Planar cell polarity signalling and development of the early mammalian nervous system

Sophie Elizabeth Pryor

Thesis submitted to University College London for the degree of Doctor of Philosophy

2013

Neural Development Unit

UCL Institute of Child Health

London

Declaration of contribution

I, Sophie Elizabeth Pryor, confirm that the work presented in this thesis is my own.

The majority of experiments were performed by me and other contributions are declared here. I was assisted by Prof. Andrew Copp during DiI labelling experiments (Chapter 4) and by Dr. Valentina Massa and Dawn Savery during neural tube explant dissections (Chapter 7).

Where information has been derived from other sources, I confirm that this has been indicated in the thesis.

_____

Sophie E. Pryor

Abstract

The vertebrate planar cell polarity (PCP) pathway is an evolutionarily conserved signalling cascade which regulates numerous developmental processes. This thesis investigates the role of PCP signalling in two events, mammalian spinal neurulation and neural crest (NC) cell migration. In mouse embryos PCP signalling is required for initiation of neural tube closure, via regulation of midline convergent extension (CE). In this thesis, a genetic modifying role for the *loop-tail* (*Vangl2*^{Lp}*)* mutation is shown to also predispose to failure of low spinal neurulation. Mutations in the core PCP gene *Vangl2* increase the frequency and severity of spina bifida in the *grainyhead-like-3* hypomorph *curly tail (Grhl3*$^{ct/ct}$*)*, a model of partially-penetrant NTDs. Affected *Vangl2*$^{Lp/+}$*;Grhl3*$^{ct/ct}$ embryos exhibit abnormalities of axis elongation, suggesting a role for CE in spinal neurulation. Investigations of the mechanism underlying the *Lp/ct* interaction reveal two distinct types of effect: 1) Effects of expression of *Vangl2*^{Lp} and *Grhl3*^{ct} in different tissues: *Vangl2* regulates midline CE and *Grhl3* regulates proliferation of tail bud progenitors. These mutant effects likely summate, leading to severe spina bifida; 2) Cell-autonomous effects of *Vangl2*^{Lp} and *Grhl3*^{ct} co-expression in the same tissue: conditional genetic experiments suggest a requirement for *Vangl2* and *Grhl3* within the same cells during neurulation and evidence for a molecular interaction at the level of Rho-GTPase signalling is presented. In amphibia and fish, early NC migration is PCP-dependent, but this has not yet been studied in mammals. *Vangl2*$^{Lp/Lp}$ embryos display normal NC cell migration, despite many severe PCP-related defects, and migration of *Vangl2*$^{Lp/Lp}$ NC *in vitro* is comparable to *Vangl2*$^{+/+}$. The closely related gene *Vangl1* does not appear to compensate for loss of *Vangl2.* Acute down-regulation of *Vangl2* specifically in the NC lineage does not cause migratory defects. Hence, the core PCP pathway is not required for early NC migration in the mouse.

Acknowledgments

Firstly, I would like to thank Andy Copp for his fantastic supervision and guidance over the last four years, and for always having time for me despite being extremely busy. I couldn't have wished for a more supportive or inspiring supervisor. I am also extremely grateful to Nick Greene for his brilliant advice and knowledge, and for putting up with me constantly popping my head around his door to ask questions!

I would like to thank all members, past and present, of the Neural Tube Defects group – I feel very lucky to have worked with such a lovely group of people. I am particularly grateful to Valentina Massa for her unending encouragement and enthusiasm and for being such a wonderful mentor to me. I am especially indebted to Dawn Savery for all things mouse-related and for patiently giving so much of her time to help me whenever I needed it. I would like to say a huge thank you to Sandra Castro and Sarah Escuin, who have both been a great inspiration to me and have taught and helped me so much. I am also grateful to the other members of my thesis committee, Paul Riley and David Wilkinson, for their helpful discussions and ideas, to all those in the Neural Development Unit who have given me advice or reagents, and to the Wellcome Trust for funding.

I am extremely thankful to my parents for providing me with so many opportunities and for their unconditional support in whatever I choose to do, and to Adam and Chloe for being such wonderful and supportive siblings! I would also like to thank the rest of my family and my amazing friends, especially Sarah and Laura for always being there and Su for all the chats and thesis-writing tips!

Finally, I am so thankful to Rich for all his love, patience and encouragement (and more recently, housework!). I couldn't have done this without him.

Table of contents

List of figures

Chapter 1 General introduction

Chapter 2 Materials and methods

Chapter 3 Severe spina bifida in the *Vangl2$^{Lp/+}$;Grhl3$^{ct/ct}$* mouse model

Chapter 4 Do *Vangl2^{Lp}* and *Grhl3^{ct}* exert distinct tissue-specific effects during spinal neurulation?

Chapter 5 Is there a molecular interaction between *Vangl2* and *Grhl3* during neurulation?

Chapter 6 A conditional genetic approach to investigate the interaction between *Vangl2* and *Grhl3*

Chapter 7 PCP and neural crest cell migration

List of tables

Chapter 1 General introduction

Chapter 2 Materials and methods

Chapter 3 Severe spina bifida in the *Vangl2*$^{Lp/+}$;*Grhl3*$^{ct/ct}$ mouse model

Chapter 4 Do *Vangl2*^{Lp} and *Grhl3*^{ct} exert distinct tissue-specific effects during spinal neurulation?

Chapter 6 A conditional genetic approach to investigate the interaction between *Vangl2* and *Grhl3*

Chapter 7 PCP and neural crest cell migration

Abbreviations

AER	apical ectodermal ridge
AFP	alpha fetoprotein
ANOVA	analysis of variance
ANP	anterior neuropore
A-P	anterior-posterior
BAC	bacterial artificial chromosome
BBS	Bardet-Biedl syndrome
BCIP	5-bromo-4-chloro-3-indolyl phosphate
BMP	bone morphogenetic protein
bp	base pair
CE	convergent extension
CIL	contact inhibition of locomotion
CNH	chordo-neural-hinge
CRL	crown-rump length
CSF	cerebro-spinal fluid
C_T	threshold cycle
DEPC	diethyl pyrocarbonate
DIG	digoxygenin
DLHP	dorsolateral hinge point
DMEM	Dulbeco's Modified Eagle Media
DMSO	dimethyl sulphoxide
DNA	deoxyribonucleic acid
dNTPs	deoxynucleotide triphosphates
dpf	days post fertilisation
DPX	dibutylphthalate polystyrene xylene
DRG	dorsal root ganglia
E	embryonic day
ECM	extra cellular matrix
EGF	epidermal growth factor
EMT	epithelial to mesenchymal transition
ENS	enteric nervous system
ENU	N-ethyl-N-nitrosourea
FBS	fetal bovine serum
FGF	fibroblast growth factor
G/A	gelatine/albumin
GAP	GTPase activating protein
GDI	guanine nucleotide dissociation inhibitor
GDP	guanosine diphosphate
GEF	guanine nucleotide exchange factor
GFP	green fluorescent protein
GTP	guanosine triphosphate
H and E	haematoxylin and eosin
HNP	hindbrain neuropore

ICM	inner cell mass
INM	interkinetic nuclear migration
JNK	Jun N-terminal kinase
LB	Luria Bertani
MHP	median hinge point
MI	mitotic index
ML	medio-lateral
MMP	matrix metalloprotease
NBT	nitro blue tetrazolium chloride
NC	neural crest
NSB	node-streak border
NTD	neural tube defect
PBS	phosphate-buffered saline
PBT	phosphate-buffered saline with 0.1% Tween-20
PCP	planar cell polarity
PCR	polymerase chain reaction
PDGF	platelet-derived growth factor
PFA	paraformaldehyde
PGC	primordial germ cell
PKC	protein kinase C
PNP	posterior neuropore
PNS	peripheral nervous system
qRT-PCR	quantitative reverse transcription PCR
RCT	randomised controlled trial
RNA	ribonucleic acid
ROCK	Rho-kinase
RQ	relative quantification
RT	room temperature
SDS	sodium dodecyl sulphate
SEM	standard error of the mean
SS	sheep serum
SSC	saline sodium citrate
TBS	tris-buffered saline
TBST	TBS with 1% Triton
TIMP	tissue inhibitor of MMP
v/v	volume per volume
VEGF	vascular endothelial growth factor
VER	ventral ectodermal ridge
w/v	weight per volume
WISH	whole mount in situ hybridisation
YFP	yellow fluorescent protein

1. General Introduction

1.1 Mammalian neurulation

During embryonic development the process of neurulation generates the neural tube, the precursor of the brain and spinal cord. The morphological events of neurulation begin during late gastrulation following the induction of the neural plate, or neuroepithelium, from a region of ectoderm on the dorsal surface of the embryo. The neural plate originates as an elliptical-shaped sheet of thickened ectodermal tissue, which is subsequently shaped and converted into a tube during two phases of neurulation, primary and secondary.

Primary neurulation generates the neural tube in the cranial and most of the spinal region and involves folding of the neuroepithelium, followed by fusion at the midline to form a closed tube (Copp et al., 2003; Greene and Copp, 2009). At low sacral and caudal levels the neural tube is formed by secondary neurulation, which does not involve bending and adhesion of neural folds. Instead, a population of mesenchymal cells within the tail bud, or caudal eminence, condense in the dorsal midline to form an epithelial rod beneath the surface ectoderm. This structure is reorganised by a process of 'canalisation' to create a secondary neural tube whose central lumen is continuous with that of the primary neural tube more rostrally (Schoenwolf, 1984). Neural tube defects (NTDs) arise when the normal processes of neurulation are disrupted (see Section 1.2).

1.1.1 Primary neurulation in the mouse

1.1.1.1 Closure sites and timing

In mammals, neural tube closure is a discontinuous process which initiates sequentially at distinct levels of the anterior-posterior (A-P) axis. Mouse neural tube closure begins at the future hindbrain/cervical boundary at embryonic day (E) 8.0 ('closure 1') and proceeds bi-directionally from this site to form the cranial and

spinal neural tube (Figure 1.1A, B). Subsequent closure events occur in the cranial region at E9: closure 2 at the forebrain/midbrain boundary, which also spreads bi-directionally, and closure 3 at the rostral end of the future forebrain, from which closure progresses caudally (Figure 1.1C). The open regions, or 'neuropores', between these sites shorten and close to form an intact tube in the cranial region by E9.5. In the spine, fusion proceeds caudally from the site of closure 1 and culminates with the closure of the posterior neuropore (PNP) at E10.5, marking the end of primary neurulation (Greene and Copp, 2009).

1.1.1.2 Shaping and folding of the neural plate

Before the onset of neural tube closure, the initially disc-shaped neuroepithelium is converted to a keyhole-shaped layer with a broad cranial area and a narrow, elongated caudal region. Different processes are thought to contribute to neural plate shaping; elongation of the pseudostratified, columnar neuroepithelial cells along their apicobasal axis contributes to narrowing, while embryonic growth contributes to the A-P elongation (Colas and Schoenwolf, 2001). Importantly, convergent extension (CE) cell movements, whereby cells intercalate mediolaterally to simultaneously narrow and lengthen to neural plate, are also essential (Ueno and Greene, 2003). As discussed later, a crucial role for the non-canonical Wnt/planar cell polarity (PCP) pathway in driving these movements has been well documented (see Section 1.4.2.1 and Chapter 4).

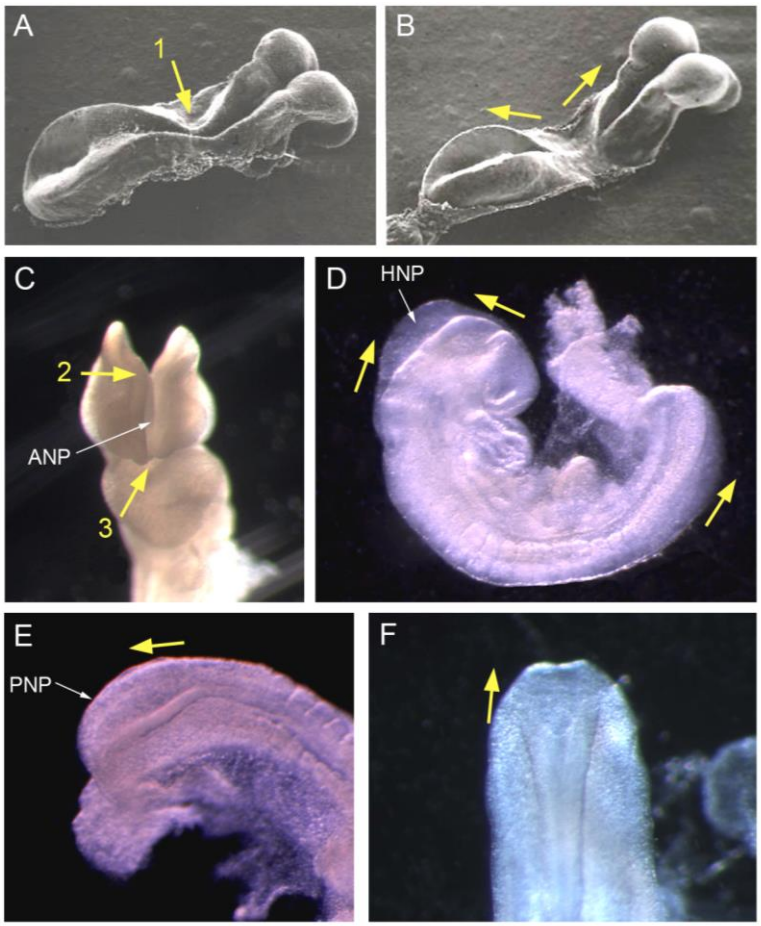

Figure 1.1 Neural tube closure is a multi-site process in mammals

Primary neurulation in the mouse embryo. (**A, B**) Closure 1 (1) occurs at the hindbrain/cervical boundary and spreads both rostrally and caudally from this site (arrows in B). (**C, D**) Two subsequent closure events occur in the cranial region (2 and 3) and progression of neurulation closes the anterior neuropore (ANP) and hindbrain neuropore (HNP). (**E, F**) Side and dorsal views of embryonic caudal regions, respectively. Spinal neurulation proceeds down the body (arrows) from the site of closure 1 to close the (PNP). A and B are modified from (Copp et al., 1990).

Neural tube closure is achieved by bending of the neuroepithelium to produce bilateral neural folds which elevate and converge towards the midline, where they meet and fuse (Figure 1.2). Bending of the neural plate varies considerably along the A-P axis. In the cranial region the neural folds initially acquire a convex

morphology, bulging outwards away from the midline, before rapidly 'flipping' around to assume a biconcave shape. The mechanisms controlling this complex bending are not well understood but are thought to involve expansion of the underlying mesenchyme and the actin cytoskeleton (Morriss-Kay, 1981). Spinal neural tube closure does not involve a biconvex phase; here, bending occurs at specific hinge points, which also vary along different levels of the neuraxis. At E8.5, bending in the upper spine is achieved solely by the formation of the median hinge point (MHP) overlying the notochord, creating a V-shaped neuroepithelium with straight neural folds (mode 1). At E9.0 the transition from mode 1 to mode 2 of neurulation, in the intermediate spine, is marked by the appearance of paired dorsolateral hinge points (DLHPs) at the point where the surface ectoderm contacts the outside of each neural fold. DLHPs bring the tips of the neural folds towards each other at the dorsal midline, producing a diamond-shaped neuroepithelium. At E10.5, when the neural tube is closing in the low spine, the MHP disappears and bending occurs solely at the DLHPs (Mode 3) (Shum and Copp, 1996).

Early studies showed that the induction of the MHP requires signals from the underlying notochord. In both mouse and chick embryos, ablation of the notochord results in loss of the MHP (Davidson et al., 1999; Smith and Schoenwolf, 1989; Ybot-Gonzalez et al., 2002), whereas pieces of notochord can induce an ectopic MHP-like bend when transplanted adjacent to the lateral neural tube (Smith and Schoenwolf, 1989). However, despite being the only site of neuroepithelial bending at E8.5, the MHP appears to be dispensable for neurulation. Following notochord ablation, spinal neural tube closure completes normally in the absence of the MHP by a 'default' mechanism involving the formation of ectopic DLHPs (Ybot-Gonzalez et al., 2002). A similar mechanism is also thought to explain the unaffected progression of neurulation in mouse embryos that lack a notochord or floor plate, such as *sonic hedgehog* (*Shh*), *Gli2* and *Foxa2* null mutants (Ang and Rossant,

1994; Chiang et al., 1996; Ding et al., 1998; Weinstein et al., 1994; Ybot-Gonzalez et al., 2002). Although *Shh* from the notochord, and later the floor plate, is required for dorsoventral patterning of the neural tube (Ulloa and Briscoe, 2007), evidence suggests that it is not the only MHP-inducing factor: *Shh*$^{-/-}$ mouse embryos are capable of forming a MHP, despite being reported to lack a floor plate (Chiang et al., 1996; Ybot-Gonzalez et al., 2002), and implanting Shh-soaked beads is not sufficient to induce a MHP in lateral E9.5 neural folds (Ybot-Gonzalez et al., 2002). Thus, it appears that the notochord also secretes other unidentified factors which induce MHP formation.

The MHP is characterised by the localised enrichment of wedge-shaped cells, which are narrow apically and expanded at their basal (non-luminal) side. This cell wedging behaviour appears to be related to interkinetic nuclear migration (INM), the process whereby nuclei move up and down between the apical and basal sides of a pseudostratified epithelium during different stages of the cell cycle (Meyer et al., 2011). Cell wedging in the MHP is correlated with the accumulation of basal, S-phase nuclei and an increase in S-phase length (Gerrelli and Copp, 1997; Smith and Schoenwolf, 1988). The mechanisms underlying the prolonged cell cycle in the MHP are not known and are currently under investigation by members of our group; of particular interest is the role of the cell cycle inhibitor, p21, which is expressed in midline neuroepithelial cells prior to floor plate differentiation (Katrin Danielsen, unpublished data). Apical constriction via the contraction of circumferential actin microfilaments has also been suggested to play a role in cell wedging (Schoenwolf and Smith, 1990). However actin microfilaments are distributed evenly along the apical surface of the neuroepithelium, irrespective of bending. Furthermore, pharmacological inhibition of the actin cytoskeleton by cytochalasin D treatment does not disrupt hinge point formation (Schoenwolf et al., 1988; Ybot-Gonzalez and Copp, 1999)

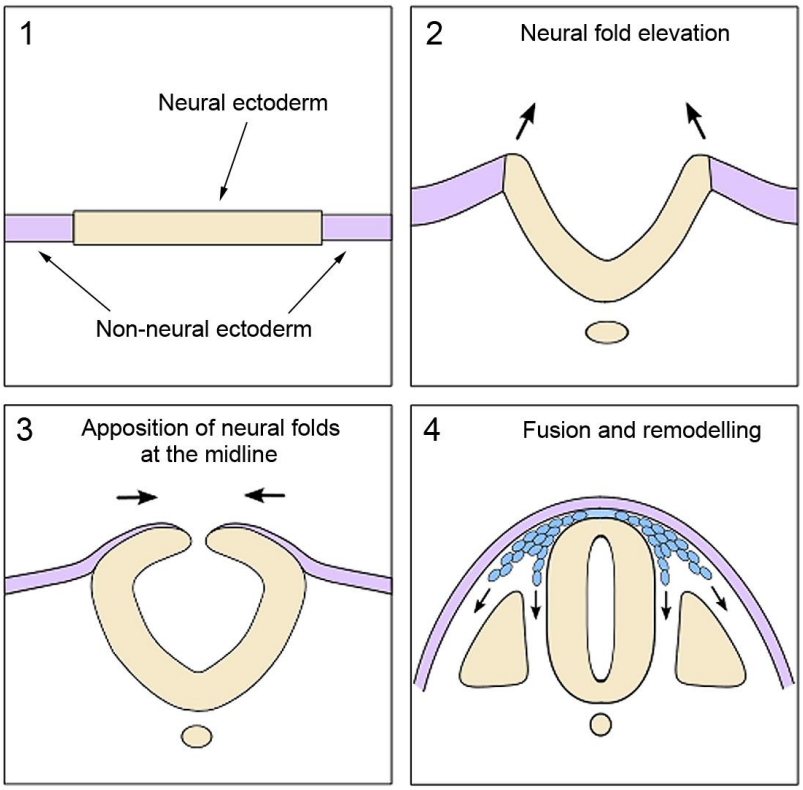

Figure 1.2 Overview of primary neurulation

Schematic diagram summarising the events of neuroepithelial bending and fusion. (**1**) Neural induction generates a thickened region of neural ectoderm, flanked by the future non-neural (epidermal) ectoderm, which undergoes shaping. (**2**) Formation and elevation of the bilateral neural folds. (**3**) The neural folds meet and appose at the dorsal midline. (**4**) Fusion of the neural folds is followed by remodelling of the neural tube and overlying ectoderm. Delamination and migration of the NC cells (blue) also begins around this stage, although the timing varies between different species and axial level (see Section 1.4.4.2).

The three stereotypical modes of neurulation mean that there is a transition from midline to dorsolateral bending as neurulation proceeds down the spine (Shum and Copp, 1996). A model has been proposed to explain the regulation of DLHP formation by the balance of antagonistic ventral and dorsal signals (Ybot-Gonzalez et al., 2007a). *Shh* is a key negative regulator of this process; the appearance of DLHPs correlates with decreasing notochordal *Shh* expression and a reduction in

strength of *Shh* signalling down the neuraxis which allows DLHPs to 'break through' when a sufficiently low threshold is reached. Furthermore, implanting Shh-soaked beads adjacent to the E9.5 neural folds suppresses DLHP formation (Ybot-Gonzalez et al., 2002). According to the model, DLHP formation is blocked during mode 1 by high levels of *Shh* from the notochord. BMP2, secreted from the dorsal surface ectoderm, also inhibits bending. In the upper spine, strong *Shh* expression from the notochord inhibits the BMP antagonist noggin, allowing BMP2 to prevent DLHP formation. In the low spine, as the level of *Shh* diminishes, noggin is de-repressed and can exert its antagonistic effects on BMP2, overcoming the inhibition of DLHPs (Ybot-Gonzalez et al., 2007a). Unlike the MHP, DLHPs are essential for the successful progression of spinal neurulation. Their absence, for example in the *Zic2* loss of function mutant, *Kumba* (*Zic2*$^{ku/ku}$), precludes neural tube closure, leading to spina bifida (Ybot-Gonzalez et al., 2007a).

1.1.1.3 Neural fold fusion

Following their bending and elevation, the neural folds become apposed at the dorsal midline. During this final stage of primary neurulation, fusion and remodelling of the two epithelia occur, resulting in an intact tube covered by future epidermal ectoderm. Several studies have described protrusions emanating from cells at the leading edge of the neural folds, which appear to extend across the gap and interdigitate as the folds contact each other (Pai et al., 2012). The nature of these protrusions appears to vary with axial level. In the spinal region, large lamellipodia-like structures, originally described as membrane ruffles, extend from the tips of the neural folds just prior to fold contact (Geelen and Langman, 1979; Pai et al., 2012; Waterman, 1976). Additionally, a recent study involving live cell imaging of the closing mouse hindbrain reported the presence of filopodia-like extensions (Pyrgaki et al., 2010). The cells from which the protrusions originate also seem to vary; ruffles apparently extend from the junction between the neural folds and ectoderm

in the trunk (Geelen and Langman, 1979; Pai et al., 2012), while in the cranial region the initial contact has been observed to be ectodermal in the midbrain and hindbrain, and neuroepithelial in the forebrain (Geelen and Langman, 1979; Pyrgaki et al., 2010). Molecularly, the regulation of these cell protrusions is poorly understood, although there is most likely a role for cytoskeletal regulation via small GTPases such as Rac1 (Camerer et al., 2010) (Ana Rolo, unpublished data).

It is unclear whether the initial contact between leading edge neural fold cells represents a distinct 'adhesion' step, or whether the mechanical bending and apposition of the neural folds is sufficient to allow their stabilisation during the subsequent remodelling phase. Studies on the role of EphA-ephrinA interactions (Abdul-Aziz et al., 2009) and the transcription factor *Grhl2* (Pyrgaki et al., 2011) do point towards an early adhesion event and future research will hopefully evaluate this further. Finally, the mechanism of remodelling of the neural tube and overlying surface ectoderm is also poorly understood. A major focus of study has been programmed cell death, however experimental evidence shows that apoptosis is dispensable for neuroepithelial fusion and remodelling in the mouse (Massa et al., 2009).

1.2 Neural tube defects

In the mouse, primary neurulation takes place around halfway through gestation, from E8.5-E10.5. If the neural tube fails to close at any of the distinct sites along the neuraxis, or closure fails to progress from these sites, it results in open neural tube defects (NTDs) (Figure 1.3). Failure of initiation of closure at the hindbrain-cervical boundary (closure 1) leads to the most severe NTD, craniorachischisis, where almost the entire neural tube from the midbrain to the low spine remains open. Incomplete closure of the cranial neural tube initially leads to exencephaly, in which the neuroepithelium appears to protrude from the developing brain. As development proceeds, the skull vault cannot form over the open region and the exposed neural tissue degenerates, leading to the appearance of anencephaly during late gestation. Failure of closure 3 is rare, but results in anencephaly combined with a 'split-face' malformation (Copp and Greene, 2010). If closure fails to progress caudally from the site of closure 1 the PNP will remain open, yielding open spina bifida which, in mice, is often accompanied by a curled or bent tail.

In human embryos, primary neurulation begins with the bending of the neural plate at 17-18 days post fertilisation (dpf) and concludes at around 28 dpf with closure of the PNP (Greene and Copp, 2009). As in mice, neural tube closure is a discontinuous process, but some differences have been reported. Events closely resembling closures 1 and 3 have been described, although the site of initial closure (at 22 dpf) appears to occur in the rhombencephalon, more rostrally than in mice (O'Rahilly and Muller, 2002). The existence of closure 2 in humans is controversial; there is evidence that an event analogous to mouse closure 2 doesn't occur, with brain formation instead achieved by the closing of a single neuropore between sites 1 and 3 (O'Rahilly and Muller, 2002). In mice, the axial level of closure 2 is known to vary between different genetic strains; those with a rostrally located closure 2 are

more highly predisposed to exencephaly, while those which exhibit closure 2 at a caudal position are more resistant. Interestingly, in the SELH/Bc strain, closure 2 appears to be absent altogether. Although 17% of these mice show exencephaly, the remaining 83% successfully complete cranial closure, demonstrating that, even in mice, it is not essential for early brain formation (Macdonald et al., 1989).

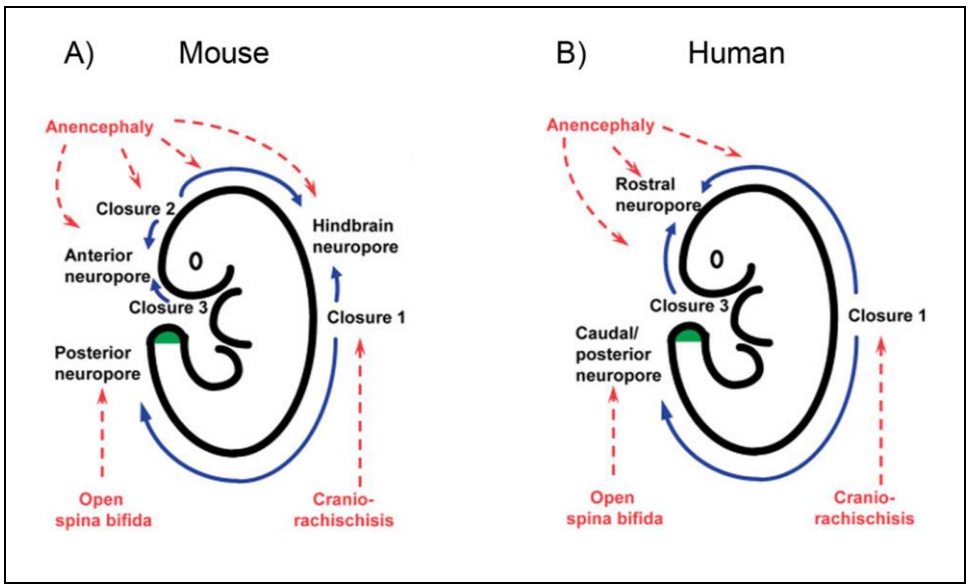

Figure 1.3 Sites of initiation of neural tube closure in mice and humans

Schematic diagram showing the multiple sites of initiation of neural tube closure in mouse (A) and human (B) embryos. Red text and arrows indicate the NTDs arising from failure of each closure event. Images taken from (Copp and Greene, 2010).

1.2.1 Classification of human NTDs

Recent estimates suggest that congenital anomalies affect approximately 2-3% of pregnancies. For example, from 2003-2007, EUROCAT (European Surveillance of Congenital Anomalies) recorded a total prevalence of major abnormalities of 24 per 1000 births (Dolk et al., 2010). NTDs are among the most common groups of birth defects, affecting 0.5-2 per 1000 established pregnancies worldwide (Copp and Greene, 2010).

1.2.1.1 Open defects

Open defects, including craniorachischisis, anencephaly and spina bifida, arise due to the primary failure of neural tube closure and are the most severe group of NTDs. Craniorachischisis is considered rare and, although the forebrain often forms normally, is incompatible with postnatal life. In anencephalic foetuses, tissue degeneration during pregnancy leads to loss of almost the entire brain by birth. Human anencephaly cases can be sub-divided into those that predominantly affect the rostral brain and skull (meroacrania) and those affecting the posterior brain and skull (holoacrania), although precisely how these defects correlate with failure of neural tube closure is unclear (Greene and Copp, 2009). Anencephaly is also lethal; affected infants are often stillborn or die shortly after birth.

Spina bifida (latin for 'split spine') represents the most common group of open NTDs and refers to the vertebral abnormalities which accompany the open lesions. Where the neural folds remains open the adjacent sclerotome cells, which normally migrate to cover the closed neural tube, cannot surround the neuroepithelium properly, leaving the midline exposed (Greene and Copp, 2009). Spina bifida varies in its clinical appearance; the more common form is myelomeningocele (spina bifida cystica), where the spinal cord tissue is contained within a meninges-covered sac which protrudes and contains cerebro-spinal fluid (CSF). Alternatively, the neural tissue may be directly exposed to the amniotic fluid, a more severe condition termed myelocele.

The survival rates of individuals with spina bifida have improved greatly, with approximately 50-90% of patients now reaching adulthood (Webb, 2010). However, the outcome of spina bifida is variable, with the severity of the condition depending on the rostral limit of the lesion. Individuals often require lifelong medical care for the numerous complications that occur; neurodegeneration frequently leads to

paralysis and loss of sensation below the lesion, while disturbed innervation of the rectum and bladder can cause incontinence and urinary tract infections (Thompson, 2009). In most cases spina bifida is accompanied by 'tethering', where the spinal cord becomes attached to the vertebral column via the surrounding tissues. Consequently, stretching of the spinal cord during growth reduces blood flow to the spinal nerves and can cause damage to the cord. Tethering, and the traction it generates on the upper spinal cord, has been suggested to contribute to Chiari II malformation, a condition where the hindbrain herniates through the foramen magnum, the large opening at the base of the skull through which the spinal cord passes (Greene and Copp, 2009). Chiari II malformation also blocks the circulation of CSF and is therefore associated with hydrocephalus, another condition that frequently accompanies spina bifida. In individuals with hydrocephalus there is an accumulation of CSF, leading to a build up of pressure and swelling of the brain. Hydrocephalus is usually treated by the insertion of a shunt to drain and divert the excess fluid, but this can itself cause problems due to blockages or infections (Thompson, 2009).

1.2.1.2 Closed and herniation defects

A milder group of NTDs, collectively referred to as closed defects, are thought to arise due to defective secondary neurulation or abnormal formation of the lower vertebrae. This group of NTDs are the least well defined, and are estimated to effect up to 10% of people, with the majority of cases being asymptomatic. Spina bifida occulta ('hidden' spina bifida) comprises the absence of one vertebra arch and is a variant of normal, although there may be visible signs on the lower back, such as a skin dimple or a patch of hair. Alternatively, 'spinal dysraphism' (thought to relate to defective secondary neurulation) comprises absence of two or more vertebral arches and is often associated with neurological abnormalities such as splitting or tethering of the lower cord. A third class of malformations, herniation defects, are

thought to arise later than open NTDs, after neural tube closure is complete. These conditions are characterised by the secondary herniation of neural tissue through a region of the skull or vertebral column, although the developmental basis of the bone defects are unclear. In the cranial region, the term ‘encephalocele’ refers to the protrusion of meninges, with or without brain tissue, through an opening in the skull, usually in the occipital region. In the spine, herniation of the meninges is called ‘meningocele’, which likely involves defective formation of the vertebrae around the closed neural tube (Copp and Greene, 2012).

1.2.2 Aetiology

NTDs appear to follow a ‘multifactorial’ pattern of inheritance, whereby interactions between multiple genes and environmental factors summate to increase the risk of the conditions (Juriloff and Harris, 2012a).

1.2.2.1 Genetic factors

The majority of NTD cases occur sporadically in families with no previous history. However, several lines of evidence indicate a genetic component in the causation of NTDs. Firstly, studies of recurrence rates within families have shown the risk of NTDs among siblings of affected individuals to be 2-5%, approximately 50-fold higher than in the general population, and this is increased further if two siblings are affected. Furthermore, concordance rates for spina bifida and anencephaly are higher in same sex twins (presumed to be monozygotic) than in opposite-sex twins (dizygotic) (Copp and Greene, 2010). NTDs also occur with chromosomal abnormalities such as aneuploidies, duplications and deletions, and have been reported in foetuses with abnormal karotypes that have spontaneously aborted (Zohn, 2012). These cases often represent one phenotypic feature of a syndrome, although it is estimated that less than 10% of human NTD cases are syndromic.

Although a strong genetic contribution is apparent, very few genes associated with NTD risk in humans have been identified to date. The sporadic nature of NTDs, along with the lethality of most forms, means there is a lack of large families with multiple affected individuals for analysis. Nevertheless, positional cloning studies have identified candidate risk loci on chromosomes two, seven and ten (Rampersaud et al., 2005; Stamm et al., 2006). The search for candidate genes has largely focused on those encoding proteins involved in folate metabolism; particularly the enzyme 5,10-methylenetetrahydrofolate reductase (*MTHFR*), for which polymorphisms have been identified. One variant, 677C>T, has been associated with increased NTD risk in some populations, although in others an association is not present or is in fact protective (Amorim et al., 2007).

Cohorts of case samples have also been screened for mutations in other genes that are known to cause NTDs in mice. In particular several putative mutations, defined as rare, nonsynonymous (amino acid-altering) sequence variants with possible defective function that are not present in controls (Juriloff and Harris, 2012a) have been identified in core PCP genes. For spina bifida cases, putative mutations have been identified in *VANGL2*, *VANGL1*, *CELSR1*, *FZD6* and *PRICKLE1* (Allache et al., 2012; Bosoi et al., 2011; De et al., 2012; Kibar et al., 2007; Kibar et al., 2009; Kibar et al., 2010). Anencephalic foetuses have been found to carry mutations in *VANGL2* (Lei et al., 2010) and craniorachischisis cases have been associated with mutations or intronic duplications in *VANGL2, CELSR1* and *SCRIBBLE* (Doudney et al., 2005; Robinson et al., 2012). Nonsynonymous PCP gene variants have also been identified in cases of closed NTDs (Juriloff and Harris, 2012a).

1.2.2.2 Non-genetic factors

Teratogenic agents have been recognised to increase the risk of NTDs. For example, valproic acid, a widely-used anti-epileptic drug, is associated with an

elevated risk of spina bifida when taken during the first trimester of pregnancy (Jentink et al., 2010). Agents that interfere with folate uptake also exacerbate NTD risk, such as the antibiotic trimethoprim, carbamazepine (another anti-convulsant) and the mycotoxin fumonisin (Copp and Greene, 2010). Fumonisin is produced by common maize-contaminating fungi and has been associated with higher NTD prevalence in populations that rely heavily on maize as a dietary staple (Gelineau-van et al., 2009). Maternal health during pregnancy is also correlated with NTD occurrence; diabetes mellitus and obesity are risk factors, as is hyperthermia following fever or excessive sauna use during the first few weeks of pregnancy (Kondo et al., 2009; Moretti et al., 2005). Some studies have reported a link between increased NTD risk and low socioeconomic status, with factors such as maternal education, household income and parental occupation being associated with NTD occurrence in offspring. Other studies have also examined the effect of ethnicity and parental age (Au et al., 2010).

Maternal nutritional status has received considerable interest, first being linked to NTDs following the Dutch Hunger Winter of 1944-1945, when increased NTD prevalence was seen in offspring of women exposed to famine during early pregnancy (Schorah, 2009). Research has predominantly focused on folates, the biological derivatives of the vitamin folic acid (see Section 1.2.3). The precise relationship between maternal folate levels and NTD risk is not fully understood; reduced serum folate and elevated plasma homocysteine (indicators of suboptimal folate status) are considered risk factors and are observed in mothers of some affected foetuses. However, for most NTD-affected pregnancies maternal folate levels fall within the ‘normal’ range (Kirke et al., 1993; Scott, 1999; Steegers-Theunissen et al., 1994). These findings led to the theory that low folate status may increase susceptibility to NTDs when combined with another environmental factor or in genetically predisposed individuals, a hypothesis which has recently been

strengthened by work in animal models (Burren et al., 2008; Burren et al., 2010). Besides folates, deficiency for two other vitamins, inositol and vitamin B12, are risk factors (Groenen et al., 2003; Kirke et al., 1993), as is high vitamin A intake (Rothman et al., 1995).

1.2.3 Treatment and prevention

Spina bifida is usually treated by surgical closure of the lesion shortly after birth, to prevent meningitis and further neurodegeneration (Thompson, 2009). Studies of mouse models of spina bifida have shown that, although failure of neural tube closure leads to neurodegeneration and loss of neurological function during late gestation, the development of the exposed spinal cord is essentially normal during early pregnancy (Stiefel et al., 2007). Such findings suggested that covering the exposed spinal cord during development might alleviate or prevent neurodegeneration and therefore provided a rationale for performing *in utero* surgery. These operations are now performed in a few specialist centres; recent assessments of outcome suggest prenatal repair can improve neurological function and hydrocephalus, but is associated with increased risk of preterm delivery (Adzick et al., 2011; Saadai and Farmer, 2012).

Over the last thirty years, primary prevention of NTDs has been a major public health issue. In the 1980s an early trial found that supplementation of women with a multivitamin preparation containing folic acid reduced NTD prevalence, although the specific effects of individual compounds were not evaluated (Smithells et al., 1981). In 1991 the MRC Vitamin Study Research Group published the findings of their pivotal study, the first randomised, placebo-controlled trial (RCT) which demonstrated that periconceptional folic acid supplementation can prevent up to 72% of NTD recurrences (MRC, 1991). Their findings were strengthened further by

the results of a Hungarian RCT demonstrating prevention of the first occurrence of NTDs by folic acid (Czeizel and Dudas, 1992) and a Chinese study showing a large decrease in NTD prevalence after introducing folic acid supplements (Berry et al., 1999). These early studies provided the impetus for international campaigns to increase dietary folate intake. In 1998 the U.S. and Canada were the first countries to introduce mandatory fortification of flour with folic acid, followed by Chile in 2000.

Today around 50 countries, including some in Africa, the Middle East, Oceania and most of America, have mandatory fortification policies. A significant decline in NTD prevalence has been seen in several of these countries post-fortification, although not in all (Crider et al., 2011; Ricks et al., 2012). In Europe, while the voluntary addition of folic acid to food products is widespread, most countries have been reluctant to introduce universal fortification. Since 1992, the UK government has recommended that all women who could become pregnant consume more folate-rich foods and supplement their diet with 0.4 mg folic acid before conceiving and until the twelfth week of pregnancy. Unfortunately these policies have been largely unsuccessful at reducing NTD rates and many women remain unprotected (Lane, 2011).

There is evidence that, even if folate levels were successfully increased in all women of child-bearing age, not all NTD cases would be prevented. No human trial has found a 100% prevention of NTDs with folic acid and there appears to be a 'floor effect' in countries that have adopted fortification policies (Heseker et al., 2009). The identification of folate-resistant animal models also implies that a proportion of human NTDs do not respond to folic acid therapy (Harris, 2009). Excitingly, the vitamin inositol is emerging as a candidate therapeutic agent for the prevention of folate-resistant NTDs (Cavalli et al., 2008). In animal studies, inositol deficiency during culture of both mouse and rat embryos increases the frequency of

cranial NTDs (Cockroft, 1988; Cockroft et al., 1992), while its administration significantly reduces the frequency of spinal NTDs in *curly tail* mouse embryos (see Section 1.3.1.2) (Cogram et al., 2002; Greene and Copp, 1997). A pilot RCT to examine the potential preventive effects of inositol is currently underway.

1.3 Modelling NTDs in the mouse

Experimental animals have provided valuable insights into the developmental events of neurulation. The mouse embryo in particular offers several advantages; the process of neurulation in mice and humans is closely similar, the accessibility of embryos during neural tube closure allows analysis of the fundamental mechanisms, and the ability to culture whole embryos throughout neurulation allows experimental and chemical manipulations which would not otherwise be possible in a mammalian system. Importantly, the abundance of mouse models of NTDs means different combinations of mutant alleles and environmental influences can be studied, in order to determine the role of gene-gene and gene-environment interactions in both normal and abnormal neural tube closure. There are currently over 240 genetic mouse models of NTDs, a figure that highlights the complexity of neurulation and the large number of cellular and morphological processes required for successful neural tube closure (Harris and Juriloff, 2007; Harris and Juriloff, 2010). This group includes mutants that display defects in neural plate shaping, in bending and elevation of the neural folds, and in the final stages of fusion and remodelling.

The analysis of mouse mutants has identified several key biological processes during neurulation. For example, regulation of the balance between continued neuroepithelial cell proliferation and neuronal differentiation appears to be important for successful neurulation. Mutations in *neurofibromin1* (*Nf1*) and *nucleoporin* (*Nup50*), which negatively regulate cell cycle inhibitors, cause exencephaly, while loss of *Pax3*, which promotes proliferation in the dorsal neuroepithelium, causes both spina bifida and exencephaly. NTDs are also seen when negative regulators of Notch signalling such as *Hes1* and *Hes3* are mutated; these are normally required to prevent premature differentiation (Copp and Greene, 2010). The role of apoptotic

cell death during neurulation is somewhat controversial. A characteristic pattern of dying cells is observed within the neural tube during its formation, particularly in dorsal regions during closure and post-fusion remodelling (Massa et al., 2009; Yamaguchi et al., 2011). A requirement for apoptosis was suggested by studies showing that suppression of apoptosis in chick leads to failure of neural tube closure (Weil et al., 1997) and from the appearance of cranial NTDs in mice when genes such as *Caspase3*, *Caspase9* and *Apaf1* are mutated (Copp and Greene, 2010). However, despite the lack of apoptosis in *Caspase3*$^{-/-}$ and *Apaf1*$^{-/-}$ mouse knockouts, neurulation in the forebrain and spinal region completes normally. Furthermore, chemical suppression of apoptosis in wild type embryos during culture does not disrupt neurulation (Massa et al., 2009).

The actin cytoskeleton also plays an important role during neurulation, particularly in the cranial region. NTDs have been observed in mice carrying mutations in several genes encoding cytoskeletal proteins, such as *Vinculin* and *Shroom*, or cytoskeleton-associated proteins, such as *Palladin* and *Marcks.* (Copp and Greene, 2010). Strikingly, most of these models exhibit exencephaly alone; only *Shroom* and *Mlp* (*Marcks-like protein*) mutants also develop spina bifida (Hildebrand and Soriano, 1999; Wu et al., 1996). The relative resistance of spinal neurulation to cytoskeletal disturbance has also been demonstrated pharmacologically; while culturing embryos with cytochalasin D, which disrupts actin polymerisation, inhibits cranial neurulation, closure of the PNP is unaffected (Ybot-Gonzalez and Copp, 1999). Recent work in our group has also shown that treatment with blebbistatin, which inhibits the formation of contractile actomyosin, does not adversely affect PNP closure. However, inhibition of Rho-kinase (ROCK) does inhibit spinal neurulation and is associated with an abnormal apical accumulation of actomyosin and components of the apical junction complex (Sarah Escuin, unpublished data).

Thus, although cranial neurulation is more dependent on the cytoskeleton, it appears that its regulation does also contribute to neural tube closure in the spine.

Mouse NTD models also allow the mechanisms underlying the protective effect of agents such as folic acid to be investigated. A number of mutants are described as 'folate-responsive', in that varying proportions (35-85%) of NTDs in these strains can be prevented by maternal administration or treatment in whole embryo culture (Greene and Copp, 2005; Harris, 2009). The most extensively studied folate-responsive NTD mutant is *Splotch* (*Sp* and *Sp2H*) which carries a null allele of the transcription factor *Pax3*. Homozygous *Splotch* embryos develop spina bifida with a penetrance of 85-100% and show variable rates of exencephaly (Greene et al., 2009). Studies have reported a reduction of both cranial and spinal NTDs in *Splotch* following folic acid treatment, by approximately 20% and 40%, respectively (Burren et al., 2008; Fleming and Copp, 1998; Wlodarczyk et al., 2006). Other folate-responsive models are *Cart1*-null and *Cited2*-null mice, the *Lrp6* hypermorph *Cd* and the *Gcn5* hypomorphic mutant (Harris, 2009).

However, similar to the folic acid resistance in an estimated 30% of human NTD cases, several mouse NTD models do not respond to folic acid treatment. These include *Ephrin-A5* knockouts, *Axial defects* (*Axd; Grhl2* hypermorph) and *curly tail* (*ct*; *Grhl3* hypomorph) (Greene and Copp, 2005). For some of these mutants, the effect of other agents has been examined. For example, methionine supplementation was found to prevent approximately 40% of spinal NTDs in *Axd* (Essien and Wannberg, 1993). In *curly tail* mice, which do not respond to either folate or methionine, a protective effect was found for inositol (see Section 1.3.1.2).

1.3.1 The *curly tail* mouse model

1.3.1.1 NTDs in *curly tail*

The *curly tail* (*ct*) mouse mutant was first described nearly 60 years ago (Gruneberg, 1954) and has since become one of the most widely studied models of partially penetrant NTDs. Homozygous *curly tail* (*ct/ct*) embryos develop apparently normally (closed neural tube and straight tail) in approximately 40-60% of cases and the remaining proportion display NTDs comprising tail flexion defects alone (40-50%) or tail defects with lumbosacral spina bifida (10-20%). Up to 5% of *ct/ct* embryos also exhibit exencephaly. Although variations in penetrance of the *curly tail* phenotype have been reported by different groups over the years, the overall incidence of NTDs has remained at around 50-60% (Gustavsson et al., 2008).

The developmental mechanism underlying the spinal defects in *curly tail* has been well characterised (Figure 1.4). Affected *ct/ct* embryos exhibit a delay or failure of PNP closure which lead to tail defects (curled and often shortened tail) or spina bifida, respectively (Copp, 1985; Van Straaten et al., 1992). Early studies showed that at E10.5, the time when delayed PNP closure can be first detected, abnormal embryos display an abnormally low rate of cell proliferation specifically in the hindgut and notochord tissues (Copp et al., 1988a; Peeters et al., 1998b). This leads to a reduction in the growth rate of the ventral tissues, creating a dorsal-ventral growth imbalance and causing excessive axial curvature in the caudal region of the embryo. In turn, the increase in ventral curvatures generates mechanical stress which opposes, and therefore delays, neural tube closure at the level of the PNP (Brook et al., 1991; Peeters et al., 1997). As described elsewhere, spinal NTDs in *curly tail* can be rescued by physically correcting the ventral curvature, or by normalising the balance between dorsal and ventral growth rates (see Chapter 3).

1.3.1.2 Similarities between *curly tail* and human NTDs

Curly tail is particularly valuable as a model for human NTDs as there are several parallels between the mutant phenotype and the human conditions. One notable similarity is the difference in NTD occurrence between the two sexes: as in human fetuses, cranial NTDs predominantly affect female *curly tail* embryos, while spina bifida is seen slightly more often in males (Juriloff and Harris, 2012b; Van Straaten and Copp, 2001). NTDs in *curly tail* are also associated with increased levels of alpha fetoprotein (AFP) in the amniotic fluid and maternal serum (Adinolfi et al., 1976) a biomarker of NTDs during human pregnancy (Cameron and Moran, 2009; Krantz et al., 2010). The penetrance of the *curly tail* phenotype is influenced by environmental factors such as temperature, anti-mitotic drugs, retinoic acid and nutrient levels which, along with the identification of modifier genes (see below), are indicative of multifactorial causation. Thus, *curly tail* appears to be a model for the complex aetiology of NTDs in humans.

The resistance of *curly tail* NTDs to folic acid highlights it as a potential model for the subset of human NTDs that don't respond to folic acid supplementation. Interestingly, a protective effect of inositol has been demonstrated for spinal NTDs in *curly tail,* both in whole embryo culture and *in vivo* by maternal administration (Cogram et al., 2002; Greene and Copp, 1997). Two inositol isomers have been evaluated; the naturally occurring form, *myo*-inositol, was found to prevent around 50% of spinal NTDs when given to pregnant mice, while *chiro*-inositol was more effective, reducing the NTD frequency by up to 86% (Cogram et al., 2002). The mechanism of inositol action is most likely regulated via the downstream mediator protein kinase C (PKC), whose isoforms are ubiquitously expressed in mouse embryos during spinal neurulation. Ultimately, the phosphorylation of substrates downstream of PKC appears to specifically stimulate proliferation in the hindgut,

correcting the *curly tail* growth imbalance and normalising spinal neurulation (Cogram et al., 2004).

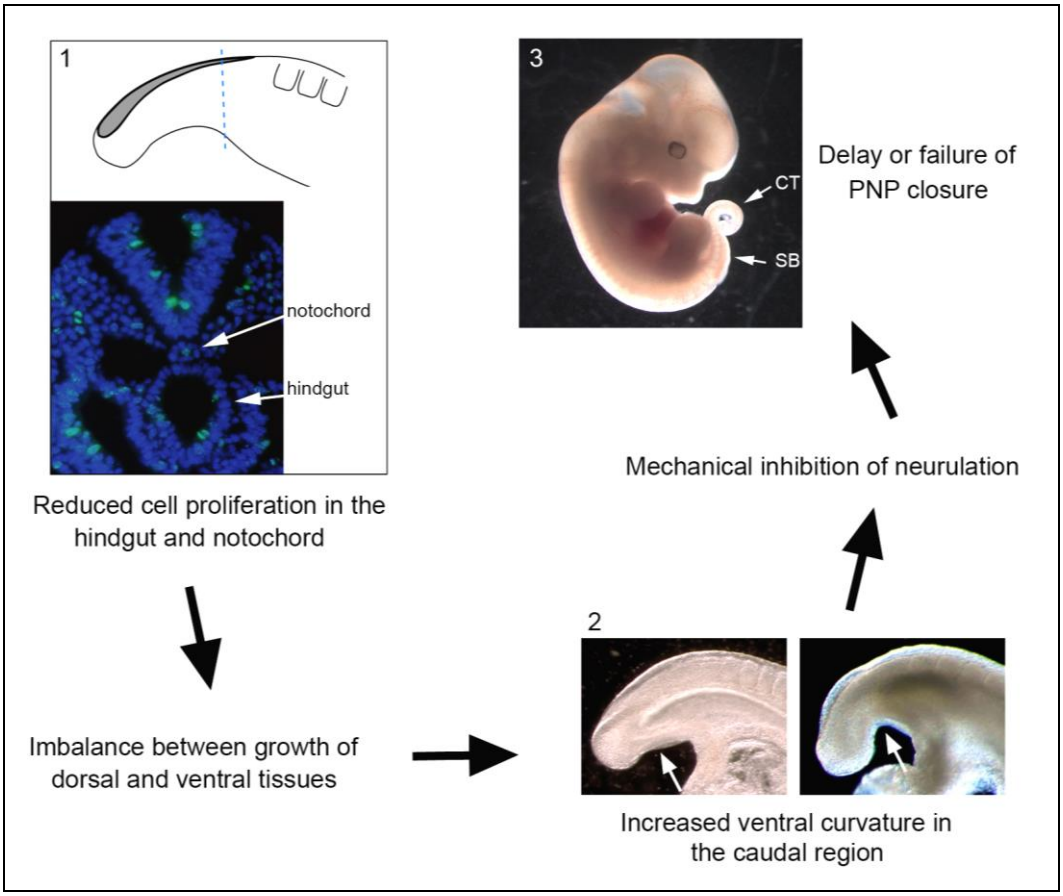

Figure 1.4 Developmental basis of *curly tail* spinal NTDs

Schematic diagram showing the mechanism underlying the delay or failure of spinal neurulation in affected *curly tail* embryos.

1.3.1.3 *ct* is a hypomorphic allele of *Grhl3*

Despite many studies of the *curly tail* phenotype, the major genetic defect remained undiscovered for many years. Mapping studies independently localised the *ct* gene to the distal region of mouse chromosome four (Beier et al., 1995; Brouns et al., 2005; Neumann et al., 1994), at a position which also contains *Grhl3*. *Grhl3* arose as a strong candidate for the *ct* gene when *Grhl3* null (*Grhl3*$^{-/-}$) embryos were found to exhibit fully penetrant spina bifida combined with reduced ventral proliferation in

the E9.5 caudal region, and low frequency exencephaly (Ting et al., 2003a). This study also reported genetic interaction between *Grhl3*$^{-}$ and *curly tail*: *Grhl3*$^{-/ct}$ mice displayed a higher incidence of spina bifida than *ct/ct* and a lower incidence than *Grhl3*$^{-/-}$. Although this result did suggest that *Grhl3* was the *ct* gene, it should be pointed out that *ct* also interacts with mutations in other genes (see Section 1.3.1.6) so the finding cannot be taken as definitive proof of allelism. *Curly tail* mice do not carry a mutation within the *Grhl3* coding sequence (Gustavsson et al., 2007; Ting et al., 2003a), however a mutation in a putative enhancer region, comprising a single nucleotide substitution approximately 21 kb upstream of the *Grhl3* start site, has been identified (Gustavsson et al., 2007). This study also showed *Grhl3* to be expressed in the hindgut of wild type embryos from the 25-26 somite stage, corresponding precisely with the time and location of the *curly tail* cell proliferation defect. Moreover, *ct/ct* embryos display reduced *Grhl3* expression in this region of the embryo during late neurulation (Gustavsson et al., 2007).

The hypothesis that spina bifida in *curly tail* results from insufficient *Grhl3* levels was tested by reinstating *Grhl3* expression in *ct/ct* embryos via a bacterial artificial chromosome (BAC). Transgenic *curly tail* embryos showed a complete rescue of the spinal NTD phenotype, along with a up-regulation of *Grhl3* and a higher mitotic index in the hindgut (Gustavsson et al., 2007). In summary, chromosome mapping, gene expression studies, the severe NTD phenotype in *Grhl3*-null embryos and the normalisation of *curly tail* neurulation by increasing *Grhl3* expression strongly support the theory that *ct* is a hypomorphic allele of the *Grhl3* gene.

1.3.1.4 Modifier genes in *curly tail*

The penetrance of the *curly tail* phenotype varies with different genetic backgrounds, suggesting that it is influenced by the presence of modifier genes (Van Straaten and Copp, 2001). Early studies identified three modifier loci that

mapped to chromosomes 3, 5 and 17, but the identity and function of these genes remain unknown (Letts et al., 1995; Neumann et al., 1994). Interestingly, one of these early studies also observed tail defects in a small proportion of heterozygous (*ct/*+) embryos implying that, despite the incomplete penetrance in homozygotes, the *ct* mutation can display dominance when inherited with particular combinations of modifiers. This finding suggested that *ct* should be thought of as a semi-dominant mutation rather than a recessive allele, as it had been previously considered (Neumann et al., 1994).

Recently, *lamin B1* was identified as a key modifier gene for NTDs in *curly tail* mice (de Castro et al., 2012). *Lamin B1* lies on mouse chromosome 18 and codes for a component of the nuclear lamina, a protein complex that lies beneath the inner nuclear membrane and serves many functions, including structural support and cell cycle regulation. *Curly tail* mice were found to carry a polymorphic variant of *lamin B1*, containing only eight glutamic acid repeat sequences compared with the normal nine repeats in wild type background-matched mice and several other wild type strains. The '8E' lamin B1 protein displayed reduced stability, was associated with abnormal nuclear morphology *in vitro* and caused reduced proliferative capacity, both in cultured cells and in embryos. When sub-strains of *curly tail* mice, carrying the different *lamin B1* variants, were generated, spina bifida and exencephaly frequency were significantly lower in the presence of the 9E (wild type) alleles compared with the 8E (mutant) variants. Thus, the mutated form of *lamin B1* confers a higher risk of NTDs in *curly tail* embryos and therefore represents a major modifier locus (de Castro et al., 2012).

1.3.1.5 *Grainyhead-like* transcription factors

Grhl3 is a member of a transcription factor family with homology to the *Drosophila grainyhead* gene (*grh*; also known as *NTF-1* or *Elf-1*). In the fly, *grh* was originally

identified as a transcriptional regulator of *Dopa decarboxylase* (*Ddc*), and has been found to play early roles in embryo patterning and later functions during neurogenesis and cuticle development (Bray et al., 1988; Wilanowski et al., 2002). The importance of *grh* during *Drosophila* development is highlighted by the embryonic lethal phenotype of mutant embryos, which also show the characteristic granular appearance of the head skeleton, flimsy cuticles and patchy tracheal tubes (Bray and Kafatos, 1991). Interestingly overexpression of *grh* causes failure of dorsal closure, the process of contact and fusion between two regions of epidermis on the dorsal surface of the embryo (Attardi et al., 1993), which has parallels with epithelial morphogenetic events such as neural tube closure and wound healing in vertebrates (Jacinto et al., 2002).

Three *grainyhead-like* family members have been identified in mammals: *Grhl1* (also called *mammalian grainyhead; MGR*), *Grhl2* (*brother of mammalian grainyhead; BOM*) and *Grhl3* (*sister of mammalian grainyhead; SOM*, or *grainyhead-like epithelial transactivator; Get1*). The proteins encoded by these three genes contain highly conserved DNA binding, protein dimerisation and activation domains, and can form homodimers and heterodimers (Kudryavtseva et al., 2003; Ting et al., 2003b; Wilanowski et al., 2002). Mouse *Grhl* genes show distinct patterns of expression during development; in particular they are highly expressed in regions of the surface ectoderm and developing epidermis, as well as in organs such as the heart, lungs, kidneys and gastro-intestinal tract (Auden et al., 2006).

Mice lacking *Grhl1* exhibit delayed hair growth, and later display coat loss due to defective anchoring of hairs within the follicles (Wilanowski et al., 2008). The recent generation of *Grhl2*-null alleles has demonstrated its crucial role during neurulation. *Grhl2*$^{-/-}$ embryos show fully penetrant cranial exencephaly and spilt face. When they die at approximately E11.5 they also display an open PNP, which would most likely

progress to spina bifida if they survived (Rifat et al., 2010). Embryos that are homozygous for either of two independently generated *Grhl2* gene trap alleles also exhibit 100% cranial NTDs and either fully penetrant or highly frequent (88%) spina bifida (Brouns et al., 2011; Werth et al., 2010). For one of these gene trap strains, a low occurrence of cranial NTDs was also reported in heterozygous (*Grhl2*$^{gt/+}$) mice (Brouns et al., 2011). Thirdly, 100% exencephaly was observed in an ENU-generated strain (*Grhl2*$^{1Nisw/1Nisw}$), although spinal neurulation was reported to occur normally in these embryos (Pyrgaki et al., 2011).

Overexpression of *Grhl2* also exerts deleterious effects on neurulation, as shown by characterisation of the *Axial defects* (*Axd*) mouse mutant. *Axd* arose spontaneously over 20 years ago and was only recently identified as a likely hypermorphic *Grhl2* allele (Brouns et al., 2011). Homozygous *Grhl2*$^{Axd/Axd}$ embryos display fully penetrant spina bifida, while tail defects are seen in a proportion of *Grhl2*$^{Axd/+}$ embryos. When *Axd/Grhl2*^{genetrap} compound heterozygotes were generated, a significant reduction in PNP length was observed compared with *Grhl2*$^{Axd/+}$ embryos, demonstrating that reducing *Grhl2* expression to near-wild type levels acts to normalise spinal neurulation (Brouns et al., 2011). The role of *Grhl2* during neurulation is not well understood, but there is emerging evidence that it regulates cell adhesion during the final stage of neural fold fusion (Pyrgaki et al., 2011; Werth et al., 2010).

Evidence for a key role of *Grhl3* during neurulation was provided by the generation of two mouse lines carrying null alleles. In the first study, homozygous embryos exhibited 100% thoracolumbosacral spina bifida and 2% exencephaly, while heterozygous embryos were indistinguishable from wild type controls (Ting et al., 2003a). The second group also observed fully penetrant spina bifida in *Grhl3*$^{-/-}$ embryos, but in this case the incidence of exencephaly was 14% (Yu et al., 2006). The reason for the difference in cranial NTD frequency is unclear, but could be due

to variation in the genetic background of the strains. Indeed, the cellular basis of exencephaly in *curly tail* and *Grhl3*-null embryos has not been elucidated; it may be related to the expression of *Grhl3* in the ventral forebrain at E8.5-E9.5 (see Chapter 5 for a detailed description of *Grhl3* expression during neurulation). Recent work in our lab has shown that over-expression of *Grhl3* can also prevent spinal neural tube closure. When *curly tail* embryos are made doubly transgenic for the *Grhl3*-containing BAC mentioned earlier ($ct^{TgGrhl3}/ct^{TgGrhl3}$), a significant increase (estimated to be ~70%) in spina bifida frequency is observed compared to *ct/ct* embryos (Sandra C.P. De Castro, unpublished data). Thus, insufficient or excessive *Grhl3* promotes failure of neurulation.

In addition to its role in neural tube closure, *Grhl3* is required during skin development in mice. $Grhl3^{-/-}$ embryos display defective epidermal terminal differentiation, with an increased number of cell layers, abnormal cellular morphology and impaired formation of the epidermal barrier (Ting et al., 2005; Yu et al., 2006). Null mutants also exhibit failed wound healing at both embryonic and adult stages (Ting et al., 2005). Expression profiling experiments revealed altered expression of several key epidermal genes in $Grhl3^{-/-}$ embryos, including those encoding structural proteins, enzymes involved in lipid metabolism and cell adhesion molecules. In particular, the cross-linking enzyme *transglutaminase 1* (*TGase1*) was identified as a direct downstream target of *Grhl3* (Ting et al., 2005; Yu et al., 2006). Open eyes were also observed in a proportion of E18.5 $Grhl3^{-/-}$ embryos (Yu et al., 2006), indicating a failure or delay of eyelid closure during development. A subsequent study found that this phenotype was fully penetrant in $Grhl3^{-/-}$ at E16.5, the stage at which the two nascent eyelid epithelia normally meet over the centre of the developing cornea and fuse (Yu et al., 2008). *Grhl3* was found to be highly expressed in keratinocytes at the leading edges of the eyelid epithelia, reminiscent of its activation in migratory cells at the epidermal wound

front. Further examination of mutant eyelids demonstrated a role for the gene in actin polymerisation and formation of cellular protrusions at the leading edges (Yu et al., 2008). Finally, *Grhl3* is also required during terminal differentiation of the stomach epithelium and bladder urothelium (Yu et al., 2006; Yu et al., 2009).

1.3.1.6 Interactions between *Grhl3* and other genes during neurulation

Several studies have examined the effects of combining mutations in *Grhl3* with those in other genes. Genetic interactions between *Grhl3* and *Grhl2* have been reported; while embryos heterozygous for either null allele develop normally, NTDs are observed in compound heterozygotes and for other allelic combinations (see Table 1.1) (Rifat et al., 2010). The $Grhl3^{ct}$ and $Grhl2^{Axd}$ alleles also interact genetically, with a 2.5-fold increase in tail defects seen in $Grhl3^{ct/+};Grhl2^{Axd/+}$ embryos compared with $Grhl3^{ct/+};Grhl2^{+/+}$ (Brouns et al., 2011).

Years before the identification of *Grhl3* as the major *ct* gene, *curly tail* was found to interact with *splotch* mutations (Estibeiro et al., 1993). While $Grhl3^{ct/+}$ and $Pax3^{Sp/+}$ embryos rarely display spinal abnormalities, 10% of compound heterozygotes develop tail flexion defects. Backcrosses of these animals to *curly tail* homozygotes also generated offspring with spina bifida; embryos with the $Grhl3^{ct/ct};Pax3^{Sp/+}$ genotype were estimated to develop spinal NTDs (spina bifida or curled tail) in almost all cases. The interaction between *curly tail* and *splotch* was not due to the exacerbation, by either allele, of the mutant effect caused by the other, suggesting that it instead represents a summation of the two effects, which promotes failure of spinal neurulation (Estibeiro et al., 1993).

Another gene known to interact with *Grhl3* is the transcriptional co-regulator *Lmo4* (*LIM domain-only 4*) (Yu et al., 2006). *Lmo4*-null mice die at birth and display

incompletely penetrant exencephaly (Lee et al., 2005). *Grhl3*$^{-/-}$;*Lmo4*$^{-/-}$ mice were found to develop 100% exencephaly, which was significantly more frequent then in either *Grhl3*$^{-/-}$ or *Lmo4*$^{-/-}$ single knockouts (14% and 55%, respectively) (Yu et al., 2006). In a later study, the loss of one *Grhl3* allele in *Lmo4*-null embryos increased the incidence of exencephaly from 58% in *Grhl3*$^{+/+}$;*Lmo4*$^{-/-}$ to 70% in *Grhl3*$^{+/-}$;*Lmo4*$^{-/-}$ and was also associated with spinal NTDs, which were not observed in either *Grhl3*$^{+/+}$;*Lmo4*$^{-/-}$ or *Grhl3*$^{+/-}$;*Lmo4*$^{+/-}$ embryos (Hislop et al., 2008). Finally, and of particular interest in this thesis, *Grhl3*^{ct} and *Grhl3*$^{-}$ interact during neurulation with mutations in *Vangl2*, a core member of the planar cell polarity (PCP) signalling pathway (Caddy et al., 2010; Stiefel et al., 2003; Stiefel et al., 2007). These interactions are investigated in subsequent chapters of this thesis.

Mutant genotype	NTD phenotype
Grhl2$^{+/-}$;*Grhl3*$^{+/-}$	EX (5%), SB (low sacral; 6%)
Grhl2$^{+/-}$;*Grhl3*$^{-/-}$	EX (mid+hindbrain; 100%) SB (thoracolumbosacral; 100%)
Grhl2$^{-/-}$;*Grhl3*$^{+/-}$	EX and split face (100%) SB (thoracolumbosacral; 100%)
Grhl2$^{-/-}$;*Grhl3*$^{-/-}$	EX and split face (100%) SB (thoracolumbosacral; 100%)

Table 1.1 NTD frequencies in embryos carrying *Grhl2* and *Grhl3* null alleles

(Rifat et al., 2010)

1.4 The planar cell polarity pathway

The term planar polarity was first used in the 1980s to describe the coordinated orientation of cells within the plane of epithelia, perpendicular to the apico-basal axis. The phenomenon has been most extensively studied in the fruitfly *Drosophila*, where it manifests as the precisely ordered arrangement of cuticular structures, such as the distally-orientated trichomes (stubbly hairs) produced by wing cells, the ommatidia (light-sensing units) of the compound eye and bristles on the legs. At the cellular level this tissue was found to be controlled by several factors, the so-called 'planar cell polarity' genes, which have since been found to be highly evolutionarily conserved (Goodrich and Strutt, 2011)

1.4.1 Vertebrate PCP genes

Studies in vertebrates have identified a group of genes homologous to the *Drosophila* 'core' PCP genes *Frizzled* (*Fzd*), *Dishevelled* (*Dvl*), *Strabismus*/*Van gogh*, *Flamingo*/*Starry night*, *Prickle* (*Pk*) and *Diego*. In contrast to *Drosophila*, several family members have been found for many of the vertebrate PCP genes. For example there are three *Dvl* genes, two *Vangl* (homologous to *Drosophila Strabismus*) genes and three *Celsr* (*Drosophila Flamingo*) genes in the mouse. Consequently, redundancy between family members means that the study of vertebrate PCP often requires knockouts of multiple genes (Simons and Mlodzik, 2008).

Planar cell polarity is established by the formation of protein complexes at the plasma membrane. Signalling is mediated through interactions between the transmembrane Fzd receptors and intracellular, multi-domain Dvl proteins, which are recruited to the membrane on activation of the pathway. Other core components include Vangl2, a four-pass transmembrane protein that contains a PDZ-binding

motif within its C-terminal domain, the transmembrane cadherin Celsr1 and the cytoplasmic protein Pk. Vertebrates also have two homologues of the *Drosophila Diego* gene, *Inversin* and *Diversin* (Simons and Mlodzik, 2008). Two further proteins for which a role in vertebrate PCP has been identified are *Scribble* (*Scrib*) (Montcouquiol et al., 2003) and *Protein tyrosine kinase 7* (*Ptk7*) (Lu et al., 2004). While *Scrib* was originally defined as a determinant of apico-basal polarity in *Drosophila*, there is increasing evidence for its involvement in PCP-regulation in vertebrates (Montcouquiol et al., 2003; Yates et al., 2013). The core components of the mammalian PCP pathway are shown in Figure 1.5.

In *Drosophila* the establishment of PCP involves interactions between the different components, resulting in the assembly of asymmetric protein complexes at opposite poles of the cell (Simons and Mlodzik, 2008). In the wing cells, a Strabismus-Pk complex localises to the proximal surface, while a complex containing Fz, Dvl and Diego forms at the distal side. Flamingo co-localises with both the proximal and distal complexes and is thought to form stabilising, homophilic adhesions to link adjacent cells (Wang and Nathans, 2007). In vertebrates the sub-cellular distributions of PCP proteins has not been well characterised, although the asymmetric localisation of factors has been reported in some tissues. For example, in the hair cells of the mouse cochlea, Dvl localises to the outer edge, the site of stereocilia formation, while Vangl2 localises to the opposite, inner side (Montcouquiol et al., 2006; Wang et al., 2005). Unlike in the fly wing, Fzd3 and Fzd6 appear to co-localise with Vangl2 in the inner ear of the mouse (Montcouquiol et al., 2006; Wang et al., 2006b). Another example is the asymmetric distribution of Dvl and Pk in the zebrafish neuroepithelium and presomitic mesoderm (Ciruna et al., 2006; Yin et al., 2008).

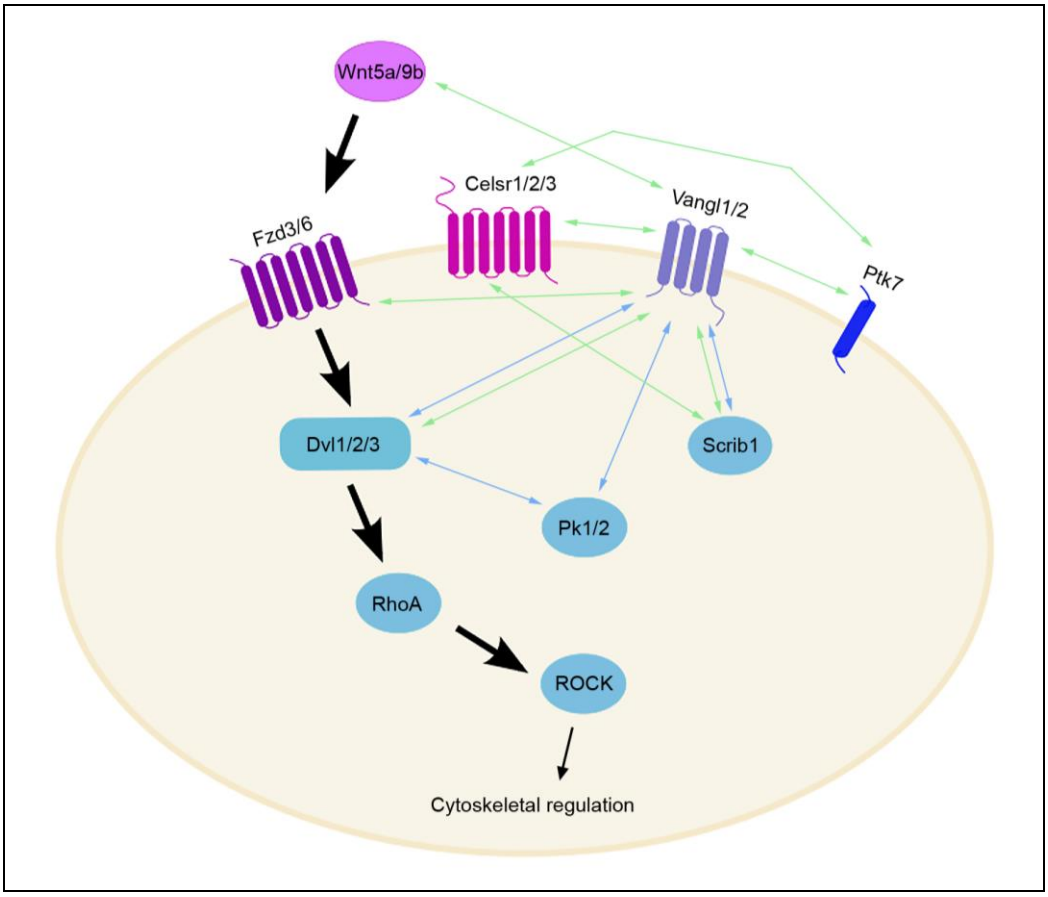

Figure 1.5 The mammalian PCP pathway

Schematic diagram showing the core PCP proteins in a mammalian cell. For each component, the family members for which a role in PCP has been described are listed. Black arrows indicate the signalling cascade, green arrows indicate known genetic interactions and blue arrows indicate known biochemical interactions.

Upstream of the Fzd/Dvl complex, vertebrate Wnt ligands have been found to regulate PCP signalling. In contrast to canonical Wnt signalling, PCP does not involve the stabilisation of cytoplasmic β-catenin, and is therefore often referred to as a 'non-canonical' branch of the Wnt signalling cascade (Yang, 2012). In particular, *Wnt5a* and *Wnt11* have been clearly linked to PCP signalling; *Wnt5a* regulates PCP and interacts genetically with *Vangl2* in mice (Gao et al., 2011; Qian et al., 2007), while roles for *Wnt5* and *Wnt11* in regulating convergent extension during zebrafish gastrulation have been identified (Heisenberg et al., 2000; Kilian et

al., 2003). *Wnt11* has also been reported to regulate the PCP-dependant orientated elongation of myocytes during early chick myogenesis (Gros et al., 2009) and the migration of neural crest cells in the *Xenopus* embryo (see Chapter 7) (De Calisto et al., 2005). Finally, there is emerging evidence that *Wnt9b* also acts via the non-canonical pathway to regulate kidney tubule morphogenesis in mice (Karner et al., 2009). In *Drosophila*, no *Wnt* ligands have been implicated in PCP pathway activity and it is not clear how fields of cells are initially polarised. One model proposes the involvement of a second group of factors, including the two large cadherins Fat (Ft) and Dachsous (Ds) as well as Four-jointed (Fj). It has been suggested that the *Ft/Ds* system could act as an upstream regulator, setting up a global polarity signal that can then be sensed and propagated by the core protein complexes. However, the relationship between the core PCP proteins and the *Ft/Ds* group is not well understood; other studies have suggested that the two act in parallel (Simons and Mlodzik, 2008).

Downstream of the vertebrate core PCP genes, an increasing number of effector proteins are emerging. The best studied PCP effectors are the family of Rho GTPases, including RhoA, Rac1 and Cdc42, which control cytoskeletal remodelling to regulate PCP-dependant processes such as orientated cell movement (Schlessinger et al., 2009). Rho GTPase signalling has been shown to be required downstream of PCP in *Xenopus*, zebrafish and mice (see Chapter 5) (Habas et al., 2001; Marlow et al., 2002; Ybot-Gonzalez et al., 2007b). Signalling via Inturned and Fuzzy has also been identified in *Xenopus* and mouse (Gray et al., 2009a; Park et al., 2006), and via Jun N-terminal kinase (JNK) in *Xenopus* (Habas et al., 2003; Yamanaka et al., 2002).

1.4.2 Roles in development

The PCP pathway regulates many aspects of vertebrate development, including CE during body axis elongation, neural tube closure in *Xenopus* and mice (see Section 1.4.2.1), cell division orientation during neurulation in zebrafish, morphogenesis of organs such as the heart, lungs and kidneys, and the orientation of scales, feathers or fur on the skin. In *Xenopus* and zebrafish embryos, PCP signalling has been found to regulate the migration of neural crest cells (see Chapter 7) (Carmona-Fontaine et al., 2008a; De Calisto et al., 2005; Matthews et al., 2008; Shnitsar and Borchers, 2008). In recent years a striking link between PCP and ciliogenesis has also emerged (Guirao et al., 2010; Park et al., 2006; Park et al., 2008; Ross et al., 2005; Song et al., 2010; Wallingford and Mitchell, 2011).

A classic example of vertebrate PCP is seen in the cochlea of the mammalian inner ear. Within the cochlea, the organ of Corti (auditory sensory organ) contains sensory epithelia composed of mechanosensory hair cells and nonsensory support cells. The hair cells are organised into four rows with each cell producing a V-shaped bundle of actin-based sterocilia that are uniformly oriented (Wansleeben and Meijlink, 2011). Cochlear hair cell polarity is commonly used as a read-out of PCP when studying mouse mutant phenotypes; for example, the precise arrangement of the stereociliary bundles is disrupted in *Vangl2*, *Celsr1*, *Scrib* and *Ptk7* mutants, as well as in mice doubly mutant for *Dvl1/2* and *Fzd3/6* (Curtin et al., 2003; Lu et al., 2004; Montcouquiol et al., 2003; Wang et al., 2005; Wang et al., 2006b). PCP also regulates CE of the cochlea during its formation (Chacon-Heszele et al., 2012; Wang et al., 2005).

1.4.2.1 PCP and NT closure

During late gastrulation, shaping of the vertebrate embryo is largely driven by the cell movements of CE, leading to narrowing and lengthening of the neural plate and

underlying mesoderm (Keller, 2002) (see Chapter 4). Work in *Xenopus* and zebrafish embryos provided the first link between PCP and CE, demonstrating a crucial role for the pathway in controlling this process. In *Xenopus* for example, over-expression of *Dvl* or *Stbm,* or disruption of their function by injecting mutant constructs or antisense morpholinos, inhibits CE in both the neural and axial mesoderm tissues. This leads to reduced elongation of the A-P axis and in some cases failure of neural tube closure (Darken et al., 2002; Wallingford et al., 2000; Wallingford and Harland, 2001). Similarly, in the zebrafish embryo, gain and loss-of-function of *Stbm* or *Prickle1* causes CE defects (Carreira-Barbosa et al., 2003; Jessen et al., 2002; Park and Moon, 2002).

The precise requirement for PCP-mediated CE during neurulation was investigated further in another study (Wallingford and Harland, 2002). Here, the authors found that the expression of mutated *Dvl* constructs produces embryos with an open neural tube phenotype (Figure 1.6) and an abnormally short, broad neural plate at early neurula stages. Despite the failure of closure the neural folds appear to form normally and move towards the midline, but are too widely spaced apart to meet and fuse. The severity of the NTD was also observed to correlate with the extent of axis elongation. When the expression of mutant *Dvl* was targeted to the ventromedial neural plate (by medial blastomere injection) or the dorsolateral neural plate (by lateral blastomere injection), only medially-injected embryos displayed NTDs. Thus, PCP-dependent CE was found to be required specifically in the midline in order to reduce the distance between the neural folds.

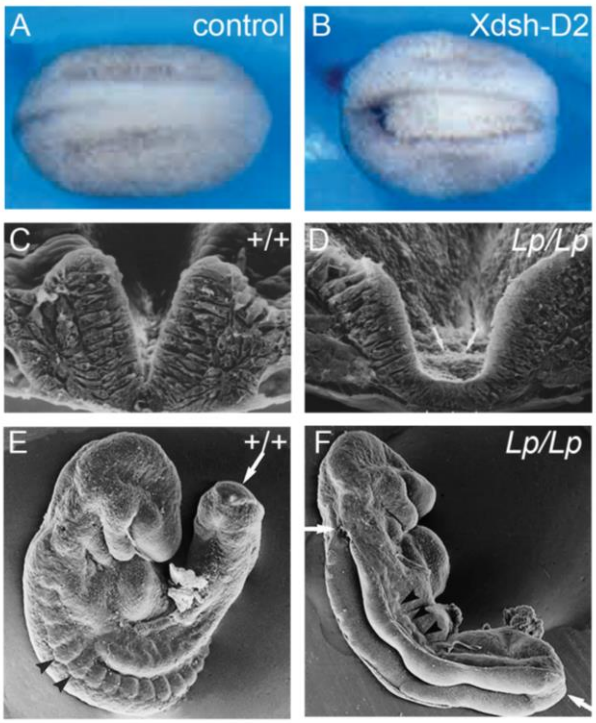

Figure 1.6 Failure of neural tube closure in *Xenopus* and mouse PCP mutants

(**A-B**) Dorsal views of stage 22 *Xenopus* embryos. The control embryo has a closed neural tube (A) while a proportion of embryos fail to achieve neural tube closure after injection of a mutant form of *Dvl* (*Xdsh-D2*; B), which disrupts PCP signalling without affecting the canonical Wnt pathway. (**C-D**) Sections through the neuroepithelium of E8.5 wild type and *Vangl2*$^{Lp/Lp}$ embryos. Arrows indicate the abnormally broad neural plate midline in the mutant. (**E-F**) E9.5 wild type and *Vangl2*$^{Lp/Lp}$ embryos. White arrows indicate the levels of the open neural tube. Images taken from (Wallingford and Harland, 2002) (A-B) and (Greene et al., 1998) (C-F).

The phenotype of *Xenopus* embryos with defective CE was realised to be highly reminiscent of the widely spaced neural folds that preclude failure of closure 1 in the mouse mutant *loop-tail* (*Lp*), indicating a conserved underlying mechanism (Figure 1.6) (Greene et al., 1998). The *loop-tail* mouse model is mutant for the core PCP gene *Vangl2* and homozygous *Vangl2*$^{Lp/Lp}$ embryos display craniorachischisis with 100% penetrance (see Section 1.4.3) (Kibar et al., 2001b; Murdoch et al., 2001a).

Gene(s)	Mutant genotype	Penetrance of CRN (%)	References
Vangl2	*Vangl2*$^{Lp/Lp}$ *Vangl2*$^{Lpm1Jus/Lpm1Jus}$	100 100	(Kibar et al., 2001a; Kibar et al., 2001b; Murdoch et al., 2001a)
Celsr1	*Celsr1*$^{Crsh/Crsh}$ *Celsr1*$^{Scy/Scy}$	100 100	(Curtin et al., 2003)
Ptk7	*Ptk7*$^{gt/gt}$ *Ptk7*$^{chz/chz}$	100 100	(Lu et al., 2004; Paudyal et al., 2010)
Scribble	*Scrib*$^{Crc/Crc}$	100	(Murdoch et al., 2001b; Murdoch et al., 2003)
Sec24b	*Sec24b*$^{Y613/Y613}$ *Sec24b*$^{krabbel/krabbel}$	100 ~100	(Merte et al., 2010; Wansleeben et al., 2010)
Dishevelled1/2	*Dvl1*$^{-/-}$;*Dvl2*$^{-/-}$	~100	(Hamblet et al., 2002; Wang et al., 2006a)
Dishevelled2/3	*Dvl2*$^{+/-}$;*Dvl3*$^{-/-}$ *Dvl2*$^{-/-}$;*Dvl3*$^{+/-}$	? (low) 100	(Etheridge et al., 2008)
Frizzled3/6	*Fzd3*$^{-/-}$;*Fzd6*$^{-/-}$	~100	(Wang et al., 2006b)
Smurf1/2	*Smurf1*$^{-/-}$;*Smurf2*$^{-/-}$	65	(Narimatsu et al., 2009)
Sfrp1/2/5	*Sfrp1*$^{-/-}$;*Sfrp2*$^{-/-}$;*Sfrp5*$^{-/-}$	100	(Satoh et al., 2008)

Table 1.2 Failure of closure 1 in mouse PCP mutants

Only single PCP gene effects and paralogous gene interactions that cause craniorachischisis (CRN) are included here. NTDs caused by interactions between *Vangl2* and other genes are listed in Chapter 3. *Smurf1* and *Smurf2* are ubiquitin ligases that have been found to regulate PCP during neurulation and inner ear development. *Sfrp1*, *2* and *5* are secreted frizzled-related proteins that regulate the PCP pathway during axis elongation. All other genes are referred to in the text.

Strikingly, since the characterisation of *loop-tail*, almost all of the loci associated with craniorachischisis in the mouse have been found to disturb PCP signalling. Closure 1 fails in several mice carrying homozygous mutations in core PCP genes

(such as *Celsr1*), in mice where transport of PCP proteins is perturbed (*Sec24b* mutants) and in mice with digenic and oligogenic PCP mutant combinations (such as *Dvl1/Dvl2* double mutants) (Juriloff and Harris, 2012a). A list of these mutants is provided in Table 1.2. Additionally, the heterozygous *Vangl2*$^{Lp/+}$ genotype causes craniorachischisis and increases the frequency of other types of NTDs when combined with mutations in other PCP, and non-PCP, genes. For more details, and a list of these genetic interactions, see Chapter 3 (Table 3.1).

1.4.3 The *loop-tail* mouse model

1.4.3.1 *Lp* alleles

The *Lp* mutation arose spontaneously within an inbred strain over 60 years ago and was named according to the appearance of a looped or kinked tail phenotype. Heterozygous mice also displayed 'wobbly' head behaviour and approximately one third of females had an imperforate vagina. When these animals were intercrossed, litters contained offspring with a severe malformation that closely resembled human craniorachischisis (Strong and Hollander, 1949; Stein and Rudin, 1953). The authors of the original study noted: 'If the parents were both abnormal, some of the fetuses were monsters, having craniorachischisis' (Strong and Hollander, 1949).

Several early positional cloning studies led to the identification of *Vangl2* (also originally called *Lpp1* and *Loop-tail associated protein*; *Ltap*) as the gene mutated in *loop-tail* mice. Two *loop-tail* alleles were initially characterised, the naturally occurring *Lp* and the N-ethyl-N-nitrosourea (ENU)-induced *Lp*^{m1Jus} (Kibar et al., 2001a; Kibar et al., 2001b; Murdoch et al., 2001a). Both alleles were identified as semi-dominant mutations, producing craniorachischisis in homozygous mice and tail defects or rare, low spina bifida in heterozygotes (Copp et al., 1994; Kibar et al., 2001a). In *Lp*, a single nucleotide substitution (G→A) was found to change serine

464 to asparagine (S464N). Similarly, a T→A missense mutation was found at position 765 of the *Lp*^{m1Jus} sequence, changing aspartate 255 to glutamate (D255E) (Kibar et al., 2001b; Murdoch et al., 2001a). Both of these mutations affect highly conserved residues within the intracellular, C-terminal portion of the Vangl2 protein (Figure 1.7).

Recently, two further *loop-tail* alleles have been reported (Figure 1.7). A second ENU-induced allele, *Lp*^{m2Jus}, was found to contain a single G→T substitution, changing arginine 259 to leucine (R259L). Despite affecting another highly conserved residue only three amino acids away from the D255E mutation, R259L was found to be recessive; homozygous mice do not exhibit craniorachischisis but show spina bifida (12%) or a looped tail (47%), while all heterozygous mice are apparently normal (Guyot et al., 2011). *Lp*^{m2Jus} does not cause a reduction in the level of *Vangl2* mRNA, but results in a 10% decrease in protein level, suggesting it is a hypomorphic allele (Guyot et al., 2011). A third chemically-induced allele, *Vangl2*^{m1Yzcm}, has also been published (Chen et al., 2013). The authors of this study observed tail defects in heterozygous mice and craniorachischisis in homozygotes. A C→T mutation was identified in the *Vangl2* sequence, which converts glutamine 449 to a stop (nonsense) codon. Although the level of *Vangl2* expression was not analysed, *Lp*^{m1Yzcm} was predicted to be a loss of function allele on the basis that its translation would produce a truncated protein lacking the PDZ-binding domain (Chen et al., 2013).

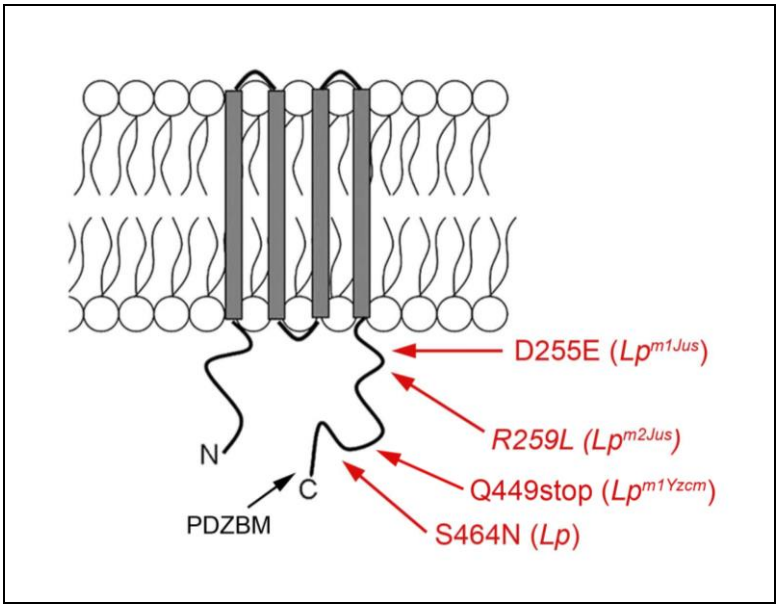

Figure 1.7 Positions of the *loop-tail* mutations

Schematic of the Vangl2 protein. All of the published *Lp* mutations map to the cytoplasmic, C-terminal tail; arrows indicate their approximate positions. Image modified from (Guyot et al., 2011).

1.4.3.2 NTDs in *loop-tail*

Loop-tail is the most extensively studied mouse model of craniorachischisis and was the first mutant to implicate a role for PCP signalling in neurulation. Early studies of the embryonic mechanism underlying NTDs in *loop-tail* embryos found that homozygous *Lp/Lp* mutants fail to initiate neural tube closure at the hindbrain-cervical boundary (closure 1) at the 5-7 somite stage. Heterozygous *Lp/+* embryos successfully close their neural tubes, but exhibit delayed PNP closure, leading to tail defects and occasional low spina bifida (Copp et al., 1994). Prior to the normal stage of closure 1, E8.5 *Lp/Lp* embryos display an abnormally broad and flat midline of the neural plate. While a sharp midline bend produces a V-shaped neural plate in wild type and *Lp/+* (Figure 1.6C), in *Lp/Lp* the sites of neuroepithelial bending are displaced to more lateral positions, producing a U-shaped neuroepithelium (Figure 1.6D) which is accompanied by an abnormally wide underlying notochord (Greene

et al., 1998). Consistent with the abnormal morphology of the midline tissues, markers of the floor plate and notochord display broadened expression domains at E8.5 and E9.5 (Greene et al., 1998; Ybot-Gonzalez et al., 2007b).

Defective axis elongation in *Lp* homozygotes was first suggested by Smith and Stein (1962), who noted that at E9.5 'their bodies are relatively shorter than normal' and that at late gestation 'the trunk of the *Lp/Lp* embryo appears compressed along the anterior-posterior axis'. Like other PCP mutants, *Lp/Lp* embryos also display an abnormally short and wide body axis at E8.5 (Lu et al., 2004; Paudyal et al., 2010; Wang et al., 2006a; Ybot-Gonzalez et al., 2007b). To directly analyse CE at pre-neurulation stages, our lab previously performed vital labelling of midline cells by injecting DiI into the node or electroporating a GFP-expressing vector into the neural plate at E7.5. After 18 hours in culture, *Lp* homozygotes displayed greatly reduced midline extension compared to wild type embryos. Heterozygous *Lp/+* embryos displayed a variable, intermediate phenotype (Ybot-Gonzalez et al., 2007b).

As described in more detail later, further experiments found this to be a cell-autonomous defect, affecting both the neural plate and underlying axial mesoderm (see Chapter 4) (Ybot-Gonzalez et al., 2007b). Together these data demonstrate that PCP-dependent CE is required prior to the initiation of mammalian neural tube closure in order to reduce the distance between the neural folds, allowing them to meet and fuse. Whether a similar mechanism underlies the delayed spinal neurulation in *Lp/+* heterozygotes, or the spina bifida in homozygous $Lp^{m2Jus};Lp^{m2Jus}$ embryos, has not been examined to date.

In addition to NTDs, *loop-tail* embryos display PCP-related defects in several other tissues. These include open eyelids, disrupted polarity of stereociliary bundles in the cochlea, defective reproductive system development and altered optic nerve trajectories (Montcouquiol et al., 2003; Rachel et al., 2000; Vandenberg and Sassoon, 2009). A complex cardiovascular phenotype has been described in *Vangl2*$^{Lp/Lp}$ mice, which includes double-outlet right ventricle (where the aorta and pulmonary artery both originate from the same ventricle), ventricular septal defects and aortic arch defects (Henderson et al., 2001; Henderson et al., 2006). *Vangl2*$^{Lp/Lp}$ embryos also exhibit aberrant lung and kidney morphogenesis (Yates et al., 2010a; Yates et al., 2010b).

1.4.3.3 Effect of the *Vang2*^{Lp} mutation

Both of the original *Lp* mutations (S464N and D255E) disturb binding of Vangl2 to Dvl proteins, suggesting this interaction is crucial for PCP signalling (Torban et al., 2004). Similarly in the zebrafish embryo, while wild type *Vangl1* is able to rescue the CE defect in *Vangl2* morphants, this phenotype cannot be rescued by injection of *Vangl1* containing either of the two *Lp* mutations (Reynolds et al., 2010). Expression studies have shown that *Lp* mutations do not alter the abundance of *Vangl2* mRNA (Guyot et al., 2011; Kibar et al., 2001b), but do cause a reduction in Vangl2 protein expression in the embryo (Belotti et al., 2012; Guyot et al., 2011; Torban et al., 2007).

In cells of the neural tube and cochlea, *Lp* mutations have been found to cause a reduction in the normal membrane localisation of Vangl2 protein (Torban et al., 2007). *In vitro* studies of the Vangl1 protein also showed that its normal membrane association is disrupted when *Lp* mutations are introduced, and that it is retained in the ER, which likely leads to its degradation by the proteasome. The authors of these studies suggested that the retention of the mutant protein could be due to

mis-folding, and when protein stability was analysed they found an approximately four-to-seven-fold reduction in half life for the mutant variants compared with wild type Vangl1 (Gravel et al., 2010; Iliescu et al., 2011). The findings that *Lp* mutations interfere with protein targeting are consistent with two reports of severe PCP phenotypes in mice carrying loss-of-function mutations in *Sec24b*, a component of COPII vesicles which play a key role in transport of proteins from the ER to the Golgi. Analysis of these mutants revealed that *Sec24b* is required for the trafficking and correct membrane localization of Vangl2 (Merte et al., 2010; Wansleeben et al., 2010). Furthermore, Vangl2^{Lp} protein fails to package into COPII vesicles and fails to reach the plasma membrane, presumably due to defective exit from the ER (Merte et al., 2010).

The data described above suggest that *Vangl2^{Lp}* represents a loss-of-function allele and that the semi-dominance of the *loop-tail* phenotype is caused by haploinsufficiency due to the partial loss of *Vangl2* in a gene-dosage dependant pathway. On the other hand, recent studies have provided strong evidence for a dominant negative effect of *Vangl2^{Lp}*, whereby the mutant protein alters the normal activity of wild type Vangl2 protein or other PCP components. The data in these reports demonstrate that the presence of the *Vangl2^{Lp}* protein has a greater phenotypic effect than the loss of wild-type Vangl2 (see Chapter 6 for more details) (Song et al., 2010; Yin et al., 2012). In summary, *Lp* mutations appear to exert complex effects on the biochemical properties of Vangl2; there is evidence for both a reduction in protein abundance and a dominant negative effect exerted by the remaining mutant protein.

1.4.3.4 *Vangl* genes

In mice, humans and zebrafish two homologues of the *Drosophila Strabismus*/*Van gogh* gene have been identified (*Vangl1* and *Vangl2*) while only one gene has been

found in *Xenopus*. Among vertebrate species, Vangl1 proteins share approximately 67% similarity, while Vangl2 proteins are 74% conserved (Torban et al., 2004). The mouse *Vangl1* and *Vangl2* genes are located on chromosomes 3 and 1, respectively and their sequence similarity is, on average, 70%, but varies at different positions. Particularly high conservation (>80%) is observed within their C-terminal cytoplasmic domain, the region to which *Lp* mutations map (Torban et al., 2004). The patterns of *Vangl1* and *Vangl2* expression during neurulation are shown later in this thesis (see Chapter 5 and Chapter 7). Briefly, the two genes are co-expressed within the neuroepithelium, but with some differences. *Vangl2* is more widely expressed, with transcripts found throughout the dorsoventral axis of the neuroepithelium prior to and during neural tube closure, while Vangl1 is largely confined to the ventral midline region (Doudney et al., 2005; Kibar et al., 2001b; Torban et al., 2007; Torban et al., 2008).

The role of *Vangl1* during development is not well understood but, like Vangl2, Vangl1 protein can bind to Dvl, suggesting functional conservation among the family members. Furthermore, this interaction is disrupted when *Lp* mutations are introduced into the *Vangl1* sequence (Torban et al., 2004). Differences in expression pattern have been suggested to underlie the lack of redundancy between the two genes during neurulation in mice (*Vangl1* doesn't compensate for the loss of *Vangl2* function in *loop-tail*) (Doudney et al., 2005). However in zebrafish ectopic expression of *Vangl1* can partially rescue the CE defect in *trilobite* (*Vangl2*) mutants (Jessen and Solnica-Krezel, 2004). Surprisingly, *Vangl1*-null mutant mice do not develop NTDs, although a proportion of double heterozygous *Vangl1*$^{genetrap/+}$;*Vangl2*$^{Lp/+}$ embryos display craniorachischisis and cochlear polarity defects, demonstrating a genetic interaction during neurulation and inner ear development (Torban et al., 2008). Interestingly, recent co-immunoprecipitation

studies have shown that Vangl1 and Vangl2 interact physically *in vitro*, forming heteromeric protein complexes (Belotti et al., 2012; Yin et al., 2012).

1.4.4 Neural crest cell migration

Another aspect of early nervous system development for which a role for PCP signalling has been described is the migration of neural crest (NC) cells. The NC is a transient, multipotent vertebrate cell population that is induced at the boundary between the future neural and non-neural ectoderm (the 'neural plate border') by a complex network of signalling pathways and transcription factors (Sauka-Spengler and Bronner-Fraser, 2008; Steventon et al., 2005; Stuhlmiller and Garcia-Castro, 2012). After their specification, NC cells undergo an epithelial to mesenchymal transition (EMT), delaminating from the dorsal neuroepithelium in a rostrocaudal wave, and migrating extensively throughout the embryo. On reaching their target locations, they give rise to a wide range of cell types, including neurons and glia of the peripheral and enteric nervous systems, heart cells, melanocytes and the bone, cartilage and smooth muscle of the head (Sauka-Spengler and Bronner-Fraser, 2008).

1.4.4.1 Delamination

Before commencing their migration, NC cells undergo an EMT in order to delaminate from the neuroepithelium and invade the surrounding mesenchyme. Pre-migratory NC cells reside within a tightly packed epithelial layer; they are joined by intercellular adherens and tight junctions, exhibit apical-basal polarity and are supported by components of the basement membrane (basal lamina). Therefore, three processes in particular are key to the EMT of the NC: alterations in cell adhesion molecules, the dissolution of cell junctions and remodelling of the surrounding extracellular matrix (ECM) (Strobl-Mazzulla and Bronner, 2012).

An early feature of the EMT, common to NC cells in different species and at varying axial levels, is a change in cell-cell adhesion via the modulation of cadherin expression. In particular, down-regulation of type I cadherins such as E-cadherin and N-cadherin and up-regulation of type II cadherins such as Cadherin7 and Cadherin11 is a hallmark of EMTs. These changes represent a switch from strong, classical cadherin-based cell-cell adhesions that are required to maintain neuroepithelial integrity, to weaker adhesions that allow increased cell motility. The regulation of cell adhesion molecules also appears to prevent mixing between pre-migratory NC and non-NC cells. For example in the chick neural tube, NC cells weakly express N-cadherin and strongly express Cadherin6B, while the surrounding cells express N-cadherin. It has been suggested that the subsequent loss of Cadherin6B and activation of Cadherin7 and 11 in the NC promotes delamination via a 'cell sorting-like mechanism' whereby NC cells are pushed out of the dorsal neural tube (Theveneau and Mayor, 2012).

The changes in cell-cell interactions that occur during the initial stages of EMT are also linked to the replacement of tight junctions by gap junctions. This involves the downregulation of major structural components of tight junctions, such as Occludins and Claudins, and the upregulation of gap junction proteins such as Connexin-43 (Cxn-43) (Kuriyama and Mayor, 2008). In the mouse, *Cxn-43* (also called *alpha-1 connexin*) is expressed in the delaminating NC at all axial levels and its knockout produces defects in NC derivatives (Lo et al., 1997; Reaume et al., 1995). In mammalian NC explant cultures, *Cxn-43* has been shown to modulate the migration of cardiac NC cells; its overexpression increases the rate of migration, while abrogation of its function causes a decrease in migration rate (Huang et al., 1998).

As NC cells separate from the neuroepithelium, they must also invade and migrate through the surrounding ECM. This element of EMT requires the controlled

digestion of ECM components, such as collagens, laminins, proteoglycans and fibronectin, in the basement membrane overlying the dorsal neuroepithelium. ECM degradation is regulated by a fine balance between the proteolytic activity of matrix metalloproteases (MMPs) and the expression of tissue inhibitors of MMPs (TIMPs) (Kuriyama and Mayor, 2008). For example, MMP2 and its natural inhibitor, TIMP-2, have been found to play important roles in chick cardiac NC migration (Cantemir et al., 2004; Duong and Erickson, 2004) and MMP-8 is expressed in the mouse NC (Giambernardi et al., 2001). NC cells also express members of the ADAM metalloprotease family, cell surface-bound enzymes that cleave extracellular portions of transmembrane proteins (Sauka-Spengler and Bronner-Fraser, 2008). In *Xenopus*, ADAM-13 is expressed in both premigratory and migratory cranial NC cells and is required for their migration (Alfandari et al., 2001) and in the chick NC cells express ADAM-10 (Hall and Erickson, 2003).

1.4.4.2 Timing and routes of early migration

After undergoing EMT, NC cells embark on defined routes of migration towards their final destinations. In general NC migration initiates around the time of neurulation, although the timing varies between species. Cranial NC cells begin their migration shortly after neural tube closure in the chick, while in mouse and *Xenopus* they depart prior to closure of the cranial neural folds (at the 4-5 somite stage in the mouse). Migration of the trunk NC starts following neural tube formation in all animal models, although the time between the end of neurulation and NC delamination can vary along the A-P axis (Theveneau and Mayor, 2012).

The cranial NC segregate into distinct streams, the pattern of which is highly conserved between species. Cells that terminate at a relatively dorsal position contribute to the cranial ganglia, while others continue further ventrally, invade the branchial arches and form the cartilage and bones of the face and neck. Caudal

forebrain (diencephalon) and midbrain-derived NC cells migrate both anteriorly to populate the periocular and frontonasal regions of the face, and ventrally to colonise the first branchial arch. In the hindbrain the NC predominantly migrate from the even-numbered rhombomere segments, creating three streams from rhombomeres two, four and six that colonise the first, second and third branchial arches (Kuo and Erickson, 2010; Trainor, 2005). The cranial streams are separated by two neural-crest free zones adjacent to rhombomeres three and five, from which relatively few NC cells emigrate. Lineage tracing studies in the mouse have shown that the cells from these odd-numbered rhombomeres migrate anteriorly or posteriorly to join the adjacent streams (Trainor et al., 2002) (Figure 1.8A). Caudal to the hindbrain, a subpopulation of cells, termed the vagal NC, arises from the axial level of somites 1-7. These cells migrate long distances, differentiating into neurons and glia of the enteric nervous system (ENS; predominantly cells from the level adjacent to somites 3-6) and cardiac cells (cells from the level of somites 1-3), as well as PNS cells and melanocytes (Kuo and Erickson, 2011).

Trunk NC cells migrate along two major pathways, a ventromedial route and a dorso-lateral route, the timings and trajectories of which show interspecies variation. In amniote embryos the NC initially migrate ventrally between the neural tube and somites, before proceeding through the anterior half of the sclerotome and along the basement membrane of the dermamyotome upon somite maturation (Figure 1.8B). Those which travel the furthest differentiate to produce neurons and glia of the sensory and sympathetic ganglia, while more dorsally-terminating NC aggregate to form the dorsal root ganglia (DRG) and boundary cap cells. Another wave of NC cells embark on a dorsolateral route between the somites and the overlying ectoderm (Figure 1.8B). These cells populate the skin and differentiate into melanocytes. In the mouse embryo NC cells travel along ventromedial and dorsolateral routes simultaneously, while in the chick the dorsolateral path is

invaded approximately 24 hours later than the ventral path (Theveneau and Mayor, 2012).

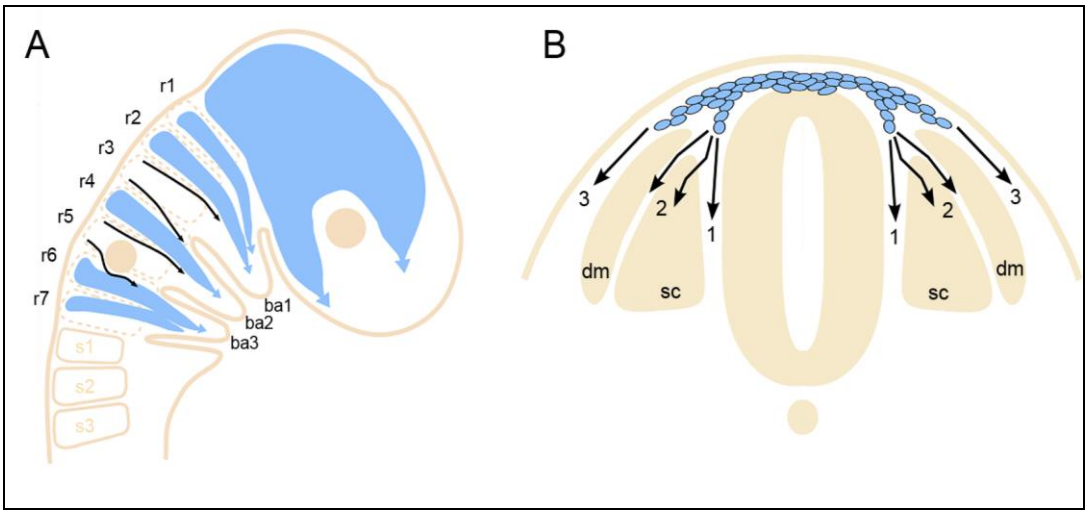

Figure 1.8 Early routes of NC cell migration in the mouse

Schematic diagram showing the major paths taken by NC cells emigrating from the cranial (A) and trunk (B) neuroepithelium. (**A**) In the cranial region, NC cells segregate into distinct streams (blue). The pattern of hindbrain NC migration is related to the rhombomere segments (r1-r7) and leads to the appearance of NC-free zones adjacent to r3 and r5. Blue arrows indicate major contributions to the branchial arches and black arrows indicate minor contributions. (**B**) In the trunk, NC cells take ventral routes (1 and 2) and dorsolateral routes (3). See text for details.

1.4.4.3 Molecular guidance of migration

Most of the molecules that are known to guide NC migration act as inhibitory cues, patterning the NC into their stereotypical streams by excluding them from restricted areas. One group of important signalling molecules are membrane-bound ephrin ligands and their Eph receptors (members of the receptor tyrosine kinase family), which are expressed in different combinations by the NC and their surrounding tissues. Interactions between ligand-receptor pairs regulates NC cell motility by inducing the collapse of cell protrusions (Theveneau and Mayor, 2012). In *Xenopus*

for example, the expression of *ephrin-B2* in the second branchial arch NC and mesoderm is complementary to that of *EphA4* and *EphB1* receptors in the third arch, targeting the NC cells to their correct destination. Blocking or ectopic activation of the receptors leads to aberrant migration and intermingling of NC cells from different streams (Smith et al., 1997). In mouse and chick embryos, the organisation of trunk NC migration involves the expression of ephrin-B ligands in the posterior half of the sclerotome, while the NC cells express EphA/B receptors and are therefore restricted to the anterior half. Inhibition of the pathway results in ectopic entry of NC cells into the posterior part of the sclerotome. Eph-ephrin interactions in the chick also regulate the early repulsion of trunk NC cells from the dorsolateral pathway (Krull et al., 1997; Santiago and Erickson, 2002).

Another important class of molecules are class3-semaphorins and their transmembrane receptors, neuropilins and plexins. Ligand-receptor binding leads to downstream signalling that can alter the cytoskeleton (Kuriyama and Mayor, 2008; Santiago and Erickson, 2002). Studies in mouse, zebrafish and chick have identified a role for semaphorin signalling in cranial NC patterning: *Sema3* genes are expressed in the NC-free zones, while their neuropilin receptors are expressed in the migratory NC cells. When signalling is impaired, cells are able to divert from their normal streams and invade adjacent NC-free regions (Gammill et al., 2007; Osborne et al., 2005; Yu and Moens, 2005). The signalling pathway is also required in the trunk to mediate the guidance of NC cells through the somites. For example, in the mouse, NC cells express *neuropilin2* (*Npn2*), while expression of its repulsive *semaphorin3F* (*Sema3F*) ligand is restricted to the posterior sclerotome. Both *Sema3F* and *Npn2* mutant mice lose their segmented pattern of trunk NC cell migration and cells are seen ectopically migrating throughout the sclerotome (Gammill et al., 2006).

Other negative regulators have also been implicated in trunk NC migration (Theveneau and Mayor, 2012). Of these, the most well understood is Slit/Robo signalling. Chick NC cells express members of the Robo receptor family and are exposed to their secreted Slit ligands as they navigate through the embryo. The expression of *Slit2* in the dermamyotome has been suggested to prevent the premature entry of *Robo1*- and *Robo2*-positive NC cells into the dorsolateral path, as overexpression of a dominant negative *Robo* receptor leads to the early invasion of this route (Jia et al., 2005). Slit/Robo signalling also appears to regulate the specific migration of vagal NC cells into the gut (De Bellard et al., 2003).

1.4.4.4 Directionality and a role for PCP signalling

The signalling molecules described above play important roles in establishing and maintaining the segregation of NC streams during their migration. Nevertheless, they do not explain how NC cells migrate collectively with such a high level of persistence and directionality. The consideration of positive regulators of NC migration has led to the identification of several candidate attractant molecules. For example, growth factors such as members of the VEGF and PDGF families are expressed in cranial regions such as the branchial arches and cause NC-related phenotypes when their signalling is impaired (Theveneau and Mayor, 2012). FGFs have also been suggested to be chemotactic factors for NC in the midbrain and heart (Kubota and Ito, 2000; Sato et al., 2011). Recently, the chemokine *stromal cell-derived factor 1* (*Sdf1*) has emerged as a strong candidate for a NC chemoattractant. Sdf1 plays well characterised roles as an attractant in other contexts and is required for migration of the cranial NC in *Xenopus* and zebrafish (see Chapter 7 for more details) (Theveneau and Mayor, 2012).

However, it has been argued that the directionality of the NC cannot simply arise from a balance of positive and negative external cues (Theveneau and Mayor,

2012). As described in Chapter 7, recent studies in *Xenopus* and zebrafish have shown that cell-cell contacts between migratory NC cells influence their directionality, and that an important driving force of polarised NC migration is a phenomenon known as contact inhibition of locomotion (CIL). In these species, PCP signalling has been found to play a key role in controlling these cell behaviours (Carmona-Fontaine et al., 2008b; De Calisto et al., 2005; Matthews et al., 2008). Whether PCP signalling is similarly required during NC cell migration in the mouse embryo has not yet been determined.

1.5 Thesis summary

This thesis aims to investigate two main questions: 1) what role does the PCP pathway play during mammalian low spinal neural tube closure, and is this equivalent to its well established role prior to closure 1, and 2) is PCP signalling required during NC cell migration in the mouse embryo? **Chapter 3** begins to address the first question by investigating the exacerbating effect of *loop-tail* (*Vangl2*^{Lp}) heterozygosity on spinal neurulation in *curly tail* (*Grhl3*$^{ct/ct}$) embryos. The spina bifida phenotype of doubly mutant *Lp/ct* embryos is described and evidence for various mutant effects is assessed. In particular, the work in this chapter identifies initial morphological evidence of defect CE in *Lp/ct* embryos.

In **Chapters 4 and 5** the developmental basis of the *Lp/ct* interaction is explored further. Chapter 4 investigates the hypothesis that mutations in *Vangl2* and *Grhl3* affect distinct processes in different tissues, namely CE in the midline and the regulation of axial progenitors in the tail bud, while Chapter 5 investigates possible molecular interactions between the two genes. In **Chapter 6** a parallel, genetic approach is taken to investigate a requirement for *Vangl2* and *Grhl3* in the same cells of the embryo. Consistent with the data in Chapters 4 and 5, the findings of this chapter suggest that the interaction between *Vangl2* and *Grhl3* during spinal neurulation predominantly reflects their tissue-specific roles.

Finally, in **Chapter 7**, a requirement for the PCP signalling pathway during mouse NC cell migration is investigated. In contrast to recent data from *Xenopus* and zebrafish, evidence that PCP signalling is dispensable for early mammalian NC migration is presented.

2. Materials and Methods

2.1 Animals

Mouse colonies were maintained by Dawn Savery in the animal facility at the UCL Institute of Child Health. The animal rooms were kept at 22^{o}C with a 24-hour cycle of 12 hours light/12 hours dark. On reaching sexual maturity (6-8 weeks of age) female mice were housed in communal cages with a maximum capacity of either 6 or 10 adult animals. Males were housed individually. Water and standard pelleted food were freely available at all times.

2.1.1 *Vangl2^{Lp}*

Loop-tail mice (Jackson Laboratories, U.S.) were maintained as a heterozygous (*Vangl2$^{Lp/+}$*) colony by backcrosses to CBA/Ca inbred mice (Harlan Laboratories, UK).

2.1.2 *Vangl2^{flox}*

Vangl2$^{flox/flox}$ mice were a gift from Prof. Deborah Henderson (Newcastle University). They were maintained as a homozygous colony; further animals were generated by crossing to C57BL/6J mice and intercrossing the heterozygous (*Vangl2$^{flox/+}$*) offspring.

2.1.3 *Grhl3^{ct}*

The *curly tail* mutation arose spontaneously in 1950 in the GFF inbred strain (Glaxo Laboratories, UK) and the original stock was derived from the offspring of a cross between an affected female and a CBA/Gr male (Van Straaten and Copp, 2001). Since then, *curly tail* mice have been maintained as a closed, random-bred colony of homozygous (*ct/ct*) individuals. Due to the lack of suitable wild type controls, a congenic (+^{ct}/+^{ct}) strain that are wild type at the *curly tail* locus, but share over 95% of the *curly tail* genetic background was generated previously (Gustavsson et al.,

2007). This strain was derived from an initial cross between *curly tail* and the SWR inbred strain, followed by successive backcrosses to *curly tail.*

2.1.4 *Grhl3^{flox}*

Grhl3$^{flox/flox}$ mice were from Dr Bogi Anderson. To generate *Grhl3$^{flox/-}$* mice for experimental crosses, heterozygous animals (*Grhl3$^{flox/+}$* on a C57BL/6J background) were crossed to *β-actin$^{Cre/+}$* mice. This produced *Grhl3$^{+/-}$;β-actin$^{Cre/+}$* (25% of offspring), which were then backcrossed to *Grhl3$^{flox/flox}$* or *Grhl3$^{flox/+}$* mice to remove the *Cre*.

2.1.5 *Grhl3^{Cre}*

Grhl3^{Cre} mice were provided by Dr Shaun Coughlin and were as described previously (Camerer et al., 2010). They were maintained as a heterozygous (*Grhl3$^{Cre/+}$*) colony on a C57BL/6J background.

2.1.6 *Wnt1-Cre*

Wnt1-Cre transgenic mice were from J.P. Martinez-Barbera and were as described previously (Jiang et al., 2000). The colony was maintained on a C57Bl/6J background.

2.1.7 *Rosa26^{YFP}*

Rosa26^{YFP} reporter mice were from the Jackson Laboratories and were as described previously (Srinivas et al., 2001). They were maintained as a homozygous colony (*R26$^{YFP/YFP}$*) on a C57BL/6J background.

2.1.8 *β-actin^{Cre}*

β-actin^{Cre} mice were from J.P. Martinez-Barbera and were maintained as a heterozygous colony (*β-actin$^{Cre/+}$*) on a C57BL/6J background.

2.2 Mouse embryology

2.2.1 Embryo collection and dissection

Experimental litters were obtained from timed matings according to the developmental stage of embryos required. Mice were paired overnight and the following morning females were checked for the presence of a copulation plug. Noon on the day of finding a plug was designated embryonic day E0.5. Alternatively, morning matings were set up and females were checked later that afternoon. In these cases, noon on the day of finding a plug was designated E0. Pregnant females were killed by cervical dislocation, the abdomen was surgically opened and the uterus was removed by cutting at the level of the cervix and below each of the ovaries. Uteri were transferred to a bijoux tube containing pre-warmed (37^{o}C) dissecting medium (Dulbeco's Modified Eagle Media containing 25 mM HEPES [DMEM, Invitrogen] supplemented with 10% heat-inactivated fetal bovine serum [FBS, Invitrogen]), transported to the laboratory and placed in a dish of fresh medium under a stereo-microscope (Zeiss SV6 or SV11) for dissection.

Embryos were dissected from the uterus using flame-sterilised watchmakers' forceps (number 5, Dumont) (Figure 2.1). Fat and blood vessels were first trimmed away from the mesometrial surface of the uterus, before opening the uterine wall at the site of each decidual implantation. The deciduae were then gently removed from the uterus and transferred to a fresh dish of dissecting medium. Each decidua was opened and dissected away to reveal the mural trophoblast layer, which envelops the embryo. Trophoblast tissue and the underlying Reichert's membrane were peeled away, exposing the embryo within its yolk sac. Finally the yolk sac and amnion were removed and the dissected embryos were numbered for future reference. Yolk sacs were washed twice in cold phosphate-buffered saline (PBS) that had been treated with 0.1% v/v diethyl pyrocarbonate (DEPC; inactivates

RNase enzymes) and stored at -20^{o}C for genotyping (see Section 2.5). Alternatively, embryos were dissected for whole embryo culture (see Section 2.2.2). In this case, the ectoplacental cone was left intact during dissection of the trophoblast layer. Reichert's membrane was trimmed up to the edges of the ectoplacental cone as it can become 'sticky' during culture, causing the embryo to adhere to the culture tube. Care was taken not to rupture the yolk sac.

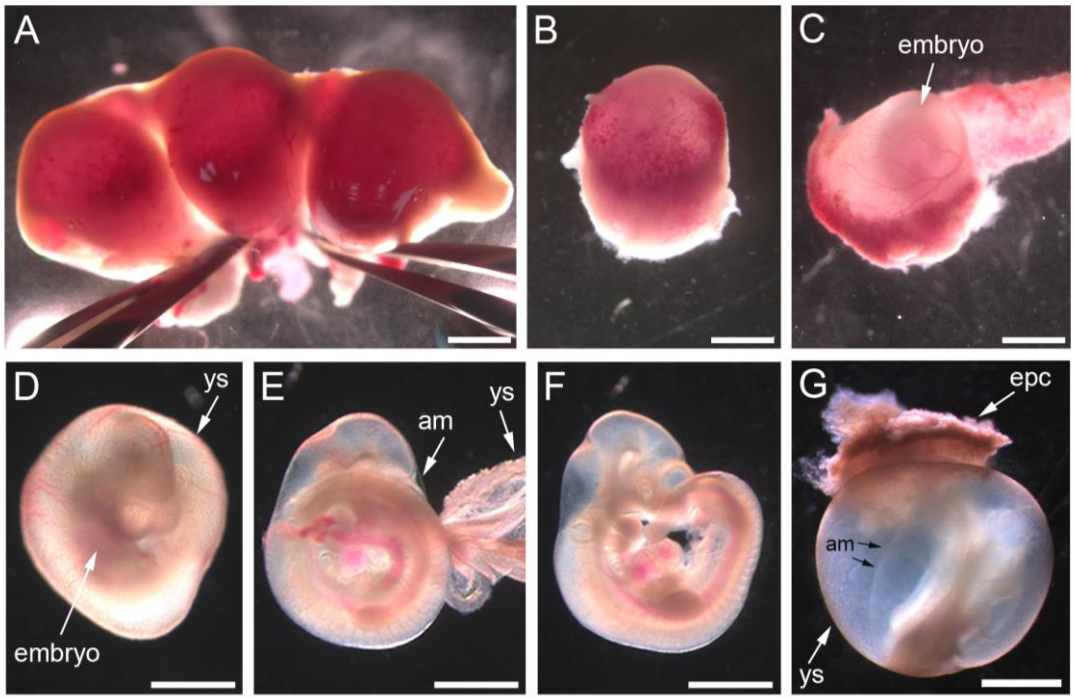

Figure 2.1 Embryo dissection

(**A**) Three implantations within the uterus. The wall of the uterus was opened to release the deciduae (B). Each individual decidua was opened to reveal the embryo within its yolk sac (C, D; in this example the trophoblast layer has been peeled back along with the decidual tissue). (**E**) The yolk sac was then removed (in this example the underlying amnion was left intact and can just be seen encasing the embryo). (**F**) Completely dissected embryo with its yolk sac and amnion removed. (**G**) Alternatively the yolk sac was left intact for whole embryo culture. Abbreviations: ys = yolk sac, am = amnion, epc = ectoplacental cone. Scale bars: 500 µm.

Dissected embryos were washed twice in cold PBS-DEPC and transferred to ice-cold paraformaldehyde (PFA) solution (4% w/v in PBS-DEPC; aliquoted and stored at -20^{o}C). Fixation was carried out at 4^{o}C for approximately 6-8 hours (E8.5) or overnight (E9-E10.5). Following fixation, embryos were washed twice in PBS-DEPC and dehydrated through a series of methanol washes (25%, 50% and 75% methanol in PBS-DEPC), followed by 2 washes in 100% methanol. All wash steps were performed on ice on a shaking platform for 20-30 minutes, depending on embryonic stage. Dehydrated embryos were stored at -20^{o}C in 100% methanol for further use. Alternatively, older embryos were fixed at room temperature (RT) overnight in Bouin's fixative (Sigma). They were then washed thoroughly in PBS, dehydrated to 70% ethanol and stored at 4^{o}C. Those required for histology were later dehydrated to 100% ethanol.

2.2.2 Whole embryo culture

The ability to culture mouse embryos throughout the stages of neurulation allows experimental studies and chemical manipulations which would not otherwise be possible in a mammalian system (Copp et al., 2000; Pryor et al., 2012). To optimise the success of culture experiments, high quality rat serum was used and embryos were carefully dissected using flame-sterilised instruments.

2.2.2.1 Preparation of rat serum

Blood serum from adult male rats was prepared at UCL Biological Services. Animals were anaesthetised by isoflurane inhalation, with anaesthesia confirmed by pinching of one of the paws. After surgical opening of the abdomen, blood was withdrawn from the abdominal aorta using a syringe, until the animal had been exsanguinated. Death was confirmed by cutting of the diaphragm. Blood was immediately centrifuged at RT for 5 minutes (10,000 g) to separate the blood cells

from the serum supernatant, which then rapidly clots. The clot was squeezed using flat-tipped forceps and the serum was transferred to a new 15 ml tube. If it appeared pink in colour rather than pale yellow, indicating contamination by red blood cells, it was centrifuged again, or discarded if persistently pink-coloured. All tubes of serum were then pooled, heat-inactivated at 56^{o}C for 30 minutes, chilled on ice and aliquoted (1-5 ml volumes) for storage at -20^{o}C. Aliquots of rat serum were thawed immediately before use, warmed to 37^{o}C and passed through a Millipore filter (0.45 µm pore size).

2.2.2.2 Culture method

After dissection for culture (Section 2.2.1), embryos were transferred to a fresh dish of pre-warmed dissecting medium. Meanwhile, 30 ml plastic culture tubes (Nunc) were prepared by smearing the outer rim with a small amount of silicone grease (Borer Chemie) to create an airtight seal. The required volume of rat serum (0.5 ml serum per E8.5 embryo, 1 ml per E9.5 embryo) was pipetted into the culture tubes and gassed for 1 minute with the appropriate mixture (Table 2.1) by attaching a glass Pasteur pipette to the cylinder with plastic tubing. Gas was blown gently on to the inner wall of the tube, causing the surface of the serum to gently ripple without bubbling. Culture tubes were then equilibrated for at least 15 minutes in a 37^{o}C roller culture incubator (B.T.C Engineering).

Embryos were transferred to the serum using a plastic Pasteur pipette, ensuring that a minimal amount of dissecting medium was introduced. Serum was then re-gassed as before and the tubes were returned to the culture incubator, with the lid covered to protect from light. For short cultures (around 6 hours) embryos did not need to be gassed again after the start of the experiment. For longer cultures embryos were re-gassed every 6-12 hours.

Embryonic day	Composition of gas mixture
E7.5-E9.5 (cranial neural tube open)	5% O_2, 5% CO_2, 90% N_2
E9.5-E10.5 (cranial neural tube closed)	20% O_2, 5% CO_2, 75% N_2
Older than E10.5	40% O_2, 5% CO_2, 55% N_2

Table 2.1 Gas mixtures administered during whole embryo culture

2.2.2.3 Assessment of embryos after culture period

At the end of the culture period, embryos were transferred into pre-warmed dissecting medium and assessed immediately. Yolk sac appearance and circulation, which develops at E8.5-E9.0, were scored as an indicator of embryonic viability. The categories used for scoring are detailed in Table 2.2; embryos with a score of 1 or 0 were excluded from further analyses. After opening the yolk sac and amnion, developmental progression was assessed by counting the number of fully-formed somite pairs. The crown-rump length (CRL) was also measured as an indicator of overall growth (see Section 2.2.3). Any gross abnormalities, for example embryos which had not turned by the appropriate stage or those with opaque tissue, were also recorded.

Yolk sac score	Description
3	Round, smooth yolk sac with a strong, unidirectional circulation
2	Moderate circulation, yolk sac surface may be slightly crinkled
1	Weak circulation, crumpled yolk sac
0	No yolk sac circulation

Table 2.2 Categories for scoring yolk sac circulation after whole embryo culture

2.2.2.4 DiI labelling

To fluorescently label cells in the midline (see Chapter 4), E9.0 embryos were injected with DiI (1,1'-dioctadecyl-3,3,3',3'-tetramethylindocarbocyanine perchlorate; Molecular Probes, USA) prior to culture. DiI solution was prepared by dissolving in DMSO (4 mg/100 µl) and diluting ten-fold in 3 mol/L sucrose. Aliquots were wrapped in foil to protect them from light and stored at −20°C; they were thawed before use and any unused DiI solution was kept at 4°C for short term storage. Glass microinjection needles were pulled on a Flaming-Brown horizontal pipette puller (Sutter Instrument Co., USA) and were prepared by breaking the end using a microforge (Narishige, Japan). Ideally, the orifice diameter was wide enough to allow DiI solution to be drawn up into the needle, but narrow enough to prevent the solution leaking when the needle was placed in the dissecting medium. Needles were attached to a hand-held mouth pipetting tube.

Embryos were dissected for culture as shown in Figure 2.1G. To prepare them for injection, embryos were then transferred to a 55 mm petri dish containing 2% agarose (w/v in PBS; 2-3 mm deep) and fresh dissecting medium. A small 'window' was made in the yolk sac overlying the PNP, taking care not to damage the amnion layer (Figure 2.2A). A drop of DiI was placed on to a petri dish lid and a small amount was drawn up into the needle. Embryos were held in place by lodging them in a small well in the agarose. Injections were made by piercing the amnion and just penetrating the dorsal surface of the neuroepithelium. Two marks were made in the midline at the level of the open PNP by releasing the DiI while slowly withdrawing the needle (Figure 2.2C).

When several embryos had been labelled, they were examined under a fluorescence stereomicroscope (Leica MZ FLIII) to check for correct DiI localisation. When viewed from the side, successful injections appeared as two marks in the

ventral region of the neural plate (Figure 2.2D). The caudal region was photographed from the dorsal side using a digital camera attached to the microscope and any additional, ectopic DiI marks in the amnion were recorded. To allow the identification of individual embryos at the end of the culture, they were labelled by pushing strands of suture thread (different combinations of long and short pieces) through a small region of the yolk sac at the opposite side to the PNP (Figure 2.2B). Embryos were then cultured as described in Section 2.2.2.2 (maximum of three per tube).

At the end of the culture period the embryos were assessed as described above (Section 2.2.2.3). Some appeared abnormal, likely due to the damage caused to the yolk sac or damage to the embryonic tissue by the injections themselves, and these were excluded from further analysis. Further photographs were taken, to allow 'before and after' measurements of the DiI marks to be made (see Chapter 4). Importantly, the localisation of DiI was evaluated by viewing the embryo from the side (Figure 2.2E) and, for some, this was confirmed by embedding the embryos in wax for transverse histological sectioning. Embryos for which DiI labelled tissues other than the neuroepithelium were excluded from the analysis.

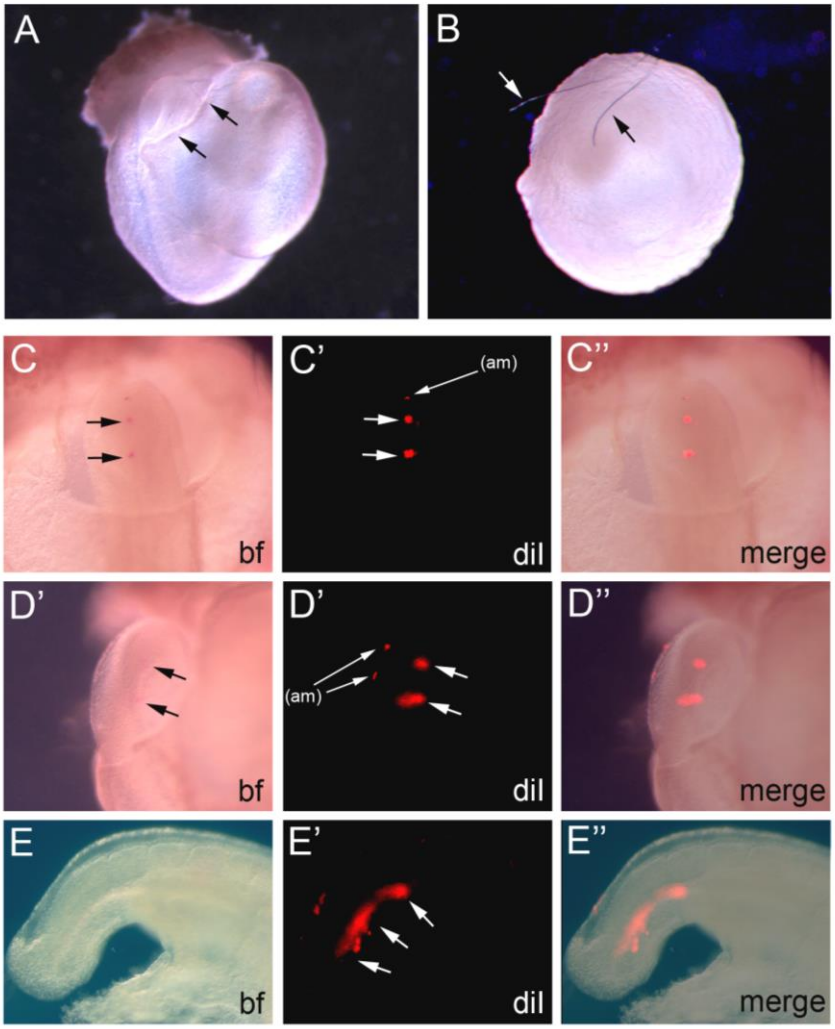

Figure 2.2 DiI labelling

(**A**) E9.0 embryo dissected for culture for which a 'window' has been cut in the yolk sac at the level of the PNP (arrows). (**B**) Embryo labelled with individual strands of suture material (arrows) ready for culture. (**C**) Dorsal view of the caudal region of an embryo immediately after DiI labelling. C' and C'' show fluorescent and merged images, respectively. Arrows point to the two midline marks; an additional, ectopic mark is visible in the amnion overlying the PNP. (**D**) The caudal region in C viewed from the side. In this orientation, the correct localisation of DiI in the ventral neural plate can be confirmed (arrows). Fluorescent and merged images are shown in D' and D''. Marks from where the needle has pierced the amnion can also be seen. (**E**) Side view of the caudal region of an embryo at the end of the culture. Arrows indicate DiI correctly localised in the (now closed) ventral neural tube. Abbreviations: bf = bright field, am = amnion.

2.2.2.5 Whole embryo culture with the ROCK inhibitor, Y27632

Inhibition of Rho-kinase (ROCK) during PNP closure was achieved by culturing E9.0 embryos with the pharmacological inhibitor Y27632 (Calbiochem; see Chapter 5). Y27632 was prepared by dissolving in sterile Milli-Q H_2O (5 mMol/L) and aliquoting on ice. Aliquots were wrapped in foil to protect them from light and stored at −20°C; they were thawed on ice before use and any unused solution was discarded due to the inhibitor's high sensitivity to light.

Intitally, a range of Y27632 concentrations (3-10 µMol/L) was tested in order to find a suitable dose. These were based on concentrations used previously for embryos with a similar genetic background (Ybot-Gonzalez et al., 2007b). Wild type (CBA/Ca) embryos were dissected for culture and evenly distributed (in terms of embryonic stage) between treatment groups. Culture serum was supplemented with Y27632 or sterile Milli-Q H_2O (vehicle control). When embryonic viability was assessed after culture, a concentration of 5 µM Y27632 (ie 1 µl of 5 mMol/L stock solution added to 1 ml of serum) was deemed suitable. It was found to be the highest dose at which normal development progressed, with higher concentrations causing toxic effects such as poor yolk sac circulation and failure of embryonic turning. As detailed later in this thesis, 5 µM Y27632 allowed normal development but had a specific effect on PNP closure in mutant embryos (Chapter 5).

2.2.3 Embryonic measurements

Throughout this project, various morphometric measurements were taken. Live embryos were measured after dissection using an eyepiece graticule on a stereo-microscope. Distance in graticule units was converted to mm for the objective used (Table 2.3). Caudal length and axial curvature were measured later from photographs using Image J software (version 1.47k).

Objective magnification	mm per 100 graticule units	mm per 1 graticule unit
0.8	12.5	0.125
1	10	0.1
1.2	8.33	0.0833
1.6	6.25	0.0625
2	5	0.05
2.5	4	0.04
3.2	3	0.03
4	2.5	0.025
5	2	0.02
6.6	1.515	0.01515

Table 2.3 Measurement conversions

Table used to convert embryonic measurements made using various microscope objectives. For example, a measurement of 20 graticule units under a 5x objective was converted to 0.4 mm (20 x 0.02).

2.2.3.1 Crown-rump length

Embryonic CRL was assessed as an indicator of overall embryonic growth. CRL was measured as the distance from the top of the head, diagonally to the furthest point along the trunk (Figure 2.3A).

2.2.3.2 Posterior neuropore size

The size of the PNP was assessed immediately after dissection. For E8.5-E9.5 embryos, PNP length was measured as the distance from the rostral limit of the open PNP to the caudal end of the embryo. At E10-E10.5, the stage at which tail bud development begins, PNP length was measured as the distance from the rostral to caudal end of the open neuroepithelium (Figure 2.3B, C). PNP width was

measured by taking a dorsal view of the caudal region and recording the longest distance between the two open neural folds (Figure 2.3D).

2.2.3.3 Caudal parameters

The width of the caudal region was measured by taking a dorsal view and measuring the widest point of the embryo, at the same axial level as the PNP width measurement (Figure 2.3D). The length of the caudal region was measured from photographs of the caudal half of the embryo, taken from a lateral view. The allantois was used as a ventral morphological marker, on the assumption that the position of this structure would not be affected by any changes in convergence and extension of dorsal tissues (see Chapters 3 and 4). A straight line was drawn up through the centre of the allantois to the dorsal surface of the embryo, and the curved distance between this point and the tip of the tail was recorded. Caudal length was also analysed by measuring the length of the region occupied by the most recently formed six somites; this was again measured from photographs (Figure 2.3E).

2.2.3.4 Axial curvature

The ventral curvature of the caudal region was measured from photographs using the method described previously (Brook et al., 1991). A straight line was drawn along the middle of the caudal end of the embryo, parallel to and equidistant from the dorsal and ventral surfaces. A second line was drawn tangential to the ventral edge of the penultimate somite, and the angle at which these two lines intersected was measured (X; Figure 2.3F).

2.2.3.5 Midline tissues

The width of the notochord and ventral neuroepithelial midline were measured from photographs of histological sections (Figure 2.3G).

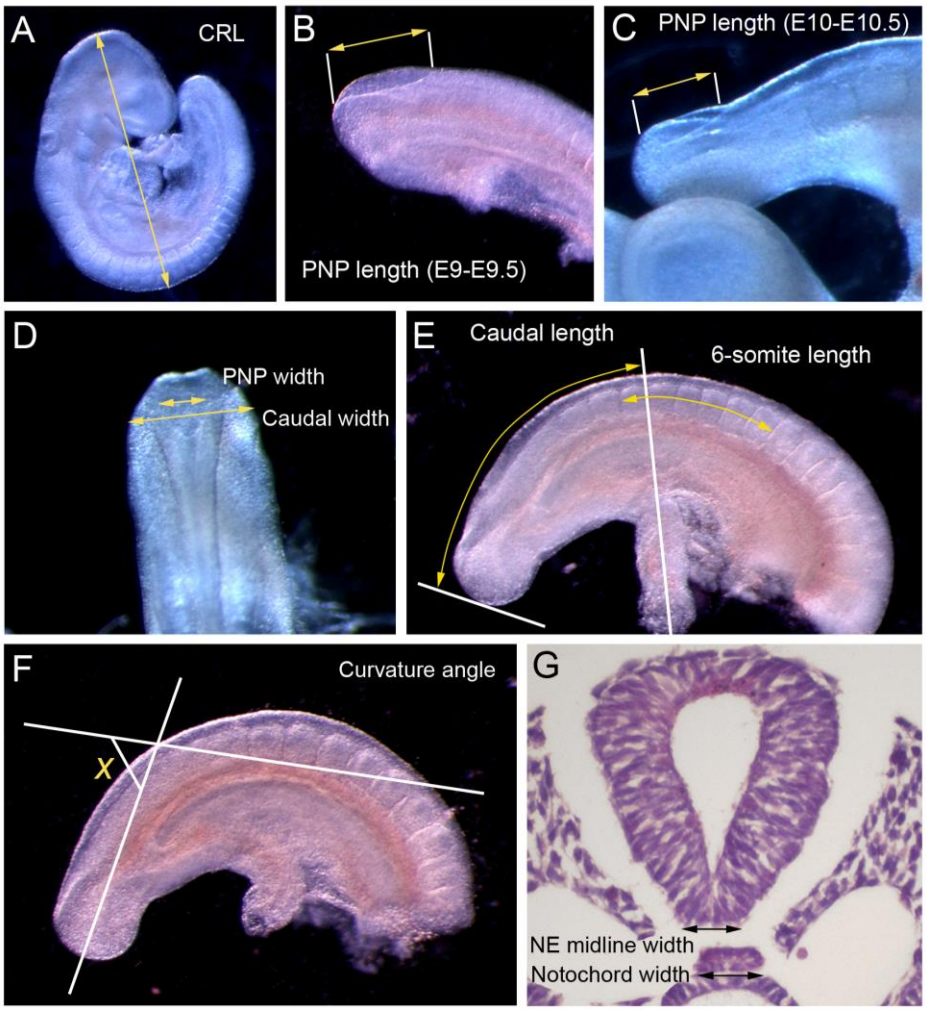

Figure 2.3 Embryonic measurements

Crown-rump length (CRL; A), PNP length (B, C), PNP width and caudal width (D) were measured immediately after dissection. Caudal length measurements (E) and the angle of ventral curvature (F) were measured from photographs of the caudal region (lateral view). The width of the ventral neuroepithelial (NE) midline and notochord was measured from photographs of haematoxylin and eosin stained histological sections (G).

2.3 Histology

Embryos were processed in one of the following ways: 1) Embryos for immunohistochemistry, haematoxylin and eosin (H and E) staining and DiI-labelled embryos were embedded in paraffin wax for microtome sectioning (see Section 2.3.1), 2) Embryos that had been used for whole mount *in situ* hybridisation were embedded in gelatine/albumin or agarose and sectioned using a vibratome (see Section 2.3.3).

2.3.1 Wax embedding

PFA-fixed embryos were taken from -20^{o}C storage in 100% methanol and washed twice in 100% ethanol for 30 minutes, rocking at room temperature. Embryos that had been fixed in Bouin's fixative were taken from 4^{o}C storage in 70% ethanol and dehydrated to 100% ethanol (80%, 90% and 100% washes for 1 hour, followed by a further wash in 100%). Embryos were then transferred to individual glass embedding moulds (Agar Scientific) and cleared by two Histo-Clear (National Diagnostics) washes, the first at room temperature and the second in a 60^{o}C oven (ThermoScientific). Histo-Clear incubation times were: 15 minutes for E8.5, 20 minutes for E9-9.5 and 30 minutes for E10-10.5 and pieces of tissue from older embryos. The Histo-Clear was replaced with molten paraffin wax and embryos were incubated in four 45-minute washes at 60^{o}C. Moulds were transported on heated metal trays during the wax changes, to prevent the wax from solidifying. After the fourth incubation, moulds were viewed under a stereomicroscope and embryos were orientated using heated forceps. The wax was then allowed to set overnight at room temperature.

2.3.2 Microtome sectioning

Solid wax blocks were removed by placing the moulds at -20°C until they could be easily pushed out (15-20 minutes). Blocks were then cut to shape, mounted on to a wooden cube using molten wax and left on ice to harden. Sections were cut on a microtome (Thermo Scientific) at a thickness of 7 µm (for immunohistochemistry) or 10 µm (for H and E staining). Ribbons or individual sections were then transferred to SuperFrost Plus slides, which had been covered with Milli-Q water and placed on a heated plate. When all the wrinkles had flattened out the water was drained from the slides, they were transferred to metal racks and then left to dry in a 37°C incubator overnight. Slides were stored in a plastic slide box at RT.

2.3.3 Gelatine/albumin and agarose embedding

Following whole mount *in situ* hybridisation, embryos in PBT (PBS-DEPC with 0.1% Tween-20) were embedded in a gelatine/albumin (G/A) mixture for vibratome sectioning. A gelatine solution (Sigma; 1.5% w/v in PBS) was added to an albumin solution (albumin from chicken egg white, Sigma; 45% w/v in PBS) and stirred by hand until smooth. Sucrose (Sigma) was then added to the mixture (20% w/v) and dissolved. Aliquots of the G/A solution were stored at -20°C until further use. Embryos were transferred into individual bijoux tubes containing G/A (0.5 ml for E8.5 embryos, 1 ml for E9.5 embryos), ensuring that no bubbles were introduced, and left overnight at 4°C. For embedding, 300 µl of G/A was pipetted into a small plastic embedding mould, again taking care not to introduce bubbles. Gluteraldehyde (30 µl) was added, quickly stirred and the embryo was immediately transferred into the well using syringe needles. The embryo was orientated and the block was left to set for approximately 1 hour. Blocks were removed from the plastic mould using a scalpel, transferred to a bijoux tube containing PBS and left at 4°C until required.

Alternatively, embryos were embedded in agarose (2% w/v in PBS). In this case warm agarose was poured into a plastic embedding mould and an embryo was transferred to the mould. The embryo was orientated using forceps as the agarose polymerised. Blocks were left on ice to allow the agarose to set completely.

2.3.4 Vibratome sectioning

Gelatine/albumin (or agarose) blocks were attached to the specimen disc of the vibratome (Leica) with super glue. The vibratome tray was filled with PBS and the specimen disc was secured within it. Sections were cut at a thickness of 40 µm (G/A blocks) or 50 µm (agarose blocks) and arranged in order on dry SuperFrost slides. When the excess PBS had dried, slides were mounted with coverslips using 50% glycerol (v/v in Milli-Q water; G/A sections) or Mowiol mounting medium (Sigma; agarose sections). Slides were sealed at the corners with nail varnish and stored at 4°C until required.

2.3.5 H and E staining

Wax was removed by incubating the slides in Histo-Clear (2 x 10 minutes). Sections were then washed twice in 100% ethanol (2 minute washes), rehydrated (95%, 75%, 50% and 25% ethanol; 2 minute washes) and incubated in tap water for at least 2 minutes. Slides were incubated in filtered Mayer's haematoxylin (to stain the nuclei) for approximately 1 minute, before washing under running tap water. Next, slides were incubated in filtered eosin (to stain the cytoplasm; 1% w/v in H_2O; Acros Organics) for approximately 3 minutes and again washed in water. After each incubation the intensity of staining was checked under a light microscope and a further incubation step was performed if necessary. The sections were then dehydrated by brief ethanol washes (25%, 50%, 75%, 100%), allowed to dry at RT and mounted with DPX mounting medium (Grale Scientific).

2.4 Neural tube explant culture

2.4.1 Preparation of cover-glasses

Circular, 13 mm cover-glasses were placed into individual wells of a 12-well tissue culture plate, under sterile conditions. A large drop (150 µl) of poly-D-Lysine (Sigma; stock solution of 0.5 mg/ml in PBS aliquoted and stored at -20^{o}C; fresh working solution of 40 µl into 1 ml PBS prepared for each experiment) was pipetted on to the centre of each cover-glass and left at RT for 30 minutes. This volume was sufficient to completely cover the surface of the glass, but not enough to overflow on to the bottom of the well. The poly-D-Lysine was then removed and the plate allowed to air dry in the tissue culture cabinet for a further 30 minutes. The same volume of fibronectin (Sigma; stock solution of 1 mg/ml in PBS stored at -20^{o}C; working solution of 50 µl into 1 ml PBS) was then pipetted on to the cover-glasses; again this was left for 30 minutes and removed. The plates were allowed to air dry again for 30 minutes; care was taken not to over dry the plates at this stage, as this was found to adversely affect the attachment of the explants.

2.4.2 Dissection and culture

To prepare embryonic neural tubes for explant culture, the cranial region was first removed, and the embryo was digested in 2% Pancreatin (Sigma) in PBS at 37^{o}C for 15 minutes to facilitate dissection. The neural tube adjacent to the most caudal five somites was then dissociated from the surrounding tissues (Figure 2.4) and transferred to a cover-glass in a 12-well tissue culture plate. Explants were cultured at 37^{o}C (5% CO_2/95% air) in a large droplet of phenol red-free DMEM (which does not auto-fluoresce) containing 10% fetal calf serum and 1% penicillin/streptomycin for 1-2 hours, until they attached to the cover-glass. A further 2 ml of medium was then added to each well. For 48 hour cultures, the culture medium was replaced after 24 hours with serum-free medium containing supplements for neural cell

culture (N2 and B27; Invitrogen) and growth factors (EGF and FGF). At the end of the culture period, explants were rinsed in PBS, fixed for 10 minutes in 4% PFA and stored in PBS at 4^{o}C.

2.4.3 Analysis

The rate of cell migration over two days was assessed by measuring the area of outgrowth of the explant as a percentage increase of the area covered by the central explant tissue at 24 hours (see dotted lines in Figure 7.13A, Chapter 7). This allowed for any variation due to differences in the original size of the explant, or to pieces of the tissue detaching and floating away during the first few hours of culture. The migration rate was also analysed by measuring the distance travelled by YFP-positive leading edge NC cells from the periphery of the central explant tissue.

The polarity of NC cells at the leading edge was assessed by measuring the distribution of cell area relative to the direction of migration, with ‘forward’ defined as the direction away from the central mass of neuroepithelial tissue. The cell area within six circular sectors, centred on the nucleus, was measured, allowing each cell to be designated ‘front’, ‘sides’ or ‘back’ based on the direction in which the majority of their area was distributed (see examples in Figure 7.18, Chapter 7). Cells which did not display a majority of at least 5% in any direction were designated ‘none’. Cells which were polarised in the direction of forward migration were therefore defined as those with the majority of their area distributed towards the front. All area and distance measurements were performed using ImageJ software.

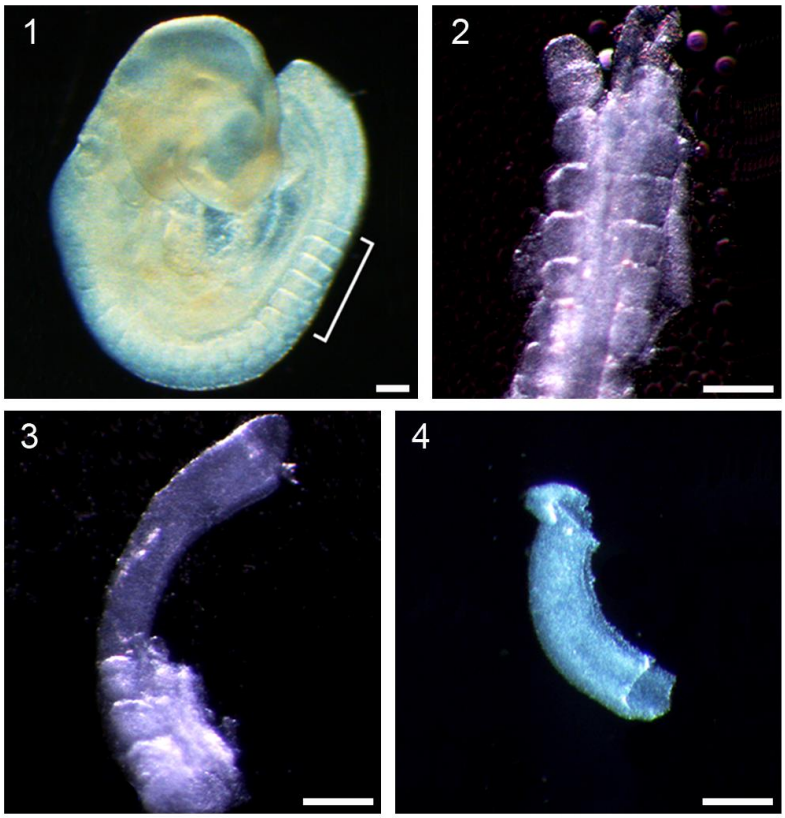

Figure 2.4 Dissection of neural tube explants

Method of preparing neural tube explants for outgrowth culture. After enzymatic digestion, the neural tube was isolated adjacent to the most posterior five somites (white bracket in 1). Surrounding surface ectoderm and somitic tissues were removed (2, 3) to produce a cleanly-dissected explant (4). Scale bars: 200 µm.

2.5 Genotyping

Genotyping of mice and embryos was carried out by polymerase chain reaction (PCR) amplification of DNA extracted from ear punches and yolk sacs respectively. Mouse genotyping was performed by Dawn Savery. A master mix of the reaction mixture was prepared and dispensed into 0.2 ml or 0.5 ml tubes before adding the DNA samples and amplifying using specific primers in a thermal cycler. Positive and negative control tubes were included for each batch of samples.

2.5.1 DNA extraction

Frozen yolk sacs were thawed at room temperature and briefly centrifuged. DNAreleasy^{TM} (Anachem), a lysing reagent which releases DNA from cells, was added to each sample (20 µl of solution, diluted 20% v/v in Sigma water) and tubes were processed in a thermal cycler (see Table 2.4 for running conditions). At the end of the programme, tubes were briefly centrifuged and stored at -20^{o}C.

Step	Temperature (^{o}C)	Duration
1	65	15 minutes
2	96	2 minutes
3	65	4 minutes
4	96	1 minute
5	65	1 minute
6	96	30 seconds
7	20	10 minutes

Table 2.4 Thermal cycler programme for cell lysis using DNAreleasy

2.5.2 *Vangl2* genotyping assays

Vangl2^{Lp} genotyping was performed by PCR amplification of the polymorphic *Crp* microsatellite region, which is closely linked to *Lp* on mouse chromosome 1 (Copp et al., 1994). The PCR reaction mixture and running conditions were as shown in Table 2.5 and Table 2.7. On the CBA background the *Vangl2*$^{+}$ and *Vangl2*^{Lp} alleles co-segregated with 150 and 140 base pair (bp) fragments, respectively. On the C57BL/6J background (that is, when *Lp* was crossed to *Wnt1-Cre* or *R26*^{YFP}; see Chapter 7) the *Vangl2*$^{+}$ and *Vangl2*^{Lp} alleles co-segregated with 95 bp and 140 bp fragments, respectively. For *Vangl2*$^{+}$, *Vangl2*^{flox} and *Vangl2*$^{-}$ genotyping, two PCRs were performed: one to detect the wild type (+) and floxed alleles and another to detect the deleted (-) allele. The PCR reaction mixtures and running conditions were as shown in Table 2.6 and Table 2.7. Amplification gave PCR products of the following bp lengths: 560 (wild type), 701 (floxed) and 203 (deleted).

Reaction component	**Volume (µl)**
10x NH_4 Reaction buffer (Bioline)	5
50 mM $MgCl_2$ (Bioline)	1.5
2 mM dNTPs (Promega)	5
40 µM Primer mix (Sigma)	0.3
5 U/µl Taq DNA polymerase (Bioline)	0.5
H_2O (Sigma)	35.7
Genomic DNA	2
Total volume:	**50**
Primers (5'-3') : Forward: GAGGGAGAAGAATTATGTCTG Reverse: AGAATCTGACTTACCCATGGT	

Table 2.5 PCR reaction mixture for *Vangl2*^{Lp} genotyping

Reaction component	Volume (µl)
5x GoTaq Flexi buffer (Promega)	4
25 mM $MgCl_2$ (Promega)	0.8
2 mM dNTPs (Promega)	2
10 µM F primer (wild type/flox or deleted)	1
10 µM common R primer	1
5 U/µl GoTaq Flexi DNA polymerase (Promega)	0.5
H_2O (Sigma)	8.7
Genomic DNA	2
Total volume:	**20**
Primers (5'-3') : Wt/flox forward: CCGCTGGCTTTCCTGCTGCTG Del forward: TTGACCTCAGTGCAGCGCCC Common reverse: TCCTCGCCATCCCACCCTCG	

Table 2.6 PCR reaction mixture for *Vangl2*$^{+}$, *Vangl2*^{flox} and *Vangl2*$^{-}$ genotyping

Step	*Vangl2*^{Lp}	Vangl2^{+}/Vangl2^{flox} and Vangl2^{-}
1. Heating	95^{o}C, 2 minutes	95^{o}C, 2 minutes
2. Denaturation	94^{o}C, 1 minute	95^{o}C, 30 seconds
3. Annealing	58^{o}C, 1 minute	67.5 ^{o}C, 30 seconds
4. Extension	72^{o}C, 1 minute	72^{o}C, 30 seconds
5. Final extension	72^{o}C, 10 minutes	72^{o}C, 10 minutes

Table 2.7 PCR running conditions for *Vangl2* genotyping

For *Lp* PCRs, steps 2-4 were repeated for 35 cycles. For wild type/flox and deleted PCRs, steps 2-4 were repeated for 16 cycles, with the annealing temperature decreasing by 0.5 ^{o}C per cycle until it reached 60 ^{o}C. Steps 2-4 were then repeated for a further 19 cycles with the annealing temperature at 60 ^{o}C.

2.5.3 *Grhl3* genotyping assays

Grhl3^{ct} genotyping was performed by PCR amplification of the region upstream of *Grhl3* containing the C21350T enhancer mutation (Gustavsson et al., 2007). The PCR reaction mixture and running conditions were as shown in Table 2.8 and Table 2.10. Amplification gave a 551 bp product for both the wild type and mutant alleles. The *curly tail* mutation causes loss of one of the two *Aci1* restriction sites (CCGC) that are normally located within the 551 bp region. Therefore, PCR products were digested with Aci1 restriction enzyme (New England BioLabs) for a minimum of 6 hours (usually overnight) at 37^{o}C. The reaction contained 1.5 µl 10x NEB3 buffer, 0.15 µl Aci1, 0.15 µl BSA, 3.2 µl H_2O and 10 µl PCR product (total volume of 15 µl). Digested samples were separated on a 2% agarose gel: the wild type *Grhl3* allele (+ or +^{ct}) produced three bands (165, 271 and 115 bp) and the mutant (*ct*) allele produced two bands (436 and 115 bp). Four bands were therefore visible for heterozygous samples.

For *Grhl3*$^{+}$, *Grhl3*^{flox} and *Grhl3*$^{-}$ genotyping, two PCRs were performed: one to detect the wild type and floxed alleles and another to detect the deleted allele. The PCR reaction mixtures and running conditions were as shown in Table 2.9 and Table 2.10. Amplification gave PCR products of the following bp lengths: 300 (wild type), 400 (floxed) and 250 (deleted).

Reaction component	Volume (µl)
10x NH_4 Reaction buffer (Bioline)	3
50 mM $MgCl_2$ (Bioline)	0.7
2 mM dNTPs (Promega)	1.5
40 µM Forward primer (Sigma)	1.5
40 µM Reverse primer (Sigma)	1.5
5 U/µl Taq DNA polymerase (Bioline)	0.15
5 M Betain (Sigma)	5
H_2O (Sigma)	15.65
Genomic DNA	1
Total volume:	**30**
Primers (5'-3'): Forward: TTGTATTTTCTTGCTTGAAACG Reverse: TCAGCGTAAGAAAGCTGTGG	

Table 2.8 PCR reaction mixture for *Grhl3*^{ct} genotyping

Reaction component	Volume (µl)
10x NH_4 Reaction buffer (Bioline)	5
50 mM $MgCl_2$ (Bioline)	1.5
2 mM dNTPs (Promega)	5
40 µM Primer mix (Sigma)	0.3
5 U/µl Taq DNA polymerase (Bioline)	0.5
H_2O (Sigma)	35.7
Genomic DNA	2
Total volume:	**50**
Wt/flox primers (5'-3'): F: CCCCTGAGCAGTTTGGAATA R: TGGCCACACTGACAAGAGAG Del primers (5'-3'): F: GAATTACAAGTCTGTGCCACCA R: ATTTGCTGACCTTTTTCTGAGC	

Table 2.9 PCR reaction mixture for *Grhl3*$^{+}$, *Grhl3*^{flox} and *Grhl3*$^{-}$ genotyping

Step	*Grhl3*^{ct}	Grhl3^{+}/Grhl3^{flox} and Grhl3^{-}
1. Heating	96^{o}C, 5 minutes	95^{o}C, 2 minutes
2. Denaturation	96^{o}C, 30 seconds	94^{o}C, 30 seconds
3. Annealing	54^{o}C, 30 seconds	60^{o}C, 30 seconds
4. Extension	72^{o}C, 45 seconds	72^{o}C, 45 seconds
5. Final extension	72^{o}C, 5 minutes	72^{o}C, 5 minutes

Table 2.10 PCR running conditions for *Grhl3* genotyping

Steps 2-4 were repeated for 35 cycles for each PCR.

2.5.4 *Cre* and sex genotyping assays

The presence of the Cre recombinase sequence was detected by PCR amplification of a 500 bp fragment. The PCR reaction mixture and running conditions were as shown in Table 2.11 and Table 2.13 and amplification gave a 500 bp product. To reliably distinguish between *Cre*-negative samples and those that had simply not amplified, primers that amplified a 145 bp fragment of the wild type *Mthfr* sequence were also added to the reaction mix (see Table 2.11).

Finally, the sex of some embryos was determined (see Chapter 6) by amplifying a fragment of the *smc* locus. The PCR reaction mixture and running conditions were as shown in Table 2.12 and Table 2.13. Female and male samples generated one and two bands, respectively (due to an intron difference between the X and Y genes).

Reaction component	Volume (µl)
10x NH_4 Reaction buffer (Bioline)	5
50 mM $MgCl_2$ (Bioline)	1.5
2 mM dNTPs (Promega)	6
40 µM Cre primer mix (Sigma)	0.3
40 µM Mthfr F primers (Sigma)	0.3
40 µM Mthfr R primer (Sigma)	0.3
5 U/µl Taq DNA polymerase (Bioline)	0.5
H_2O (Sigma)	35.7
Genomic DNA	2
Total volume:	**50**
Primers (5'-3'): Cre F: ACCCTGATCCTGGCAATTTCGGC Cre R: GATGCAACGAGTGATGAGGTTCGC Mthfr F: GAAGCAGAGGGAAGGAGGCTTCAG Mthfr R: GACTAGCTGGCTATCCTCTCATCC	

Table 2.11 PCR reaction mixture for *Cre* genotyping

Reaction component	Volume (µl)
10x NH_4 Reaction buffer (Bioline)	5
50 mM $MgCl_2$ (Bioline)	1.5
2 mM dNTPs (Promega)	5
40 µM Forward primer (Sigma)	0.3
40 µM Reverse primer (Sigma)	0.3
5 U/µl Taq DNA polymerase (Bioline)	0.25
H_2O (Sigma)	35.65
Genomic DNA	2
Total volume:	**50**
Primers (5'-3'): Forward: CCGCTGCCAAATTCTTTGG Reverse: TGAAGCTTTTGGCTTTGAG	

Table 2.12 PCR reaction mixture for sex genotyping

Step	*Cre* PCR	Sex PCR
1. Heating	94^{o}C, 2 minutes	94^{o}C, 5 minutes
2. Denaturation	94^{o}C, 30 seconds	94^{o}C, 1 minute
3. Annealing	63^{o}C, 30 seconds	58^{o}C, 1 minute
4. Extension	70^{o}C, 45 seconds	72^{o}C, 1 minute
5. Final extension	72^{o}C, 5 minutes	72^{o}C, 5 minutes

Table 2.13 PCR running conditions for *Cre* genotyping and sexing of embryos

Steps 2-4 were repeated for 30 cycles for the *Cre* PCR and 35 cycles for the sex PCR

2.5.5 Agarose gel electrophoresis

PCR products were separated by agarose gel electrophoresis and analysed by comparison to appropriate molecular weight markers (Bioline Hyperladders; ladder V for 25-500 bp bands and ladder I for 200-10,000 bp bands). Gel concentrations were 1-4 % w/v agarose dissolved in TAE buffer (40 mM Tris acetate and 1 mM EDTA in water) with ethidium bromide dye added. Orange G (Sigma) solution was used as a loading buffer (50% glycerol and 50% 1x TE buffer [10 mM Tris EDTA pH 8.0] with Orange G powder added to colour).

2.6 Quantitative reverse transcription PCR

For qRT-PCR whole embryos, or the embryonic caudal region containing the last two somites, were washed twice in cold PBS-DEPC following dissection and transferred to sterile eppendorf tubes. Excess PBS-DEPC was removed and samples were immediately frozen on dry ice, before storing at -80°C.

2.6.1 RNA extraction and purification

Total RNA was extracted using TRIzol Reagent (Invitrogen). Volumes given are for an E9-E9.5 caudal sample and were doubled for whole embryos. Samples were taken from storage and kept on dry ice before being homogenised with 500 µl TRIzol by pipetting up and down (tubes were left on wet ice until the whole batch had been processed). Samples were then incubated at RT for 5 minutes, 100 µl of chloroform was added and the tubes were vigorously shaken by hand for 15 seconds. They were then incubated at RT for a further 2-3 minutes, centrifuged at 4^{o}C for 15 minutes (12,000 g) and the upper aqueous phase (containing the RNA) was transferred to a clean eppendorf tube. To precipitate the RNA, 250 µl of isopropanol was added, samples were shaken and incubated at RT for 10 minutes and then centrifuged at 4^{o}C for 10 minutes (14,000 g). The supernatant was removed, taking care not to disturb the gel-like RNA pellet, which was then washed with 500 µl of 75% ethanol in DEPC-H_2O, briefly vortexed and centrifuged at 4^{o}C for 5 minutes (10,000 g). The RNA pellet was dried at RT for no longer than 10 minutes and re-suspended in 15 µl DEPC-H_2O and 0.5 µl RNase inhibitor. Unless immediately proceeding to DNase treatment, RNA samples were frozen on dry ice and stored at -80^{o}C.

To remove DNA contamination from samples, DNase treatment was performed using the DNA-free Kit (Ambion): 1.5 µl of 10x DNase I buffer and 1 µl of DNase I

enzyme was added to the tube, followed by incubated at 37°C for 30 minutes. The reaction was stopped by the addition of 2 µl DNase inactivation buffer, incubating at RT for 2 minutes with occasional flick-mixing. Samples were centrifuged at 4°C for 2 minutes (10,000 g) and the supernatant was transferred to a new tube. RNA concentration was measured using a spectrophotometer (NanoDrop 1000; Thermo Scientific). RNA purity was also assessed by recording the ratio of sample absorbance at 260 and 280 nm (a 260/280 ratio of 2.0 is considered to be pure). Samples generally had a ratio of 1.6-1.8; those with lower values were discarded.

2.6.2 Complementary (c) DNA synthesis

First-strand cDNA was synthesised using the Superscript VILO cDNA Synthesis Kit (Applied Biosystems). RNA samples were thawed on ice and 300 ng was transferred to a clean eppendorf tube (on ice; made up to a volume of 14 µl with DEPC-H_2O), before 4 µl of 5x VILO Reaction Mix and 2 µl of 10x SuperScript Enzyme Mix were added (total volume of 20 µl). Tubes were run in a thermal cycler using the following programme: 25°C for 10 minutes, 42°C for 60 minutes and 85°C for 5 minutes. cDNA samples were diluted by adding 40 µl DEPC-H_2O.

To check that the reverse transcription reaction had worked, cDNA samples were amplified in a standard PCR reaction using primers against the housekeeping gene *glyceraldehyde-3-phosphate dehydrogenase* (*Gapdh*), which produced a 177 bp product. The PCR reaction mixture and running conditions were as shown in Table 2.14 and Table 2.15. cDNA quality was also assessed by running a test qRT-PCR plate, again using *Gapdh* primers.

Reaction component	Volume (µl)
10x NH_4 Reaction buffer (Bioline)	3
50 mM $MgCl_2$ (Bioline)	0.7
2 mM dNTPs (Promega)	1.5
10 µM Forward primer (Sigma)	1.5
10 µM Reverse primer (Sigma)	1.5
5 U/µl Taq DNA polymerase (Bioline)	0.15
H_2O (Sigma)	20.65
cDNA	1
Total volume:	**30**

Table 2.14 Standard PCR reaction mixture

Step	Temperature, Duration
1. Heating	94^{o}C, 5 minutes
2. Denaturation	94^{o}C, 30 seconds
3. Annealing	60^{o}C, 30 seconds
4. Extension	72^{o}C, 30 seconds
5. Final extension	72^{o}C, 10 minutes

Table 2.15 Running conditions for a standard PCR

Steps 2-4 were repeated for 35 cycles

2.6.3 qRT-PCR

2.6.3.1 Primers

The primers used for qRT-PCR were all from Sigma and are listed in Table 2.16. Primers were designed in NCBI Primer-BLAST to amplify an approximately 200 bp fragment of the target gene, with an optimum annealing temperature of 60^{o}C. This programme was also used to ensure that primers would amplify unique products as

it highlighted other potential targets within the mouse genome (by running against the RefSeq RNA database). All primers were tested on a qRT-PCR run using a control cDNA sample (from a wild type embryo); amplification and dissociation (melting) curves were analysed as described in Section 2.6.3.3.

Gene name	Sequence (5'-3')	PCR product size
ArhGEF3	F: GAAGTGCGGCTGGGTGGCTC R: TGGCCGGCAGCAGACAGAAC	194 bp
ArhGEF7	F: CCGGCTGGTTCCCCAGCAAC R: GCAGTGGCCGCAGGTAGGTG	216 bp
Gapdh	F: ATGACATCAAGAAGGTGGTG R: CATACCAGGAAATGAGCTTG	177 bp
Grhl3	F: CCAGACTCCAGTAACAATG R: AAGGGTGAGCAGGTTCGCTT	218 bp
p190RhoGAP	F: TGGATGCGTGGTCAAGCCAAGG R: CAAACCGCCCCAGGCGAGTG	233 bp
RhoGEF19	F: AGCGAAGGCGTTTCTCGGCCTCA R: CTTGCGTGTCCAGCCTGGGTTCC	243 bp
ROCK1	F: CTGCCGGGTGGGATGCGACT R: CCGCGGTGGGTTTGTAGCCG	173 bp
Vangl2	F: CCGGGGATTGGGTAGCGTGT R: GGTCCCACAGCCACCTCCTTCA	214 bp

Table 2.16 Primers for qRT-PCR

2.6.3.2 Sample preparation

qRT-PCR was performed using a fluorescence-based method to measure the amplification of a target gene normalised to an endogenous reference control gene. Here, *Gapdh* was used as the reference gene for all experiments. qRT-PCR plates (Optical 96-Well Fast Thermal Cycling Plate; Applied Biosystems) were prepared on ice using designated pipettes and pipette tips to prevent contamination of samples with genomic DNA. Each sample was analysed in triplicate for both target gene and

Gapdh amplification. A master mix was prepared on ice for each set of primers (see Table 2.17); 23 µl was dispensed into each well after loading 2 µl of the relevant cDNA. A negative control well (2 µl water instead of cDNA) was also included for each primer pair. Plates were then sealed with an adhesive film (MicroAmp Optical Adhesive Film; Applied Biosystems), taking care to keep the surface clean and seal all the wells, before being briefly vortexed and centrifuged.

Reaction component	Volume (µl)
Mesa Blue*	12.5
10 µM Forward primer	2
10 µM Reverse primer	2
H_2O (Sigma)	6.5
Total volume:	**23**

Table 2.17 Master mix for qRT-PCR

*The Mesa Blue qPCR Master Mix Plus for SYBR Assay (Eurogentec) contains a fluorescent reporter dye that binds to double stranded DNA. As the DNA is amplified, the dye is incorporated into newly synthesised DNA. The fluorescent signal can therefore be measured to quantify the level of target gene expression, relative to the *Gapdh* control.

2.6.3.3 Thermal cycling

The qRT-PCR plate was run on a 7500 Fast Real-Time PCR System (Applied Biosystems) using a standard thermal cycling programme consisting of a pre-run (50^{o}C for 2 minutes, 95^{o}C for 5 minutes) and 40 cycles (denaturation at 95^{o}C for 15 seconds, annealing/extension at 60^{o}C for 1 minute). At the end of the programme a dissociation (melting) curve analysis was run; this programme gradually reheated the plate to 95^{o}C while continually monitoring the fluorescence emitted, producing a dissociation curve of fluorescence against temperature. Separation of the two cDNA

strands causes a rapid decrease in fluorescence and, as all PCR products for a primer pair should have the same melting temperature, a single sharp peak should be seen on the graph.

2.6.3.4 Analysis

Analysis of data (amplification and dissociation) was performed using 7500 Software (Applied Biosystems). The dissociation curves for each well were checked first; the presence of additional peaks indicates unwanted PCR products (contamination or primer dimmer) which emit fluorescence and can therefore interfere with the results. Wells with a poor dissociation curve were excluded from further analysis at this point. The amplification graph, showing fluorescence against cycle number, was then examined for each well. The baseline (cycles during which background fluorescence is emitted prior to amplification) and 'threshold' levels (see below) were adjusted for each target gene and *Gapdh*.

The analysis of gene expression levels was based on the principle that, as the target gene is amplified, the level of fluorescence emitted will at some point begin to increase exponentially. This is manually designated as the threshold level on the amplification curve, with the cycle at which the fluorescence reaches this threshold defined as C_T ('threshold cycle'). The C_T value varies depending on the initial level of gene expression and can therefore be used to calculate the relative quantity of the target gene in each sample (with each normalised to *Gapdh*). The consistency of C_T values for triplicates was checked, as were the negative control wells. One wild type sample was also selected as a reference for the relative quantification (RQ) of all other samples on the plate; this was given an RQ value of 1 by the software. Data were exported to Microsoft Excel and the mean RQ value for each sample triplicate was tabulated to allow comparisons of mRNA expression level.

2.7 Whole mount *in situ* hybridisation

RNA probes for whole mount *in situ* hybridisation (WISH) were transcribed from DNA templates, obtained from various sources (Table 2.18).

2.7.1 Plasmid DNA templates

Plasmid DNA was first transformed into competent DH5α cells in order to grow up bacterial cultures. Eppendorf tubes were placed on ice and the appropriate volume of plasmid DNA was added (0.5-1 µl; approximately 0.1 µg DNA). Single use, 50 µl aliquots of competent cells were taken from -80^{o}C storage and placed on ice to thaw for approximately 5 minutes before being transferred to the plasmid DNA tube and gently flick-mixed. A negative control tube (no DNA) was also included. Tubes were then placed on ice for 20 minutes, incubated at 42^{o}C for 50 seconds to heat shock the cells and immediately returned to the ice for a further 2 minutes. Next, 950 µl of RT Luria Bertani broth (LB broth; Invitrogen) was added to each tube and cells were incubated at 37^{o}C, shaking, for 60-90 minutes. Samples were plated on to LB agar (Invitrogen) plates containing 50 µg/ml ampicillin (Sigma; all plasmids contained an ampicillin resistance gene). Two plates, containing 50 µl and 200 µl of the culture, were spread for each sample. Plates were incubated upside down at 37^{o}C overnight (12-16 hours).

The following morning, plates were removed from the incubator and checked for bacterial colonies. The negative plate was examined to ensure that no colonies were present. Pipette tips were used to pick individual colonies (minimum of two per plate) and were dropped into 50 ml falcon tubes containing 5 ml LB broth (and ampicillin). Cultures were incubated at 37^{o}C overnight, shaking. The bacterial cells were then harvested by centrifugation at 4^{o}C (4,600 rpm for 20 minutes); a 0.5 ml

aliquot of the culture was also taken in case larger cultures (for midi preps) were later required.

Plasmid DNA was purified using a mini prep kit (Qiagen) according to the manufacturer's protocol (QIAprep Spin Miniprep Kit using a microcentrifuge). Briefly, cells were resuspended in 250 µl of Buffer P1 (containing RNase A and Lyse Blue reagent) and lysed by addition of 250 µl Buffer P2 (inverted to mix; solution turns blue if Lyse Blue is included). The samples were neutralised by adding 350 µl Buffer N3 (mixed thoroughly until the solution becomes colourless), than cleared by centrifugation at 13,000 rpm for 10 minutes. The supernatant was transferred to a QIAprep spin column; this was centrifuged for 1 minute and the flow-through discarded (DNA remains bound to the membrane). The column was washed with 750 µl Buffer PE, again the column was centrifuged for 1 minute and the flow through was discarded before centrifuging for a further 1 minute. Plasmid DNA was eluted into a clean eppendorf in 50 µl Buffer EB or Sigma water and the concentration was measured using a spectrophotometer.

2.7.2 Preparation of RNA probes

Purified plasmid DNA was linearised by restriction enzyme (restriction endonuclease) digestion. Where possible, small scale digests were initially used to verify the expected insert. In these cases a 20 µl reaction mixture was set up (0.2-0.5 µg DNA, H_2O, 2 µl 10x buffer, 1 µl BSA and 1 µl [10U] enzyme) and incubated at the required temperature for 1-2 hours. Half of the sample was then run on an agarose gel. For large scale digests the volume was scaled up to 200 µl (5-10 µg DNA, H_2O, 20 µl 10x buffer, 10 µl BSA and ~5 µl [50U] enzyme) and the digest was incubated for 2-4 hours.

After checking a sample of the linearised plasmid on a gel, the DNA was purified by phenol-chloroform extraction. An equal volume of phenol chloroform isoamyl alcohol (Sigma) was added to the digest, vortexed briefly and centrifuged for 2 minutes at 13,000 rpm. The upper aqueous layer was transferred to a clean eppendorf tube and the DNA was precipitated by adding 1/10 volume of 3 M sodium acetate (pH 5.2) and 3 times the volume of 100% ethanol and incubating at -80^{o}C for 30-60 minutes (or -20^{o}C overnight). DNA was pelleted by centrifuging at 4^{o}C for 15 minutes (13,000 rpm), the supernatant was removed and the pellet was washed with 500 µl of 70% ethanol. The pellet was allowed to dry at RT for approximately 10 minutes before being resuspended in 20 µl Sigma water.

In general, mini preps yielded 0.2-1 µg/µl of plasmid DNA. Digoxygenin (DIG) labelled, single stranded RNA probes were transcribed in a 20 µl reaction containing: 1 µg linearised plasmid DNA, H_2O, 2 µl DIG labelling mix (Roche), 2 µl 10x transcription buffer (Roche), 0.5 µl RNAse inhibitor and 2 µl RNA polymerase. Reactions were incubated at 37^{o}C for 2-4 hours and the efficiency of transcription was assessed by running 0.5 µl of the sample on a gel. Finally, the sample volume was increased by adding 40 µl of DEPC-water and probes were purified by passing through Chroma Spin-1000 DEPC-H2O columns (Clontech), according to the manufacturer's instructions. Approximately 50 µl of clean probe was collected from the column, to which 40 µl formamide and 1 µl RNase inhibitor was added. Probes were stored at -20^{o}C.

Probe name	Vector	Insert size	RE and RNA polymerase for AS probe	RE and RNA polymerase for S probe	Source	Reference
Brachyury	M13	1660 bp	SacII, T7	-	R. Beddington	(Wilkinson et al., 1990)
Erbb3	pBlueScript - DR3	1400 bp	EcoRI, T7	XhoI, T3	C. Birchmeier	(Meyer and Birchmeier, 1995)
FoxD3	pBlueScript	558 bp	BamHI, T3	HindIII, T7	P. Labosky	(Hanna et al., 2002)
Grhl3	pGEM-T	494 bp	SalI, T7	SP6, NcoI	N. Greene	(Gustavsson et al., 2007)
Sox9	pBlueScript SK	500 bp	EcoRI, T3	XbaI, T7	R. Lovell-Badge	(Morais da et al., 1996)
Vangl1	pGEM-T easy	324 bp	PstI, T7	Apa1, SP6	D. Henderson	(Doudney et al., 2005)
Vangl2	pGEM-T easy	554 bp	ApaI, Sp6	PstI, T7	D. Henderson	(Doudney et al., 2005)
Wnt3a	pGEM 3Zf	1250 bp	ScaI, Sp6	BamHI, T7	A. McMahon	(Takada et al., 1994)
Wnt5a	pGEM 7Zf	2500 bp	XhoI, Sp6	-	A. McMahon	(Takada et al., 1994)

Table 2.18 Probes used for whole mount *in situ* hybridisation

All probes were directed against mouse transcripts. Abbreviations: RE = restriction enzyme, AS = antisense, S = sense.

2.7.3 *In situ* hybridisation

All solutions used were DEPC-treated until after the hybridisation step. Washes were performed on ice on a rocking platform, unless otherwise stated.

2.7.3.1 Tissue pre-treatment and hybridisation

Embryos were taken from -20 ^{o}C storage and placed on ice. For those which had completed cranial neural tube closure, small holes were made in the hindbrain and ventral forebrain to prevent trapping of the probe. If direct comparison of gene expression between genotypes was required, stage-matched embryos were processed in the same tube. Embryos were then rehydrated in bijoux tubes in a series of methanol washes (75%, 50% and 25% methanol in PBT), washed twice in PBT and bleached for 1 hour in 6% hydrogen peroxide (30% stock solution, Sigma) in PBT to inactivate endogenous phosphatases and remove pigmentation. Embryos were then washed 3 times in PBT before being treated with 5 µg/ml proteinase K in PBT at RT to permeabilise the tissue. Treatment times depended on embryonic stage and were: 1 minute for E8.5 embryos, 2-5 minutes for E9.5 and 5-8 minutes for E10.5. The reaction was stopped by briefly washing in glycine (2 mg/ml in PBT), followed by a further wash in PBT and re-fixation in freshly prepared 0.2% v/v gluteraldehyde (25% stock) in 4% PFA for 20 minutes at RT.

After fixation, embryos were washed twice in PBT and transferred to a tube containing 1 ml pre-hybridisation solution, pre-heated to 70^{o}C (50% formamide, 1% sodium dodecyl sulphate [SDS], 5x SSC pH 4.5, 50 µg/ml yeast RNA and 50 µg/ml heparin in DEPC-H_2O). When the embryos had sunk to the bottom of the tube, the pre-hybridisation solution was replaced and the embryos were incubated at 70^{o}C for 2-4 hours (HB-1000 Hybridiser oven; UVP). For hybridisation, 10 µl (approximately 1 µg) of DIG-labelled probe was added and gently mixed by inverting the tube several times. Alternatively, recycled probe solution was used, in which case it was

pre-heated for 30 minutes and used to replace the pre-hybridisation solution after the 2-4 hour incubation period. Embryos were hybridised at 70^{o}C overnight.

2.7.3.2 Post-hybridisation and immunohistochemistry

The following day any unbound probe, which had not hybridised to the target mRNA, was removed through a series of stringent washes. The hybridisation solution was carefully removed and kept at -20^{o}C for further use, before being replaced with pre-heated 'solution 1' (50% formamide, 1% SDS and 5x SSC pH 4.5 in DEPC-H_2O). Embryos were then transferred back to bijoux tubes, washed twice in solution 1 at 70^{o}C for 30 minutes each, followed by two 30-minute washes at 65^{o}C in 'solution 2' (50% formamide, 1% SDS and 2x SSC pH 4.5 in DEPC-H_2O). Next, embryos were washed 3 times at room temperature for 10 minutes each in Tris-buffered saline containing 1% v/v Tween-20 (TBS-T) before being gently rocked at room temperature in TBST containing 10% heat-inactivated sheep serum (SS; Sigma) to block non-specific antibody binding sites. After 90 minutes, the blocking solution was replaced with alkaline phosphatase-conjugated sheep anti-DIG Fab fragments (AP-anti-DIG, Roche), diluted 1:2000 in TBST containing 1% SS, and gently rocked at 4^{o}C overnight. Binding of the AP-anti-DIG antibody to the DIG-labelled RNA probe therefore allowed detection and localisation of the bound probe.

2.7.3.3 Post-antibody washes and developing

To remove unbound antibody, embryos were washed 3 times in TBST for 5 minutes each, rocking at RT, followed by five 60-minute washes. They were then left washing in TBST at 4^{o}C overnight. The following day embryos were washed three times for 10 minutes each in freshly-prepared NTMT solution (100 mM NaCl, 100 mM Tris HCl pH 9.5, 50 mM $MgCl_2$ and 1% Tween-20 in H_2O). The *in situ* signal was then developed using a reaction for the colorimetric detection of alkaline

phosphatase activity. For this reaction embryos were incubated at room temperature, gently shaking and wrapped in aluminium foil to protect them from light, in a developing solution of NTMT containing 4.5 µl/ml nitro blue tetrazolium chloride (NBT, Roche) and 3.5 µl/ml 5-bromo-4-chloro-3-indolyl phosphate (BCIP, Roche). During this step, alkaline phosphatase catalyses the hydrolysis of BCIP, generating an intermediate compound which is oxidised by NBT to produce an insoluble, dark blue precipitate.

Embryos were checked regularly for colour development and the developing solution was replaced when it began to turn pink. For probes which developed very rapidly, the developing solution was diluted to half-strength with NTMT. Conversely, if the staining had not developed sufficiently after one day, embryos were returned to TBST and incubated overnight at 4^{o}C. The following day they were re-washed in NTMT and transferred into fresh developing solution. When the signal had developed to the desired extent, the reaction was stopped by washing twice in PBT, followed by a further wash overnight at 4^{o}C. Embryos were then re-fixed in 4% PFA and stored in the fridge in PBT for further processing.

2.8 Immunohistochemistry

Primary and secondary antibodies and the concentrations used are listed in Table 2.19 and Table 2.20, respectively. All primary antibodies were immuno-reactive against mouse tissue.

2.8.1 Immunofluorescence on tissue sections

Immunofluorescence was performed on 7 µm paraffin wax sections. Before beginning the protocol, one of the following two methods was used to de-wax and rehydrate the sections and to retrieve the antigen:

1) Declere method: Slides were placed in cold Declere solution (Cell Marque; 20x stock diluted to 1x in Milli-Q H_2O) in a plastic slide trough and steamed for 45 minutes in a kitchen steamer. Five minutes before the end, a second trough containing fresh Declere was placed in the steamer to warm. Slides were then transferred to the fresh solution and allowed to cool to RT (approximately 2 hours).

2) Citrate method: Wax was removed with Histo-Clear incubations (2 x 10 minutes) and sections were rehydrated in an ethanol series (100%, 75%, 50% and 25% ethanol followed by tap water; 2 minutes each). Antigen unmasking was then carried out by gently boiling the slides in citric acid buffer (2.1g per litre Milli-Q H_2O, adjusted to pH6) in a microwave (3 mins. medium heat, allow to cool for 1 min., 3 mins. medium, allow to cool for 1 min., 3 mins, high). Slides were left to cool to RT.

For blocking and antibody incubations, 100-200 µl of solution was applied to the surface of the slide and overlaid with a piece of parafilm. All incubations were carried out in a humid chamber (containing tissue soaked in Milli-Q H2O); this was covered in foil during secondary antibody incubations to prevent photobleaching. Washing steps were performed in a plastic slide trough (approximately 200 ml

volume), gently rocking at RT for 10 minutes; this was also foil-covered following the secondary antibody incubation. A negative control slide (no primary antibody) was included for each experiment. Protocols varied slightly for individual antibodies and the steps were as follows:

1) Anti-GFP/YFP: 3 washes in TBST (TBS with 1% Triton), RT for 90 minutes in blocking solution (2 mg/ml BSA, 0.15% glycine and 5% heat inactivated sheep serum in TBST), primary antibody at 4^{o}C overnight, 3 washes in TBST, secondary antibody (fluorescein-labelled goat anti-chicken IgY) at RT for 1 hour.

2) Anti-PH-H3: 3 washes in TBST, RT for 90 minutes in blocking solution (2 mg/ml BSA, 0.15% glycine and 5% heat inactivated sheep serum in TBST), primary antibody at 4^{o}C overnight, 3 washes in TBST, secondary antibody (goat anti-rabbit IgG Alexa-488) at RT for 1 hour.

3) Anti-Casp3: 3 washes in TBST, RT for 90 minutes in blocking solution (5% heat inactivated sheep serum in TBST), primary antibody at 4^{o}C overnight, 3 washes in TBST, secondary antibody (biotinylated goat anti-rabbit) at RT for 1 hour, 3 washes in TBST, streptavidin (green; 1;250; Invitrogen) at RT for 90 minutes.

4) Anti-Ki67: 3 washes in TBST, RT for 90 minutes in blocking solution (5% heat inactivated sheep serum in TBST), primary antibody at 4^{o}C overnight, 3 washes in TBST, secondary antibody (biotinylated goat anti-rabbit) at RT for 1 hour, 3 washes in TBST, streptavidin at RT for 90 minutes.

Finally, slides were washed 3 times in TBST, incubated with DAPI solution (1:10,000 in PBS) at RT for 5 minutes to stain the nuclei, washed 3 times in TBST and mounted with Mowiol.

Target	Species raised in	Dilution and method	Supplier
Cleaved-caspase 3 (Casp3)	Rabbit (polyclonal)	1:250 (wax sections, citrate method)	Cell signalling technology
GFP/YFP	Chicken (polyclonal)	1:100 (wax sections, citrate method) 1:250 (explant cultures)	Abcam
Ki67	Rabbit (polyclonal)	1: 250 (wax sections, Declere method)	Nova-Castra
Phospho-Histone H3 (PH-H3)	Rabbit (polyclonal)	1:250 (wax sections, Declere method)	Miilipore
P75	Rabbit (polyclonal)	1:200 (explant cultures)	Santa Cruz

Table 2.19 Primary antibodies used for immunofluorescence

Target	Species raised in	Conjugate	Dilution	Suppier
Rabbit IgG	Goat	Alexa-488 (green)	1:400	Invitrogen
Rabbit IgG	Goat	Alexa-568 (red)	1:400	Invitrogen
Chicken IgG	Goat	Alexa-488 (green)	1:400	Invitrogen
Rabbit IgG	Goat	Biotin	1:300	Invitrogen
Chicken IgY	Goat	Fluorescein	1:200	Aves Lab inc.

Table 2.20 Secondary antibodies used for immunofluorescence

2.8.2 Immunofluorescence on neural tube explant cultures

Immunocytochemistry was performed on *Wnt1-Cre/YFP* neural crest cell cultures (see Section 2.4 and Chapter 7) after culturing explants for 24 hours. The culture medium was carefully removed from the wells of the tissue culture plate and migratory cells were fixed in 4% PFA at RT for 10 minutes. Cells were washed twice with PBS, gently rocking at RT for 10 minutes, and blocked at RT for 1 hour (1% BSA, 0.15% glycine and 10 % goat serum in PBS).

Primary antibody incubation was carried out (anti-P75 at 4^{o}C overnight followed by/or anti-GFP/YFP at RT for 2.5 hours), followed by two further PBS washes. Secondary antibody incubations were at RT for 1 hour and were performed simultaneously where relevant (mixture of goat anti-rabbit IgG Alexa-568 and goat anti-chicken IgG Alexa-488). After final PBS washes, cover-glasses were removed from the wells using forceps, turned upside down and mounted with Vectashield mounting medium with DAPI (Vector Labs).

2.9 RhoA activation assay

To measure the level of activated (GTP-bound) RhoA in the embryonic caudal region (see Chapter 5), the G-LISA RhoA Activation Assay Biochem Kit was used (Absorbance Based; Cytoskeleton Inc.). This assay consists of individual wells, to which a Rho-GTP binding protein is linked. GTP-bound Rho in a cell/tissue lysate binds to the well during an incubation step and can then be detected with an antibody against RhoA, while inactive (GDP-bound) Rho is removed during washes. Compared to traditional pull-down methods, the assay is quicker, requires less cellular material (10-50 µg protein rather than 1-2 mg) and allows more samples to be processed simultaneously.

2.9.1 Sample preparation

Assay components and other required reagents were prepared prior to beginning the experiment, according to the manufacturer's instructions. Tissue samples were E9.5 embryonic caudal regions that had been immediately snap-frozen on dry ice after dissection and stored at -80^{o}C (see Section 2.6). Throughout the protocol, tissue samples and lysates were processed rapidly on ice to prevent the hydrolysis of GTP, which results in Rho inactivation.

Frozen tissue samples were homogenised by sonication (High Intensity Ultrasonic Processor, Sonics and Materials Inc) in lysis buffer containing a cocktail of protease inhibitors. Samples were removed from -80^{o}C storage and placed on dry ice. Immediately prior to sonication they were thawed in a RT water bath for a few seconds and placed on ice. Sonication was also performed on ice; four PNP samples for each genotype were combined into one of the sample eppendorf tubes (in a total volume of 100 µl lysis buffer). A 20 µl aliquot was retained for protein

quantification and the remaining lysate was snap frozen in liquid nitrogen before being returned to -80^{o}C storage.

2.9.2 Protein quantification

Protein concentration was measured using a spectrophotometer (UVmini-1240, Shimadzu) and Precision Red^{TM} Advanced Protein Assay Reagent. Samples were prepared by transferring 20 µl of lysate and 1 ml of Precision Red to disposable cuvettes and incubating at RT for 1 minute. A blank (lysis buffer and Precision Red) was also prepared. The absorbance of the blank and sample cuvettes was measured at a wavelength of 600 nm, and was then multiplied by five to obtain the protein concentration (mg/ml). Samples generally contained 0.7-0.9 mg/ml protein, with a concentration of 0.5-2 mg/ml required for the assay. The lysis buffer dilutions required to equalise the sample protein concentrations were then calculated, in preparation for the G-LISA assay.

2.9.3 G-LISA assay protocol

The assay was performed according to the instructions provided. For clarity the manufacturer's protocol (as found at www.cytoskeleton.com/bk124) is provided below, with some notes omitted. Each sample was processed in duplicate.

1. Aliquot 60 µl of Lysis Buffer into a labeled microfuge tube and dilute with 60 µl of ice cold Binding Buffer. Vortex for 3-5 s on high and place on ice. This is your buffer blank sample. It is normal for the buffer blank to have a raw reading between 0.1 – 0.4.

2. Aliquot 12 µl of Rho Control Protein into a labeled microfuge tube and dilute with 48 µl of Cell Lysis Buffer and 60 µl of Binding Buffer. Vortex for 3-5 s on high and place on ice. This is your positive control sample.

3. Take the Rho plate out of its bag. Gently peel up the seal from the strips and pull out the number of strips required. Place strips in the extra strip holder provided, and place on ice. Immediately after removing the assay strips, put the rest of the plate back in the pouch with desiccant, seal well and place back in storage.

4. Dissolve the powder in the wells with 100 µl ice cold water, keeping the plate on ice.

5. Thaw the snap frozen cell lysates in a ROOM TEMPERATURE water bath. Immediately place on ice after they are thawed.

6. Based on the calculation of equalization, add required amount of Lysis Buffer to respective tubes to equalize all lysate concentration.

7. Immediately aliquot sufficient lysate for duplicate (60 µl) or triplicate (90 µl) assays into fresh ice cold microcentrifuge tubes.

8. Add an equal volume of ice-cold Binding Buffer to each tube. Vortex each tube for 3-5 s on a high setting and return tubes to ice. Keep on ice.

9. Completely remove the water from the microplate wells by patting on a paper towel

10. Put plate back on ice.

11. Immediately add 50 µl of equalized cell lysate to duplicate or triplicate wells.

12. Pipette 50 µl of buffer blank control into duplicate wells.

13. Pipette 50 µl of RhoA positive control into duplicate wells.

14. Immediately place the plate on a cold orbital microplate shaker (400 rpm recommended, 200 rpm minimum) at 4°C for exactly 30 min.

15. During the incubation, dilute the anti-RhoA primary antibody to 1/250 in Antibody Dilution Buffer by adding 2 µl of antibody to every 500 µl Antibody Dilution Buffer.

16. After 30 min, flick out the solution from the wells and wash twice with 200 µl Wash Buffer at room temperature using a multi-channel pipettor. Do not leave this plate unattended at this time. Vigorously remove the Wash Buffer after each wash by flicking and patting the plate as detailed in step 9.

17. Place plate on the bench.

18. Immediately pipette 200 µl of room temperature Antigen Presenting Buffer into each well using a multi-channel pipettor and incubate at room temperature for exactly 2 min.

19. Vigorously flick out the Antigen Presenting Buffer, patting the inverted plate 5-7 times on a stack of paper towels as outlined in step 9.

20. Immediately wash the wells three times with 200 µl of room temperature Wash Buffer. Vigorously remove Wash Buffer after each wash as detailed in step 9.

21. Add 50 µl of diluted anti-RhoA primary antibody to each well and leave the plate on the orbital microplate shaker (200-400 rpm) at room temperature for 45 min.

22. During the primary antibody incubation, dilute the secondary HRP labeled antibody to 1/62.5 by adding 8 µl of antibody to every 500 µl Antibody Dilution Buffer.

23. Vigorously flick out the anti-RhoA primary antibody, patting the inverted plate 5-7 times on a paper towel as outlined in step 9.

24. Immediately wash the wells three times with 200 µl of room temperature Wash Buffer. Vigorously remove Wash Buffer after each wash as detailed in step 9.

25. Add 50 µl of diluted Secondary antibody to each well and leave the plate on a microplate shaker (200–400 rpm) at room temperature for 45 min.

26. During the secondary antibody incubation thaw HRP detection reagents A and B in a room temperature water bath and remove as soon as they are thawed. Components A and B should be mixed in equal volumes immediately prior to use. Unused mixed solution should be discarded.

27. Immediately prior to the end of the secondary antibody incubation, mix HRP detection reagents A and B in equal volumes.

28. Vigorously flick out the secondary antibody, patting the inverted plate 5-7 times on a paper towel as outlined in step 9.

29. Wash the wells three times with 200 µl of Wash Buffer, patting the inverted plate 5-7 times on a paper towel as outlined in step 9.

30. Pipette 50 µl of the mixed HRP detection reagent into each well and incubate at 37°C for 10-15 min.

31. Add 50 µl of HRP Stop Buffer. Check that the wells are free of bubbles.

2.9.4 Analysis

The colorimetric signal for each well was read by measuring the absorbance (490 nm wavelength) using a microplate spectrophotometer. The mean value (minus the negative control value) was then calculated for each genotype sample and the positive control (see Chapter 5).

2.10 Image processing and statistics

Photographic images were analysed in Image J (version 1.47k) where relevant. Figures were compiled in Photoshop (CS3) and Inkscape (version 0.48). Statistical analyses were performed in SigmaStat (version 3.5).

3. Severe spina bifida in the *Vangl2*$^{Lp/+}$;*Grhl3*$^{ct/ct}$ mouse model

3.1 Introduction

3.1.1 NTDs caused by genetic interactions between *Vangl2* and other genes

As described in Chapter 1, homozygous *Vangl2*$^{Lp/Lp}$ embryos fail to initiate neural tube closure at E8.5, leading to the appearance of the severe NTD, craniorachischisis (Greene et al., 1998; Kibar et al., 2001b; Murdoch et al., 2001a). Additionally, several genetic studies have demonstrated that the *Vangl2*^{Lp} allele interacts with mutations in a number of other genes to cause NTDs in mice. Such interactions have been reported in mice with digenic and oligogenic mutant combinations, and are listed in Table 3.1. An interesting pattern emerging from these studies is that, while craniorachischisis is the predominant NTD phenotype produced by combinations of core PCP gene mutations (for example in *Vangl2*$^{Lp/+}$*;Vangl1*$^{gt/+}$*, Vangl2*$^{Lp/+}$*;Celsr1*$^{Crsh/+}$ and *Vangl2*$^{Lp/+}$*;Wnt5a*$^{-/-}$), it is not the only NTD that mutations in PCP genes can cause. The heterozygous *Vangl2*$^{Lp/+}$ genotype also increases susceptibility to failure of neurulation at other axial levels when inherited with mutations in other, often non-PCP, genes.

Vangl2^{Lp} interacts genetically with mutations in the transcription factor *Grhl3* (Caddy et al., 2010; Stiefel et al., 2003; Stiefel et al., 2007), the cargo-binding protein *Sec24b* (Merte et al., 2010) and the PCP-regulator *Ptk7* (Lu et al., 2004; Paudyal et al., 2010) to produce spina bifida. *Vangl2*^{Lp} also promotes exencephaly, for example in combination with mutations in the Wnt co-factor *Cthrc1* (Yamamoto et al., 2008) and the actin nucleator *Cordon-bleu* (Carroll et al., 2003). It is not well understood why a combination of *Vangl2*^{Lp} with mutant alleles of other genes can produce such variable phenotypes.

Mutant genotype	Mouse chromosome	NTD Phenotype (penetrance)	Other phenotypes reported	References
Vangl2$^{Lp/+}$;*Vangl1*$^{gt/+}$	1, 3	CRN (63%)	Tail flexion defects, inner ear defects, heart defects	(Torban et al., 2008)
Vangl2$^{Lp/+}$;*Celsr1*$^{Crsh/+}$	1, 15	CRN (54-100%, depending on background)	Some gastroschisis/omphalocele	Dr Jennifer Murdoch, (unpublished data)
Vangl2$^{Lp/+}$;*Dvl2*$^{-/-}$	1, 4	CRN (100%)	Inner ear defects, heart defects, tail flexion defects	(Wang et al., 2006a)
Vangl2$^{Lp/+}$;*Dvl3*$^{-/-}$ *Vangl2*$^{Lp/+}$;*Dvl3*$^{+/-}$	1, 16	CRN (38%) CRN (23%), EX (9%)	Heart defects, inner ear defects Inner ear defects	(Etheridge et al., 2008)
Vangl2$^{Lp/+}$;*Scrib*$^{Crc/+}$	1, 15	CRN (54%), SB (4%)	Tail flexion defects, heart defects	(Murdoch et al., 2001b) (Phillips et al., 2007)
Vangl2$^{Lp/+}$;*Wnt5a*$^{-/-}$	1, 14	CRN (100%)	Inner ear defects, eyelid closure defects	(Qian et al., 2007)
Vangl2$^{Lp/+}$;*Ptk7*$^{gt/+}$ *Vangl2*$^{Lp/+}$;*Ptk7*$^{chz/+}$	1, 17	SB (94%) CRN (6%), SB (23%)	None described None described	(Lu et al., 2004) (Paudyal et al., 2010)
Vangl2$^{Lp/+}$;*Sfrp1*$^{-/-}$;*Sfrp2*$^{+/-}$;*Sfrp5*$^{-/-}$ *Vangl2*$^{Lp/+}$;*Sfrp1*$^{-/-}$;*Sfrp2*$^{-/-}$;*Sfrp5*$^{+/-}$	1, 8, 3, 19	SB (62%) CRN (% not reported)	None described None described	(Satoh et al., 2008)
Vangl2$^{Lp/+}$;*Fzd1*$^{+/-}$ *Vangl2*$^{Lp/+}$;*Fzd2*$^{+/-}$ *Vangl2*$^{Lp/+}$;*Fzd2*$^{-/-}$ *Vangl2*$^{Lp/+}$;*Fzd1*$^{+/-}$;*Fzd2*$^{+/-}$	1, 5 1, 11 1, 11 1, 5, 11	SB (4%), EX (44%) SB (29%), EX (25%) SB (100%), EX (33%) EX (43%)	Heart defects Inner ear defects	(Yu et al., 2010)

Vangl2$^{Lp/+}$;*Ror2*$^{-/-}$	1, 13	SB and EX (‘>50%’)	Inner ear defects	(Gao et al., 2011)
Vangl2$^{Lp/+}$;*Sec24b*$^{Y613/+}$	1, 3	SB (68%)	None described	(Merte et al., 2010)
Vangl2$^{Lp/+}$;*Grhl3*$^{+/-}$	1, 4	SB (67%)	Inner ear defects, defective wound repair	(Caddy et al., 2010)
Vangl2$^{Lp/+}$;*Grhl3*$^{ct/ct}$	1, 4	SB (86%)	Tail flexion defects	(Stiefel et al., 2003; Stiefel et al., 2007), W.Damith Jayatilake, unpublished.
Vangl2$^{Lp/+}$;*Zic2*$^{ku/+}$	1, 14	SB (59%)	None described	Valentina Massa, unpublished.
Vangl2$^{Lp/+}$;*Cthrc1*$^{LacZ/LacZ}$	1, 15	EX (100%)	Inner ear defects	(Yamamoto et al., 2008)
Vangl2$^{Lp/+}$;*Cobl*$^{C101/C101}$	1, 2	EX (20%)	None described	(Carroll et al., 2003)

Table 3.1 *Vangl2* genetic interactions causing NTDs in mouse mutants

CRN = craniorachischisis, EX = exencephaly, SB = spina bifida

3.1.2 PCP and spinal neurulation post-closure 1

The modifying effect of *Vangl2*^{Lp} towards later neurulation events raises questions about the role of PCP signalling during low spinal neural tube closure. In particular it is unclear whether the reported genetic interactions represent defects of convergence and extension, as has been described for closure 1. If so, this would implicate CE cell movements as an essential feature of low spinal neurulation in addition to their recognised role during post-gastrulation shaping.

Heterozygous *Vangl2*$^{Lp/+}$ mice never display craniorachischisis under normal developmental conditions. However PNP closure is delayed in *Vangl2*$^{Lp/+}$ embryos compared with their wild type littermates, which is likely to be responsible for the rare spina bifida and the frequent tail flexion defects seen in heterozygotes (Copp et al., 1994). Furthermore, embryos which are homozygous for the more recently identified hypomorphic *Vangl2*^{Lpm2Jus} mutation also display spinal phenotypes; 12% develop spina bifida and 47% have tail defects (Guyot et al., 2011). It is currently unknown whether the spinal defects in *Vangl2*$^{Lp/+}$ and *Vangl2*$^{Lpm2Jus/Lpm2Jus}$ embryos result from a CE defect.

3.1.3 *Vangl2*^{Lp} interacts with *Grhl3*^{ct} to cause severe spina bifida

To investigate potential genetic interactions between *Vangl2* and *Grhl3*, mice doubly mutant for the *loop-tail* and *curly tail* alleles were previously bred in our laboratory. The *Vangl2*$^{Lp/+}$*;Grhl3*$^{ct/ct}$ genotype was found to be highly predisposing to spina bifida (86% penetrance), whereas on the same genetic background only 7% of *Vangl2*$^{+/+}$*;Grhl3*$^{ct/ct}$ mice displayed this phenotype (W.Damith Jayatilake, 1997; unpublished data). The spina bifida in *Vangl2*$^{Lp/+}$*;Grhl3*$^{ct/ct}$ embryos was also more severe than in *Vangl2*$^{+/+}$*;Grhl3*$^{ct/ct}$, with the rostral limit of the open region extending

further up the body, often as far as the level of the hindlimb buds at E11.5. Thus, these data identified the *loop-tail* mutation as a genetic modifier which increases the frequency and severity of the partially penetrant spina bifida observed in homozygous *curly tail* embryos. Notably the defect manifests as failure of PNP closure, while craniorachischisis is never seen. Since these findings, *Vangl2*$^{Lp/+}$*;Grhl3*$^{ct/ct}$ fetuses have been used to study pathological features of myelomeningocele, such as spinal cord tethering and *in utero* neurodegeneration (Stiefel et al., 2003; Stiefel et al., 2007), but the developmental mechanisms underlying spina bifida in this model are not understood.

The *Vangl2*$^{Lp/+}$*;Grhl3*$^{ct/ct}$ mutant provides a model to examine the role of the PCP pathway during low spinal neural tube closure. Is the genetic predisposing effect of PCP mutations towards failure of spinal neurulation mediated via CE, as during closure 1, or does it reflect other functions for PCP genes? This mouse model also raises the question of how *Vangl2* and *Grhl3,* two key genes which when mutated cause distinct NTD phenotypes with different underlying mechanisms, interact during neurulation?

This chapter begins to elucidate the developmental mechanism(s) underlying the *loop-tail/curly tail* interaction. The phenotypes of embryos with different combinations of *Vangl2* and *Grhl3* mutant alleles are assessed and the following initial hypotheses are considered: (1) *Vangl2*^{Lp} heterozygosity increases the frequency of spina bifida in *Grhl3*$^{ct/ct}$ embryos by a mechanism involving diminution of convergent extension; (2) *Vangl2*^{Lp} heterozygosity increases the frequency of spina bifida in *Grhl3*$^{ct/ct}$ embryos via a non-PCP mechanism, involving exacerbation of the known *curly tail* mutant phenotype; (3) *Vangl2*^{Lp} heterozygosity affects other events of spinal neurulation, thereby summating with the *curly tail* mutant pathway to increase the tendency towards spina bifida.

3.2 Results

3.2.1 Spina bifida in Vangl2$^{Lp/+}$;Grhl3$^{ct/ct}$ embryos

Given that the previous data on the *loop-tail/curly tail* interaction was collected over 15 years ago, the breeding was repeated to assess the *Vangl2$^{Lp/+}$;Grhl3$^{ct/ct}$* phenotype using our current mouse colonies. To generate experimental litters for analysis, *Vangl2$^{Lp/+}$;Grhl3$^{ct/+}$* male mice were bred with *Grhl3$^{ct/ct}$* females, producing offspring with the following four genotypes: *Vangl2$^{+/+}$;Grhl3$^{ct/+}$*, *Vangl2$^{+/+}$;Grhl3$^{ct/ct}$*, *Vangl2$^{Lp/+}$;Grhl3$^{ct/+}$* and *Vangl2$^{Lp/+}$;Grhl3$^{ct/ct}$* (Figure 3.1). Embryos were collected between E11 and E12.5 and genotypes were obtained in the expected Mendelian ratios (Table 3.2).

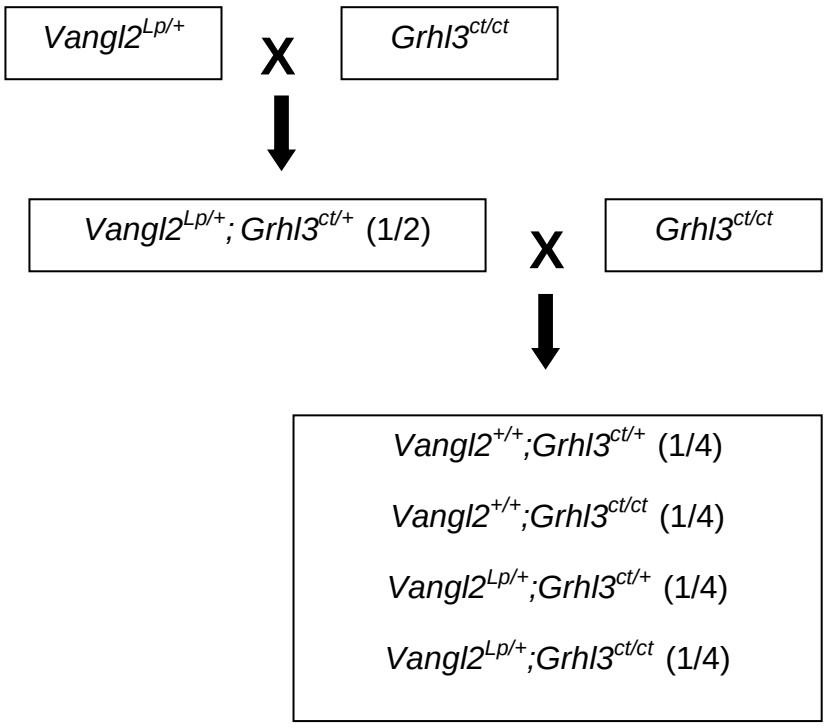

Figure 3.1 Breeding scheme for the generation of experimental litters

Matings between *Vangl2$^{Lp/+}$;Grhl3$^{ct/ct}$* and *Grhl3$^{ct/ct}$* mice produce embryos with one of four possible genotypes. Numbers in brackets indicate the expected proportion of offspring for each genotype.

Genotype	Expected		Observed	
	%	Freq.	%	Freq.
Vangl2$^{+/+}$;*Grhl3*$^{ct/+}$	25.00	21/85	30.59	26/85
Vangl2$^{+/+}$;*Grhl3*$^{ct/ct}$	25.00	21/85	22.35	19/85
Vangl2$^{Lp/+}$;*Grhl3*$^{ct/+}$	25.00	21/85	20.00	17/85
Vangl2$^{Lp/+}$;*Grhl3*$^{ct/ct}$	25.00	21/85	27.06	23/85
Deviation from Mendelian ratios:	χ^2=1.138 with 3 degrees of freedom (p = 0.768)			

Table 3.2 Genotype frequencies of offspring from *Vangl2*$^{Lp/+}$;*Grhl3*$^{ct/+}$ X *Grhl3*$^{ct/ct}$ matings.

Embryos were collected at E11-E12.5 and genotypes were obtained in the expected Mendelian ratios (p = 0.768, Chi-square test).

Embryos were examined for NTDs at E11-E12.5, by which time spina bifida can be clearly identified, and as expected various spinal phenotypes were observed within litters. Embryos which had successfully completed neural tube closure were categorised according to the appearance of their tail; a straight tail was indicative of normal spinal development (Figure 3.2A) while a tail flexion defect ('curly tail') was suggestive of delayed neurulation (Figure 3.2B). Embryos which had failed to achieve PNP closure and had an open spina bifida were grouped according to the axial severity of the lesion. Somites 26 to 31 correspond to the future lumbar region, so an opening extending as far rostrally as the 31st somite pair or higher was defined as a 'large spina bifida' (lumbo-sacral; Figure 3.2D). An opening from the 32nd somite pair or lower was defined as 'small' (sacral; Figure 3.2C). Somite 32 marks the upper extremity of the future sacral region (somites 32-35). All embryos with spina bifida also displayed tail flexion defects.

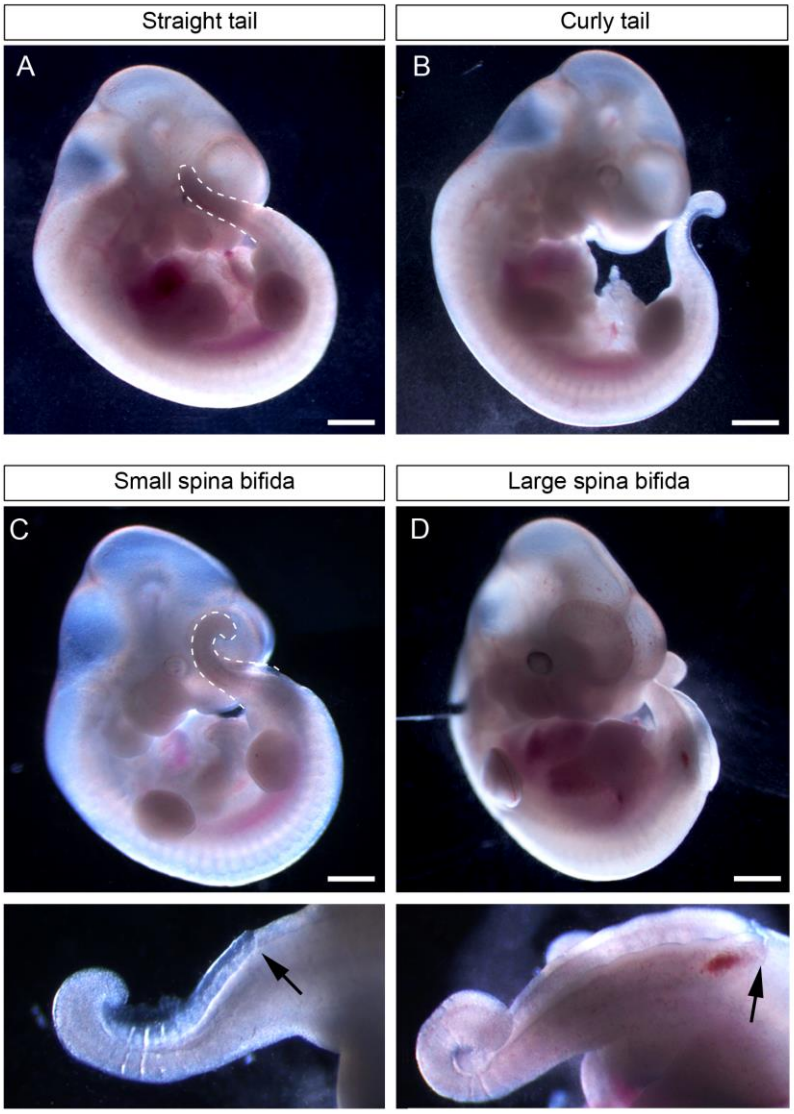

Figure 3.2 Spectrum of spinal phenotypes observed in E11-12.5 litters from *Vangl2*$^{Lp/+}$;*Grhl3*$^{ct/+}$ X *Grhl3*$^{ct/ct}$ matings

(A) Phenotypically normal embryo with a straight tail. **(B)** Embryo which has completed primary neurulation but has a curly tail, most likely due to delayed PNP closure. **(C, D)** Appearance of the spina bifida at E11-E12.5. Arrows indicate the rostral limit of the open region. Higher magnification images are shown in the lower panels. Small and large spina bifidas correspond to sacral and lumbo-sacral lesions in humans, respectively. Scale bars: 500 µm.

All of the *Vangl2*$^{+/+}$;*Grhl3*$^{ct/+}$ embryos collected had closed neural tubes, the majority in combination with a normal, straight tail and a small proportion (1/26 embryos) with a curly tail. *Vangl2*$^{+/+}$;*Grhl3*$^{ct/ct}$ embryos displayed partially penetrant defects, manifesting as tail defects in approximately 30% of embryos and small spina bifida in 5%. The *Vangl2*^{Lp} allele was associated with spinal defects in all cases, with no phenotypically normal *Vangl2*$^{Lp/+}$;*Grhl3*$^{ct/+}$ or *Vangl2*$^{Lp/+}$;*Grhl3*$^{ct/ct}$ embryos recorded. Compound heterozygous *Vangl2*$^{Lp/+}$;*Grhl3*$^{ct/+}$ embryos exhibited 59% tail defects and 41% spina bifida, while in *Vangl2*$^{Lp/+}$;*Grhl3*$^{ct/ct}$ the penetrance of spina bifida was increased to 74%, with the remaining 26% of embryos displaying a curled tail (Table 3.3; Figure 3.3). The difference in NTD frequency between the four genotypes was statistically significant ($p < 0.001$, Chi-square test).

In summary, a shift in the severity of the spinal phenotype was observed in the presence of more mutant alleles, particularly the *Lp* mutation. All *Vangl2*$^{Lp/+}$;*Grhl3*$^{ct/ct}$ embryos displayed defective spinal neurulation, with an incidence of 74% spina bifida compared to 5% in their *Vangl2*$^{+/+}$;*Grhl3*$^{ct/ct}$ littermates. These data are similar to the frequencies of 86% vs 7% which were previously observed (W.Damith Jayatilake, 1997; unpublished data). Conversely, *Vangl2*^{Lp} did not appear to exacerbate cranial NTDs in *curly tail* embryos; 5% exencephaly (1/19 embryos) was observed in *Vangl2*$^{+/+}$;*Grhl3*$^{ct/ct}$ and no exencephalic *Vangl2*$^{Lp/+}$;*Grhl3*$^{ct/ct}$ embryos were recorded (Table 3.3).

Genotype	Caudal phenotype			
	Straight tail **%** (freq.)	**Tail flexion defects** **%** (freq.)	**Spina bifida** **%** (freq.)	**Exencephaly** **%** (freq.)
Vangl2$^{+/+}$;*Grhl3*$^{ct/+}$	**96.15** (25/26)	**3.85** (1/26)	**0** (0/26)	**0** (0/26)
Vangl2$^{+/+}$;*Grhl3*$^{ct/ct}$	**63.16** (12/19)	**31.58** (6/19)	**5.26** (1/19)	**5.26** (1/19)
Vangl2$^{Lp/+}$;*Grhl3*$^{ct/+}$	**0** (0/17)	**58.82** (10/17)	**41.18** (7/17)	**0** (0/17)
Vangl2$^{Lp/+}$;*Grhl3*$^{ct/ct}$	**0** (0/23)	**26.09** (6/23)	**73.91** (17/23)	**0** (0/23)

Table 3.3 NTD phenotypes observed in E11-E12.5 embryos from *Vangl2*$^{Lp/+}$;*Grhl3*$^{ct/+}$ X *Grhl3*$^{ct/ct}$ matings

The percentage and frequency of each phenotype is shown. The proportion of embryos with tail defects and spina bifida varies significantly between genotypes (Chi-square test; χ^2=75.003 with 6 degrees of freedom; $p < 0.001$).

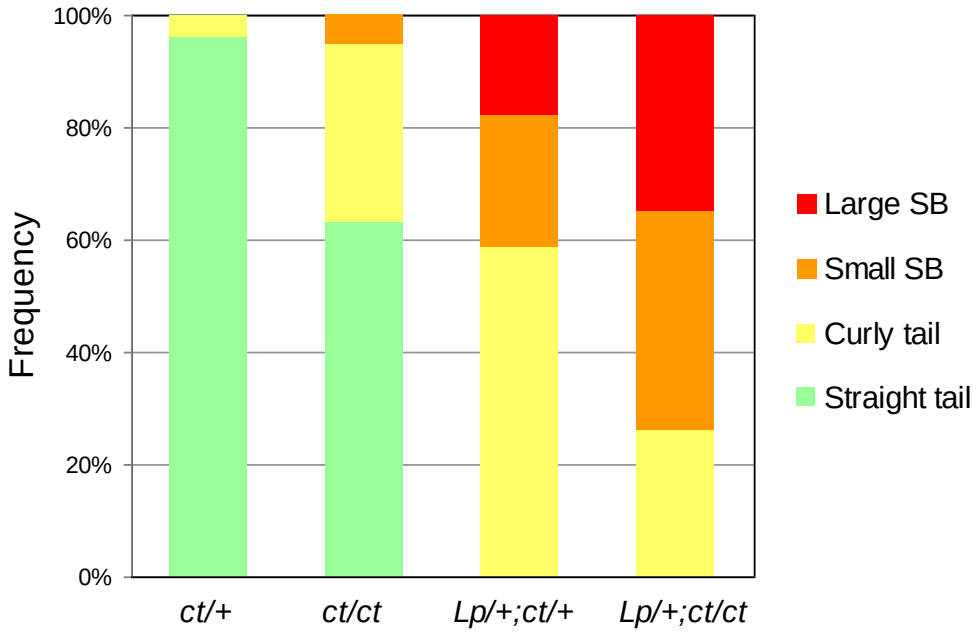

Figure 3.3 Spinal NTD frequency at E11-E12.5

Graph illustrating an association between the number of mutant alleles and the frequency and severity of spinal NTDs. *Vangl2*$^{Lp/+}$;*Grhl3*$^{ct/ct}$ is the most severely affected genotype, with a frequency of 74% spina bifida. Among these embryos, approximately half of the spina bifida cases observed are classified as 'large' (right-hand column).

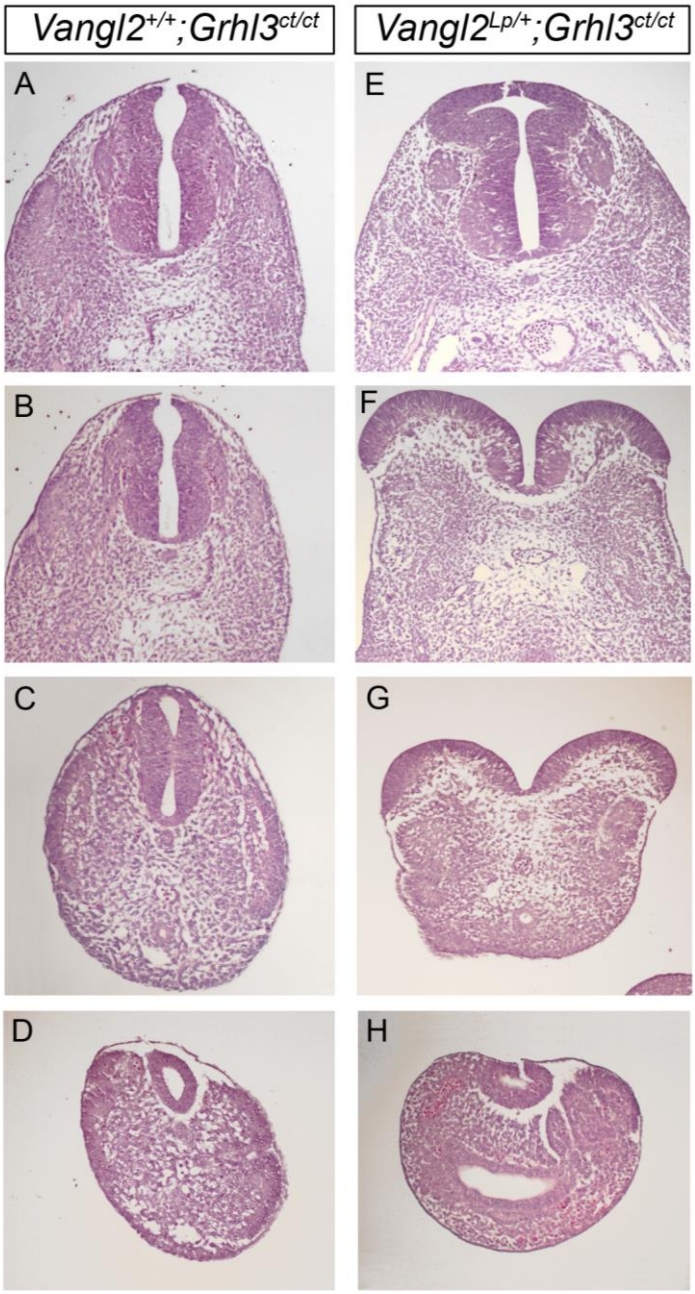

Figure 3.4 Sections through the spina bifida in *Vangl2$^{Lp/+}$;Grhl3$^{ct/ct}$*

Transverse, H and E-stained sections through a *Vangl2$^{+/+}$;Grhl3$^{ct/ct}$* embryo with a closed neural tube (A-D; rostral to caudal) and a *Vangl2$^{Lp/+}$;Grhl3$^{ct/ct}$* embryo with a large spina bifida (E-H). Failure of PNP closure leads to widely splayed open neural folds in the double mutant (F, G). Panels D and H show a closed neural tube in embryos of both genotypes at the level of secondary neurulation. The slight opening in H is a histology artefact.

Sections through the caudal region of a phenotypically normal *Vangl2*$^{+/+}$;*Grhl3*$^{ct/ct}$ embryo and a *Vangl2*$^{Lp/+}$;*Grhl3*$^{ct/ct}$ with spina bifida are shown in Figure 3.4. In the lower trunk the neural tube of both embryos is closed, although the *Vangl2*$^{Lp/+}$;*Grhl3*$^{ct/ct}$ neuroepithelium appears dysmorphic (Figure 3.4A, E). Further caudally, the widely open neural folds can be seen in the double mutant (Figure 3.4F, G). In the tail, secondary neurulation appears to be ongoing in the *Vangl2*$^{Lp/+}$;*Grhl3*$^{ct/ct}$ embryo, despite the failure of primary neurulation; indeed a lumen can be seen and the neural tube appears to be covered by surface ectoderm, as in the control (Figure 3.4D, H).

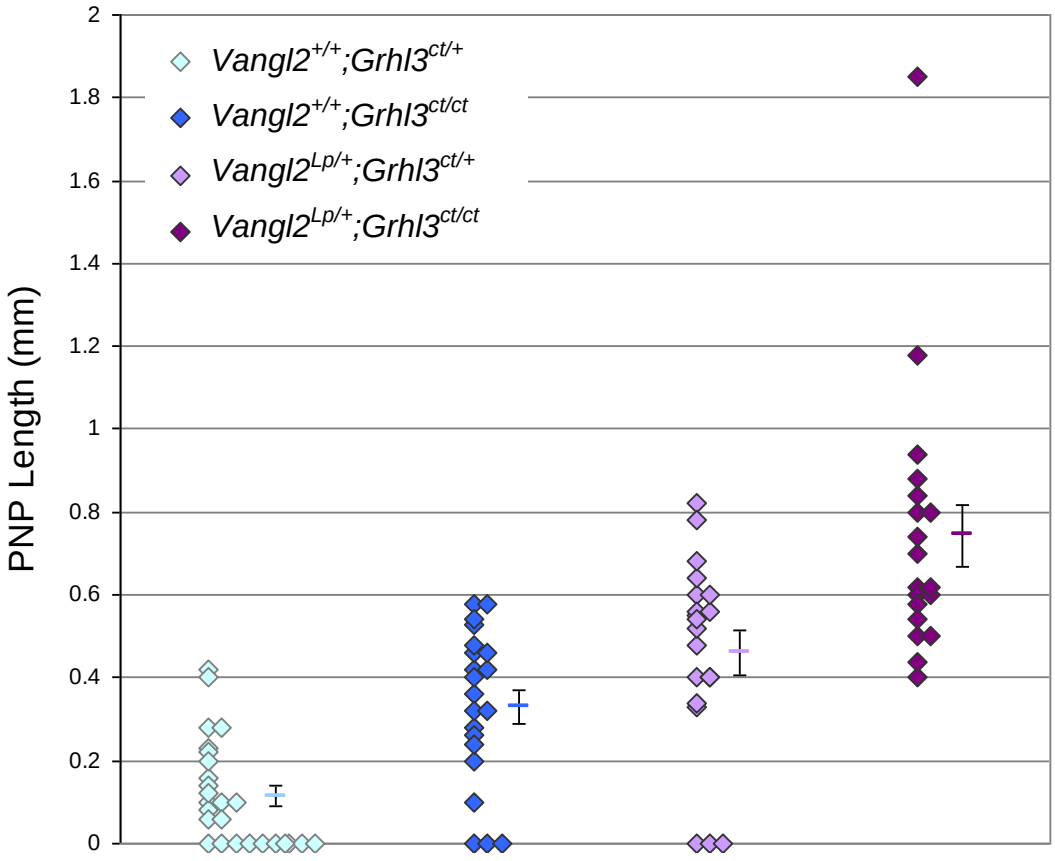

Figure 3.5 PNP length of embryos at the 29-33 somite stage

Each individual embryo is represented by a single data point, with the mean ± SEM shown to the right of each group. A measurement of 0 indicates that PNP had completely closed. The mean PNP length varies significantly between genotypes ($p < 0.001$, Kruskal-Wallis 1-Way ANOVA on Ranks).

To confirm that the observed defects were due to the failure of primary neurulation and not, for example, a re-opening event, litters were also collected at E10-E10.5 for examination of the PNP. An enlarged PNP is associated with the progression of spina bifida (Copp, 1985) so it was predicted that the *Vangl2*$^{Lp/+}$*;Grhl3*$^{ct/ct}$ genotype would exhibit such a delay in neurulation. At the 29-33 somite stage, the difference in mean PNP length between genotypes was evident (Figure 3.5; see examples in Figure 3.7). PNP length in the *Vangl2*$^{Lp/+}$*;Grhl3*$^{ct/ct}$ genotype was significantly increased compared to *Vangl2*$^{+/+}$*;Grhl3*$^{ct/ct}$ and *Vangl2*$^{+/+}$*;Grhl3*$^{ct/+}$, and was larger than in *Vangl2*$^{Lp/+}$*;Grhl3*$^{ct/+}$, although this latter comparison did not reach statistical significance. *Vangl2*$^{+/+}$*;Grhl3*$^{ct/ct}$ and *Vangl2*$^{Lp/+}$*;Grhl3*$^{ct/+}$ embryos had significantly larger PNPs than *Vangl2*$^{+/+}$*;Grhl3*$^{ct/+}$ embryos, many of which had completed PNP closure by this stage. In contrast, none of the *Vangl2*$^{Lp/+}$*;Grhl3*$^{ct/ct}$ embryos had achieved closure.

In general, a wide range of values was observed within each genotype group (Figure 3.5), consistent with the partial penetrance of the NTDs in older embryos (Figure 3.3). Embryonic crown-rump length and somite number did not differ between genotypes, indicating that the difference in PNP size does not simply reflect changes in overall growth or developmental stage (Figure 3.6).

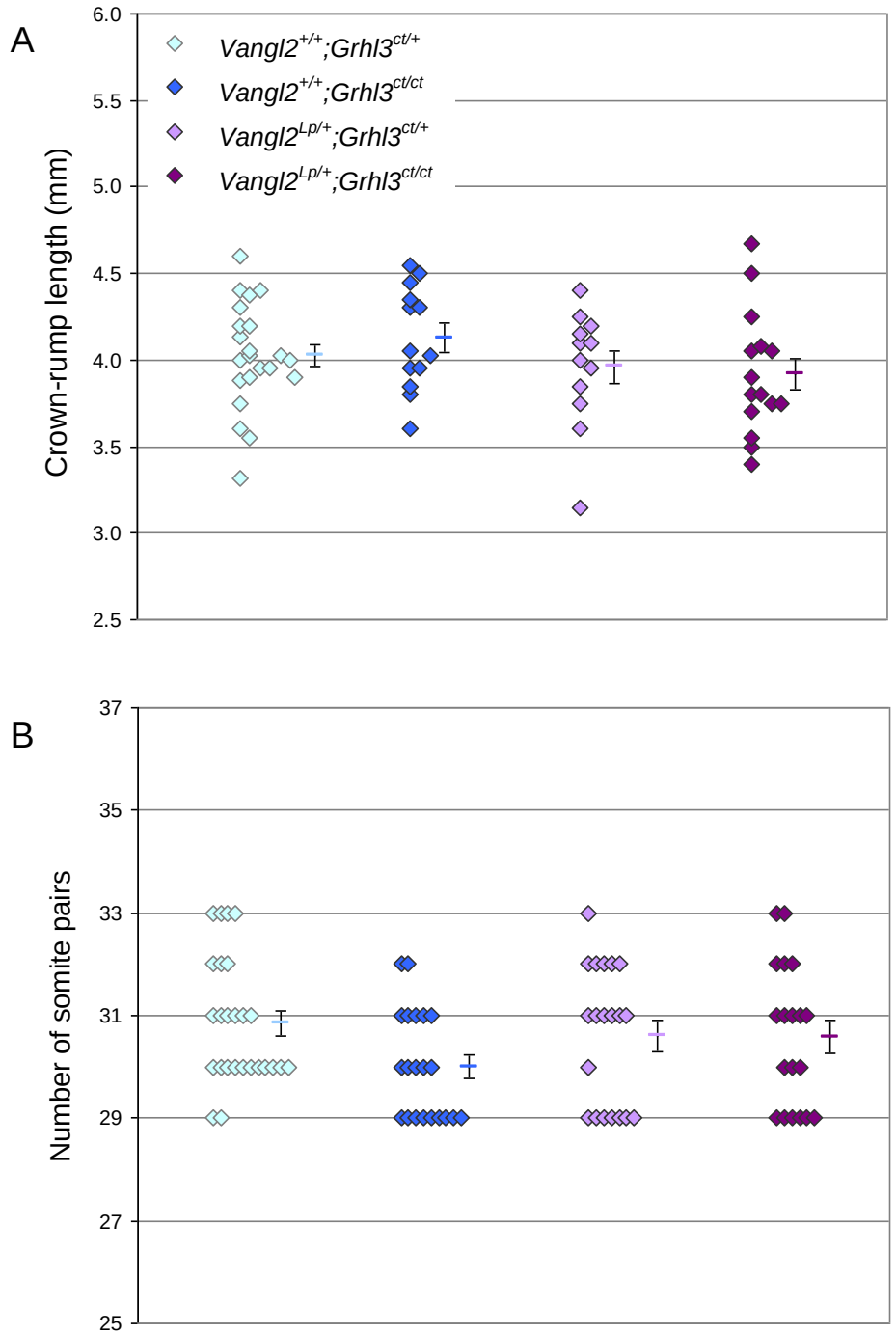

Figure 3.6 Embryonic crown-rump length and somite number

(**A**) Crown-rump length (CRL) for embryos with 29-33 somites. (**B**) Number of somite pairs for embryo data in Figure 3.5. Individual embryos for each genotype are shown as before. Error bars represent the mean ± SEM. CRL and somite number do not vary significantly with genotype (p = 0.35 and p = 0.163, respectively, 1-Way ANOVA).

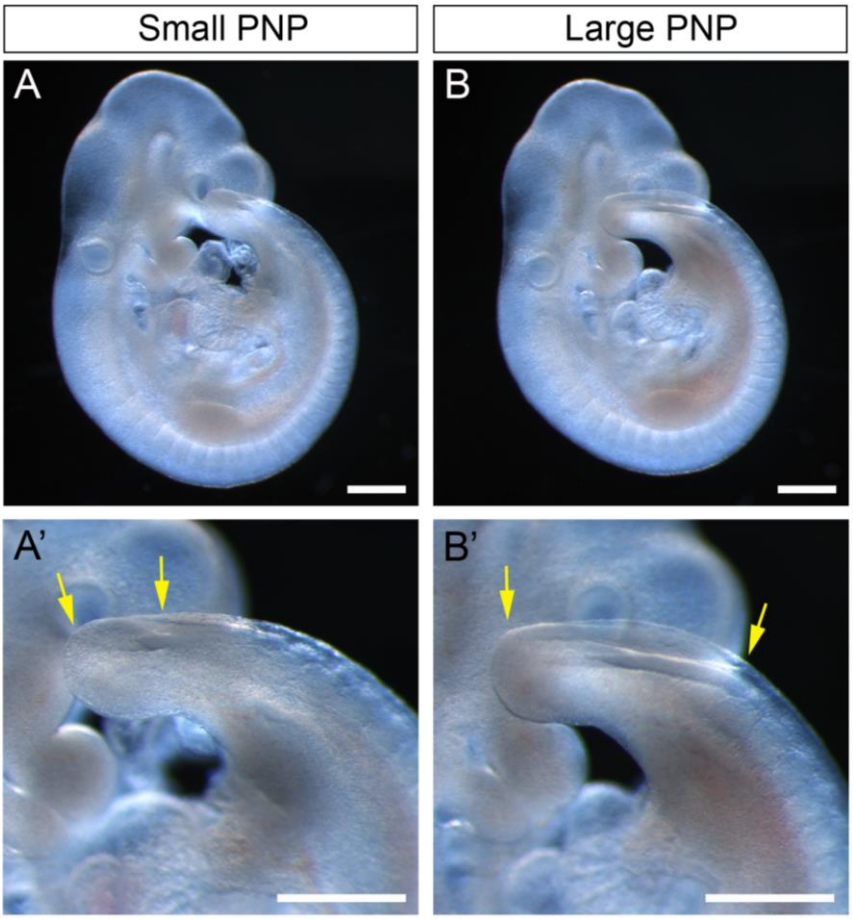

Figure 3.7 Examples of the different PNP sizes at E9.5

(**A, A'**) Embryo with a small PNP. (**B, B'**) Stage-matched embryo with a large PNP, which extends as far rostrally as the somite rows. This delay in closure is associated with the appearance of spina bifida and/or tail flexion defects. Arrows indicate the open region. Scale bars: 500 µm.

3.2.2 DLHP formation in *Vangl2*$^{Lp/+}$;*Grhl3*$^{ct/ct}$ embryos

Bending of the neuroepithelium at DLHPs is a key feature of neurulation at low spinal levels. Failure of DLHP formation, for example in the *Zic2* loss-of-function mouse mutant, *Kumba* (*Zic2*$^{ku/ku}$), is incompatible with the caudal progression of neural tube closure, resulting in severe spina bifida (Ybot-Gonzalez et al., 2007a). Therefore, a detrimental effect of *Vangl2*^{Lp} on events that regulate dorsolateral

bending, but are not primarily abnormal in *curly tail* (*Grhl3*$^{ct/ct}$) embryos, could mediate its exacerbation of spina bifida in the double mutants.

However, histological analysis of embryos at E9, shortly after the stage when DLHPs first appear (Shum and Copp, 1996) revealed apparently normal dorsolateral bending in *Vangl2*$^{Lp/+}$;*Grhl3*$^{ct/ct}$ mutants (Figure 3.8). Neural plate morphology was characteristic of mode 2 of spinal neurulation in both *Vangl2*$^{Lp/+}$;*Grhl3*$^{ct/ct}$ and *Vangl2*$^{+/+}$;*Grhl3*$^{ct/ct}$ controls. At the level of PNP closure the tips of the folds were apposed at the midline, while more caudal sections showed comparable DLHPs and neural fold elevation at the PNP. Thus, the *loop-tail* mutation does not appear to have a deleterious effect on DLHP formation.

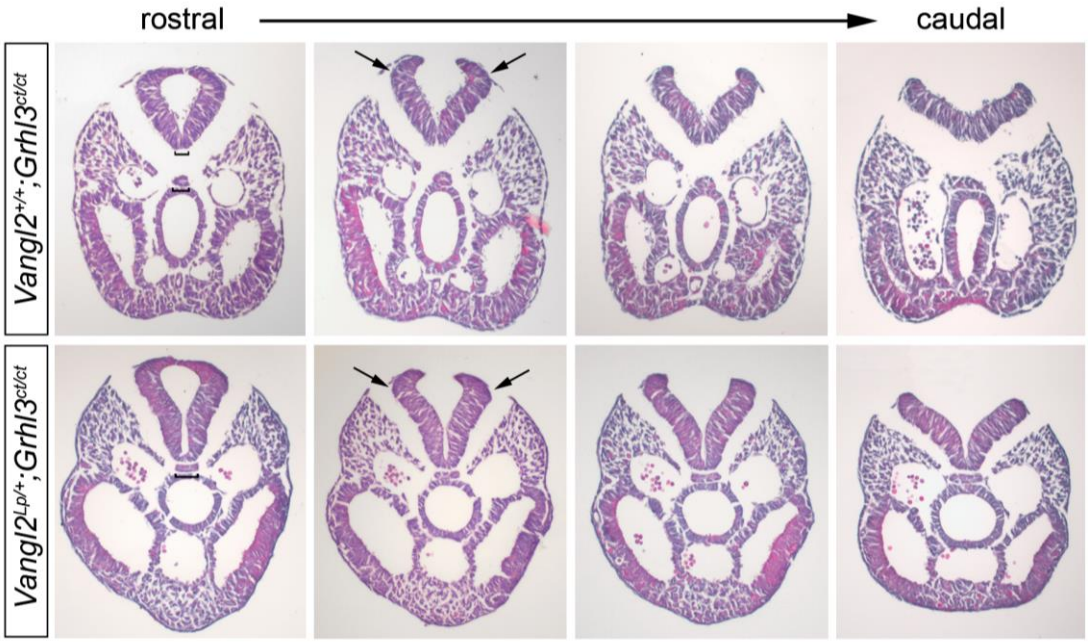

Figure 3.8 DLHPs form normally in *Vangl2*$^{Lp/+}$;*Grhl3*$^{ct/ct}$ embryos at E9

Transverse sections through the caudal region of a control *Vangl2*$^{+/+}$;*Grhl3*$^{ct/ct}$ embryo (upper panels) and a *Vangl2*$^{Lp/+}$;*Grhl3*$^{ct/ct}$ embryo (lower panels). DLHPs appear to form normally in the double mutant. N = minimum of 3 embryos per genotype. Arrows indicate DLHPs and brackets indicate the width of the floor plate and notochord (see Section 3.2.4).

3.2.3 Spina bifida in *Vangl2$^{Lp/+}$;Grhl3$^{ct/ct}$* is not due to an exacerbation of the *curly tail* defect

Affected *curly tail* embryos exhibit an abnormally low rate of cell proliferation in the hindgut endoderm and notochord at E9.5. This imbalance between the growth of ventral and dorsal tissues precedes the increase in ventral curvature of the caudal region, and the resulting mechanical opposition of neural fold closure, that leads to spina bifida and tail flexion defects (Brook et al., 1991; Copp et al., 1988a). We therefore considered the possibility that the *Lp* mutation causes an additional increase in ventral curvature, perhaps by exerting a similar cell-type-specific effect on proliferation.

Interestingly however, the *Vangl2^{Lp}* allele was associated with a reduction in the angle of axial curvature (Figure 3.9, Figure 3.10). At each developmental stage analysed (14-19 somites, 20-25 somites and 26-31 somites), *Vangl2$^{Lp/+}$;Grhl3$^{ct/+}$* and *Vangl2$^{Lp/+}$;Grhl3$^{ct/ct}$* embryos displayed significantly less ventral curvature than their *Vangl2$^{+/+}$;Grhl3$^{ct/+}$* and *Vangl2$^{+/+}$;Grhl3$^{ct/ct}$* littermates ($p < 0.001$ for each stage, 1-Way ANOVA). In general, embryos without the *Lp* mutation showed an increase in axial curvature as development proceeded, while the curvature in embryos with the *Lp* mutation remained rather more constant over time (Figure 3.9). These data indicate that the spina bifida in *Vangl2$^{Lp/+}$;Grhl3$^{ct/ct}$* does not arise due to increased ventral curvature of the caudal region during spinal neurulation.

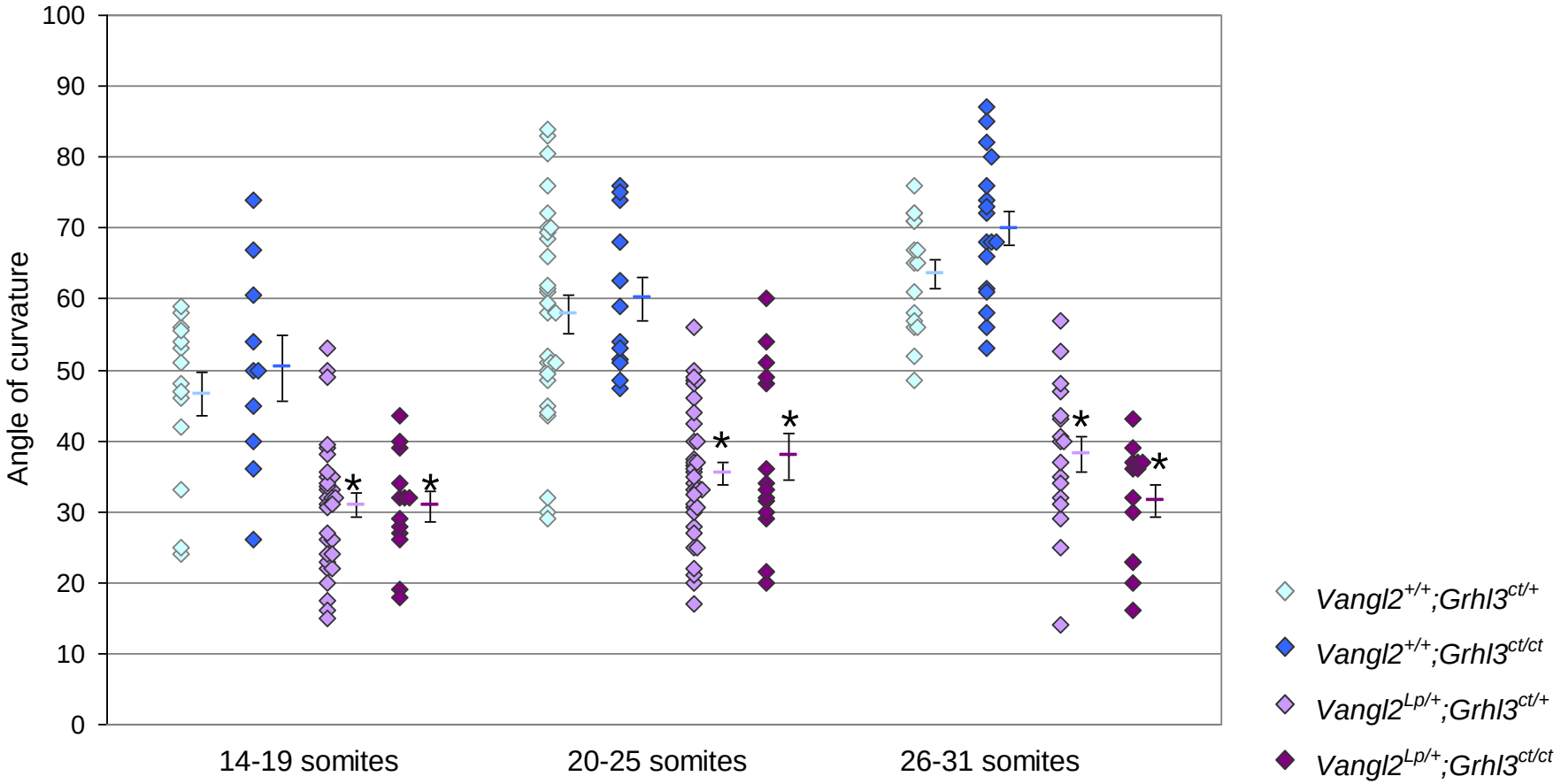

Figure 3.9 *Vangl2*^{Lp} is associated with a reduction in ventral axial curvature

Each embryo is represented by a single data point, with the mean ± SEM to the right of each group. The mean PNP angle of curvature varies significantly between genotypes ($p < 0.001$ for each stage, 1-Way ANOVA). *Significantly reduced compared with *Vangl2*$^{+/+}$;*Grhl3*$^{ct/+}$ and *Vangl2*$^{+/+}$;*Grhl3*$^{ct/ct}$ ($p < 0.05$).

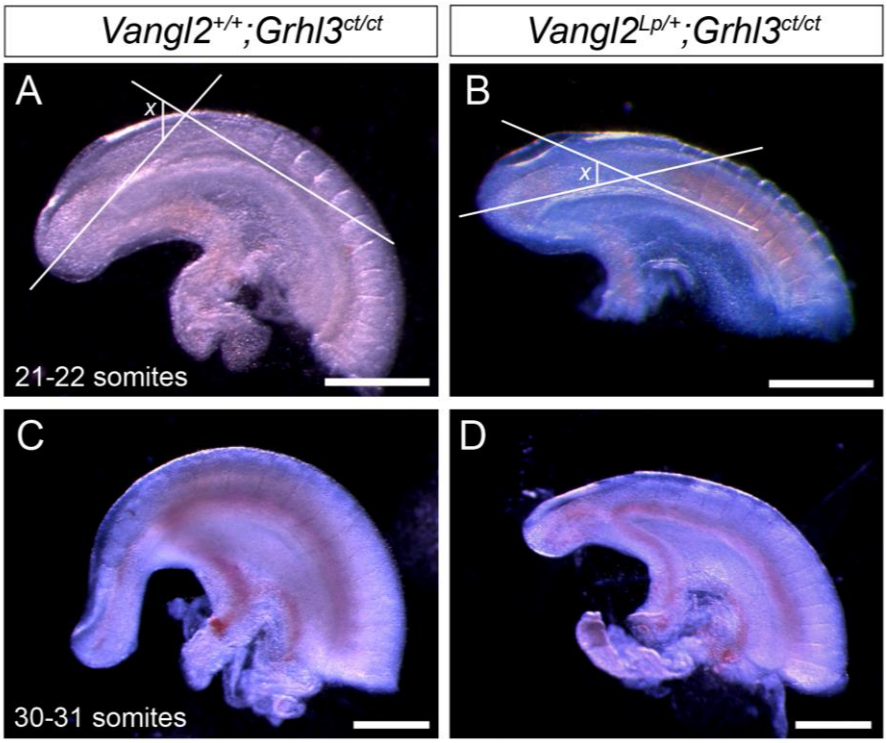

Figure 3.10 Reduced axial curvature in *Vangl2$^{Lp/+}$;Grhl3$^{ct/ct}$*

The angle of axial curvature (*X*) of the caudal region was measured as shown in A and B (and see Chapter 2). Curvature was reduced in *Vangl2$^{Lp/+}$;Grhl3$^{ct/ct}$* compared to *Vangl2$^{+/+}$;Grhl3$^{ct/ct}$*. Representative 21-22 and 30-31 somite stage samples are shown in A-B and C-D, respectively. Scale bars: 500 µm.

In an early study of the *curly tail* mutant mechanism (Copp et al., 1988a), 27-29 somite stage embryos were examined for changes in cell proliferation at different sites along the caudal axis. An informative comparison was made between the distal site of active neural fold elevation in unaffected ('Category 1/2') *curly tail* embryos versus the relatively more proximal site of active neurulation in *curly tail* embryos with severely enlarged neuropores ('Category 4/5'). This approach revealed affected *curly tail* embryos to exhibit a significantly lower mitotic index (MI) in hindgut endoderm and notochord than their normally developing littermates.

Figure 3.11 Analysis of proliferation in the 27-29 somite stage hindgut endoderm

(**A, B**) Schematic of the comparison between the equivalent distal and proximal regions of embryos with small and large PNPs, respectively. Dotted lines indicate the level of active neural fold elevation, through which transverse sections were cut.

(**C, D**) Sections through representative control (C) and double mutant (D) embryos at the level of PNP closure, following immunofluorescence for PH-H3 (green). Nuclei are stained with DAPI (blue). White boxes outline the hindgut endoderm, within which a few mitotic nuclei can be seen. Scale bars: 100 μm.

(**E**) Mitotic indices in the hindgut. Each data point represents the mean MI for four-seven sections through an individual embryo. Error bars represent the mean MI ± SEM for all sections of the same genotype. Squares correspond to embryos with a smaller than average PNP and triangles denote those with a larger than average PNP. Mean MI did not vary significantly with genotype (p = 0.876, 1-Way ANOVA).

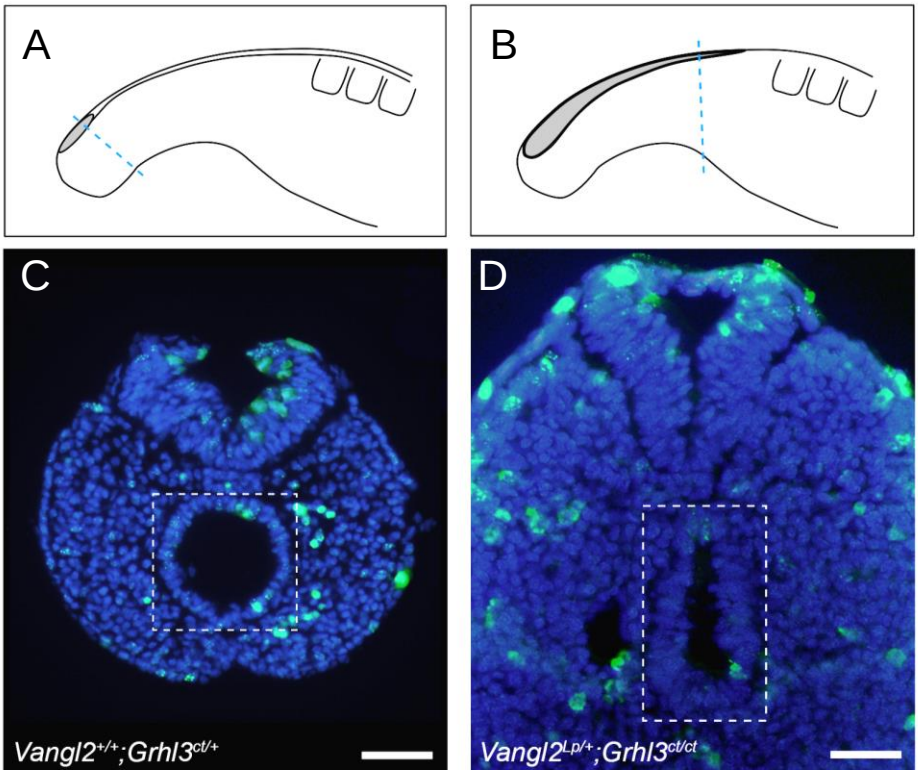
A
B
C
D
Vangl2+/+;Grhl3ct/+
Vangl2Lp/+;Grhl3ct/ct

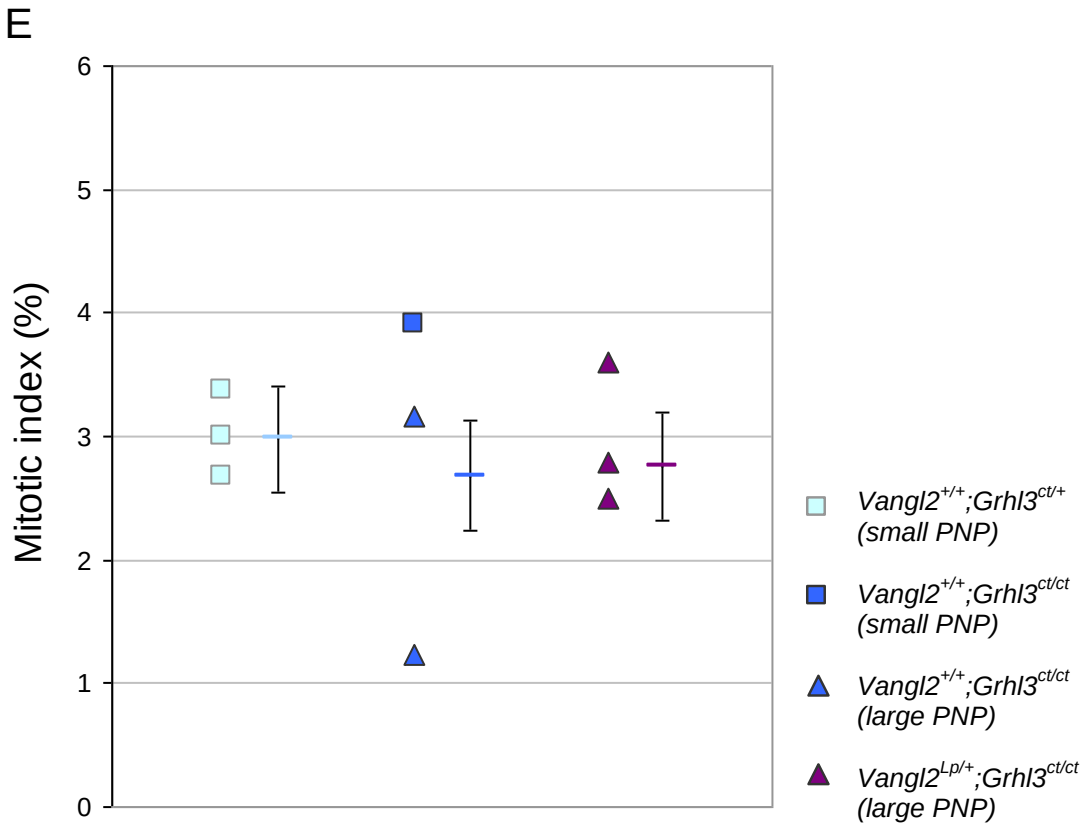
E
Mitotic index (%)
0
1
2
3
4
5
6
Vangl2+/+;Grhl3ct/+ (small PNP)
Vangl2+/+;Grhl3ct/ct (small PNP)
Vangl2+/+;Grhl3ct/ct (large PNP)
Vangl2Lp/+;Grhl3ct/ct (large PNP)

A similar method was used here (Figure 3.11), with an investigation of hindgut proliferation performed at 27-29 somites using the late-G2/M-phase marker, phospho-histone H3 (PH-H3). Control *Vangl2*$^{+/+}$;*Grhl3*$^{ct/+}$ embryos had a mean hindgut MI of 2.98 (± 0.43) and, while *curly tail* (*Vangl2*$^{+/+}$;*Grhl3*$^{ct/ct}$) mean MI was unaltered overall, individual embryos did show the expected trend towards reduced proliferation with increasing PNP size. MI was not significantly reduced in *Vangl2*$^{Lp/+}$;*Grhl3*$^{ct/ct}$ compared to either of the other genotypes, indeed the mean MI was 2.76 (± 0.44), despite the presence of the *ct* alleles (Figure 3.11C). These data therefore demonstrate further that the exacerbating effect of the *Vangl2*^{Lp} allele is not via the developmental mechanism demonstrated previously for the *curly tail* mutant.

3.2.4 Morphological evidence of defective CE in *Vangl2*$^{Lp/+}$;*Grhl3*$^{ct/ct}$

Prior to failure of closure 1 and the appearance of craniorachischisis, PCP mutant mouse embryos exhibit morphometric features that are indicative of defective CE. Typically they display an abnormally short and wide body axis during late gastrulation (Paudyal et al., 2010; Wang et al., 2006a; Ybot-Gonzalez et al., 2007b), and abnormally broad floor plate and notochord tissues at E8.5 (Greene et al., 1998; Lu et al., 2004; Wang et al., 2006a). Abnormal somite morphology has also been described as evidence of defective CE: for example, *Ptk7*$^{gt/gt}$ embryos have wider somites with shorter spacing at E8.5 (Lu et al., 2004). Does *Vangl2*^{Lp}, which increases susceptibility to defects later in neurulation, induce a similar 'PCP phenotype' at E9-E9.5?

The length of the caudal embryonic axis was reduced in *Vangl2*$^{Lp/+}$;*Grhl3*$^{ct/ct}$ by approximately 20% compared to *Vangl2*$^{+/+}$;*Grhl3*$^{ct/ct}$ embryos (Figure 3.12A, B; p =

0.017, t-test). In addition, the embryonic length occupied by the most-recently formed 6 somites was measured. The somites in *Vangl2*$^{Lp/+}$*;Grhl3*$^{ct/ct}$ appeared shorter along the A-P axis and wider mediolaterally than in *Vangl2*$^{+/+}$*;Grhl3*$^{ct/ct}$, and this reduction in length was statistically significant (Figure 3.12C, D; p = 0.007, t-test). As well as the overall reduction in length, the morphology of the *Vangl2*$^{Lp/+}$*;Grhl3*$^{ct/ct}$ caudal region did not look entirely normal: it appeared less well defined, lacking the ventral narrowing that give the appearance of a 'waist' just caudal to the allantoic insertion in *Vangl2*$^{+/+}$*;Grhl3*$^{ct/ct}$ (Figure 3.12B).

Measurements of the midline tissues were also collected from histological sections at E9.5. An apparent increase in the width of the *Vangl2*$^{Lp/+}$*;Grhl3*$^{ct/ct}$ floor plate can be seen in Figure 3.8; at the level of PNP closure the ventral midline neuroepithelium is U-shaped, in contrast to the normal V-shaped appearance in *Vangl2*$^{+/+}$*;Grhl3*$^{ct/ct}$. Similarly, while the notochord becomes progressively narrower and rounder in more rostral sections through *Vangl2*$^{+/+}$*;Grhl3*$^{ct/ct}$ embryos, it displays an abnormally flat and broad appearance at all levels in *Vangl2*$^{Lp/+}$*;Grhl3*$^{ct/ct}$ (Figure 3.8). Quantification of these observations revealed a significantly greater width of both tissues in *Vangl2*$^{Lp/+}$*;Grhl3*$^{ct/ct}$ embryos compared with *Vangl2*$^{+/+}$*;Grhl3*$^{ct/ct}$ (Figure 3.13A; p = 0.003 and p < 0.001 for the neuroepithelium and notochord, respectively). The overall width of the caudal end was unchanged (Figure 3.13B), suggesting that the midline tissues are specifically affected at this stage.

Taken together, these data indicate that heterozygosity for the *Vangl2*^{Lp} mutation causes a disruption of the normal lengthening of the embryonic axis and narrowing of the midline tissues during spinal neurulation.

Figure 3.12 Diminished length of the caudal region in *Vangl2$^{Lp/+}$;Grhl3$^{ct/ct}$* during spinal neurulation

(**A, B**) The caudal end (measured from the level at which a straight line drawn up from the allantois intersects the dorsal surface) is approximately 20% shorter in E9.5 *Vangl2$^{Lp/+}$;Grhl3$^{ct/ct}$* compared to *Vangl2$^{+/+}$;Grhl3$^{ct/ct}$* (**p* = 0.017, t-test; n = minimum of eleven E9.5 embryos per genotype). Representative embryo caudal regions are shown in B; white arrows indicate the measured region and the yellow arrow in the upper panel indicates the 'waist' seen caudal to the allantoic insertion (absent in *Vangl2$^{Lp/+}$;Grhl3$^{ct/ct}$*).

(**C, D**) The region corresponding to the last six somites is approximately 14% shorter in *Vangl2$^{Lp/+}$;Grhl3$^{ct/ct}$* (**p* = 0.007, t-test; n = minimum of eleven E9.5 embryos per genotype). Arrows in D indicate the measured region. Graphs in A and C show the mean length ± SEM. Scale bars: 200 µm.

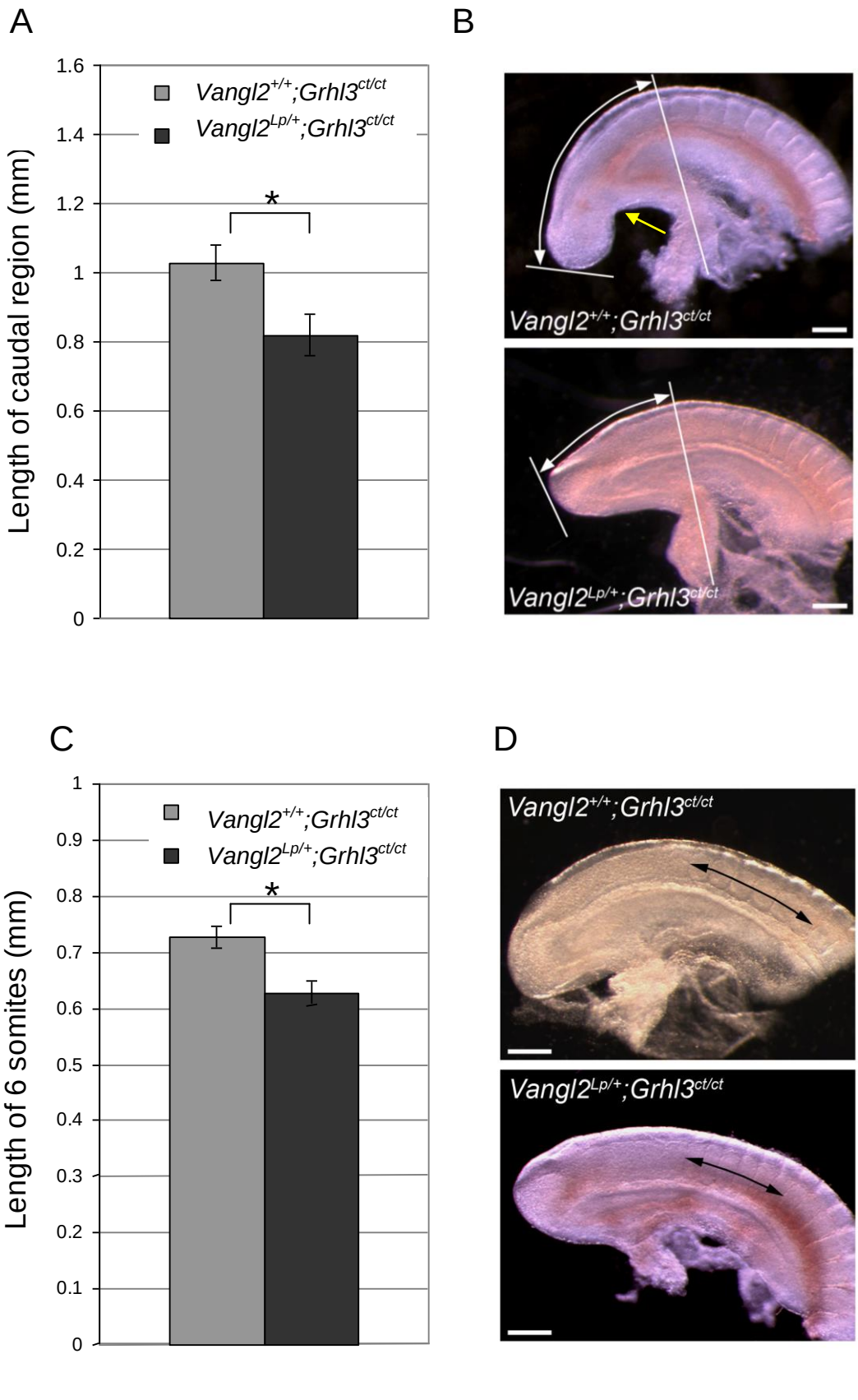
A
B
C
D
Length of caudal region (mm)
Length of 6 somites (mm)
Vangl2+/+;Grhl3ct/ct
Vangl2Lp/+;Grhl3ct/ct
*
0
0.2
0.4
0.6
0.8
1
1.2
1.4
1.6
0.1
0.3
0.5
0.7
0.9

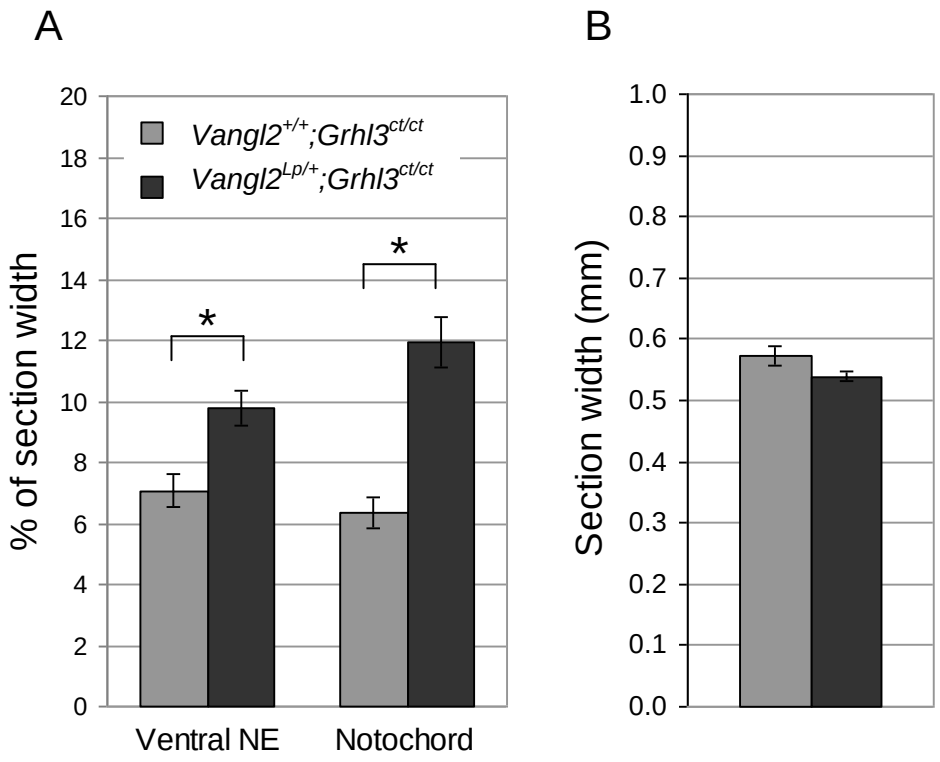

Figure 3.13 Increased relative width of axial tissues in *Vangl2$^{Lp/+}$;Grhl3$^{ct/ct}$* embryos

(**A**) The relative width of the midline ventral neuroepithelium (NE) and the notochord, as a proportion of total body width, is significantly increased in *Vangl2$^{Lp/+}$;Grhl3$^{ct/ct}$*. Measurements are from transverse histological sections as shown in Figure 3.8 (*p = 0.003 and $p < 0.001$, respectively; Mann Whitney Rank Sum test). Bars represent the mean ± SEM (n = minimum of 22 sections from 3 embryos). (**B**) The overall width of the caudal end, measured as the total width of the section, does not vary between genotypes (p = 0.081; Mann Whitney Rank Sum test; n = minimum of 24 sections from 3 embryos).

3.3 Discussion

3.3.1 The *loop-tail/curly tail* interaction is not due to an exacerbation of the *Grhl3*$^{ct/ct}$ mutant phenotype

The observations that *Vangl2*$^{Lp/+}$*;Grhl3*$^{ct/ct}$ embryos display a reduction in ventral axial curvature compared to *Vangl2*$^{+/+}$*;Grhl3*$^{ct/ct}$, and a similar hindgut mitotic index to control embryos, strongly suggest that the deleterious effect of the *Lp* allele is not via the known *curly tail* mutant mechanism. The pathogenesis of NTDs in *curly tail* embryos was elucidated by several studies in the 1980s and 1990s that investigated the connection between the observed caudal proliferation imbalance and the development of NTDs (Copp et al., 1988a; Peeters et al., 1998b). In normally developing embryos, ventral curvature progressively declines in the caudal region from the 27-29 somite stage as the PNP completes closure, and it has been proposed that this 'unbending' facilitates the final stages of primary neurulation (Brook et al., 1991). Abnormally developing *curly tail* embryos display enhanced curvature at this stage and, although a degree of axial unbending is observed, this occurs at a more caudal level than normal (Brook et al., 1991; Peeters et al., 1997). This increased curvature is not simply a secondary effect of delayed PNP closure, as experimentally inducing a delay in non-mutant embryos by physically reopening the PNP does not lead to an increase in curvature (Brook et al., 1991). Together, these early studies suggested a correlation between decreased curvature and successful PNP closure, and that stress forces generated by enhanced curvature in *curly tail* embryos impede the mechanical movements of the neural folds during neurulation.

This hypothesis of a direct causal relationship was also tested experimentally. Firstly, ventral curvature was reduced by inserting the tip of a human eyelash into the hindgut lumen of *curly tail* embryos via the caudal end. After a period of whole

embryo culture, the normal 'unbending' was seen to be enhanced and the delay in PNP closure was significantly rescued (Brook et al., 1991). In another study caudal explants, in which the neuroepithelium was mechanically separated from the surrounding tissues, were cultured *in vitro* and displayed apparently normal closure, further demonstrating that the defect was extrinsic to the neuroepithelium (Van Straaten et al., 1993). In a third report, curvature was increased by culturing embryos with a collapsed, and therefore more tightly wrapped, amnion, which was found to promote ventral curvature and the incidence of open PNP (Peeters et al., 1996). Besides physical manipulations, the *curly tail* defect can also be ameliorated by restoring the balance between the growth rates of dorsal and ventral structures. Embryonic growth retardation *in vivo* by maternal food deprivation, or *in vitro* culture by hyperthermia (40.5^{o}C), normalises PNP closure and reduces the incidence of SB (Copp et al., 1988b; Peeters et al., 1996), as do the stimulation of hindgut proliferation by inositol treatment and the restoration of *Grhl3* function via BAC transgenesis (Cogram et al., 2004; Gustavsson et al., 2007).

The progression of neural tube closure also appears to correlate with curvature at other levels of the mouse neuraxis. For example, initiation of closure at the hindbrain-cervical boundary occurs before embryonic turning, in a region where the embryo exhibits concave (dorsal) bending. In the cranial region, closure correlates with axial unbending, with the last part to close being the midbrain, the most curved part of the cephalic neuroepithelium (Jacobson and Tam, 1982; Peeters et al., 1997). An association between axial curvature and rate of neural tube closure has also been described in other vertebrate species, including chick, rabbit and human embryos (Peeters et al., 1998a).

Given this generalised phenomenon, it would seem that the severe spina bifida phenotype in *Vangl2*$^{Lp/+}$*;Grhl3*$^{ct/ct}$ embryos, despite their 'straighter' caudal regions,

must be the result of another, overriding defect. Indeed, the degree of straightening observed in *Vangl2*$^{Lp/+}$*;Grhl3*$^{ct/ct}$ embryos would be predicted to normalise PNP closure in *curly tail* mutants yet, in contrast, closure is drastically diminished in *Vangl2*$^{Lp/+}$*;Grhl3*$^{ct/ct}$ double mutants. Reasons for the straighter caudal region in embryos with the *Lp* mutation could include: (1) an increase in proliferation rate in the hindgut and notochord, (2) diminished proliferation in the neuroepithelium and (3) reduced CE in the neuroepithelium. Consistent with the reduction in curvature, no further decrease in hindgut proliferation was found in *Vangl2*$^{Lp/+}$*;Grhl3*$^{ct/ct}$*.* In fact, the hindgut mitotic index was found to be comparable to that in control (*Vangl2*$^{+/+}$*;Grhl3*$^{ct/+}$ and unaffected *Vangl2*$^{+/+}$*;Grhl3*$^{ct/ct}$) embryos (Figure 3.11E), which could be interpreted as support for explanation 1. Curvature is reduced from as early as 14-19 somites in embryos with the *Lp* mutation (Figure 3.9), suggesting that, if *Vangl2*^{Lp} does promote ventral proliferation, it does so hours before the *curly tail* defect normally appears. With regards to explanation 2, the expression domains of *Vangl2* and *Grhl3* overlap in the neuroepithelium during spinal neurulation (see Chapter 5), so it will be interesting to determine cell proliferation in this region. However, the morphological data in Figure 3.12 and Figure 3.13 appear to support explanation 3: that is, the *Lp* mutation results in reduced caudal elongation and wider axial tissues, indicative of CE defects.

3.3.2 Does *Vangl2*^{Lp} promote failure of spinal neurulation by inducing a 'PCP' phenotype?

The hypothesis that heterozygosity for *Vangl2*^{Lp} impedes low spinal neurulation via a 'PCP effect' is consistent with CE studies of E8.5 *Vangl2*$^{Lp/+}$ heterozygotes, which do achieve closure 1 but display tail defects and rare spina bifida (Copp et al., 1994). *Vangl2*$^{Lp/+}$ embryos show an intermediate length-to-width ratio and a mild axis elongation phenotype prior to the initiation of closure (Wang et al., 2006a; Ybot-

Gonzalez et al., 2007b) and a slight delay in closure 1 compared to wild type embryos (Copp et al., 1994). Here, the *Vangl2*$^{Lp/+}$ genotype strongly correlates with the severity of the spinal phenotype, with *Vangl2*$^{Lp/+}$;*Grhl3*$^{ct/+}$ embryos being the second-most severely affected genotype after *Vangl2*$^{Lp/+}$;*Grhl3*$^{ct/ct}$ (Figure 3.3, Figure 3.5).

The occurrence of NTDs in *loop-tail* heterozygotes does differ slightly within the literature, presumably due to differences in the genetic background of the strains used and the number of embryos analysed. For example one study observed a spina bifida frequency of 5% (Merte et al., 2010), while this was reportedly as high as 13% in other studies (Lu et al., 2004; Satoh et al., 2008). The variability of spinal defects in *Vangl2*$^{Lp/+}$ embryos suggests that they are sensitive to sub-optimal genetic background conditions when bred with other strains. Moreover, as described in Chapter 1, modifier genes which increase susceptibility to NTDs are indeed present in the *curly tail* background. This raises the question of whether the *Vangl2*$^{Lp/+}$;*Grhl3*$^{ct/ct}$ phenotype could be influenced by non-specific background effects. Genetic background-matched *Vangl2*$^{Lp/+}$;*Grhl3*$^{+/+}$ and *Vangl2*$^{+/+}$;*Grhl3*$^{+/+}$ embryos are, therefore, included as important controls in further analyses of this thesis (Chapter 4 and Chapter 5).

Nonetheless the penetrance of NTDs in *Vangl2*$^{Lp/+}$;*Grhl3*$^{ct/ct}$ is particularly high (74% spina bifida), and is considerably more so than in *Vangl2*$^{Lp/+}$;*Grhl3*$^{ct/+}$ (41%). Thus, the *Grhl3*$^{ct/ct}$ genotype appears to make a specific contribution to the *Vangl2*$^{Lp/+}$;*Grhl3*$^{ct/ct}$ phenotype. As the known *curly tail* mutant developmental defect appears not to play a role in this interaction, the role of *Grhl3* here is intriguing. The abnormal tail bud morphology in *Vangl2*$^{Lp/+}$;*Grhl3*$^{ct/ct}$ (Figure 3.12B) is of particular interest, given the presence of *Grhl3* transcripts in a population of cells within the caudal end at E8.5-E9.5. This observation is pursued further in Chapter 4.

3.3.3 Spina bifida in *Vangl2$^{Lp/+}$;Grhl3$^{ct/ct}$* embryos is not due to failed DLHP formation

At E9.0, *Grhl3* is expressed in the neuroepithelium at the level of the open PNP, the region where DLHPs will form (see Chapter 5). However *curly tail* embryos develop DLHPs normally (Van Straaten and Copp, 2001), indicating that a reduction in *Grhl3* does not adversely affect the signals that regulate dorsolateral bending. The rescue of PNP closure in *curly tail* embryos by physically straightening the tail or abrogating the mechanical stress imposed by surrounding tissues (Brook et al., 1991; Van Straaten et al., 1993) further demonstrates that the defect in *curly tail* is not intrinsic to the neuroepithelium. DLHPs in *Vangl2$^{Lp/+}$;Grhl3$^{ct/ct}$* embryos appear comparable to *Vangl2$^{+/+}$;Grhl3$^{ct/ct}$*, indicating that the *Lp/ct* interaction does not involve disrupted DLHP formation.

Grhl3 null mice (*Grhl3$^{-/-}$*) display 100% penetrant spina bifida (Ting et al., 2003a; Yu et al., 2006) and it has been reported that these embryos fail to form DLHPs at E9.5 (Rifat et al., 2010). However, the authors of this study only examined neural fold elevation at a distal level of the open PNP, away from the closure region where DLHP are normally seen. It is therefore possible that the absence of DLHPs they described is a secondary effect of the widely splayed open neural folds. Indeed, our group has consistently observed DLHPs in *Grhl3$^{-/-}$* embryos at E9.0 (Caroline Hirst, unpublished data).

4. Do *Vangl2*^{Lp} and *Grhl3*^{ct} exert distinct tissue-specific effects during spinal neurulation?

4.1 Introduction

4.1.1 Convergent extension during axis elongation

During development, many embryonic tissues actively narrow in one axis (convergence) while simultaneously lengthening along the perpendicular axis (extension). Early studies of the amphibian gastrula revealed that as the presumptive axial (notochordal) and paraxial (somitic) mesoderm is internalised, cells undergo such convergent extension (CE) movements to close the blastopore and elongate the anterior-posterior (A-P) body axis. Meanwhile the overlying neural tissue also simultaneously converges and extends. The morphogenetic process of CE has since been shown to control body axis elongation in fish, worms, birds and mammals, as well as regulating processes such as germ band extension and imaginal leg disc evagination in the fruit fly (Keller et al., 2000) and elongation of the mammalian cochlea and limb buds (Gao et al., 2011; Wang et al., 2005).

During *Xenopus* gastrulation, CE in neural and mesodermal tissues is driven by cell rearrangements, whereby cells intercalate with each other to change the tissue shape. Two distinct types of cell intercalation have been described: radial intercalation, as cells move between one another along the superficial-deep axis of the embryo leading to thinning of the tissue, and medio-lateral (ML) intercalation along the ML axis to produce a tissue which is narrower and longer. The movements of *Xenopus* CE are believed to be tissue-autonomous, as isolated explants continue to converge and extend in culture independently of external forces and surrounding tissues (Keller et al., 2000).

While cell rearrangement represents a common type of movement driving CE, it is not the only mechanism employed by embryos to elongate their body (Tada and Heisenberg, 2012). During gastrulation in zebrafish, mesodermal cells display both

similar and different behaviours to *Xenopus*: progenitors of the prechordal plate migrate as a cohesive cluster without exchanging their neighbours, while later internalising notochord progenitors undergo ML intercalations to extend the body axis. At the same time, more lateral mesodermal precursors (somitic progenitors) first display collective migration towards the midline, followed by both ML and radial intercalation when they arrive near to the presumptive notochord. Thus, collective mesodermal cell migration is another important aspect of CE in zebrafish (Tada and Heisenberg, 2012). Orientated cell division has also been shown to contribute to CE in some systems. For example, divisions have been reported to predominantly occur in the A-P dimension in the presumptive neural plate of zebrafish embryos (Gong et al., 2004). In addition to cell intercalation, orientated divisions are also a feature of *Drosophila* germband epithelium morphogenesis and neural plate shaping in the chick embryo (Keller, 2002).

CE processes also drive the shaping of the body axis in mouse embryos. After emerging from the node, the population of chordamesoderm cells narrows to form the mature notochord, while presomitic mesoderm derived from the primitive streak caudal to the node also undergoes CE movements. At the same time the overlying neurectoderm cells converge towards the midline, lengthening and narrowing the neural plate (Yamanaka et al., 2007; Ybot-Gonzalez et al., 2007b; Yen et al., 2009). The cellular behaviours underlying CE of the mammalian neural plate and underlying mesoderm are not fully understood although, as discussed in more detail later, labelling experiments and time lapse imaging have provided evidence of cell intercalation (Yamanaka et al., 2007; Yen et al., 2009).

4.1.2 A stem cell population in the tail bud

During elongation of amniote embryos, the axial tissues of the body (neural tube, notochord and somites) are laid down in a rostral-to-caudal sequence. During gastrulation the cells generating these structures are predominantly derived from the primitive streak and the surrounding epiblast which, together, will later form the tail bud. Regional organisation of progenitors within the primitive streak has been demonstrated by detailed fate-mapping and lineage analysis: at the rostral tip of the streak, cells emerging from the node generate the notochord, while cells from the 'node-streak border' (NSB), the region encompassing the caudal end of the node and a portion of the rostral streak, additionally contribute to somitic tissue and the ventral midline of the neuroepithelium. More caudal regions of the primitive streak and the adjacent epiblast contain precursors of the lateral neural plate and somites (Cambray and Wilson, 2002; Selleck and Stern, 1991; Wilson and Beddington, 1996). Later in development, the fate map of progenitors within the tail bud is similar to the map of the early streak and surrounding tissues. During low spinal neurulation the region at the caudal junction of the neural tube and notochord, termed the 'chordo-neural-hinge' (CNH), is considered to be homologous to the NSB, as it contains progenitors of the ventral neural tube, notochord and somites (Figure 4.1) (Cambray and Wilson, 2002; McGrew et al., 2008).

As A-P development proceeds, most regional progenitors within the primitive streak are laid down and incorporated into axial tissues. Intriguingly, labelling studies have provided evidence that a small population of cells also remains within the streak and later comes to reside in the tail-bud, and that these cells constitute a self-renewing stem cell population (Cambray and Wilson, 2002; Cambray and Wilson, 2007; Wilson and Beddington, 1996). Early transplantation experiments demonstrated that small groups of cells isolated from the tail buds of mouse embryos at stages up to

E13.5 could contribute to axial tissue when grafted to the primitive streak of E8.5 host embryos (Tam and Tan, 1992). It was later shown in both mouse and chick embryos that this potency is specifically a property of cells within the CNH, and that progeny from this region can be serially transplanted through the streaks of multiple embryos (Cambray and Wilson, 2002; McGrew et al., 2008).

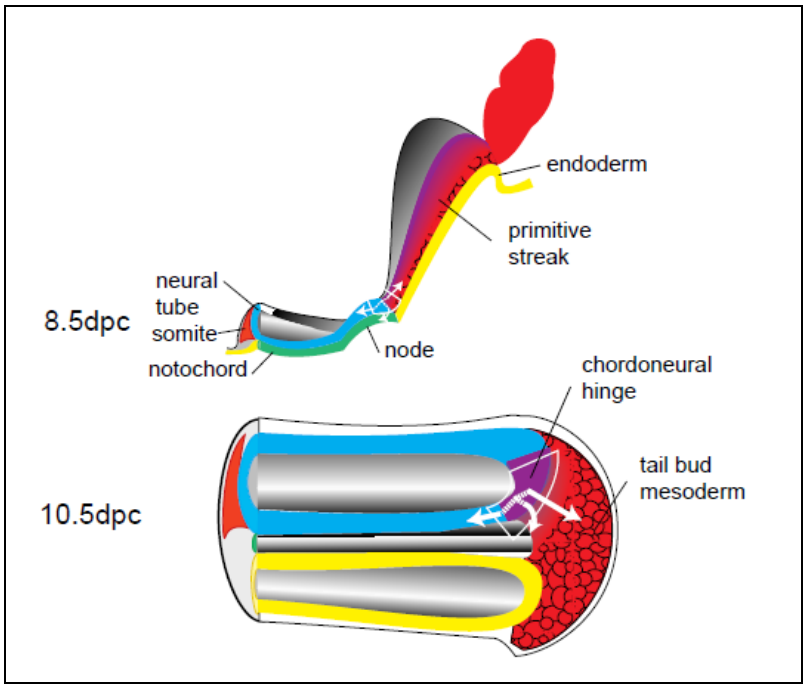

Figure 4.1 Location of progenitor cells during axis elongation

A stem-cell like population has been proposed to reside at the node-streak border, which is analogous to the chordo-neural-hinge at later stages (white boxes in the upper and lower images, respectively). Image taken from (Cambray and Wilson, 2002).

The reports described above did not investigate whether individual cells of the CNH are indeed multipotent, or whether this region instead consists of a mixture of pre-specified precursors. However, single cell labelling experiments have indicated that at least some cells within this region are multipotent; in both chick and mouse labelled cells were found to contribute progeny to more than one tissue (Forlani et

al., 2003; McGrew et al., 2008; Selleck and Stern, 1991). The contribution of the CNH to the elongation of the body axis is not fully understood (Wilson et al., 2009) although, recently, termination of body axis elongation in the chick was shown to be associated with a progressive reduction in size of this cell population (Olivera-Martinez et al., 2012).

In the previous chapter, evidence of defective CE and abnormal tail bud morphology were identified in *Vangl2*$^{Lp/+}$*;Grhl3*$^{ct/ct}$ embryos during spinal neurulation. Here, the possibility that the *Lp* and *ct* alleles cause distinct mutant effects in different tissues, which then summate to cause failure of neural tube closure, was considered. In particular, I investigated whether *Vangl2*^{Lp} causes defective CE in the midline, and whether *Grhl3*^{ct} affects tail bud development.

4.2 Results

4.2.1 When do the genotypes diverge phenotypically?

In *Vangl2*$^{Lp/+}$*;Grhl3*$^{ct/ct}$ embryos, a delay in spinal neurulation is evident at E10-E10.5 (see Chapter 3). To determine the developmental stage at which this defect initiates, and when *Vangl2*$^{Lp/+}$*;Grhl3*$^{ct/ct}$ embryos first differ phenotypically from *Vangl2*$^{+/+}$*;Grhl3*$^{ct/ct}$*,* a more detailed analysis of PNP size was performed. The findings of the previous chapter show that, after *Vangl2*$^{Lp/+}$*;Grhl3*$^{ct/ct}$*,* the genotype with the most severe effect is *Vangl2*$^{Lp/+}$*;Grhl3*$^{ct/+}$, raising the additional question of whether non-specific effects of the *curly tail* background may contribute to the *Lp/ct* interaction, in addition to the *Grhl3*^{ct} mutation. To address this possibility, *Vangl2*$^{Lp/+}$ mice were bred with congenic wild type mice, which share over 95% genetic background with the *curly tail* strain (+^{ct}/+^{ct}; see Chapter 2). This cross generated background-matched wild type and *loop-tail* heterozygous embryos. The following embryos were therefore used for all analyses in this chapter, and in Chapter 5: wild type (*Vangl2*$^{+/+}$*;Grhl3*$^{+/+}$); 'single mutants' (*Vangl2*$^{Lp/+}$*;Grhl3*$^{+/+}$ and *Vangl2*$^{+/+}$*;Grhl3*$^{ct/ct}$); 'double mutants' (*Vangl2*$^{Lp/+}$*;Grhl3*$^{ct/ct}$).

For each of the four genotypes the length of the PNP at different developmental stages was measured (Table 4.1, Figure 4.2). The PNP length of *Vangl2*$^{Lp/+}$*;Grhl3*$^{ct/ct}$ embryos was first significantly increased compared to the other three genotypes at the 26-28 somite stage, when both single mutants displayed a milder delay in closure. At 29-33 somites none of the *Vangl2*$^{Lp/+}$*;Grhl3*$^{ct/ct}$ embryos had completed closure, while *Vangl2*$^{+/+}$*;Grhl3*$^{ct/ct}$ PNPs were variable (Figure 4.2; also see Chapter 3), likely reflecting the spectrum of spinal phenotypes observed in this strain. By this stage there was no difference between *Vangl2*$^{+/+}$*;Grhl3*$^{+/+}$ and *Vangl2*$^{Lp/+}$*;Grhl3*$^{+/+}$ PNP length and a proportion of embryos of both genotypes had achieved closure

(Figure 4.2). At early stages (14-16 and 17-19 somites) the *Lp* allele was actually associated with a reduction in PNP length compared to wild type embryos.

When PNP width was assessed, *Vangl2*$^{Lp/+}$;*Grhl3*$^{ct/ct}$ diverged from *Vangl2*$^{+/+}$;*Grhl3*$^{ct/ct}$ at an earlier stage than was observed for PNP length (Table 4.2, Figure 4.3). At 17-19 and 20-22 somites the double mutants had wider PNPs than wild type or *curly tail* embryos. Interestingly this difference was also observed in *Vangl2*$^{Lp/+}$;*Grhl3*$^{+/+}$ embryos, suggesting that the *Lp* allele causes an increase in PNP width regardless of the *Grhl3* genotype. Finally, embryonic crown-rump length (CRL) was measured to check that the differences in PNP size were not secondary effects of differences in overall embryonic growth. Embryos of all genotypes displayed a comparable growth rate (Figure 4.4), with no difference in the CRL of embryos at 14-25 somites (1-Way ANOVA; $p > 0.18$ for each stage-category). At 26-28 somites a small difference between genotypes was observed, likely due to the presence of outliers and the relatively small number of embryos ($p = 0.04$, 1-Way ANOVA; no individual comparisons were significant). However by 29-33 somites, when PNP size is dramatically increased in *Vangl2*$^{Lp/+}$;*Grhl3*$^{ct/ct}$ compared to the other genotypes, no differences in CRL were observed.

Together these data show that, in terms of PNP length, *Vangl2*$^{Lp/+}$;*Grhl3*$^{ct/ct}$ embryos display larger neuropores than wild type and single mutant embryos at the 26-28 somite stage. However, before this difference becomes apparent, both *Vangl2*$^{Lp/+}$;*Grhl3*$^{ct/ct}$ and *Vangl2*$^{Lp/+}$;*Grhl3*$^{+/+}$ embryos display an increase in PNP width. The finding that *Vangl2*$^{Lp/+}$;*Grhl3*$^{ct/ct}$ embryos are phenotypically much more severe than background-matched *Vangl2*$^{Lp/+}$;*Grhl3*$^{+/+}$ embryos suggests that the *curly tail* genetic background does not make a significant contribution to the *Lp/ct* phenotype, independently of the *Grhl3*^{ct} mutation.

Genotype	Number of somite pairs					
	14-16	**17-19**	**20-22**	**23-25**	**26-28**	**29-33**
1) *Vangl2*$^{+/+}$; *Grhl3*$^{+/+}$	0.59 ± 0.01	0.55 ± 0.01	0.52 ± 0.02	0.29 ± 0.09	0.26 ± 0.03	0.10 ± 0.02
2) *Vangl2*$^{+/+}$; *Grhl3*$^{ct/ct}$	0.55 ± 0.02	0.54 ± 0.01	0.57 ± 0.02	0.54 ± 0.02	0.47 ± 0.06	0.33 ± 0.04
3) *Vangl2*$^{Lp/+}$; *Grhl3*$^{+/+}$	0.52 ± 0.01	0.46 ± 0.03	0.49 ± 0.02	0.44 ± 0.03	0.43 ± 0.08	0.12 ± 0.03
4) *Vangl2*$^{Lp/+}$; *Grhl3*$^{ct/ct}$	0.50 ± 0.02	0.51 ± 0.01	0.55 ± 0.02	0.52 ± 0.02	0.66 ± 0.04	0.79 ± 0.08
*Statistical differences ($p < 0.05$)	1 > 3, 4	1 > 3	2 > 3	2 > 1	2 > 1 4 > 1, 2, 3	2 > 1 4 > 1, 2, 3

Table 4.1 Comparison of PNP length between genotypes

Table showing the mean PNP length (mm) ± SEM for progressive developmental stages. The difference between genotypes was significant at each stage analysed (1-Way ANOVA analysis; $p < 0.03$ for each somite category). * Significant differences revealed by multiple comparison testing.

Genotype	Number of somite pairs					
	14-16	**17-19**	**20-22**	**23-25**	**26-28**	**29-33**
1) *Vangl2*$^{+/+}$; *Grhl3*$^{+/+}$	0.16 ± 0.02	0.16 ± 0.01	0.20 ± 0.02	0.13 ± 0.04	0.09 ± 0.01	0.04 ± 0.01
2) *Vangl2*$^{+/+}$; *Grhl3*$^{ct/ct}$	0.21 ± 0.02	0.19 ± 0.01	0.20 ± 0.01	0.19 ± 0.04	0.17 ± 0.03	0.11 ± 0.02
3) *Vangl2*$^{Lp/+}$; *Grhl3*$^{+/+}$	0.18 ± 0.03	0.24 ± 0.02	0.32 ± 0.01	0.32 ± 0.04	0.27 ± 0.05	0.10 ± 0.03
4) *Vangl2*$^{Lp/+}$; *Grhl3*$^{ct/ct}$	0.24 ± 0.02	0.29 ± 0.02	0.32 ± 0.02	0.35 ± 0.03	0.39 ± 0.03	0.42 ± 0.02
*Statistical differences ($p < 0.05$)	4 > 1	4 > 1, 2	3 > 1, 2 4 > 1, 2	3 > 1 4 > 1, 2	3 > 1 4 > 1, 2, 3	2 > 1 4 > 1, 2, 3

Table 4.2 Comparison of PNP width between genotypes

Table showing the mean PNP width ± SEM for progressive developmental stages. The difference between genotypes was significant at each stage analysed (1-Way ANOVA analysis; $p < 0.03$ for each somite category). *Significant differences revealed by multiple comparison testing.

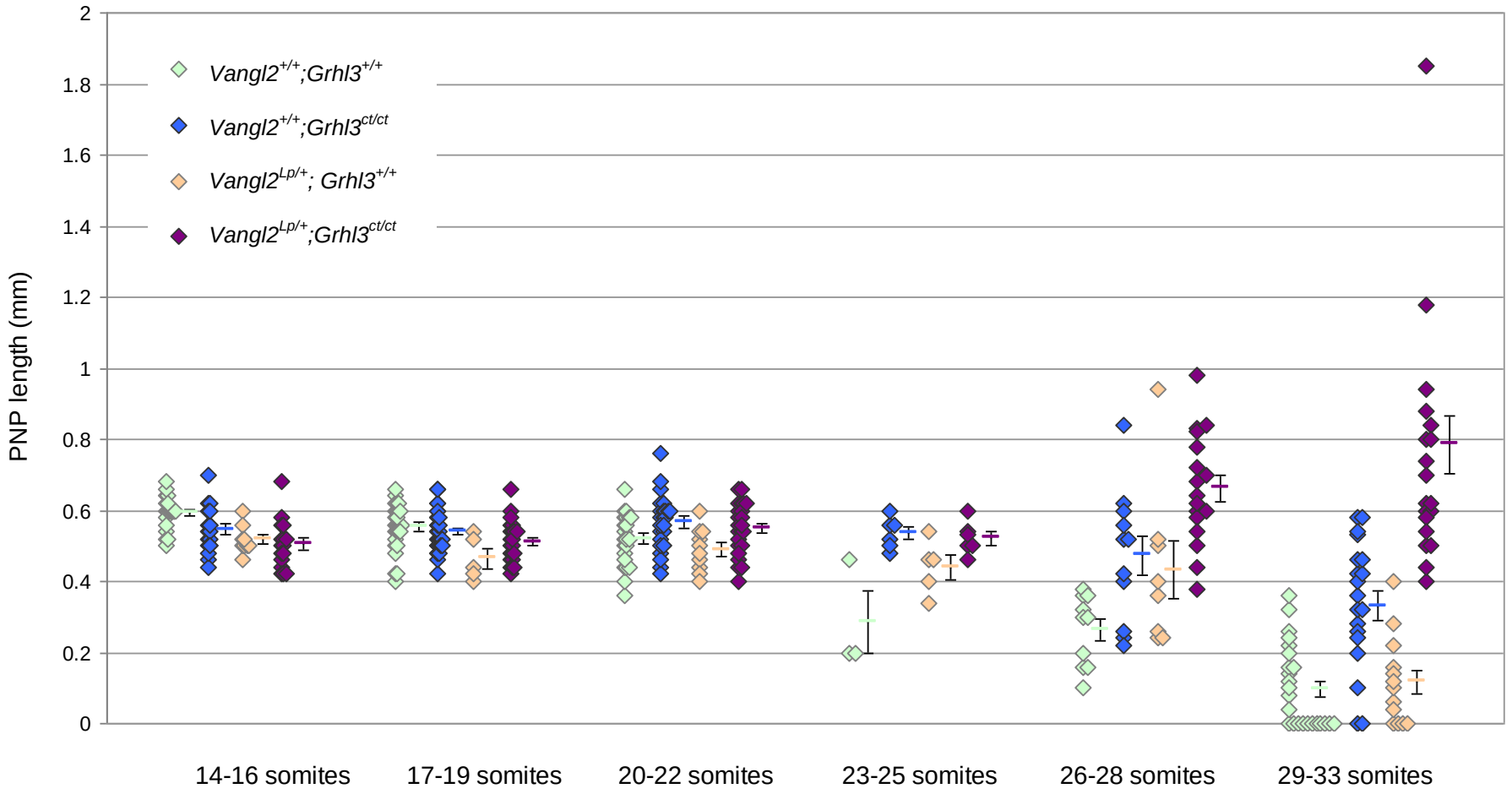

Figure 4.2 Graph of PNP lengths for each genotype.

Individual embryos are represented by a single data point, with the mean ± SEM shown to the right of each group.

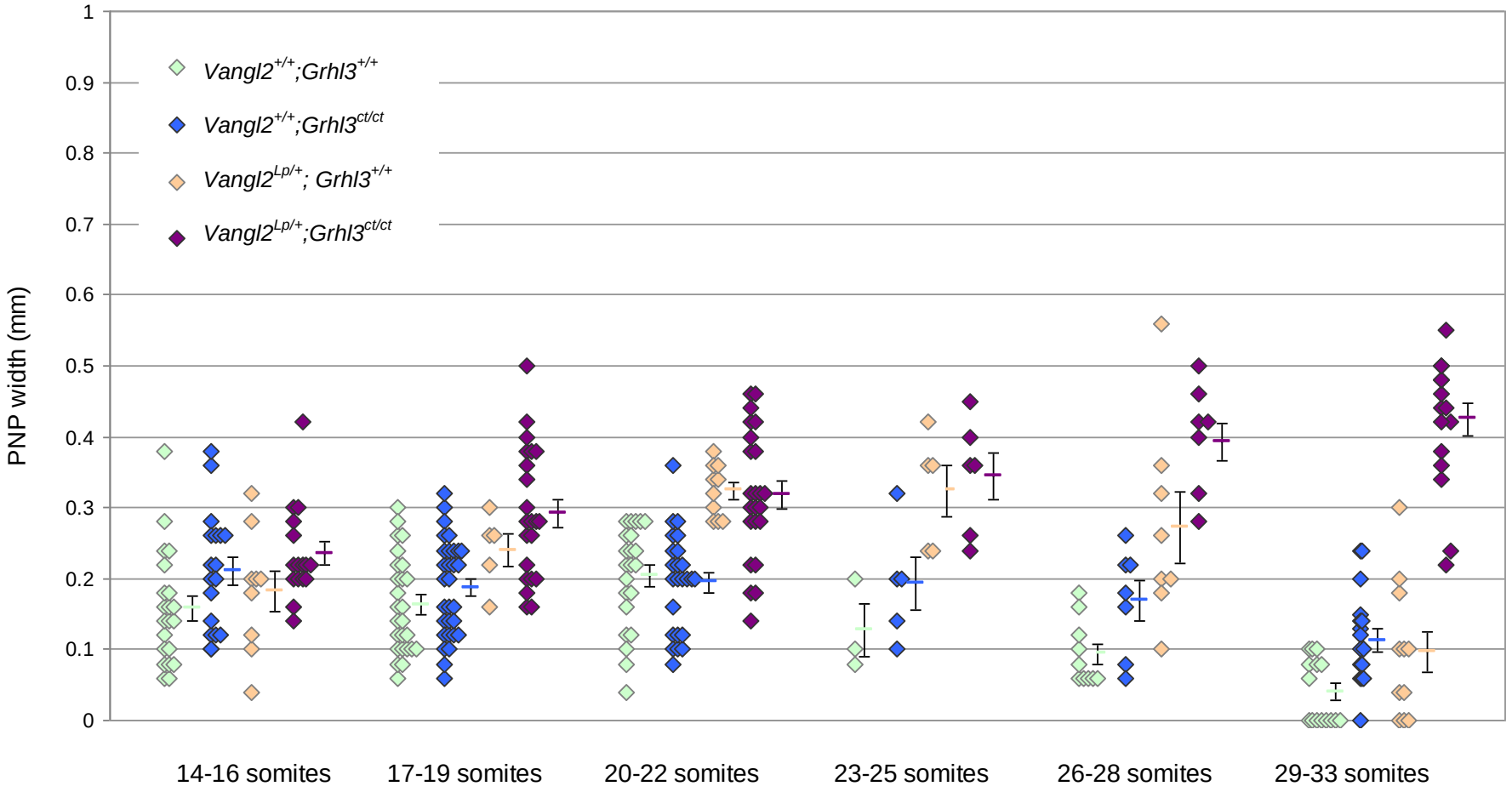

Figure 4.3 Graph of PNP widths for each genotype.

Individual embryos are represented by a single data point, with the mean ± SEM shown to the right of each group.

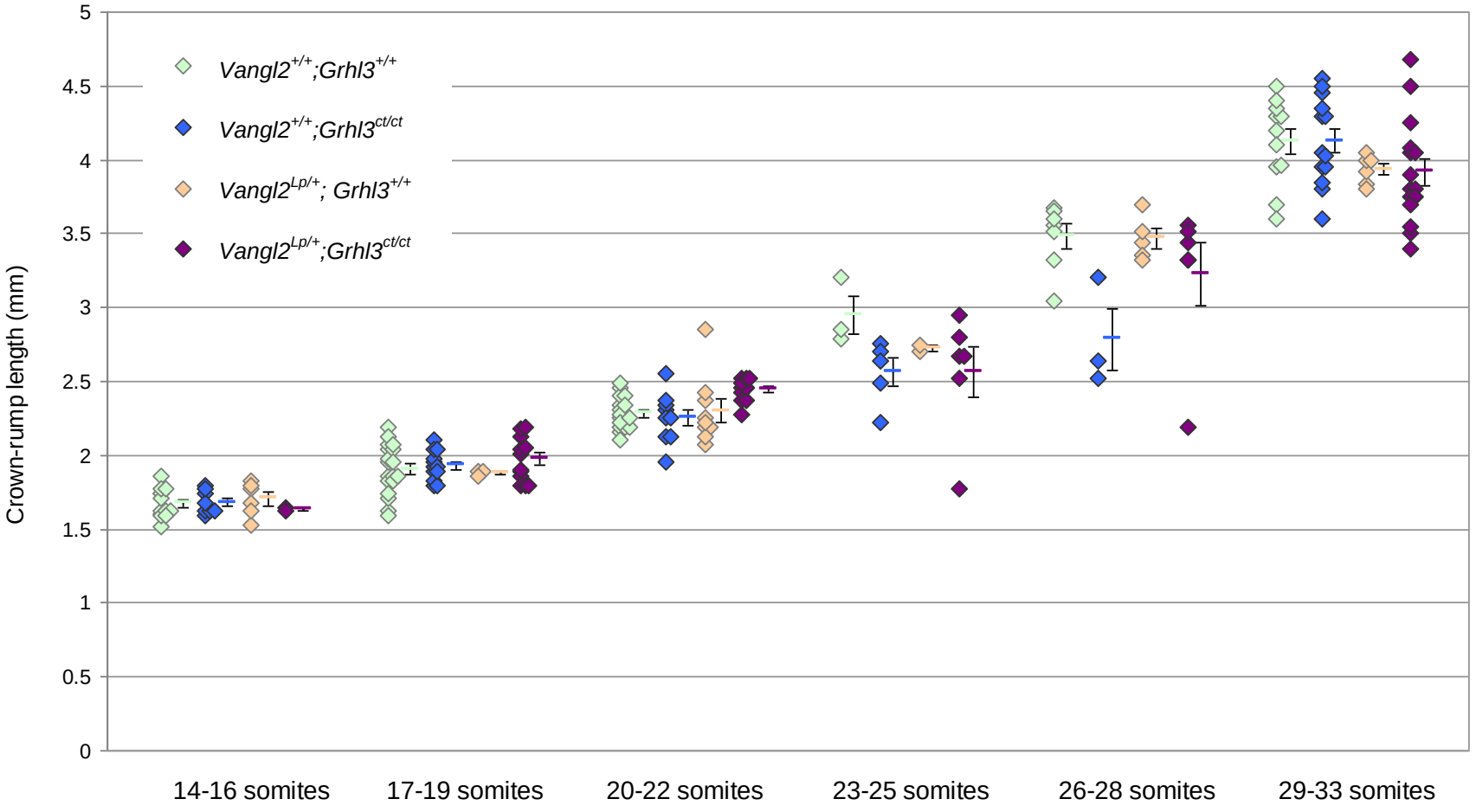

Figure 4.4 Graph of crown-rump lengths for each genotype.

Individual embryos are represented by a single data point, with the mean ± SEM shown to the right of each group.

4.2.2 *Vangl2*^{Lp} causes defective midline convergent extension during spinal neurulation

As described in Chapter 3, initial morphometric analyses indicate that *Vangl2*$^{Lp/+}$*;Grhl3*$^{ct/ct}$ embryos exhibit a reduction in the normal lengthening of the embryonic axis and narrowing of the midline tissues during spinal neurulation. As *loop-tail* heterozygotes, like the double mutants, display abnormally wide posterior neuropores (Figure 4.3), I investigated whether they too display evidence of defective CE. As discussed earlier, *Vangl2*$^{Lp/+}$ embryos show a mild CE phenotype at E8.5, prior to the initiation of neural tube closure (Wang et al., 2006a; Ybot-Gonzalez et al., 2007b).

As in *Vangl2*$^{Lp/+}$*;Grhl3*$^{ct/ct}$ embryos, the length of the *Vangl2*$^{Lp/+}$*;Grhl3*$^{+/+}$ caudal region was reduced, as was the length of the region occupied by the most-recently formed six somites (Figure 4.5A, B). For both of these parameters, no difference was found between *Vangl2*$^{+/+}$*;Grhl3*$^{ct/ct}$ and wild type. Similarly, a reduction in the angle of ventral curvature was observed in the posterior region of *Vangl2*$^{Lp/+}$*;Grhl3*$^{+/+}$ embryos, to a similar extent as that seen in *Vangl2*$^{Lp/+}$*;Grhl3*$^{ct/ct}$ (Figure 4.5C). These measurements demonstrate that the caudal axis is significantly shorter and straighter in embryos that are heterozygous for *Vangl2*^{Lp}, and that these phenotypes are not affected by the presence of *Grhl3*^{ct} alleles.

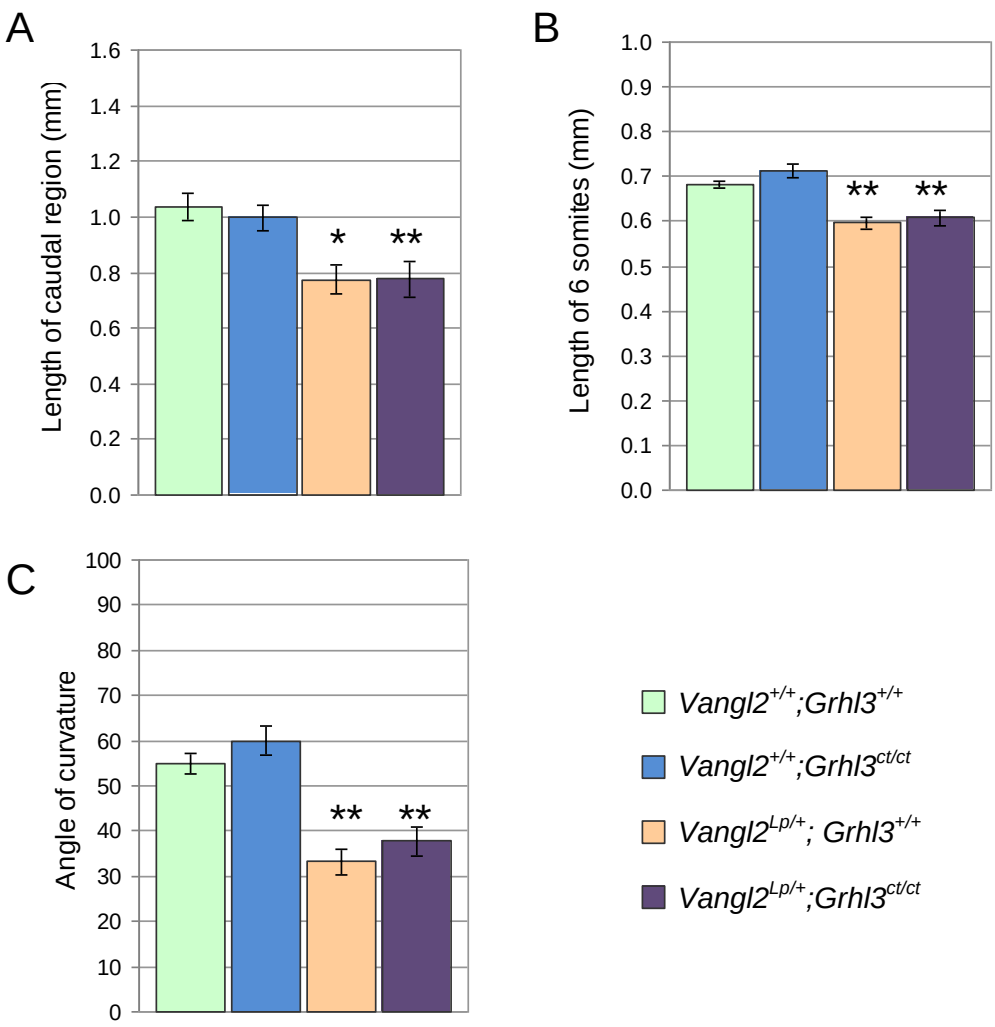

Figure 4.5 *Vangl2*^{Lp} is associated with a reduction in caudal axis length and ventral curvature

Data shown are for embryos with 20-25 somite pairs. Parameters were measured as shown in Chapter 2 with the data for *Vangl2*$^{+/+}$*;Grhl3*$^{ct/ct}$ and *Vangl2*$^{Lp/+}$*;Grhl3*$^{ct/ct}$ as shown before (see Chapter 3). (**A**) The *Lp* allele is associated with an approximately 20% reduction in caudal length compared to wild type and *curly tail* embryos (p = 0.001; n = min. of 8 embryos per genotype). (**B**) The *Lp* allele is associated with an approximately 14% reduction in length of the most recently formed 6 somites compared to wild type and *curly tail* embryos (p < 0.001; n = min. of ten embryos per genotype). (**C**) Axial curvature is also reduced in *Vangl2*$^{Lp/+}$*;Grhl3*$^{+/+}$ and *Vangl2*$^{Lp/+}$*;Grhl3*$^{ct/ct}$ (p < 0.001; n = min. of ten embryos per genotype). Bars represent the mean ± SEM. Genotypes were compared by 1-Way ANOVA and asterisks indicate results of multiple comparison testing: **signifcantly reduced compared to wild type and *curly tail*; *significantly reduced compared to wild type (p < 0.05).

The width of the midline tissues was assessed by examining transverse sections of embryos following WISH for the notochord marker, *Brachyury*. Previous analysis of this gene, and of *sonic hedgehog* (*Shh*), has revealed broader domains of notochordal expression in PCP mutant embryos prior to closure 1 (Greene et al., 1998; Paudyal et al., 2010; Ybot-Gonzalez et al., 2007b). As observed for the histological sections shown previously (Chapter 3), *Vangl2*$^{Lp/+}$*;Grhl3*$^{ct/ct}$ embryos displayed an abnormal widening of the notochord at the axial level of PNP closure, compared to both wild type and *Vangl2*$^{+/+}$*;Grhl3*$^{ct/ct}$*,* and this was accompanied by an increase in the width of the overlying ventral neuroepithelium. A similar phenotype was seen in *Vangl2*$^{Lp/+}$*;Grhl3*$^{+/+}$ (see yellow arrows in Figure 4.6), whereas *Vangl2*$^{+/+}$*;Grhl3*$^{ct/ct}$ embryos appeared similar to wild type.

A proportion of E9.0-E10.5 mutant embryos also displayed an unusual phenotype whereby the ventral neuroepithelium appeared to protrude dorsally through the open posterior neuropore, producing a convex neural plate. The appearance of this defect ranged in severity, from a slight ‘bulge’ at the caudal end to a distinct dorsal protrusion (Figure 4.7A). The phenotype was not seen in wild type embryos, became more frequent with an increasing number of mutant alleles, and was predominantly associated with the *Vangl2*^{Lp} mutation (Figure 4.7B). Transverse sections through the abnormal region revealed an excess of neuroepithelial tissue, in which the neural folds appeared to have buckled and become displaced dorsally (Figure 4.8F, I). The phenotype was not a feature of an enlarged PNP *per se*, as it was not observed in affected *curly tail* embryos (Figure 4.8E, H).

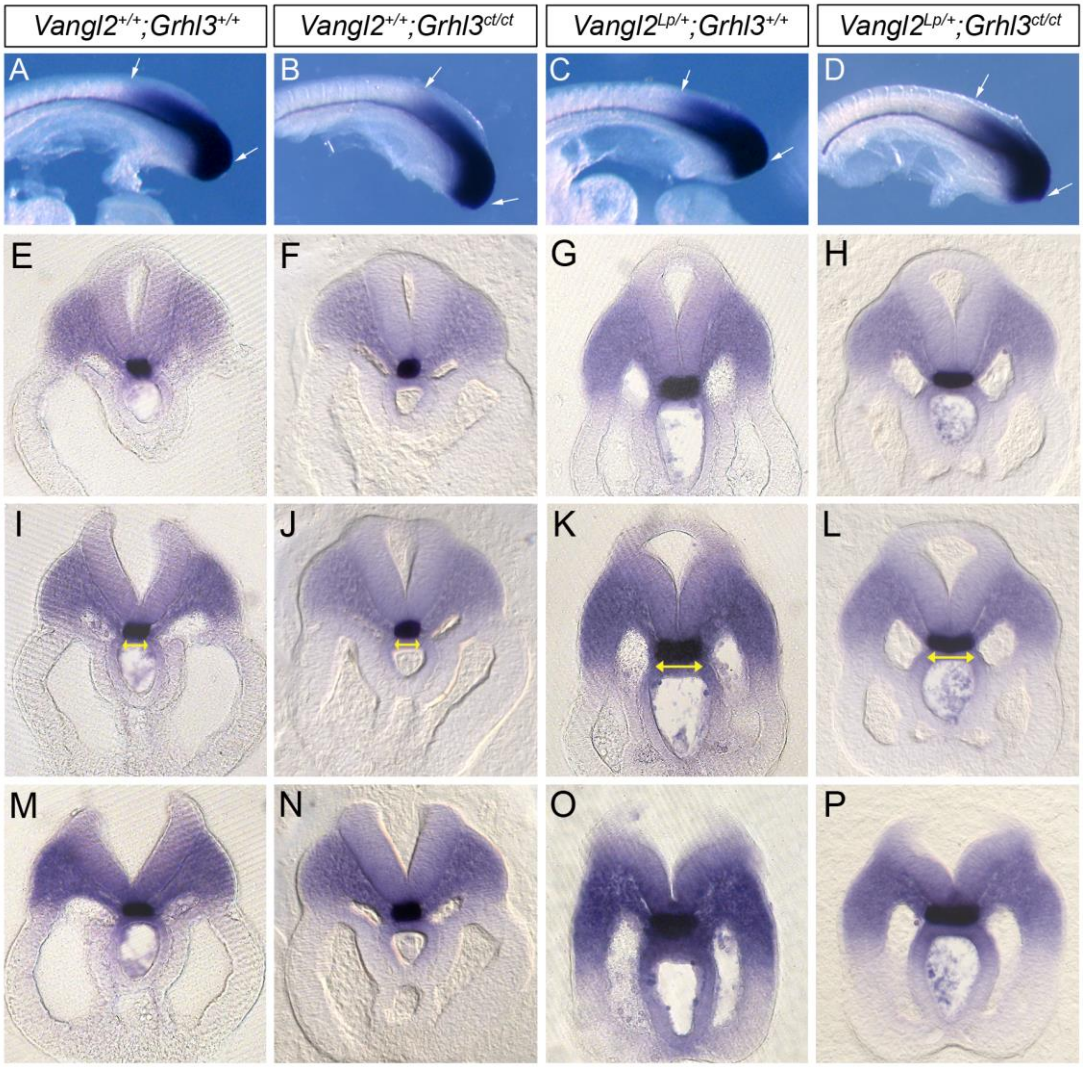

Figure 4.6 *Vangl2*^{Lp} is associated with increased width of the midline tissues

(**A-D**) Caudal regions of 20-25 somite stage embryos following whole-mount *in situ* hybridisation for *Brachyury*. Although no overt differences in expression were observed between genotypes, the length of the expression domain appeared slightly shorter for both genotypes carrying the *Lp* mutation, likely reflecting the shorter body axis in these embryos (arrows). (**E-P**) Transverse sections through the embryo in A-D at the level of the recently closed neural tube (E-H), the point of closure (I-L) and the level of active neurulation caudal to the closure point (M-P. Arrows in I-L indicate the width of the *Brachyury*-positive notochord.

A

B

Genotype	Normal PNP appearance **%** (freq.)	'Bulging' PNP **%** (freq.)
Vangl2$^{+/+}$;*Grhl3*$^{+/+}$	**100** (81/81)	**0** (0/81)
Vangl2$^{+/+}$;*Grhl3*$^{ct/+}$	**98.73** (78/79)	**1.27** (1/79)
Vangl2$^{+/+}$;*Grhl3*$^{ct/ct}$	**97.96** (48/49)	**2.04** (1/49)
Vangl2$^{Lp/+}$; *Grhl3*$^{+/+}$	**81.48** (22/27)	**18.52** (5/27)
Vangl2$^{Lp/+}$; *Grhl3*$^{ct/+}$	**83.52** (76/91)	**16.48** (15/91)
Vangl2$^{Lp/+}$;*Grhl3*$^{ct/ct}$	**76.60** (36/47)	**23.40** (11/47)

Figure 4.7 Dorsal bulging at the level of the PNP

(**A**) Examples of the different phenotypes observed in the E9.5 embryonic caudal region. Scale bars: 200 µm. (**B**) Frequency of a 'bulging' PNP phenotype in embryos of each genotype at E9.0-E10.5. The *Vangl2*$^{+/+}$;*Grhl3*$^{ct/+}$ and *Vangl2*$^{Lp/+}$; *Grhl3*$^{ct/+}$ genotypes from the breeding strategy described in Chapter 3 are also included for comparison (grey text). A low frequency (1-2%) was observed in embryos carrying the *Grhl*^{ct} mutation, while the *Vangl2*^{Lp} allele was associated with a higher occurrence of the defect (>16%). *Vangl2*$^{Lp/+}$;*Grhl3*$^{ct/ct}$ embryos displayed the highest frequency, with nearly a quarter of embryos affected (23%).

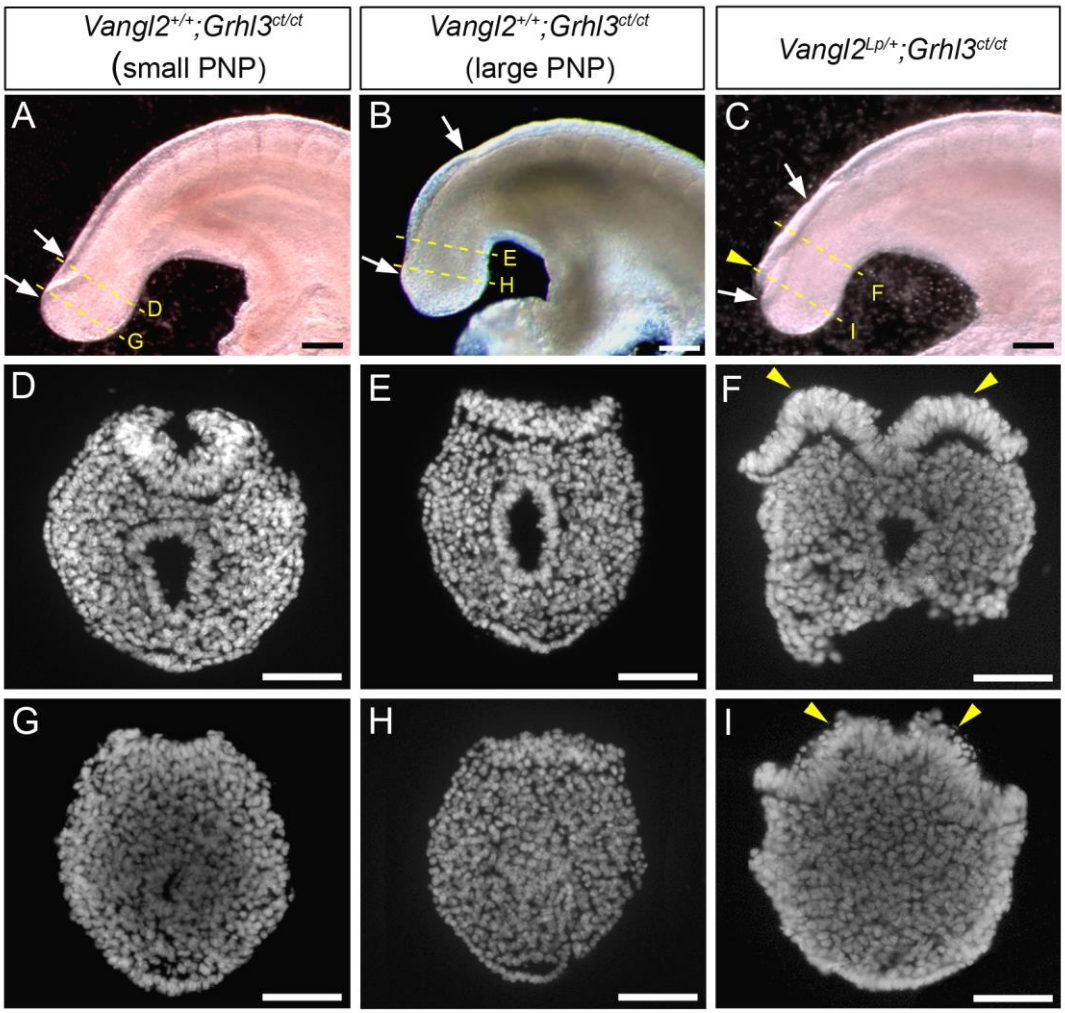

Figure 4.8 Dorsal bulging is associated with an excess of neural tissue

(**A-C**) Caudal regions from E10.5 unaffected *curly tail* (A), affected *curly tail* (B) and *Lp/ct* double mutant embryos. (**D-I**) Sections through the caudal regions shown in A-C. In *curly tail* embryos, a delay in neurulation does not lead to the observed phenotype, as both unaffected and affected embryos display normal neural plate morphology at the level of the PNP and tail bud (D-E and G-H, respectively). White arrows indicate the level of the open PNP. Dotted lines indicate the level of the sections in D-I. The appearance of a bulging PNP appears to be due to excessive, dysmorphic neural tissue (yellow arrowheads). Scale bars: 200 µm (A-C) and 50 µm (D-I).

Could the bulging PNP and apparent excess of neural tissue seen in individual sections occur due to defective CE cell movements in the caudal region? An alternative explanation is that *Vangl2*^{Lp} causes an increase in neuroepithelial proliferation, leading to an increase in neuroepithelial cell number. The latter possibility was investigated by immunofluorescence for PH-H3 (Figure 4.9). Consistent with the sections shown above, the number of DAPI-stained nuclei was higher in the neuroepithelium of embryos carrying the *Lp* mutation than those which were wild type for *Vangl2*. Both *Vangl2*$^{Lp/+}$*;Grhl3*$^{+/+}$ and *Vangl2*$^{Lp/+}$*;Grhl3*$^{ct/ct}$ had, on average, over 200 cells per section compared to approximately 175 cells in *Vangl2*$^{+/+}$*;Grhl3*$^{+/+}$ and *Vangl2*$^{+/+}$*;Grhl3*$^{ct/ct}$ embryos (Figure 4.9A). However, this increase in neuroepithelial cell number was not associated with a higher proliferation rate; in fact, while *Vangl2*$^{Lp/+}$*;Grhl3*$^{+/+}$ embryos were comparable to wild type, a lower mitotic index was observed in both *Vangl2*$^{+/+}$*;Grhl3*$^{ct/ct}$ and *Vangl2*$^{Lp/+}$*;Grhl3*$^{ct/ct}$ (Figure 4.9B).

Further evidence for a reduction in axis extension downstream of *Vangl2*^{Lp} was provided by analysing the pattern of caudally-expressed genes in wild type and mutant embryos. As shown in Figure 4.6A-D, the region occupied by *Brachyury* was slightly shorter in the *Vangl2*$^{Lp/+}$*;Grhl3*$^{+/+}$ and *Vangl2*$^{Lp/+}$*;Grhl3*$^{ct/ct}$ caudal region. Similarly, the caudal region occupied by expression of the canonical Wnt ligand, *Wnt3a*, was also slightly reduced in both of these genotypes compared to wild type and *curly tail* embryos (Figure 4.10). For both genes, the overall intensity of staining and distribution of transcripts was unaltered.

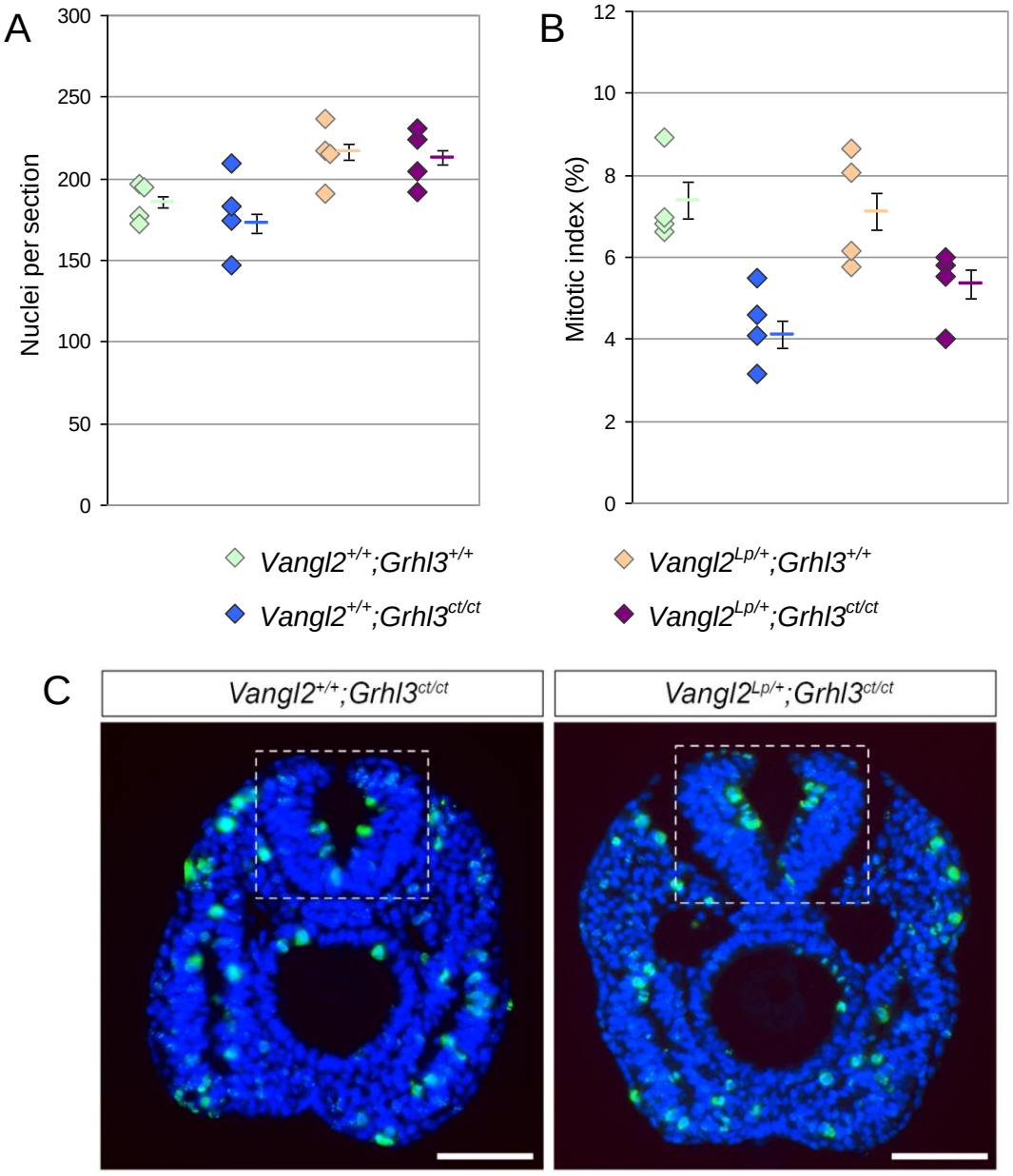

Figure 4.9 *Vangl2*^{Lp} does not cause an increase in neuroepithelial proliferation

(**A**) Comparison of neuroepithelial cell number at the 17-19 somite stage, counted from DAPI-stained sections. Each data point represents the mean number of nuclei per section, for a minimum of four sections through an individual embryo at the level of active neurulation (shown in C). Error bars represent the mean cell number ± SEM for all sections of the same genotype. An increase in cell number was observed in *Vangl2*$^{Lp/+}$;*Grhl3*$^{+/+}$ and *Vangl2*$^{Lp/+}$;*Grhl3*$^{ct/ct}$ ($p < 0.001$, 1-Way ANOVA). (**B**) Mitotic indices in the neuroepithelium. Mean MI was reduced in embryos with the *Grhl3*$^{ct/ct}$ genotype, but did not vary significantly between wild type and *Vangl2*$^{Lp/+}$;*Grhl3*$^{+/+}$, or between *Vangl2*$^{+/+}$;*Grhl3*$^{ct/ct}$ and *Vangl2*$^{Lp/+}$;*Grhl3*$^{ct/ct}$ ($p < 0.001$, 1-Way ANOVA).

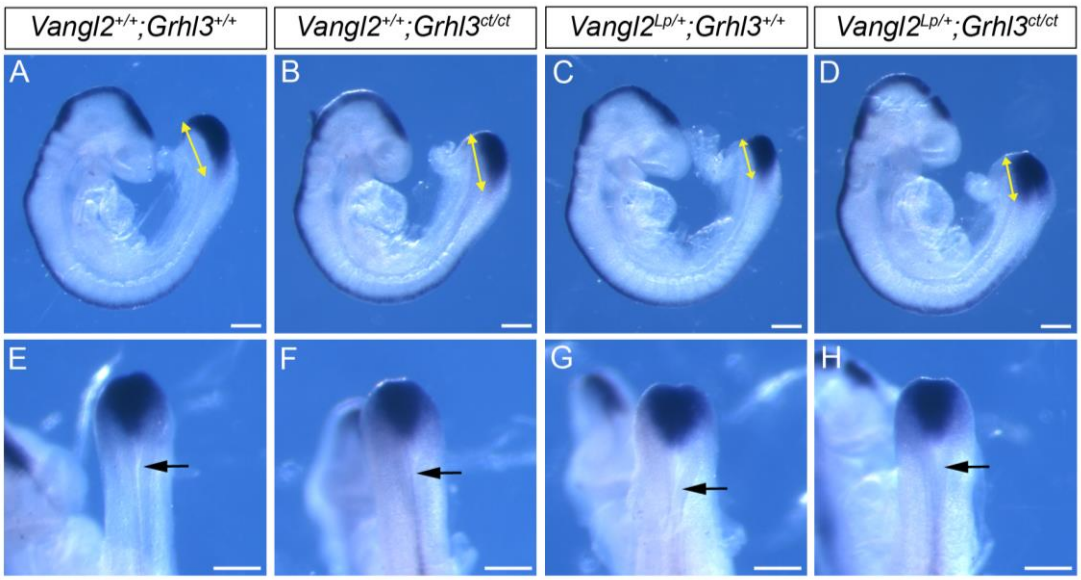

Figure 4.10 *Wnt3a* expression in the caudal region

(**A**-**D**) Whole-mount *in situ* hybridisation for *Wnt3a* at E9.5. Arrows indicate the embryonic region occupied by *Wnt3a* transcripts, which appears shorter in both *Vangl2*$^{Lp/+}$;*Grhl3*$^{+/+}$ and *Vangl2*$^{Lp/+}$;*Grhl3*$^{ct/ct}$. (**E**-**H**) Higher magnification dorsal views of the caudal regions in A-D. Besides the shorter body axis in embryos with the *Lp* mutation, no differences in *Wnt3a* are apparent and in each genotype the rostral limit of the expression domain is positioned at a similar level relative to the closure point (arrows).

The data described so far suggest that embryos carrying the *loop-tail* mutation display defective midline convergent extension during low spinal neurulation. In pre-neurulation stage embryos, CE can be studied by labelling the E7.5 midline tissues, either by microinjecting DiI (1,1'-dioctadecyl-3,3,3',3'-tetramethylindocarbocyanine perchlorate) into the node or electroporating a GFP-expressing vector into the neural plate (Pryor et al., 2012; Ybot-Gonzalez et al., 2007b). After continued development in whole embryo culture, the majority of wild type embryos exhibit striking axis extension, with a streak of labelled cells observed along the midline rostral to the node. In contrast, a large proportion of *Vangl2*$^{Lp/Lp}$ embryos display very limited rostral extension and labelled cells persist at the caudal site of injection

or electroporation. Heterozygous *Vangl2*$^{Lp/+}$ embryos generally display a variable, intermediate phenotype (Ybot-Gonzalez et al., 2007b)

To directly evaluate axis extension during PNP closure, DiI injection was used to label the cells in the midline of the caudal region at E9.0 (see Chapter 2). As it was first important to establish whether CE cell movements are indeed detectable in the midline at this stage, wild type embryos were initially labelled and cultured for different lengths of time (Figure 4.11). Two DiI marks were made in the midline via injections through the dorsal surface of the open neural plate, with the original prediction that these marks would move apart in the rostro-caudal dimension as development proceeds. After six hours in culture the distance between the labelled regions was not markedly increased, although the normal closure of the PNP did appear to have progressed (Figure 4.11A). Interestingly however, after 18 hours, a streak of fluorescently labelled cells was visible along the midline from the level of the closed neural tube to the open PNP more caudally. The distance between the most rostral and caudal labelled cells was approximately twice that of the original marks (Figure 4.11B). Correct localisation of DiI in the midline was confirmed by histological sectioning (Figure 4.11C).

Next, DiI labelling was performed in *Vangl2*$^{+/+}$*;Grhl3*$^{+/+}$, *Vangl2*$^{+/+}$*;Grhl3*$^{ct/ct}$, *Vangl2*$^{Lp/+}$*;Grhl3*$^{+/+}$ and *Vangl2*$^{Lp/+}$*;Grhl3*$^{ct/ct}$ E9.0 embryos to compare the degree of axis extension in the different mutant genotypes. The invasive nature of this technique meant that a proportion of embryos appeared abnormal at the end of the culture period and unfortunately had to be excluded from the analysis (Table 4.3). Nevertheless, consistent differences were seen between genotypes for the healthy embryos (Figure 4.12, Figure 4.13). In *Vangl2*$^{+/+}$*;Grhl3*$^{ct/ct}$ embryos the streak of labelled cells appeared closely similar to wild type, with an approximately two-fold increase in the distance between the most rostral and caudal fluorescent cells

(Figure 4.12B, Figure 4.13). However in both *Vangl2*$^{Lp/+}$;*Grhl3*$^{+/+}$ and *Vangl2*$^{Lp/+}$;*Grhl3*$^{ct/ct}$ embryos the midline DiI streak was shorter and did not extend as far into the caudal region (Figure 4.12C, D). In these two genotypes the length of the labelled region was only 1.5 times that of the distance between the original marks (Figure 4.13).

Together these results demonstrate that CE is indeed a feature of neurulation in the low spine, as has been shown previously for neurulation prior to closure 1, and that this process is compromised in the presence of the *Vangl2*^{Lp} allele. On the other hand *curly tail* embryos display normal midline extension, showing that this process is not inhibited by mutations in *Grhl3*.

Genotype	No. of labelled embryos cultured	Excluded from analysis (%)	Reason for exclusion
Vangl2$^{+/+}$;*Grhl3*$^{+/+}$	14	7 (50%)	Abnormal development (3), Mis-labelling (4)
Vangl2$^{+/+}$;*Grhl3*$^{ct/ct}$	9	5 (56%)	Abnormal development
Vangl2$^{Lp/+}$;*Grhl3*$^{+/+}$	8	4 (50%)	Abnormal development
Vangl2$^{Lp/+}$;*Grhl3*$^{ct/ct}$	5	2 (40%)	Abnormal development

Table 4.3 Viability of DiI-labelled embryos

Table showing the number of embryos successfully labelled and cultured for each genotype (second column) and the proportion excluded from further analysis at the end of the culture period (third column). Embryos were excluded if they appeared morphologically abnormal, or if cells had been mis-labelled.

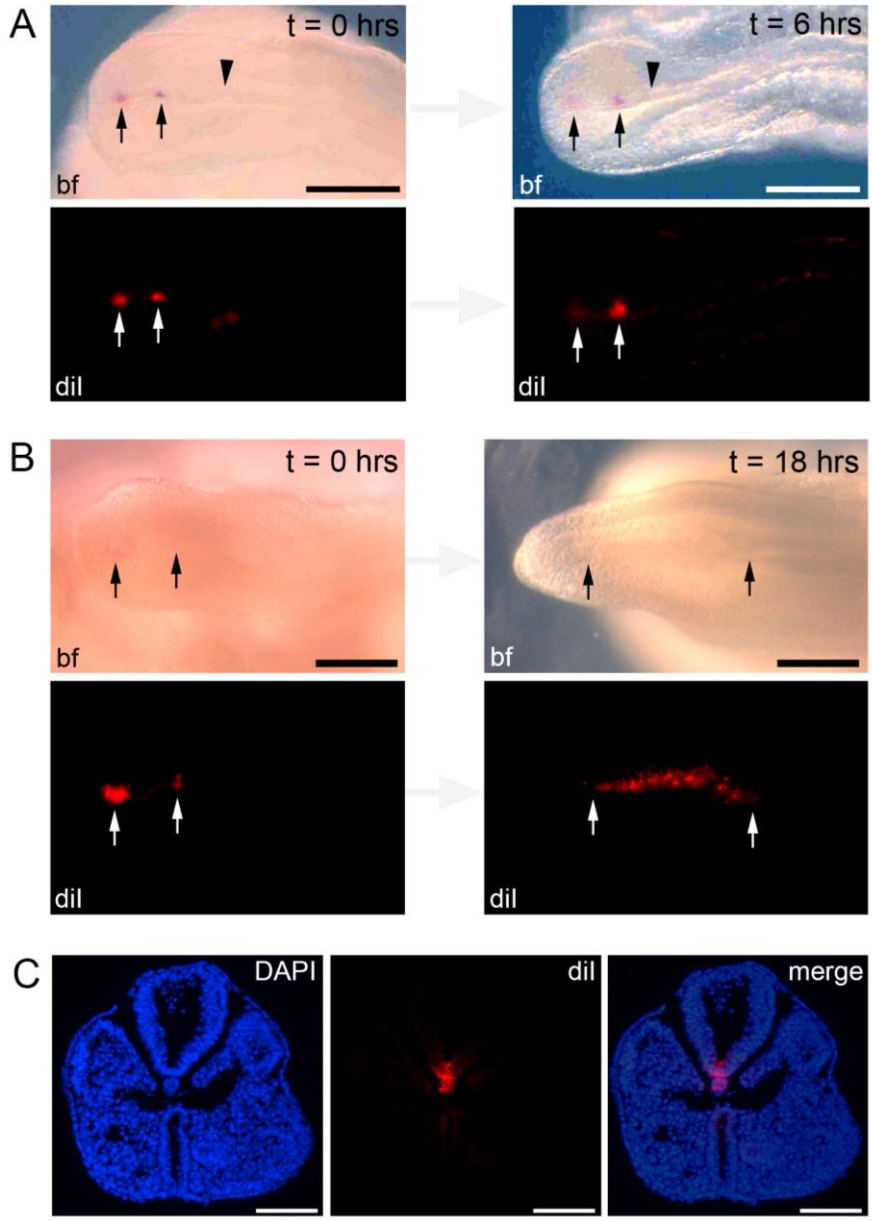

Figure 4.11 Fluorescent labelling of the midline during PNP closure

(**A**) Representative wild type caudal region immediately after labelling (t=0 hrs; left panels) and following six hours in culture (t=6 hrs; right panels). Bright field (bf) and fluorescent (dil) images are shown in the upper and lower panels, respectively. After six hours PNP closure has progressed (arrowheads indicate the points of closure) but the distance between the labels has not increased (arrows). (**B**) After 18 hours a rostrocaudal streak of DiI-labelled cells can be seen in the midline (right panels; arrows indicate the most rostral and caudal labelled cells). (**C**) Transverse sections through the caudal region of a labelled embryo, showing DiI in both neural tube floor plate and underlying notochord. Scale bars: 100 µm (A-B) and 50 µm (C).

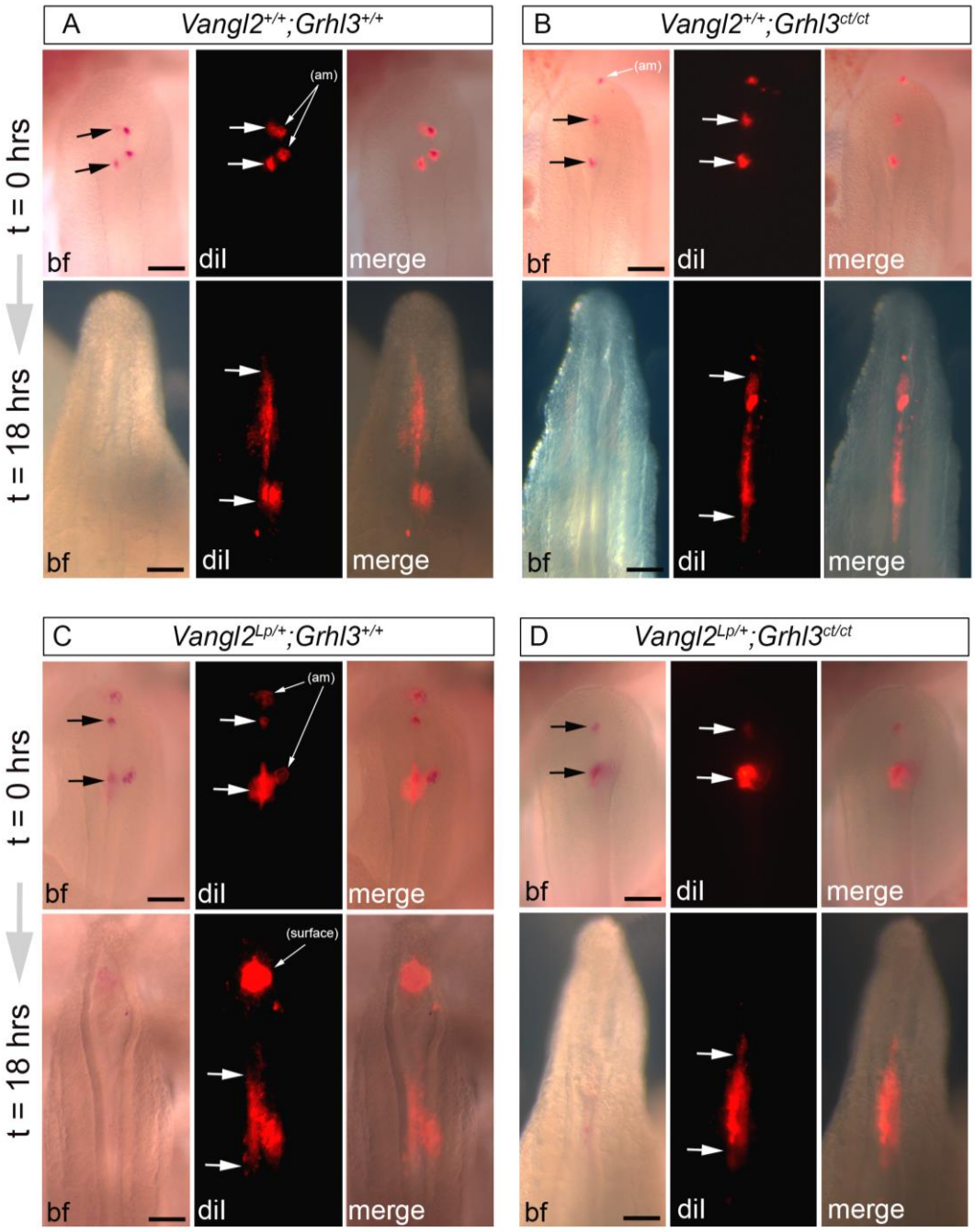

Figure 4.12 Defective CE in *Vangl2$^{Lp/+}$;Grhl3$^{+/+}$* and *Vangl2$^{Lp/+}$;Grhl3$^{ct/ct}$* embryos

Panels show dorsal views of the caudal region immediately after labelling (t=0 hrs; top row of A-D) and following 18 hours in culture (t=18 hrs; bottom row of A-D). Arrows indicate the position of the DiI marks prior to culture, and the limits of the labelled region at the end of the culture period. Ectopic marks, in either the amnion (am) or on the surface of the embryo, are also indicated. (**A**-**B**) Wild type and *curly tail* embryos display comparable midline extension. (**C**-**D**) In *Vangl2$^{Lp/+}$;Grhl3$^{+/+}$* and *Vangl2$^{Lp/+}$;Grhl3$^{ct/ct}$* embryos axis extension is reduced. Scale bars: 50 µm

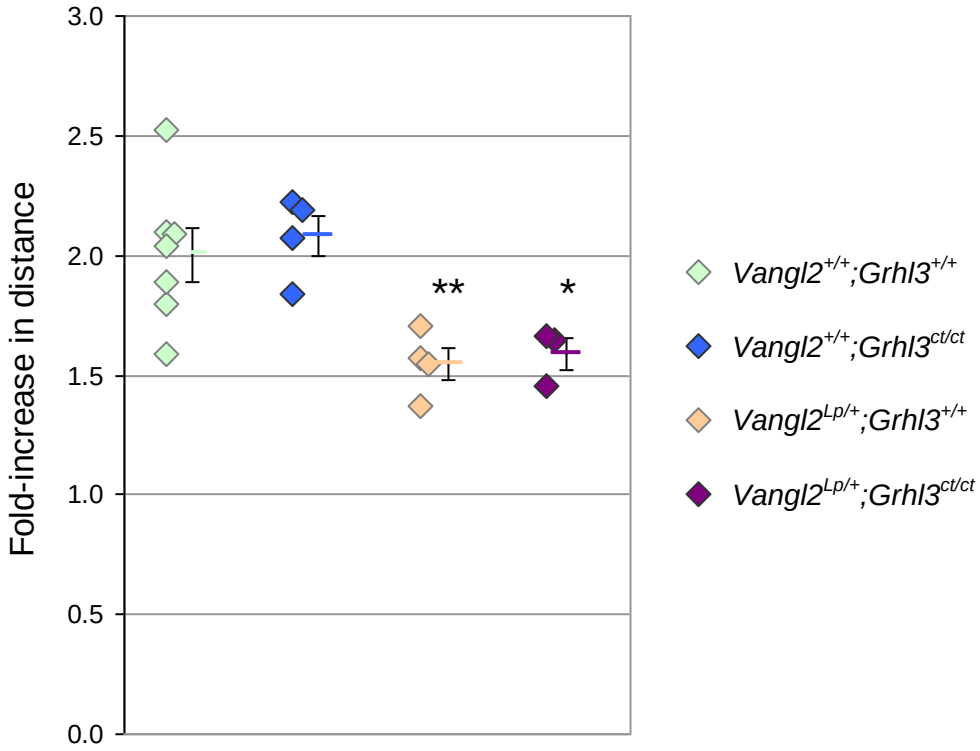

Figure 4.13 Quantification of DiI labelling experiments

Comparison of axis elongation in the different genotypes during spinal neurulation. Each data point represents the length of the fluorescently labelled region in individual embryos after 18 hours in culture, expressed as the fold change of the distance between the original DiI marks. Error bars represent the mean MI ± SEM for each genotype. A reduction in axis extension was observed in both *Vangl2*$^{Lp/+}$*;Grhl3*$^{+/+}$ and *Vangl2*$^{Lp/+}$*;Grhl3*$^{ct/ct}$ (p = 0.006, 1-Way ANOVA) Asterisks indicate results of multiple comparison testing: **signifcantly reduced compared to wild type and *curly tail*; *significantly reduced compared to *curly tail* (p < 0.05).

4.2.3 A possible tail bud defect downstream of *Grhl3*^{ct}

If *Grhl3* is not required for CE in the midline tissues during spinal neurulation, what contribution do the *curly tail* alleles make to the *Lp/ct* phenotype? Is their role in the interaction specific to another tissue? As introduced earlier, a population of multipotent progenitor cells is believed to reside in the caudal region of the embryo and contribute to the axial tissues as the trunk elongates (Cambray and Wilson,

2002). Interestingly, *Grhl3* is expressed in a population of caudal cells which closely corresponds to this region from late E8.5-E9.5 (for a more detailed description of *Grhl3* expression during neurulation see Chapter 5). WISH analysis revealed a strong patch of *Grhl3* expression ventral to the neuroepithelium at the level of the open PNP (Figure 4.14A-C). This region presumably corresponds to the notochord expression described previously (Gustavsson et al., 2007), although at this axial level the notochord is not well defined morphologically and *Grhl3* was not detected in the mature notochord more rostrally (see Chapter 5). Sagittal sections through the caudal region further suggested that this expression corresponds to the chordo-neural-hinge (CNH; Figure 4.14D; compare to Figure 4.1), raising the intriguing question of whether *Grhl3* plays a role in regulating or maintaining the putative population of caudal stem cells. Conversely, *Vangl2* transcripts were not detected in this region (Figure 4.14E).

The reduced rates of cell proliferation in the E10.5 *curly tail* hindgut (Copp et al., 1988a) and in the E9.5 $Vangl2^{+/+};Grhl3^{ct/ct}$ and $Vangl2^{Lp/+};Grhl3^{ct/ct}$ neuroepithelium (Figure 4.9B) both correspond to the expression of *Grhl3* in these tissues. With this in mind, it was hypothesised that the cell cycle dynamics of the E9.5 caudal progenitor population might also be altered in embryos carrying the $Grhl3^{ct/ct}$ genotype. Immunofluorescence for the proliferation marker Ki67 showed this region to contain cycling cells (Figure 4.15E). The rate of proliferation in different genotypes was evaluated by calculating the mitotic index (MI) within a defined region ventral to the neuroepithelium, corresponding to the domain of *Grhl3* expression identified by WISH (Figure 4.16A; compare boxed areas to those in Figure 4.14B, C). While there was no difference in the mean MI between wild type and $Vangl2^{Lp/+};Grhl3^{+/+}$ (4.0 ± 0.52 and 3.7 ± 0.40, respectively), a nearly 2-fold reduction in the rate of proliferation was observed in both $Vangl2^{+/+};Grhl3^{ct/ct}$ and $Vangl2^{Lp/+};Grhl3^{ct/ct}$ E9.5 embryos (Figure 4.16B).

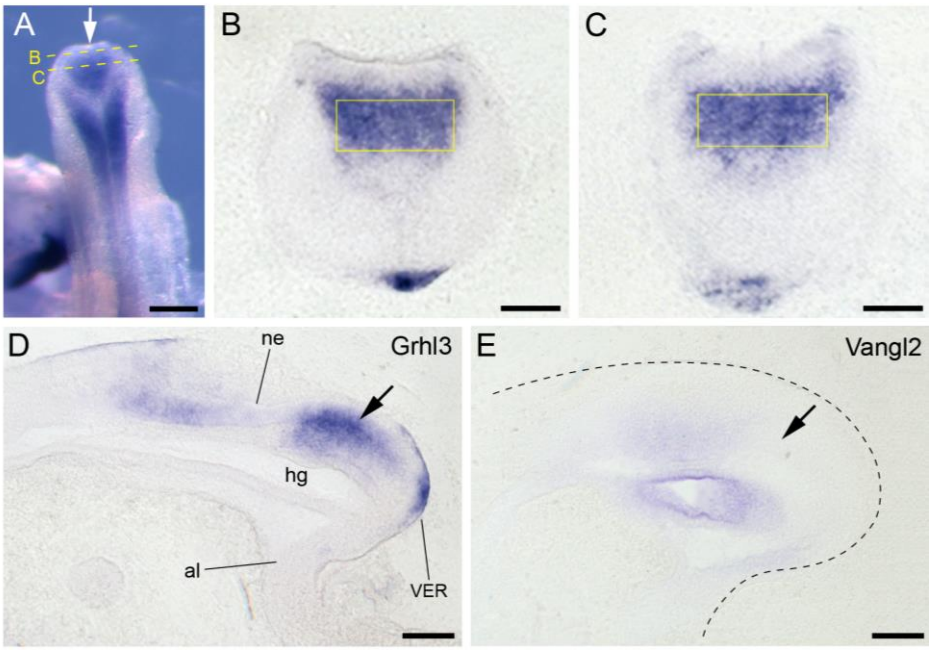

Figure 4.14 *Grhl3* expression in the E9.5 caudal region

(**A**-**C**) Whole-mount *in situ* hybridisation for *Grhl3* in an E9.5 wild-type embryo. In addition to expression in the neural folds, transcripts are detected medially in a distinct region of the caudal end (arrow in A). Transverse sections through this region show a population of *Grhl3*-expressing cells ventral to the open neural plate (boxed region in B and C). This expression domain extends to a level where the notochord and hindgut are no longer morphologically distinguishable. (**D**) Sagittal section through another embryo showing the location of the *Grhl3*-positive population relative to the caudal tissues. (**E**) *Vangl2* expression, shown for comparison; it is not strongly expressed in this region (arrow). Abbreviations: ne = neuroepithelium, hg = hindgut, al = allantois, VER = ventral ectodermal ridge. Scale bars: 200 µm (A) and 50 µm (B-E).

Finally, to investigate possible changes in the survival rate of cells within the *Grhl3*-expressing region, programmed cell death was analysed using immunofluorescence for the apoptotic marker activated Caspase3 (Casp3). In general the number of Casp3-positive nuclei in the caudal region was low (Figure 4.17). In the E9.5 spinal region a few apoptotic cells were observed within the neuroepithelium (Figure 4.17A, 1-2), particularly at the dorsal midline of the recently closed neural tube as described previously (Massa et al., 2009). Further caudally, a small number of dying

cells were seen in the hindgut (Figure 4.17A, 3). Within the caudal *Grhl3* expression domain the apoptotic index was generally less than 1% and was not significantly different between genotypes (Figure 4.17B). Together these results show that *Grhl3* is expressed within the caudal region of the embryo where a population of axial stem cells has been proposed to reside, and that it appears to regulate the proliferation of cells within this area. The observed reduction in the MI of this region was specific to embryos with the *Grhl3*$^{ct/ct}$ alleles.

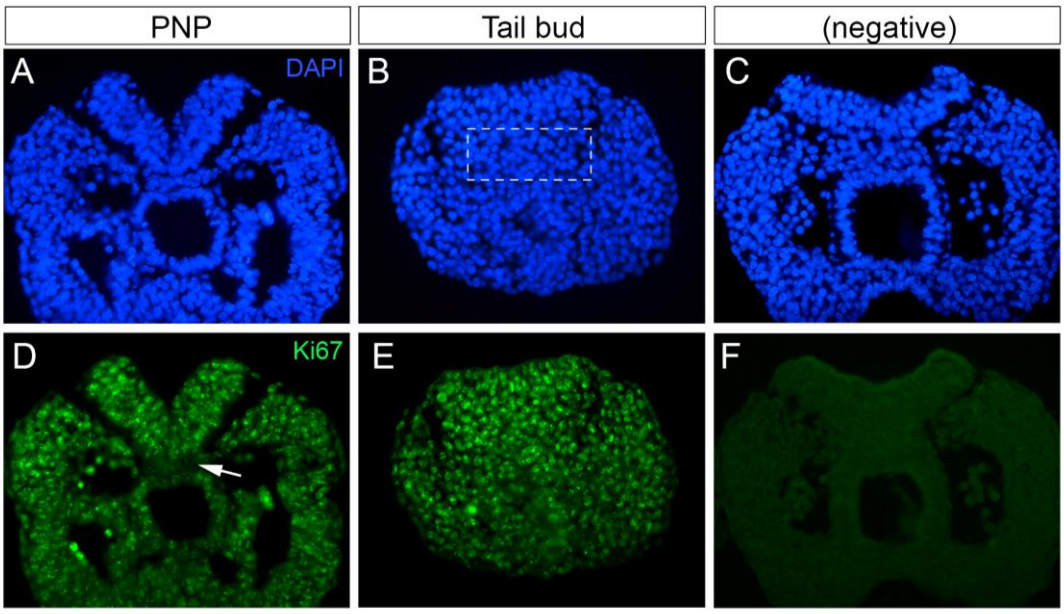

Figure 4.15 Ki67 immunofluorescence in the wild type caudal region

(**A**-**B**) DAPI-stained sections through the caudal region of an E9.5 wild type embryo at the level of the PNP and tail bud. The boxed region in B corresponds to the location of *Grhl3* transcripts, as identified by WISH (compare to Figure 4.14). (**D**) Ki67-positive cells can be seen in numerous tissues at the level of the PNP, particularly throughout the neuroepithelium. In contrast, the notochord contains very few proliferative cells (arrow). (**E**) Further caudally, the majority of cells within the progenitor-containing region are Ki67-positive (compare E to boxed region in B). Fluorescent signal was not observed in negative controls (C and F; no primary antibody).

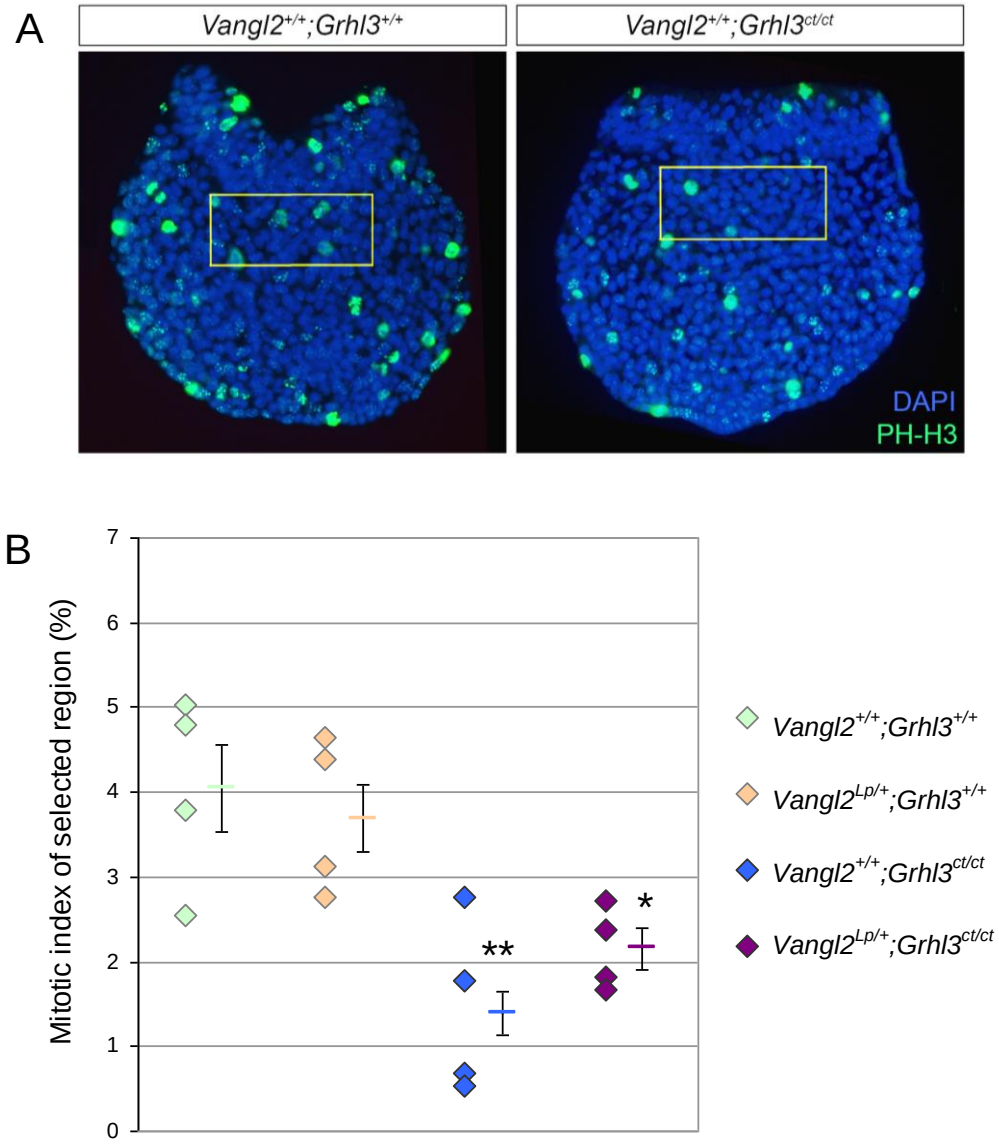

Figure 4.16 Analysis of proliferation in the caudal progenitor region

(**A**) Sections through representative wild type and *curly tail* embryos at the level of the caudal *Grhl3* expression domain. Sections are stained for PH-H3 (green) and nuclei are stained with DAPI (blue). The boxed regions correspond to the location of *Grhl3* transcripts, shown in Figure 4.14. Boxes were scaled to occupy an equivalent region of the tissue for each section. (**B**) Comparison of mitotic index within the selected region, calculated from DAPI-stained sections. Each data point represents the mean MI for an individual embryo with the mean MI ± SEM for all sections of the same genotype shown to the right (minimum total of 24 sections, across four embryos). MI was significantly reduced in embryos with the *Grhl3*$^{ct/ct}$ genotype ($p < 0.001$, Kruskal-Wallis 1-Way ANOVA on Ranks). Asterisks indicate results of multiple comparison testing: **signifcantly reduced compared to wild type and *Vangl2*$^{Lp/+}$*;Grhl3*$^{+/+}$; *significantly reduced compared to wild type ($p < 0.05$).

Figure 4.17 Analysis of apoptosis in the caudal progenitor region

(**A**) Sections through the caudal region of an E9.5 wild type embryo, from the level of the recently-closed neural tube (1) to the tail bud (4), following immunofluorescence for activated Caspase3 (green). Nuclei are stained with DAPI (blue; inset). Arrows in 1 and 2 indicate dying cells within the neuroepithelium. The boxed region in 4 corresponds to the *Grhl3*-expression domain; no apoptotic cells were detected in this region of the section. Abbreviation: hg = hindgut.

(**B**) Apoptotic indices (AI) within the boxed region in A4. Each data point represents the mean AI for an individual embryo with the mean AI ± SEM for all sections of the same genotype shown to the right. n = minimum total of 19 sections from 4 embryos for *Vangl2*$^{+/+}$*;Grhl3*$^{+/+}$, *Vangl2*$^{+/+}$*;Grhl3*$^{ct/ct}$ and *Vangl2*$^{Lp/+}$*;Grhl3*$^{ct/ct}$, and *n* = 16 total sections from 3 embryos for *Vangl2*$^{Lp/+}$*;Grhl3*$^{+/+}$. Mean AI did not vary significantly with genotype (p = 0.596, Kruskal-Wallis 1-Way ANOVA on Ranks).

A

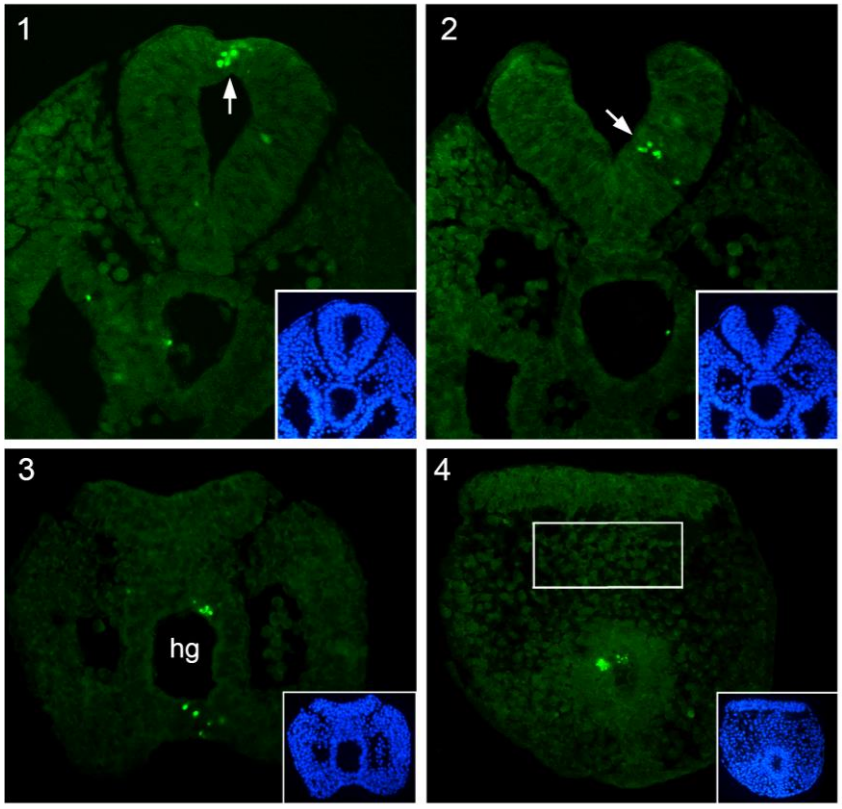
1
2
3
hg
4

B

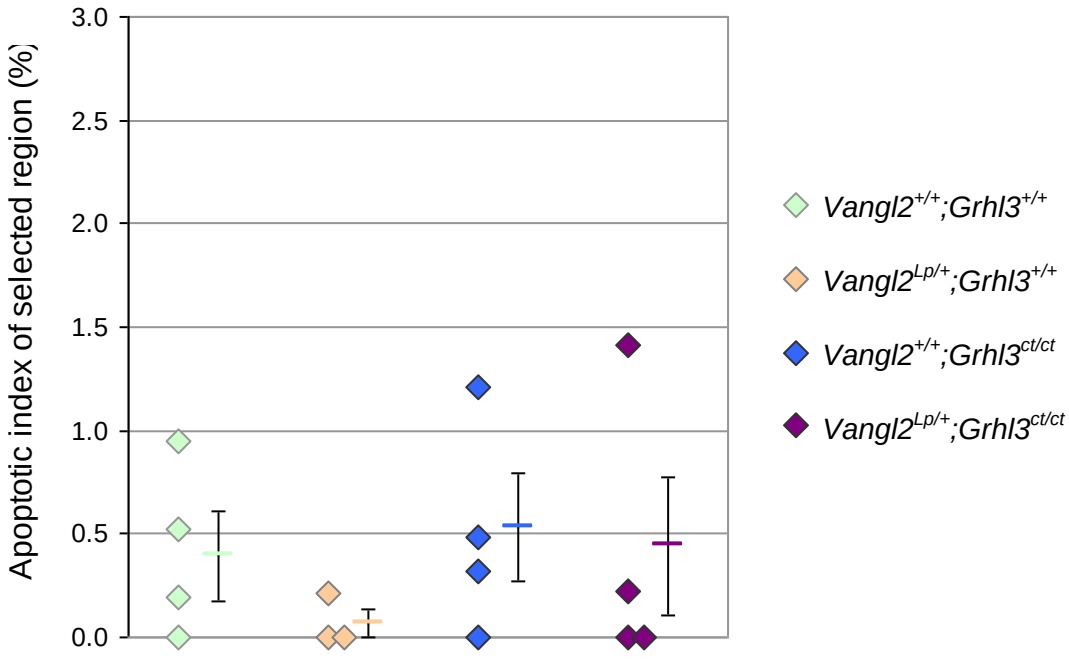
Apoptotic index of selected region (%)
3.0
2.5
2.0
1.5
1.0
0.5
0.0
Vangl2+/+;Grhl3+/+
Vangl2Lp/+;Grhl3+/+
Vangl2+/+;Grhl3ct/ct
Vangl2Lp/+;Grhl3ct/ct

4.3 Discussion

4.3.1 Evidence of a caudal CE defect downstream of *Vangl2^{Lp}*

The DiI labelling experiments described here indicate that convergent extension movements do contribute to elongation of the axial midline during low spinal neurulation, as has been described prior to the initiation of neural tube closure at E8.5. The current analyses of mutant embryos show that the presence of one *Vangl2^{Lp}* allele is sufficient to perturb this process, indicating that it is PCP-dependent. In this chapter, various lines of evidence support a role for *Vangl2* in caudal CE: 1) both *Vangl2$^{Lp/+}$;Grhl3$^{+/+}$* and *Vangl2$^{Lp/+}$;Grhl3$^{ct/ct}$* embryos display abnormally wide midline tissues, and an increase in PNP width, at E9-E9.5; 2) embryos of these two genotypes exhibit shortening of the caudal body axis, as shown by morphometric analyses and gene expression studies; 3) fluorescently-labelled midline cells display diminished extension along the A-P axis during culture in embryos harbouring the *Lp* mutation. These data are reminiscent of the CE phenotypes reported in PCP mutant embryos at the time of closure 1 (Paudyal et al., 2010; Wang et al., 2006a; Ybot-Gonzalez et al., 2007b).

Additionally, the *Vangl2$^{Lp/+}$;Grhl3$^{+/+}$* and *Vangl2$^{Lp/+}$;Grhl3$^{ct/ct}$* genotypes were associated with a dysmorphic and dorsally-protruding neuroepithelium that contained more cells per transverse section than embryos which were wild type for *Vangl2*. This phenotype does not appear to be a consequence of increased cell proliferation, as neuroepithelial MI was not found to correlate with *Vangl2* genotype. Similarly, no differences in cell proliferation were previously observed between the wild type and *Vangl2$^{Lp/Lp}$* neuroepithelium (Gerrelli and Copp, 1997). Could an increase in cell number at a particular axial level instead reflect the ‘bunching up’ of the neural plate when CE is disrupted?

Labelling techniques such as the electroporation of GFP-expression vectors and DiI microinjection enable the examination of CE in living mouse embryos (Pryor et al., 2012; Ybot-Gonzalez et al., 2007b). For the current study, the latter approach offered two main advantages over the former: DiI injections can be targeted to small groups of cells in the midline in a more precise manner than electroporation, and the fluorescence can be immediately detected. The second point crucially allows 'before and after' measurements to be taken when evaluating the extent of axis elongation over a culture period. However, the experiment itself is not without difficulties. One particular challenge was producing microinjection needles with an appropriately-sized aperture; the tip needed to be sharp enough to pierce the amnion, cause minimal damage to the embryo and prevent DiI leakage, but the opening had to be large enough to allow DiI to be drawn up and expelled using a mouth pipette. It is therefore likely that the observed abnormal development of some cultured embryos is attributable to damage caused by the injections, along with the necessary opening of the yolk sac overlying the PNP. Nevertheless, there are a number of further experiments which could be performed using this technique. For example, it would be interesting to examine the movement of cells within more lateral regions of the neural plate and compare the extent of CE at different rostral-caudal levels of the PNP.

4.3.2 Cellular behaviours underlying mammalian CE

As mentioned earlier, the mechanisms of CE during axis elongation in the mouse embryo are not fully understood, although in recent years studies have demonstrated a role for cell intercalation (Yamanaka et al., 2007; Yen et al., 2009). A role for the cell-autonomous rearrangement of cells at the midline was also suggested by examination of chimeric mouse embryos containing a mixture of wild type and *Vangl2*$^{Lp/Lp}$ cells (Ybot-Gonzalez et al., 2007b). In this study wild type

embryonic stem (ES) cells were injected into blastocysts from *Vangl2*$^{Lp/+}$ X *Vangl2*$^{Lp/+}$ matings, which were also homozygous for the ROSA26 beta-galactosidase (β-gal) locus. In E8 +/+ ↔ +/+ chimeras a random mixture of host (β-gal positive) and donor (β-gal negative) cells were observed throughout the neuroepithelium and notochordal plate, while +/+ ↔ *Lp/Lp* chimeras displayed a reduction in the proportion of PCP mutant cells at the midline. Quantification of this effect in the +/+ ↔ *Lp/Lp* neural plate revealed a predominance of up to 45% wild type cells in the midline compared with lateral regions. Consistent with the variable and intermediate elongation defects observed in heterozygous *Vangl2*$^{Lp/+}$ embryos prior to neurulation, a range of phenotypes was seen +/+ ↔ *Lp/*+ chimeras (Ybot-Gonzalez et al., 2007b).

This study also demonstrated that lengthening of the notochord at positions more rostral to the node is less dependent on CE, with the authors suggesting that oriented cell divisions could account for the majority of elongation in this region (Ybot-Gonzalez et al., 2007b). A more detailed examination of mammalian notochord formation, involving live imaging and lineage analysis, revealed that distinct morphological processes form the node at different axial levels. In the trunk, the notochord is extended by CE driven by ML intercalation, while different mechanisms are employed during formation of the head process (prechordal plate) and tail notochord (Yamanaka et al., 2007). It would be interesting to investigate whether the rate of notochordal CE also varies at different rostro-caudal levels of the PNP during low spinal neurulation in the mouse.

Together, the findings described above suggest a role for ML intercalation in the neural plate and underlying mesoderm prior to closure 1. As the data in the current chapter (and Chapter 3) appear to show a deleterious effect of *Vangl2*^{Lp} on both of these tissues during PNP closure, it is tempting to speculate that analogous events

also occur later in neurulation. It would be interesting to assess whether the mechanisms controlling CE of cells emerging from the node are similar to those for cells recently laid down from the tail bud.

The forces driving ML cell intercalation are thought to be generated within tissues by directional cell motility. In many systems this is controlled at the cellular level by the production of polarised protrusions (Keller et al., 2000). Such cell behaviours have been most extensively studied in the frog embryo, where mesoderm cells elongate and align along the ML axis, forming medially and laterally directed lamellipodia that appear to provide traction as the cells 'crawl' along their neighbours and intercalate (Shih and Keller, 1992). In the *Xenopus* neural plate, CE appears to be largely driven by monopolar, medially directed protrusions that pull the cells between each other towards the midline in a similar way to that seen for the bipolar mode (Elul and Keller, 2000). An analysis of CE in the mouse also points towards a mechanism involving cell intercalation driven by polarised protrusions. Cells of the presomitic mesoderm were observed to elongate mediolaterally and become aligned perpendicular to the midline, before extending bipolar, ML-orientated protrusions and undergoing ML intercalation (Yen et al., 2009). Interestingly, this study also reported a role for radial intercalation in the presomitic mesoderm. Whether similar cell behaviours drive intercalation in the mammalian neural plate and notochord remains to be investigated.

4.3.3 Role of *Grhl3* in the caudal region

The CE defects described here were exclusively associated with the presence of the *Vangl2*^{Lp} allele. CE in *Vangl2*$^{+/+}$*;Grhl3*$^{ct/ct}$ embryos appeared comparable to wild type, and was no more severe in *Vangl2*$^{Lp/+}$*;Grhl3*$^{ct/ct}$ than in *Vangl2*$^{Lp/+}$*;Grhl3*$^{+/+}$. These findings raise the question of whether *Grhl3* plays a specific role in another

tissue of the caudal region at E9.5. Interestingly *Grhl3* was expressed within the CNH region at late E8.5-E9.5 (Figure 4.14; also see WISH analysis in Chapter 5) and the *Grhl3*$^{ct/ct}$ genotype was associated with reduced proliferation in this area a few hours before the spinal defect in the double mutants becomes apparent.

The molecular characteristics of the caudal stem cell population have not been well defined. Several genes have been found to mark distinct subpopulations of cells within the primitive streak and adjacent epiblast during late gastrulation in both mouse and chick, and continue to be expressed in equivalent regions of the tail bud at later stages (Cambray and Wilson, 2007; Gofflot et al., 1997; Wilson et al., 2009). However these do not reliably label the stem cell population in both species. For example, in mouse embryos the node-streak border and CNH are marked by the transition between the posterior limit of the *Foxa2* expression domain and the anterior limit of *Fgf8* expression. However, such a molecular boundary cannot be used to locate these regions in avian embryos as *Fgf8* extends further rostrally in the chick than in the mouse (Wilson et al., 2009). Recently, *Sox2* and *Brachyury* were found to be uniquely co-expressed in the chick CNH and, intriguingly, also in a discrete group of cells in an equivalent caudal region of the human embryo (Olivera-Martinez et al., 2012). It would be interesting to determine whether their expression also defines the CNH in the mouse and, if so, to perform co-labelling with *Grhl3.*

Breeding *Grhl3*$^{Cre/+}$ mice with the *Rosa26*^{YFP} reporter strain also reveals the presence of *Grhl3*-positive cells and their descendents in the caudal region during late neurulation (see Chapter 6) and these embryos could be further examined, perhaps in combination with DiI labelling and whole embryo culture. The observed reduction of cell proliferation in the caudal region of *curly tail* embryos warrants further investigation. Double immunostaining for Grhl3 and cell cycle markers should be performed to precisely characterise cell cycle dynamics within sub-

domains of the posterior tissues, and to specifically determine the phase of the cell cycle that is elongated/blocked in *curly tail* embryos. This could also be achieved via injections of the thymidine analogues BrdU (5-bromo-2-deoxyuridine) or EdU (5-ethynyl-2-deoxyuridine); an examination of stained sagittal sections might reveal regions of proliferative heterogeneity.

Finally, the significance of *Grhl3* expression in the ventral ectodermal ridge (VER) is not understood and has not been addressed here. The VER was first described in the 1950s as a thickening of the ectoderm on the ventral side of the E10.5-E11.5 mouse embryo tail bud. Given its morphological similarity to the apical ectodermal ridge (AER) of the developing limb bud, it was speculated that the VER is a source of signals for tail development (Gruneberg, 1956). Later studies showed that the VER first appears ventral to the PNP at the 17-18 somite stage, extends posteriorly to almost reach the tail tip by 30-33 somites and finally regresses at approximately E13, when tail elongation ceases (Gofflot et al., 1997; Goldman et al., 2000). VER ablation experiments revealed that the structure is required for somitogenesis and tail elongation, as well as the morphology of the neural tube, notochord and hindgut (Goldman et al., 2000). Signalling molecules including *BMP2*, *BMP7*, *FGF17* and *Wnt5a* are expressed in the VER, as are components of the ECM (Gofflot et al., 1997; Goldman et al., 2000; Lopez-Escobar et al., 2012; Ohta et al., 2007), but the expression of *Grhl3* in this structure has not been previously reported.

4.3.4 How do the mutant effects summate during neurulation?

If *Vangl2* regulates CE in the midline and *Grhl3* plays a role in regulating proliferation of caudal progenitors, then how might the effects of mutations in these two genes interact? It could be that reduced proliferation downstream of *Grhl3*^{ct}

reduces the size of the putative stem cell pool, so that fewer cells are available to exit this region and contribute to the midline tissues as the axis elongates. A combination of this effect with subsequent defects of CE, as seen for the *Vangl2*^{Lp} allele, could produce a more severe phenotype than either of the single effects and contribute to the severe spinal defects in *Vangl2*$^{Lp/+}$*;Grhl3*$^{ct/ct}$ (Figure 4.18).

Further exploration of this hypothesis would require investigations of the specific requirements for *Grhl3* at each of its sites of expression. A genetic approach would be to generate *Vangl2*$^{Lp/+}$*;Grhl3*$^{flox/+}$ mice and breed these with *Sax1*-Cre animals, which have recently been generated (Professor Kate Storey, personal communication). *Sax1* (also called *Nkx1-2*) appears to be specifically expressed in the caudal neural plate during low spinal neurulation [Valentina Massa and Sandra C.P. De Castro, unpublished data; (Schubert et al., 1995)] so in *Vangl2*$^{Lp/+}$*;Grhl3*$^{flox/+}$*;Sax1*$^{Cre/+}$ offspring *Grhl3* would be reduced in this tissue. If the phenotype of these embryos was found to be milder than in *Vangl2*$^{Lp/+}$*;Grhl3*$^{+/-}$ embryos, it would further suggest a requirement for *Grhl3* in the CNH (and/or VER).

Ultimately, to test the hypothesis that a 'tissue-tissue' interaction contributes to the spina bifida in *Vangl2*$^{Lp/+}$*;Grhl3*$^{ct/ct}$, it would be necessary to demonstrate a recapitulation of this severe phenotype in the *Vangl2*$^{Lp/+}$ single mutant. One approach would be to attempt the targeted electroporation of a *Cre*-expression vector into the caudal region of *Vangl2*$^{Lp/+}$*;Grhl3*$^{flox/+}$ embryos, followed by whole embryo culture, to specifically ablate the CNH expression domain of *Grhl3*. Alternatively, siRNAs specific for *Grhl3* could be introduced into CNH cells of cultured *Vangl2*$^{Lp/+}$ embryos using chemical or viral transfection, or by electroporation. In either case, the prediction would be that *Vangl2*$^{Lp/+}$ embryos in which *Grhl3* was locally inactivated in the tail bud would exhibit delayed PNP closure compared with mock-treated controls.

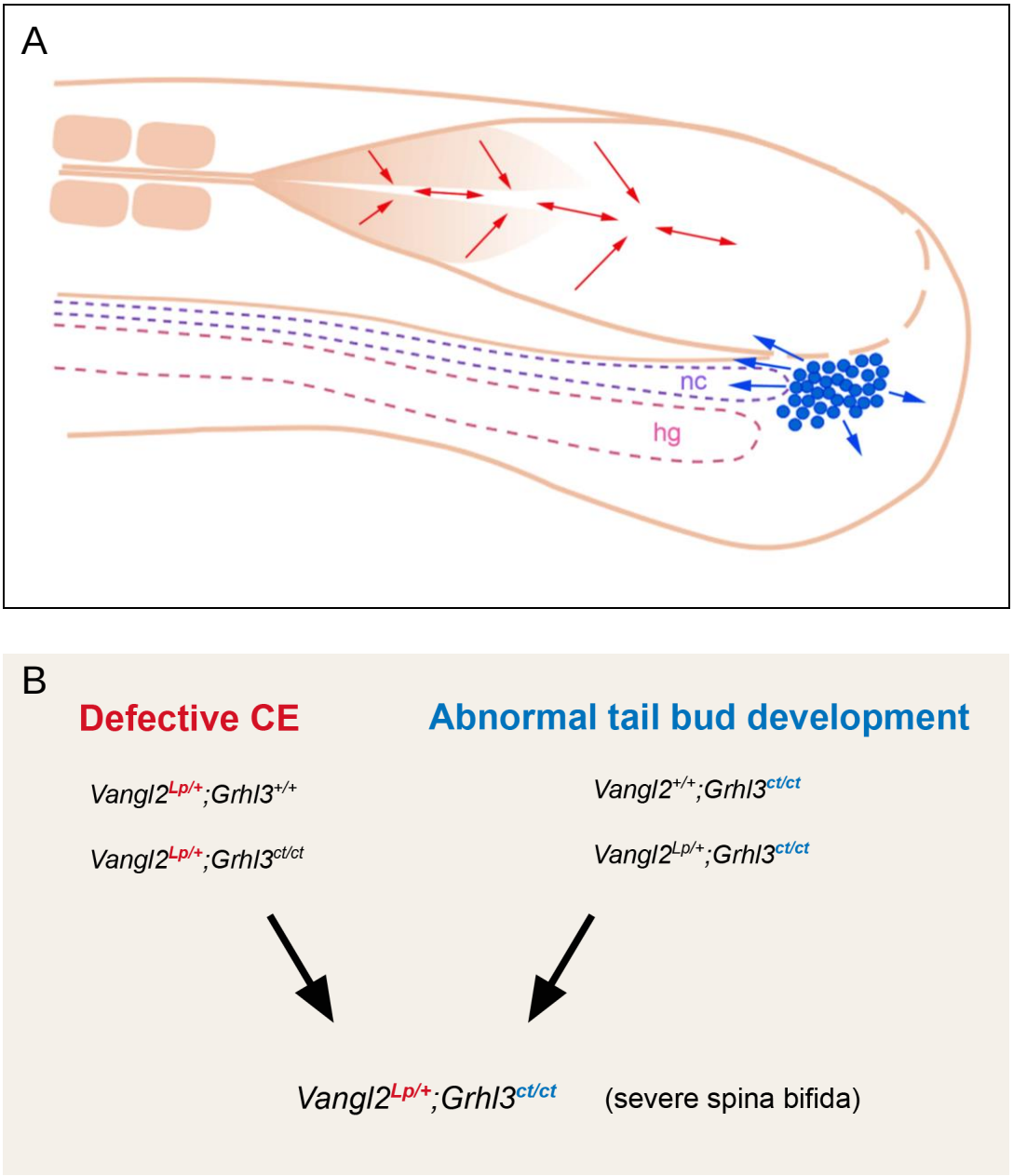

Figure 4.18 Proposed tissue-tissue interaction during spinal neurulation

(**A**) Schematic diagram of caudal development. Red arrows indicate midline convergent extension. The CNH stem cells (blue) have been shown to contribute to the ventral neural tube, somitic mesoderm and notochord, as well as tail bud mesoderm progenitors more caudally (blue arrows) (Olivera-Martinez et al., 2012; Wilson et al., 2009). Abbreviations: nc = notochord, hg = hindgut. (**B**) Summary of the hypothesis that distinct mutant effects in the midline and tail bud contribute to the severe spinal defects in *Vangl2*$^{Lp/+}$;*Grhl3*$^{ct/ct}$ embryos.

5. Is there a molecular interaction between *Vangl2* and *Grhl3* during neurulation?

5.1 Introduction

5.1.1 Published links between PCP and *grainyhead* genes

In *Drosophila*, the *grainyhead (grh)* transcription factor is essential for the development of normal tissue polarity. This function was identified from a genetic screen for genes involved in the *frizzled* (*fz*) pathway, which revealed that mutations in *grh* produce polarity phenotypes in the wing, eye, abdomen and thorax (Lee and Adler, 2004). This work also demonstrated a strong interaction between *grh* and several *fz* pathway genes, including *fz*, *Van Gogh* (*vang / strabismus*) and *Starry night* (*stan / flamingo*). In each case the interaction caused disrupted polarity over a much larger region of the wing than was seen for either of the single mutants. *Grh* was found to be required for the normal localisation of *fz* pathway components in the wing cells, with a disruption of the normal Fz, Dsh, Vang and Stan accumulation observed in regions of abnormal hair morphology. Interestingly, reduced levels of Stan protein were also observed in *grh* mutant clones (Lee and Adler, 2004).

In mice, a molecular link between PCP signalling and *Grhl3* has been described during embryonic wound repair. *Grhl3* was found to interact genetically with *Vangl2* during early (E12.5) and late (E16.5) wound healing and with *Scribble* during early wound healing (Caddy et al., 2010). The authors of this study found that *Grhl3* regulates the PCP pathway via direct transcriptional activation of *RhoGEF19*, a homologue of the *Xenopus* and human WGEF genes that have been shown to activate RhoA (Tanegashima et al., 2008; Wang et al., 2004). In *Xenopus* embryos, WGEF connects PCP signalling and RhoA activation; it can bind to Dvl and Dishevelled-associated activator of morphogenesis (Daam1), is required for PCP-mediated CE and axis elongation and can rescue CE defects induced by expression of dominant negative *Wnt11* (Tanegashima et al., 2008). In *Grhl3* null mice, E18.5 epidermal expression of *RhoGEF19* is reduced, while *in vitro* transfection of *Grhl3*

leads to an upregulation of *RhoGEF19* mRNA. Furthermore, knockdown of *Grhl3* or *RhoGEF19* in keratinocytes causes failure of RhoA activation and defective wound healing, a phenotype which can be rescued by overexpression of RhoGEF19 (Caddy et al., 2010).

Interactions between mammalian *Grhl3* and PCP genes during neurulation and cochlea development were also reported by Caddy et al. (2010; see Chapter 3), though the molecular basis of these interactions was not investigated. Although these findings have led to the consideration, by some, of *Grhl3* as a novel component of the mammalian PCP pathway (Dworkin et al., 2011), its wider role has not yet been characterized. It is possible therefore, that *Grhl3*-dependent regulation of signaling downstream of PCP is not a feature of all developmental events which require this pathway. Indeed, unlike the core PCP members, *Grhl3* does not regulate the initiation of neural tube closure (Rifat et al., 2010).

Another possible link between PCP and *Grhl3* is via *Wnt5a,* which functions in mammalian PCP signalling and interacts genetically with *Vangl2* (Qian et al., 2007). Loss of *Wnt5a* in mouse embryos leads to gross morphological defects and perinatal lethality. Homozygous null embryos display caudal truncation, shortening of the A-P axis and outgrowth defects affecting multiple structures, such as the limbs, snout and external ear (Yamaguchi et al., 1999). Other studies of *Wnt5a*$^{-/-}$ embryos have also reported cochlear defects, low penetrance NTDs, defective septation of the cardiac outflow tract and abnormal lung and sexual development (Chawengsaksophak et al., 2012; Oishi et al., 2003; Qian et al., 2007; Schleiffarth et al., 2007).

Wnt5a can signal through the receptor tyrosine kinase, Ror2 (Oishi et al., 2003) and Gao et al. showed that Wnt5a regulates PCP by inducing the formation of a Ror2-

Vangl2 receptor protein complex at the plasma membrane (Gao et al., 2011). This Wnt5a signalling activity appears to be required for the cellular distribution of Vangl2, as in *Wnt5*$^{-/-}$ mice its normal localisation is lost (Gao et al., 2011; Qian et al., 2007). Furthermore Wnt5a acts through Ror2 to induce Vangl2 phosphorylation, which is required for its function. Vangl2^{Lp} protein, which remains trapped in the ER and cannot correctly localise to the plasma membrane, fails to form a complex with Ror2, leading to dramatically reduced levels of phosphorylation, both *in vitro* and in *Vangl2*$^{Lp/Lp}$ embryos (Gao et al., 2011).

Interestingly, *Wnt5a* mRNA was previously found to be reduced in the caudal region of *curly tail* embryos during spinal neurulation (Gofflot et al., 1998). In this study, WISH revealed lower levels of *Wnt5a* expression in around 70% of affected *ct/ct* embryos at the 28-30 somite stage compared with their unaffected littermates. At 20-22 somites, before a delay in PNP closure is detectable, 45% of *ct/ct* embryos showed a reduction compared to non-mutant controls. Closer examination revealed that *Wnt5a* was diminished in the ventral mesoderm, hindgut, VER, and to a lesser extent within the neuroepithelium. Whether *Grhl3* regulates *Wnt5a* expression has not been investigated.

In this chapter, the possibility of a molecular interaction between *Vangl2* and *Grhl3* within the same cells of the caudal region during spinal neurulation is investigated. The following initial questions were considered: 1) Does the *Lp/ct* interaction involve a further change in the level or site of *Grhl3* expression?; 2) Does the *Lp/ct* interaction involve a transcriptional effect of *Grhl3* on the PCP genes?; 3) Could the interaction involve a transcriptional effect of *Grhl3* downstream of the PCP pathway?

5.2 Results

5.2.1 Comparison of *Vangl2* and *Grhl3* expression during spinal neurulation

Grhl3 exhibits a dynamic pattern of expression during the period of neurulation. At E8.0 its transcripts are confined to a small region of non-neural ectoderm cells immediately adjacent to the folding neural plate (Auden et al., 2006; Ting et al., 2003). By late E8.5-E9.0, expression is also detected in the ventral forebrain, caudal neural folds, and at the tip of the caudal end. As described in Chapter 4, *Grhl3* transcripts are also abundant in a population of cells ventral to the caudal neural plate, which is hereafter referred to as the CNH (chordo-neural-hinge) expression domain (Figure 5.1). Expression in the neuroepithelium is downregulated by E10-E10.5, when *Grhl3* appears in the hindgut ventral to the PNP and the allantois (Gustavsson et al., 2007; Gustavsson et al., 2008). This hindgut expression corresponds to the time and location of the cell proliferation defect in *Grhl3*$^{ct/ct}$ embryos (Gustavsson et al., 2007).

Vangl2 is more widely expressed throughout the neuroepithelium during neural tube closure. At E8 it is restricted to the hindbrain and upper spine (Doudney et al., 2005; Ybot-Gonzalez et al., 2007b), the level at which neural tube closure initiates, before being expressed throughout the closed neural tube, the hindgut endoderm and the base of the allantois by E9-E9.5 (Kibar et al., 2001; Murdoch et al., 2001; Torban et al., 2007). At this stage *Vangl2* expression diminishes in a rostral to caudal direction, with transcripts confined to the ventral neural plate at the level of the open PNP (see Chapter 7).

We hypothesised that, if a molecular or cellular interaction between *Vangl2* and *Grhl3* within the cells of the same tissue(s) does contribute to the severe spina

bifida in *Vangl2*$^{Lp/+}$;*Grhl3*$^{ct/ct}$ embryos, the two genes would be co-expressed in the relevant tissue(s) at the appropriate developmental stage. Therefore the spatiotemporal pattern of *Vangl2* and *Grhl3* expression during PNP closure was compared using WISH. In E9.0 wild-type embryos the two genes appeared to be co-expressed in a region of the neuroepithelium at the level of the open PNP and most-recently closed neural tube (arrows in Figure 5.2A', F'). Transverse sections through this region revealed expression of both genes throughout the closed neural tube, with the exception of the dorsal-most cells (Figure 5.2B, G). *Vangl2* expression appeared progressively weaker and ventrally-restricted in more caudal sections (Figure 5.2C-E), while *Grhl3* expression persisted, most strongly at the basal side of the neuroepithelium (Figure 5.2H, I) and in the CNH (Figure 5.2J).

At E9.5 the apparent co-expression of *Vangl2* and *Grhl3* in the neuroepithelium persisted (Figure 5.3) and by this stage both genes also appeared to be expressed in the hindgut endoderm, albeit quite weakly (Figure 5.3C, H). *Grhl3* transcripts were also detected in the allantois (Figure 5.3F) and ventral ectodermal ridge (VER; Figure 5.3J). These data indicate that the expression domains of *Vangl2* and *Grhl3* do overlap in the neuroepithelium and hindgut during PNP closure, potentially allowing a functional interaction within these tissues.

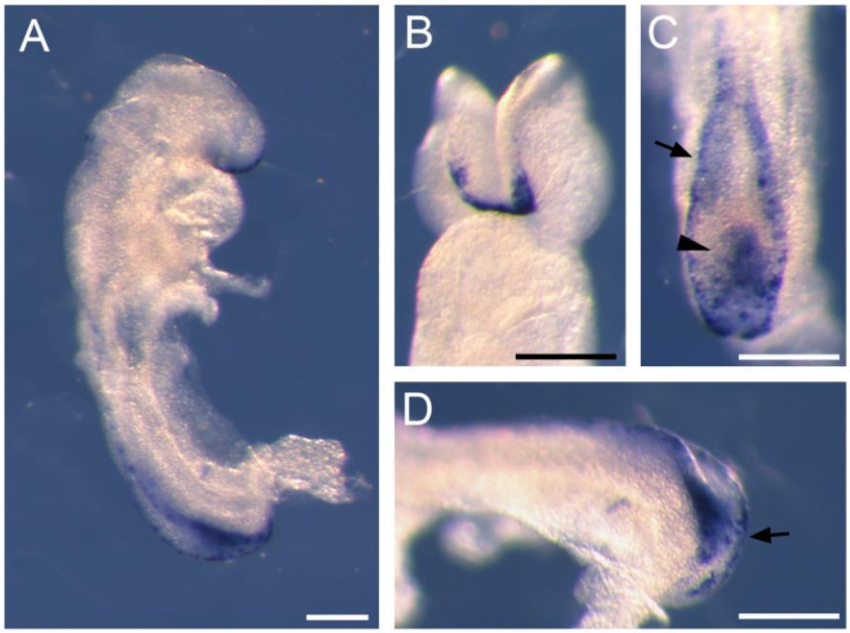

Figure 5.1 *Grhl3* expression domains at late E8.5

Whole-mount *in situ* hybridisation for *Grhl3* in a wild-type embryo with 10 somite pairs. Transcripts are detected in the neuroepithelium of the ventral forebrain (B) and in the surface ectoderm surrounding the PNP (C). *Grhl3* is also beginning to be expressed in the neural folds of the PNP (arrow in C). More caudally, expression can be seen in a population of cells in the caudal region ('tail bud' expression domain; arrowhead in C) and in the surface ectoderm at the tip of the caudal end (arrow in D). Scale bars: 200 µm.

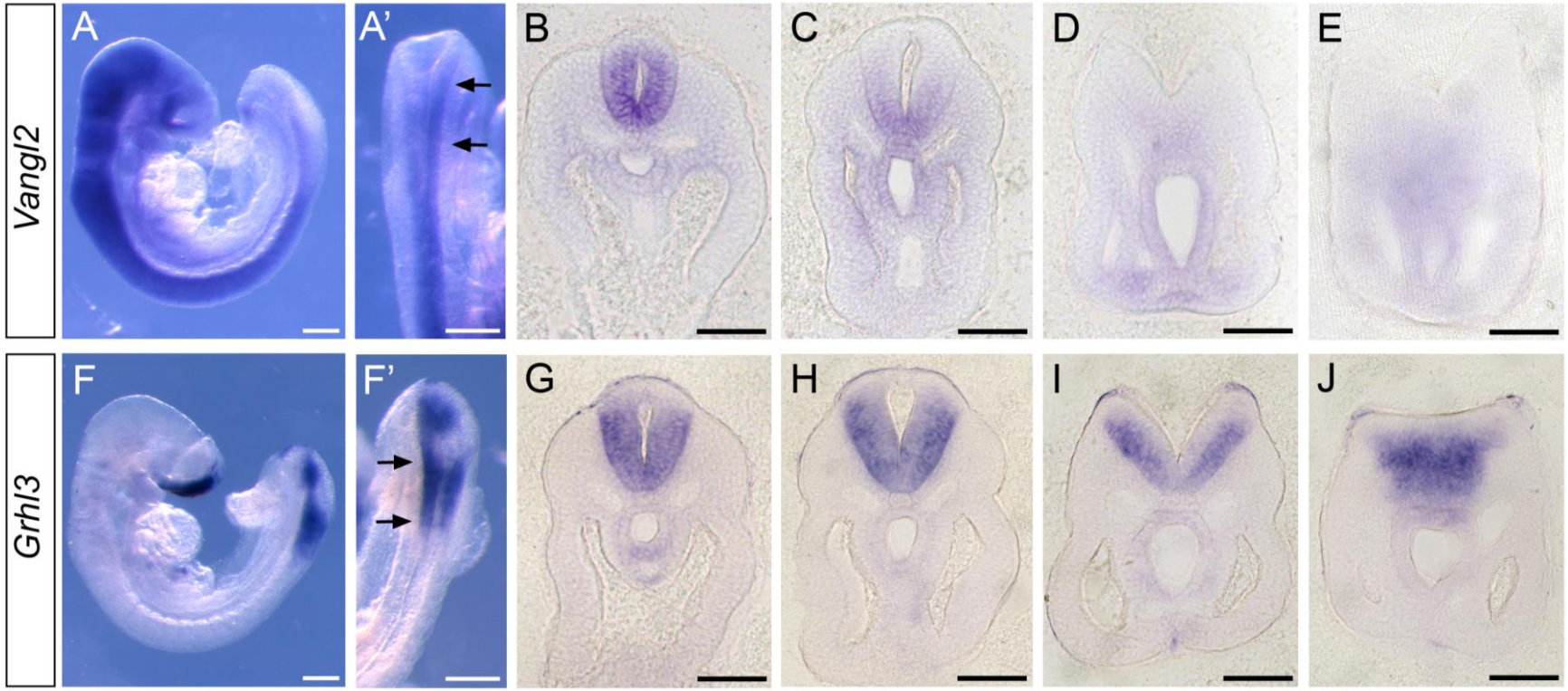

Figure 5.2 Overlapping expression of *Vangl2* and *Grhl3* at E9.0

Whole-mount *in situ* hybridisation for *Vangl2* (A-E) and *Grhl3* (F-J) in E9.0 wild type embryos. Both genes are expressed in the neuroepithelium at the level of the PNP at this stage (arrows in A' and F'). Transverse sections at the level of neural tube closure reveal a region of apparent co-expression (B-C and G-H). Further caudally *Vangl2* expression is reduced (D-E) and *Grhl3* expression is also seen in the tail bud (J). Scale bars: 200 µm (A, F) and 50 µm (B-E, G-J).

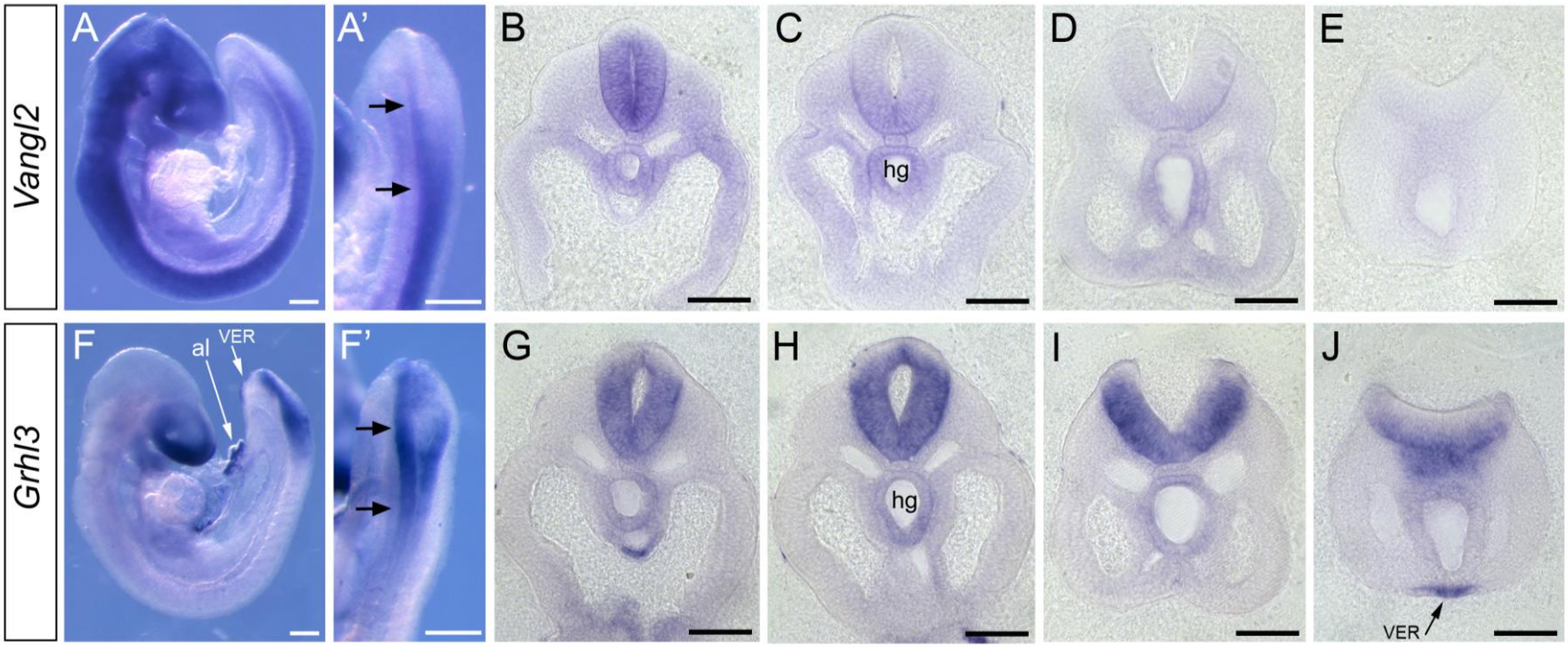

Figure 5.3 Overlapping expression of *Vangl2* and *Grhl3* at E9.5

Whole-mount *in situ* hybridisation for *Vangl2* (A-E) and *Grhl3* (F-J) in E9.5 wild type embryos. The apparent co-expression of the two genes persists at this stage (arrows in A' and F'). Transverse sections show reduced *Vangl2* expression in the caudal region (B-E) and *Grhl3* expression at various sites (G-J). Abbreviations: al = allantois, hg = hindgut, VER = ventral ectodermal ridge. Scale bars: 200 µm (A, F) and 50 µm (B-E, G-J).

5.2.2 Does the *Lp/ct* interaction involve further changes in *Grhl3* expression?

In a previous report from our laboratory, quantitative RT-PCR (qRT-PCR) was used to determine the level of *Grhl3* expression in the caudal region of E10.5 *Grhl3*$^{ct/ct}$ embryos. At the 28-29 and 30-31 somite stages, when *Grhl3* is strongly expressed in the hindgut, mRNA levels were reduced in *curly tail* embryos compared with wild type by 56% and 41%, respectively (Gustavsson et al., 2007). However the reduction of *Grhl3* in *curly tail* embryos has not been investigated at earlier stages of neurulation. Here, *Grhl3* expression in the caudal region at 19-20 somites was examined in order to answer the following questions: 1) What is the level of *Grhl3* expression in *curly tail* embryos at E9.5, when it is normally expressed in the neuroepithelium and tail bud? and 2) Is there a further alteration in *Grhl3* expression in *Vangl2*$^{Lp/+}$*;Grhl3*$^{ct/ct}$ embryos?

Using qRT-PCR*, Grhl3* expression was found to be reduced by approximately 20% in the *Vangl2*$^{+/+}$*;Grhl3*$^{ct/ct}$ caudal region compared with wild type (Figure 5.4). No further decrease was observed in *Vangl2*$^{Lp/+}$*;Grhl3*$^{ct/ct}$, consistent with the findings that the *Lp/ct* interaction does not arise due to an exacerbation of the known *curly tail* mutant phenotype (see Chapter 3). Interestingly, *Grhl3* was increased in *loop-tail* heterozygotes by around 20% compared to wild type embryos (Figure 5.4). To investigate how the changes in mRNA level correlate with the different *Grhl3* expression domains at this stage, WISH was also performed (Figure 5.5). For the accurate comparison of different genotypes, all embryos were processed together within the same tube and incubated in developing solution for the same length of time. In *Vangl2*$^{+/+}$*;Grhl3*$^{ct/ct}$ and *Vangl2*$^{Lp/+}$*;Grhl3*$^{ct/ct}$ embryos, expression was diminished in the neuroepithelium at the level of the PNP compared to wild type (Figure 5.5, arrowheads in A'-C'; also see E-G). In the tail bud however, the

expression domain was similar in these three genotypes (Figure 5.5, arrows in A'-C'; also see I-K). Consistent with the qRT-PCR experiment, *Grhl3* expression appeared to be increased in *loop-tail* heterozygotes; more intense staining was observed in the neuroepithelium (Figure 5.5D', H) and the tail bud expression domain extended more laterally compared to wild type (Figure 5.5L). Transcripts were also observed in the surface ectoderm adjacent to the PNP in *Vangl2*$^{Lp/+}$;*Grhl3*$^{+/+}$ at this stage (Figure 5.5L). Similar changes in expression were seen in the ventral forebrain (Figure 5.6). Weaker and more spatially restricted staining could be seen in both *Vangl2*$^{+/+}$;*Grhl3*$^{ct/ct}$ and *Vangl2*$^{Lp/+}$;*Grhl3*$^{ct/ct}$ embryos compared to wild type (Figure 5.6B, C, F, G), while the signal was expanded and more intense in *Vangl2*$^{Lp/+}$;*Grhl3*$^{+/+}$ (Figure 5.6D, H). Together these results demonstrate that *Grhl3* expression is reduced in *curly tail* embryos at E9.5, and that there is no further decrease in *Vangl2*$^{Lp/+}$;*Grhl3*$^{ct/ct}$.

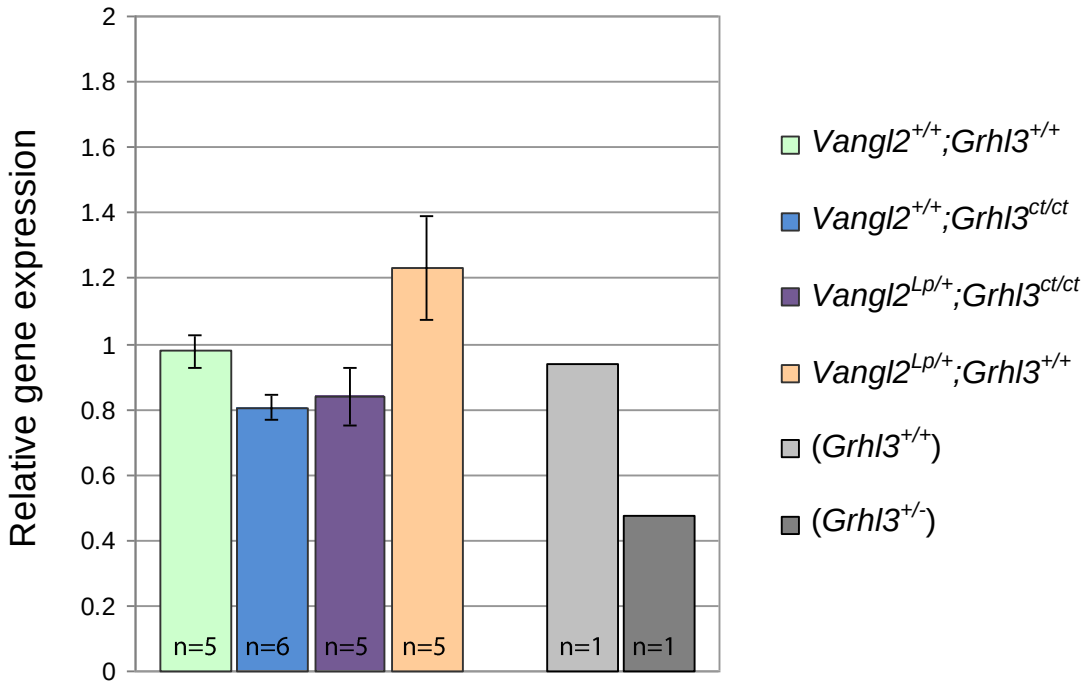

Figure 5.4 Quantification of *Grhl3* expression in the caudal region at 19-20 somites

Bars represent the mean ± SEM for each genotype. The level of expression varies significantly between the four genotypes (p = 0.019, 1-Way ANOVA). *Grhl3*$^{+/+}$ and *Grhl3*$^{+/-}$ samples, from independently collected litters, were also included as controls.

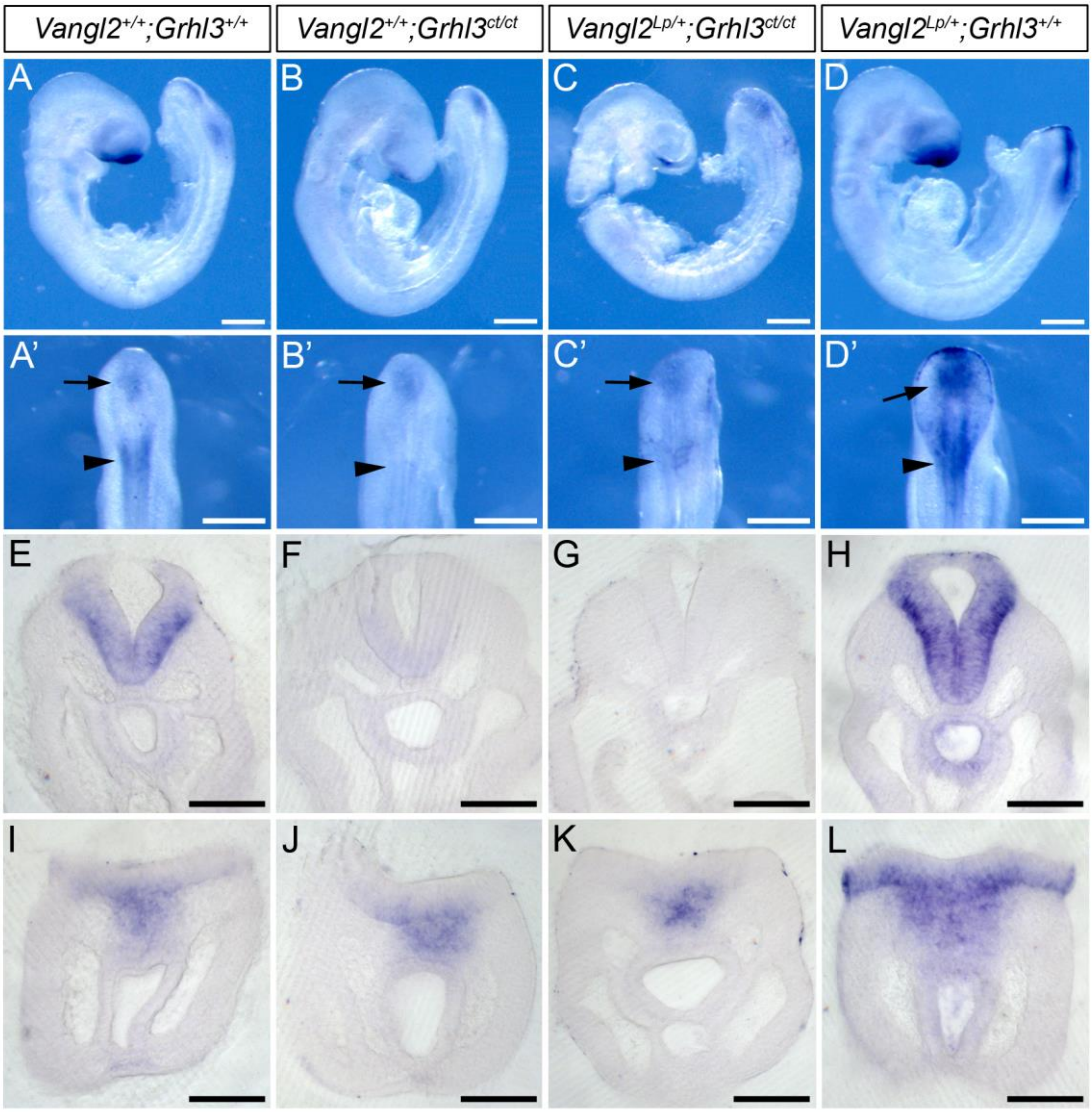

Figure 5.5 Expression pattern of *Grhl3* in the E9.5 caudal region

WISH for *Grhl3* in *Vangl2*$^{+/+}$;*Grhl3*$^{+/+}$ (A, E, I), *Vangl2*$^{+/+}$;*Grhl3*$^{ct/ct}$ (B, F, J), *Vangl2*$^{Lp/+}$;*Grhl3*$^{ct/ct}$ (C, G, K) and *Vangl2*$^{Lp/+}$;*Grhl3*$^{+/+}$ (D, H, L) embryos. Lateral views of whole embryos are shown in A-D, with higher magnification dorsal views of the caudal region shown in A'-D'. Arrowheads indicate the axial level at which *Grhl3* is normally expressed in the neuroepithelium (see wild type expression in A'). Arrows indicate the region of CNH expression. Transverse sections at the level of the neuroepithelial and tail bud expression are shown in E-H and I-L, respectively. n = four embryos per genotype. Scale bars: 200 µm (A-D) and 50 µm (E-L).

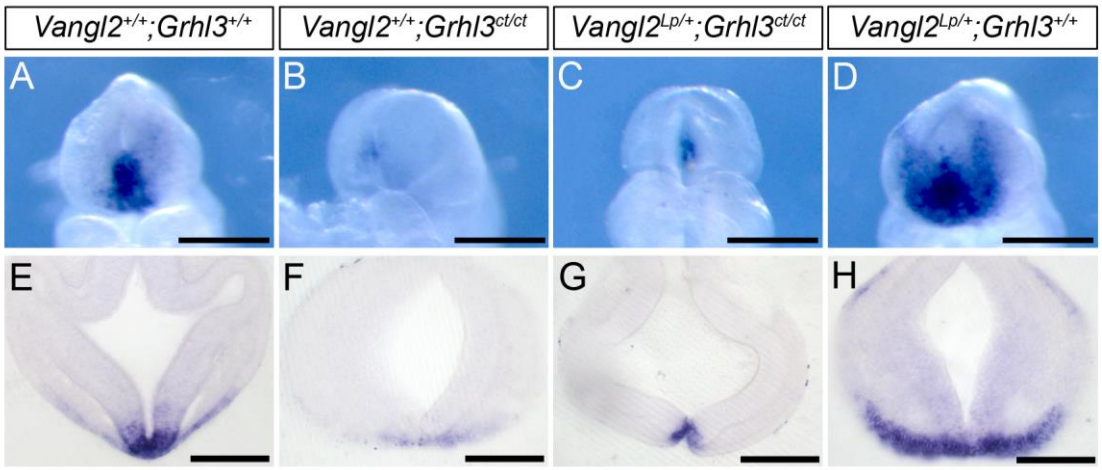

Figure 5.6 Expression pattern of *Grhl3* in the E9.5 cranial region

(**A**-**D**) Ventral views showing *Grhl3* expression in the forebrain of the embryos in Figure 5.5. (**E**-**H**) Transverse sections through the brains of the embryos in A-D. Transcripts are present in the neuroepithelium and surface ectoderm in *Vangl2*$^{+/+}$;*Grhl3*$^{+/+}$ (E) and are reduced in *Vangl2*$^{+/+}$;*Grhl3*$^{ct/ct}$ (F) and *Vangl2*$^{Lp/+}$;*Grhl3*$^{ct/ct}$ (G). Expression appears increased in *Vangl2*$^{Lp/+}$;*Grhl3*$^{+/+}$, particularly in the surface ectoderm (H). Scale bars: 200 µm (A-D) and 50 µm (E-H).

5.2.3 Does the *Lp/ct* interaction involve changes in PCP gene expression?

5.2.3.1 *Vangl2* expression

The level of *Vangl2* expression in the caudal region at E9.5 was examined by qRT-PCR. No significant changes were found between genotypes, although there was a trend towards slightly higher levels of expression in embryos carrying the *Grhl3*^{ct} mutation (Figure 5.7). When wild type and *curly tail* embryos were examined by WISH, no apparent changes in the pattern of expression were observed (Figure 5.8). As shown earlier in wild type embryos, *Vangl2* was widely expressed throughout the neuroepithelium and in the hindgut. This pattern of expression was comparable in embryos of both genotypes and at the level of the PNP the expression appeared weaker, and was absent from the dorsal neural folds, in both

Vangl2$^{+/+}$;*Grhl3*$^{+/+}$ and *Vangl2*$^{+/+}$;*Grhl3*$^{ct/ct}$ (Figure 5.8A', B'). The similarity between the level of *Vangl2* mRNA in wild type and *Vangl2*$^{Lp/+}$;*Grhl3*$^{+/+}$ embryos (Figure 5.7) is consistent with previous reports that the *Lp* mutation does not cause a reduction in the total level of *Vangl2* mRNA, but rather leads to a decrease in the amount and stability of Vangl2 protein (Gravel et al., 2010; Guyot et al., 2011; Torban et al., 2007).

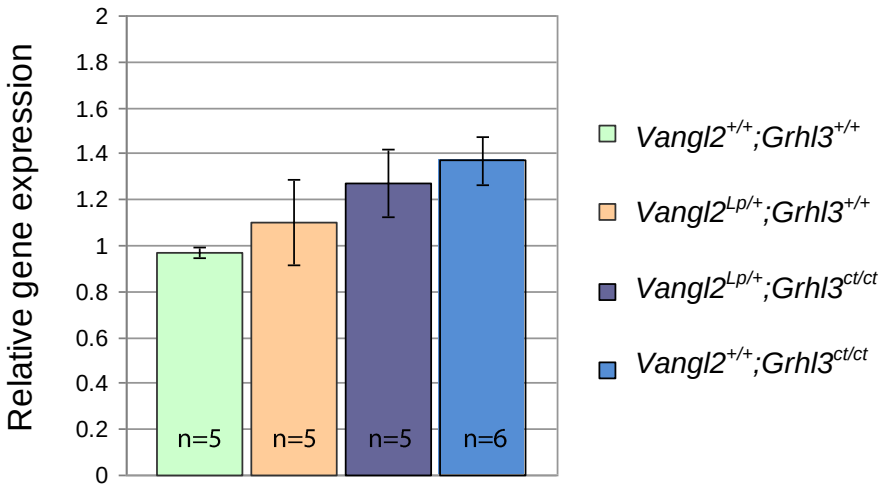

Figure 5.7 Quantification of *Vangl2* expression in the caudal region at 19-20 somites

Bars represent the mean ± SEM for each genotype. The level of expression does not vary significantly between the four genotypes (p = 0.156, 1-Way ANOVA).

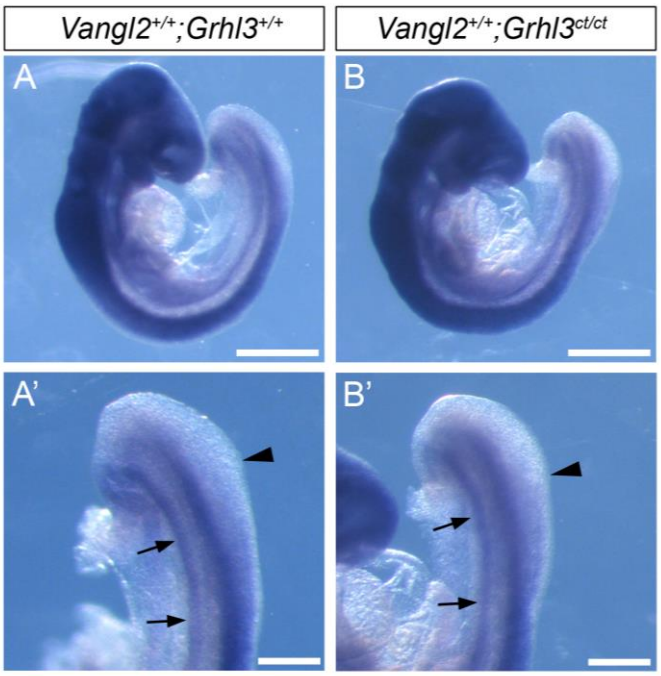

Figure 5.8 Expression pattern of *Vangl2* in E9.5 wild type and *curly tail* embryos

WISH for *Vangl2* in *Vangl2*$^{+/+}$;*Grhl3*$^{+/+}$ (A) and *Vangl2*$^{+/+}$;*Grhl3*$^{ct/ct}$ (B). Higher magnification views of the caudal regions are shown in A' and B' (arrows indicate *Vangl2* expression in the hindgut) Vangl2 becomes ventrally restricted within the neuroepithelium at a comparable level in both genotypes (arrowheads indicate the rostral limit of the PNP). n = three embryos per genotype. Scale bars: 500 µm (A-B) and 200 µm (A'-B').

5.2.3.2 *Wnt5a* expression

As described earlier, Wnt5a was previously found to induce Vangl2 activation *in vitro*. *In vivo*, Wnt5a dosage correlates with the level of Vang2 activity, as measured by the degree of its asymmetrical localisation and phosphorylation (Gao et al., 2011). The finding that *Wnt5a* expression is reduced in a proportion of *curly tail* embryos during neurulation (Gofflot et al., 1998), therefore raises the question of whether Vangl2 activity is also diminished in these mice. If reduced *Wnt5a* expression in *curly tail* causes a reduction in Vangl2 activation, could this summate with the reduction in PCP signalling in *Vangl2*$^{Lp/+}$, thus contributing to the severe spina bifida in *Vangl2*$^{Lp/+}$;*Grhl3*$^{ct/ct}$ embryos?

As previously reported (Gofflot et al., 1998; Yamaguchi et al., 1999), *Wnt5a* transcripts were abundant within the caudal region of wild type embryos at E10.0 (Figure 5.9A). Transverse sections at the level of the hindlimb buds revealed strong expression in the AER and moderate expression throughout the limb bud mesenchyme, ventral neural tube and somites, and around the bilateral nephric ducts. Transcripts appeared to be absent from the dorsal neuroepithelium, dermamyotome and hindgut (Figure 5.9D). Further caudally, *Wnt5a* was strongly expressed throughout several tissues, with the exception of the dorsal neural tube and notochord (Figure 5.9J). In the most distal region expression appeared ubiquitous, with the neuroepithelium being the most intensely stained region (Figure 5.9M).

Contrary to previous findings, alterations in *Wnt5a* expression were not detected in *curly tail* (or in $Vangl2^{Lp/+};Grhl3^{ct/ct}$) embryos by WISH (Figure 5.9B, C). When transverse sections through both $Vangl2^{+/+};Grhl3^{ct/ct}$ and $Vangl2^{Lp/+};Grhl3^{ct/ct}$ caudal regions were analysed, the pattern and intensity of staining was closely similar to $Vangl2^{+/+};Grhl3^{+/+}$ at all axial levels examined (Figure 5.9). To examine quantitatively *Wnt5a* expression in the caudal region, qRT-PCR analysis was also performed. Consistent with the WISH data, no difference in mRNA level was detected between genotypes at E10.0, or at E9.5 (Figure 5.10). These results suggest that *Wnt5a* is expressed normally in the $Vangl2^{+/+};Grhl3^{ct/ct}$ and $Vangl2^{Lp/+};Grhl3^{ct/ct}$ caudal region during neurulation.

Figure 5.9 Pattern of *Wnt5a* expression in the E10.0 caudal region

WISH for *Wnt5a* in 27-29 somite stage *Vangl2*$^{+/+}$;*Grhl3*$^{+/+}$ (A, D, G, J, M), *Vangl2*$^{+/+}$;*Grhl3*$^{ct/ct}$ (B, E, H, K, N) and *Vangl2*$^{Lp/+}$;*Grhl3*$^{ct/ct}$ (C, F, I, L, O) embryos. Transverse sections of the caudal regions in A-C are shown in D-O. A comparable pattern of expression is observed in embryos of all three genotypes. In the hindlimb buds, *Wht5a* is strongly expressed in the VER and more weakly expressed in the underlying mesenchyme (D-F; the asterisk in D indicates absence of the AER, a histological artefact). In the neuroepithelium, expression is restricted to the ventral region (D-I), despite the open neural folds in *Vangl2*$^{Lp/+}$;*Grhl3*$^{ct/ct}$ (I). At this level, transcripts appear to be weakly expressed or absent from the notochord and hindgut. In the tail bud, Wnt5a was not reduced in *Vangl2*$^{+/+}$;*Grhl3*$^{ct/ct}$ and *Vangl2*$^{Lp/+}$;*Grhl3*$^{ct/ct}$ compared to wild type (J-O). The embryo in B had an open PNP; the altered morphology and appearance of closed neural tube in N is due to the slightly different angle of sectioning. n = minimum of four embryos per genotype; the *Vangl2*$^{+/+}$;*Grhl3*$^{ct/ct}$ and *Vangl2*$^{Lp/+}$;*Grhl3*$^{ct/ct}$ embryos all had larger than average PNPs. Abbreviations: hg = hindgut, AER = apical ectodermal ridge, nd = nephric duct, VER = ventral ectodermal ridge. Scale bars: 100 µm.

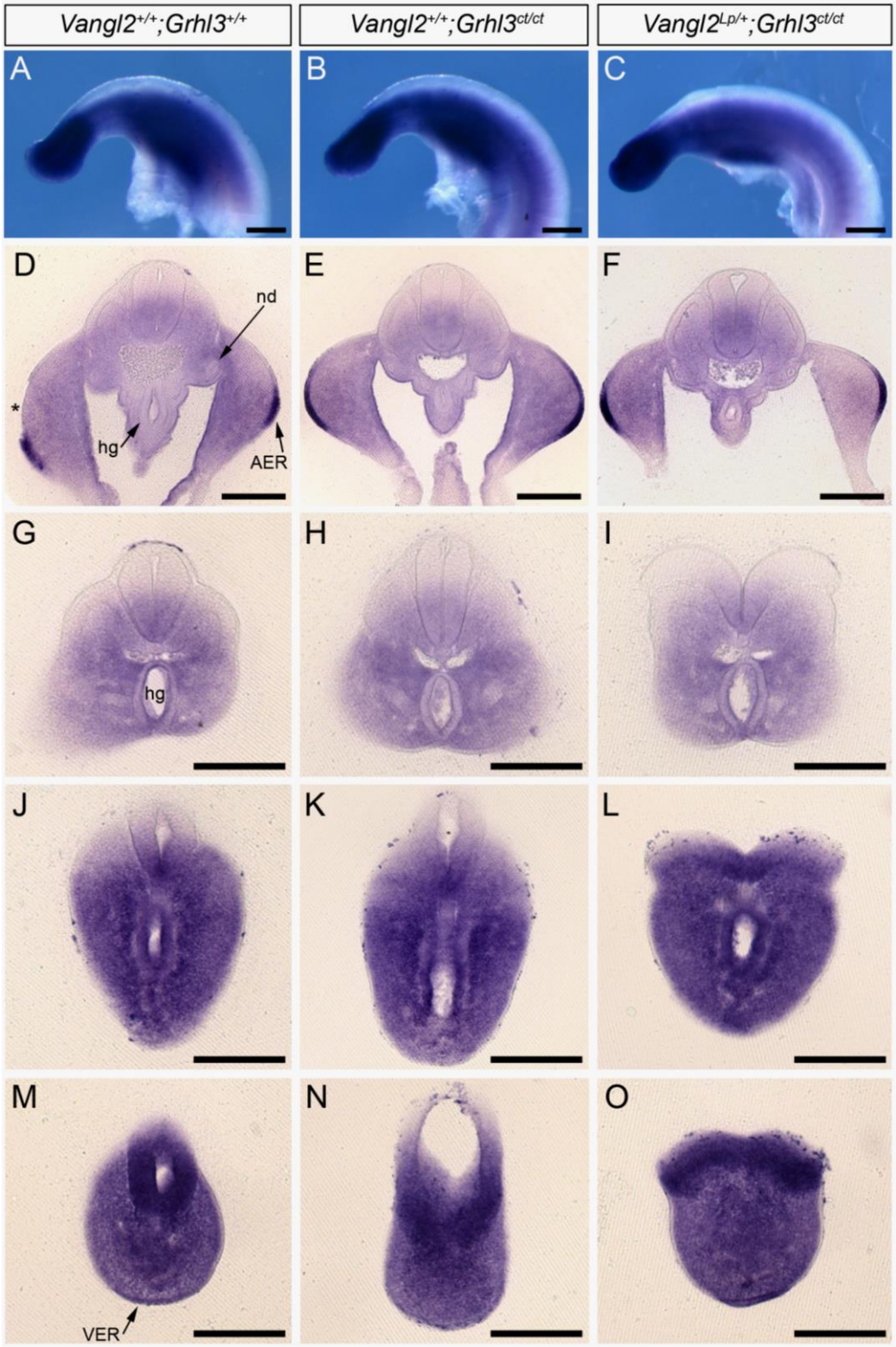
Vangl2+/+;Grhl3+/+
Vangl2+/+;Grhl3ct/ct
Vangl2Lp/+;Grhl3ct/ct
A
B
C
D
nd
*
hg
AER
E
F
G
hg
H
I
J
K
L
M
VER
N
O

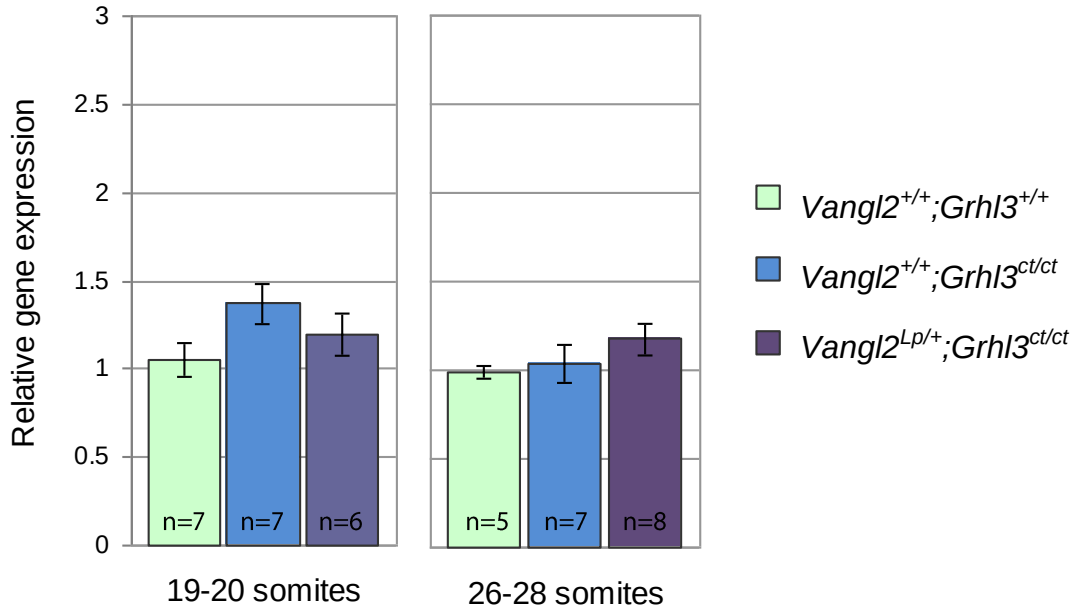

Figure 5.10 Quantification of *Wnt5a* in the caudal region by qRT-PCR

Bars represent the mean ± SEM for each genotype. *Wnt5a* mRNA was measured at two embryonic stages. The level of expression does not vary between the three genotypes (1-Way ANOVA; $p = 0.133$ for 19-20 somites and $p = 0.323$ for 26-28 somites).

5.2.4 Does *Grhl3* have a transcriptional effect downstream of the PCP genes?

In parallel to the work described above, a possible transcriptional effect of *Grhl3* downstream of the PCP genes was considered. Could the misregulation of *Grhl3* target genes downstream of PCP signalling in $Grhl3^{ct/ct}$ contribute to the *Lp/ct* interaction? To investigate this question a candidate gene approach was taken, with potential targets selected based on the literature and a microarray comparison of E9.5 $Grhl3^{+/+}$ and $Grhl3^{ct/ct}$ caudal regions that was previously performed in our laboratory (Nick Greene, unpublished data). The expression of each gene in the caudal region of E9.5 $Vangl2^{+/+};Grhl3^{+/+}$, $Vangl2^{+/+};Grhl3^{ct/ct}$ and $Vangl2^{Lp/+};Grhl3^{ct/ct}$ embryos was examined by qRT-PCR.

As described above, *RhoGEF19* was recently identified as a direct target of *Grhl3* in the E18.5 epidermis and was found to be downregulated in the skin of *Grhl3*$^{-/-}$ embryos at late gestation (Caddy et al., 2010). Here, however, an approximately two-fold increase in *RhoGEF19* expression was observed in *Vangl2*$^{+/+}$*;Grhl3*$^{ct/ct}$ embryos compared to wild type, with a similar increase also seen in *Vangl2*$^{Lp/+}$*;Grhl3*$^{ct/ct}$ (Figure 5.11A; $p = 0.05$, 1-Way ANOVA). The second gene to be analysed was *Rho kinase 1* (*ROCK1)*, a downstream effector of RhoA that was previously reported to be significantly upregulated (1.8-fold increase) in the back skin of E18.5 *Grhl3*$^{-/-}$ mice (Yu et al., 2006). In agreement with this study, an increase of around 50% was seen in the *Vangl2*$^{+/+}$*;Grhl3*$^{ct/ct}$ caudal region. An intermediate level of expression was observed in *Vangl2*$^{Lp/+}$*;Grhl3*$^{ct/ct}$ (Figure 5.11B; $p = 0.032$, 1-Way ANOVA).

Two further GEF genes, *ArhGEF3* and *ArhGEF7*, emerged from the microarray performed by Dr Nick Greene. In this previous study, the expression of *ArhGEF3* was increased by approximately two-fold in the caudal region of affected *curly tail* embryos (those with a large PNP) compared to wild type (Nick Greene, unpublished data). Mouse *ArhGEF3* was identified in a screen for candidate genes involved in Hirschsprung's disease (Heanue and Pachnis, 2006) but its function has not been studied. However, human ARHGEF3 has been shown to activate RhoA *in vitro* (Thiesen et al., 2000). Here, *ArhGEF3* displayed an approximately two-fold upregulation in *Vangl2*$^{+/+}$*;Grhl3*$^{ct/ct}$ samples, consistent with the previous microarray data. Again, the increase in gene expression was not as marked in *Vangl2*$^{Lp/+}$*;Grhl3*$^{ct/ct}$ embryos (Figure 5.11C; $p = 0.02$, 1-Way ANOVA).

Mouse *ArhGEF7* (also called *Beta-pix*) has been shown to recruit and activate *Rac1* (ten Klooster et al., 2006). More recently, its role in promoting lamellipodia and negatively regulating focal adhesion maturation was documented (Kuo et al., 2011).

ArhGEF7 previously displayed a 2.2-fold increase in *curly tail* (affected and unaffected pooled) compared to wild type (Nick Greene, unpublished data). Here, however, no difference in ArhGEF7 expression was detected between genotypes (Figure 5.11D; p = 0.417, 1-Way ANOVA).

The final gene to be analysed, *P190RhoGAP* (also called *Grlf1*), was included due to its association with NTDs in mice. *P190RhoGAP* is highly expressed within the nervous system during development and embryos homozygous for a loss-of-function allele display numerous abnormalities, including 30% exencephaly, eye defects and low penetrance omphalocele (failure of abdominal cavity fusion) (Brouns et al., 2000). However, no alterations in *P190RhoGAP* expression were observed in the $Vangl2^{+/+};Grhl3^{ct/ct}$ or $Vangl2^{Lp/+};Grhl3^{ct/ct}$ caudal region at E9.5 (Figure 5.11E).

Figure 5.11 Quantification of potential *Grhl3* targets in the E9.5 caudal region

Graphs show the results of qRT-PCR analysis using samples from embryos with 19-21 somites. Bars represent the mean ± SEM for each genotype. (**A**) Expression of *RhoGEF19* varied significantly between genotypes (p = 0.05, 1-Way ANOVA) although individual pairwise comparisons did not quite reach significance. (**B**) Expression of *ROCK1* varied significantly between genotypes (p = 0.032, Kruskal-Wallis One Way ANOVA on Ranks) * p < 0.05 (pairwise comparison). (**C**) Expression of ArhGEF3 varied significantly between genotypes (p = 0.02, Kruskal-Wallis One Way ANOVA on Ranks) * p < 0.05 (pairwise comparison). Conversely, no difference in the abundance of *ArhGEF7* (D) or *p190RhoGAP* (E) mRNA was detected (1-Way ANOVA; p = 0.417 and p = 0.695, respectively).

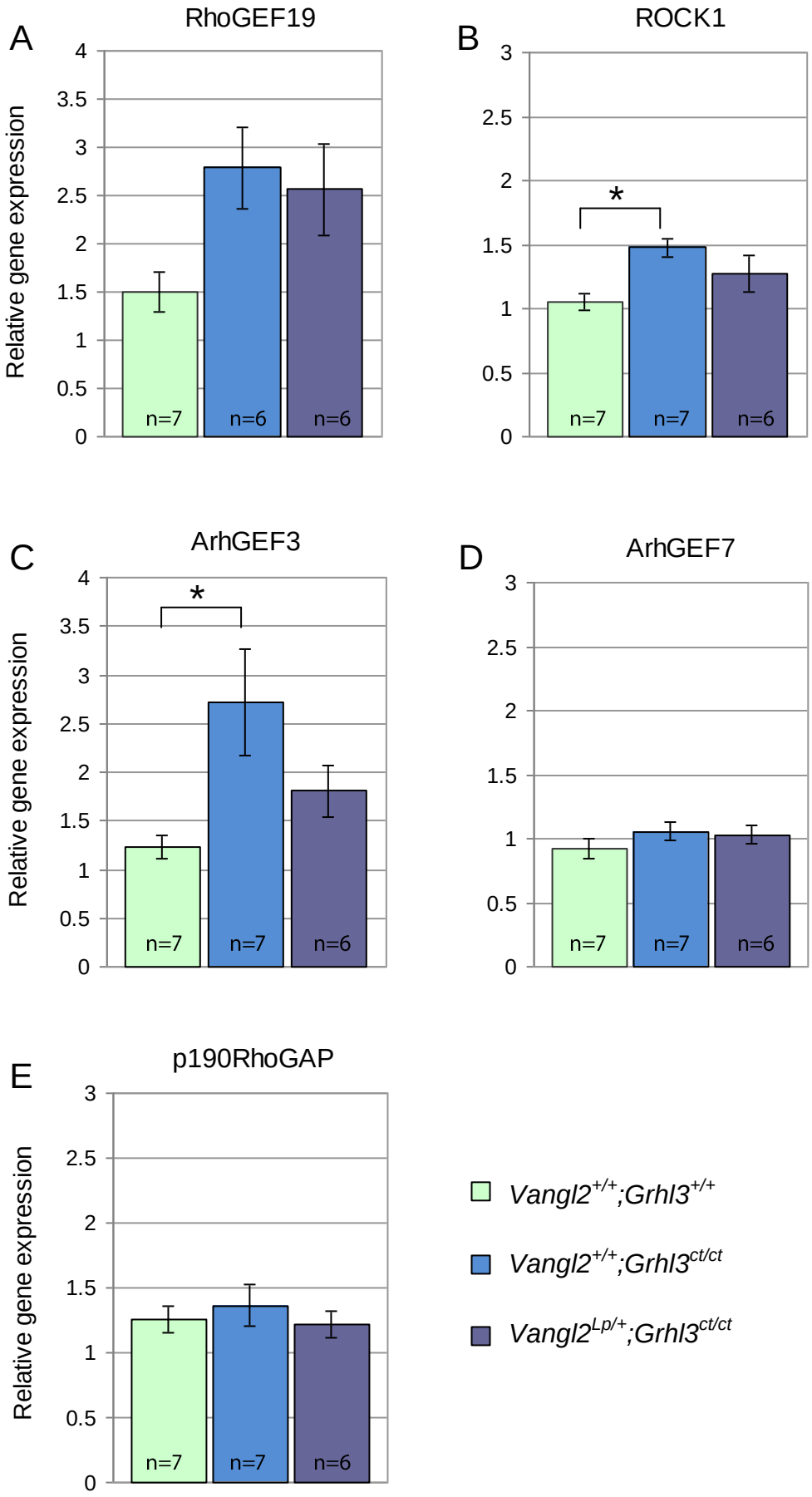
A
RhoGEF19
Relative gene expression
4
3.5
3
2.5
2
1.5
1
0.5
0
n=7
n=6
n=6
B
ROCK1
3
2.5
2
1.5
1
0.5
0
*
n=7
n=7
n=6
C
ArhGEF3
Relative gene expression
4
3.5
3
2.5
2
1.5
1
0.5
0
*
n=7
n=7
n=6
D
ArhGEF7
3
2.5
2
1.5
1
0.5
0
n=7
n=7
n=6
E
p190RhoGAP
Relative gene expression
3
2.5
2
1.5
1
0.5
0
n=7
n=7
n=6
Vangl2+/+;Grhl3+/+
Vangl2+/+;Grhl3ct/ct
Vangl2Lp/+;Grhl3ct/ct

5.2.5 Signalling downstream of the PCP genes

5.2.5.1 Level of active Rho protein

If the presence of *ct* mutations leads to the misregulation of genes involved in RhoGTPase signalling, what are the consequences downstream? In mouse embryos a requirement for RhoA-ROCK signalling has been demonstrated downstream of the PCP genes during the initiation of neural tube closure (Ybot-Gonzalez et al., 2007b): whole embryo culture from E7.5 with a pharmacological inhibitor of ROCK, Y27632, revealed a strong interaction between ROCK inhibition and the *Lp* mutation. Almost all *Vangl2*$^{Lp/+}$ mice treated with a low dose of the inhibitor displayed failure of closure 1, a phenotype which is not seen in *loop-tail* heterozygotes under normal developmental conditions. *Vangl2*$^{+/+}$ embryos were much less affected, with open neural tubes only observed in around 50% of embryos when using a near-toxic dose. Following inhibitor cultures, *Vangl2*$^{+/+}$ and *Vangl2*$^{Lp/+}$ embryos were also found to display morphological features characteristic of *loop-tail* homozygotes. In addition to *Vangl2*, ROCK inhibition summated with mutations in *Celsr1* and *Scribble*. Nearly 100% of treated *Celsr1*$^{Crsh/+}$ embryos had an open neural tube, as did a proportion of *Scribble*$^{Crc/+}$, although embryos of the latter genotype were more resistant to higher doses of the inhibitor (Ybot-Gonzalez et al., 2007b).

To investigate a possible alteration in RhoA signalling downstream of *Grhl3*$^{ct/ct}$, the level of active (GTP-bound) RhoA was measured using a G-LISA RhoA activation assay (Figure 5.12; see Chapter 2 for details). We hypothesised that a change in the level of activated RhoA in *ct/ct* could interact with a reduction of RhoA signalling downstream of *Lp*, thus contributing to the interaction in *Vangl2*$^{Lp/+}$*;Grhl3*$^{ct/ct}$ embryos. When normalised to wild type samples, a reduction of around 25% was observed in the *Vangl2*$^{Lp/+}$*;Grhl3*$^{+/+}$ caudal region. Similarly the level of GTP-RhoA was reduced in *Vangl2*$^{+/+}$*;Grhl3*$^{ct/ct}$, this time by nearly 40%. Consistent with the

observed reduction in each of the single mutants, a reduction of around 55% was seen in *Vangl2*$^{Lp/+}$*;Grhl3*$^{ct/ct}$ samples (Figure 5.12C). This result suggests that there is a reduction in GTP-RhoA in the *Vangl2*$^{Lp/+}$*;Grhl3*$^{ct/ct}$ caudal region, and that this is a cumulative effect of reduced active Rho for each of the single mutant genotypes. Unfortunately there was insufficient lysate leftover to measure the total level of Rho protein in the samples. However, as detailed in Chapter 2, samples were normalised for the total amount of cellular protein.

5.2.5.2 ROCK inhibitor cultures

As described above, RhoA-ROCK signalling is required downstream of PCP signalling prior to closure 1. The observed reduction in activated RhoA in *Vangl2*$^{Lp/+}$*;Grhl3*$^{+/+}$, *Vangl2*$^{+/+}$*;Grhl3*$^{ct/ct}$, and *Vangl2*$^{Lp/+}$*;Grhl3*$^{ct/ct}$ at E9.5 suggests that this pathway also plays a role during low spinal neurulation. To investigate this further, Y27632 was applied to E9.0 embryos in whole embryo culture. If a reduction in RhoA signalling in *Vangl2*$^{Lp/+}$*;Grhl3*$^{ct/ct}$ contributes to the failure of neurulation, and this is a cumulative effect of reduced GTP-RhoA downstream of both *Lp/+* and *ct/ct*, then would inhibition of this pathway summate with either single mutant genotype to delay PNP closure?

A concentration of 5 μM Y27632 was deemed to be suitable, based on toxicity assays (see Chapter 2) and previous analyses (Ybot-Gonzalez et al., 2007b). Wild type embryos cultured in 5 μM Y27632 from E9.0 developed normally and appeared morphologically comparable to controls (Figure 5.13A-D). Somite number and CRL did not differ between control and inhibitor-treated embryos, indicating that Y27632 did not retard embryonic development or growth (Figure 5.13E). Treatment with Y27632 did not delay closure of the wild type PNP after seven hours in culture (Figure 5.13F).

When mutant embryos (*Vangl2*$^{Lp/+}$*;Grhl3*$^{+/+}$, *Vangl2*$^{+/+}$*;Grhl3*$^{ct/ct}$ and *Vangl2*$^{Lp/+}$*;Grhl3*$^{ct/ct}$) were cultured, an effect of 5 µM Y27632 on PNP size was observed. PNP length was significantly increased with inhibitor treatment (p = 0.026, 2-Way ANOVA). For both *Vangl2*$^{Lp/+}$*;Grhl3*$^{+/+}$ and *Vangl2*$^{+/+}$*;Grhl3*$^{ct/ct}$ embryos, treatment with Y27632 increased the mean PNP length to a size which was similar to that seen in *Vangl2*$^{Lp/+}$*;Grhl3*$^{ct/ct}$ embryos (Figure 5.14A). The effect of ROCK inhibition on PNP width appeared more pronounced: the mean values for *Vangl2*$^{Lp/+}$*;Grhl3*$^{+/+}$ and *Vangl2*$^{+/+}$*;Grhl3*$^{ct/ct}$ embryos were higher for treated embryos than for controls (Figure 5.14B; p < 0.001, 2-Way ANOVA). For both PNP parameters, inhibitor treatment appeared to affect *Vangl2*$^{Lp/+}$*;Grhl3*$^{+/+}$ and *Vangl2*$^{+/+}$*;Grhl3*$^{ct/ct}$ embryos more dramatically than *Vangl2*$^{Lp/+}$*;Grhl3*$^{ct/ct}$, although this observation could not be confirmed as only one control embryo was recovered for the latter genotype. The mean number of somite pairs did not differ between control and inhibitor-treated embryos, indicating that the differences in PNP size did not simply reflect differences in developmental stage (Figure 5.14D).

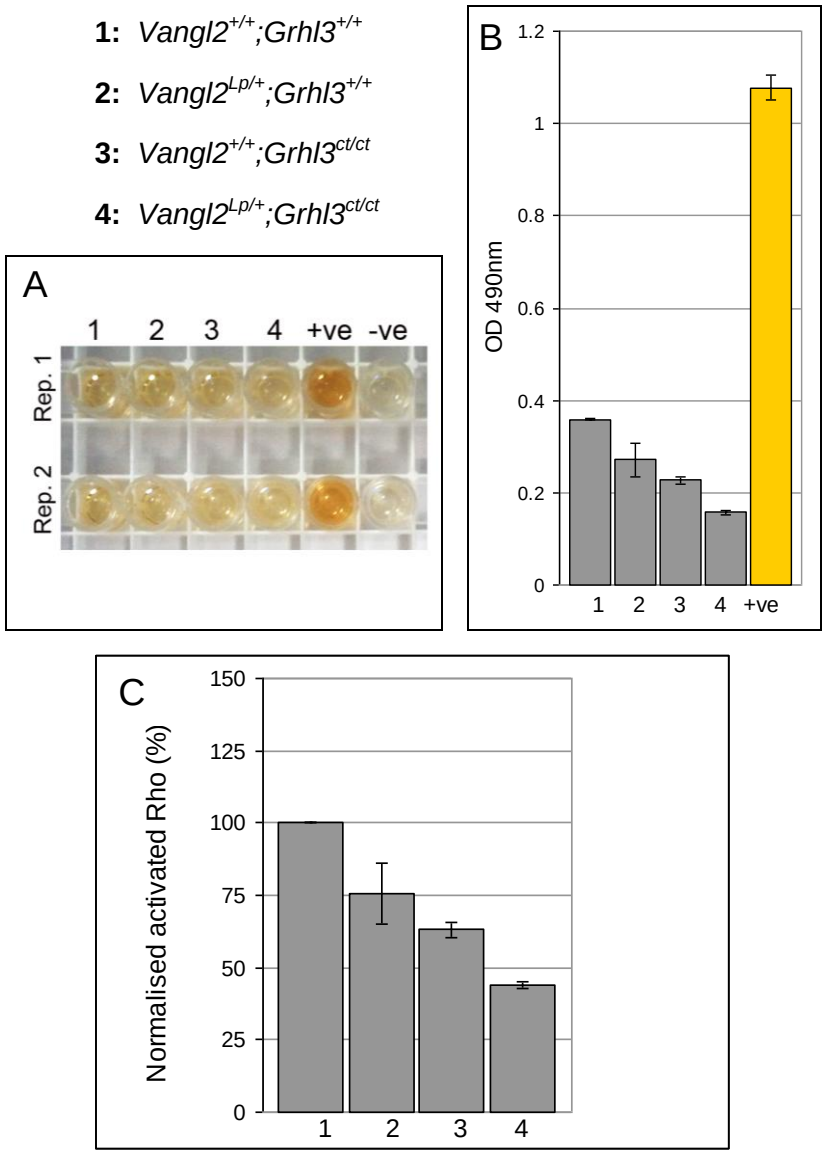

Figure 5.12 RhoA activation assay

An absorbance based G-LISA assay was performed. For each genotype, protein lysates from four E9.5 caudal regions were pooled into one sample tube. Samples were normalised for total cellular protein prior to performing the experiment. Two replicates were processed for each sample. (**A**) Photograph of the experimental plate following incubation with HRP detection reagent. +ve control wells contain constitutively active RhoA, -ve controls were lysis buffer blanks for background readings. (**B**) Absorbance readings at 490nm for each genotype. Bars represent the mean and SEM after subtraction of the background values for each of the two replicates. The difference between the four genotypes was statistically significant (p = 0.010, Kruskal-Wallis 1-way ANOVA on ranks). The positive control shows a mean absorbance of around 1, as expected from the assay protocol. (**C**) Level of activated-RhoA, normalised to wild type (*Vangl2*$^{+/+}$;*Grhl3*$^{+/+}$) samples.

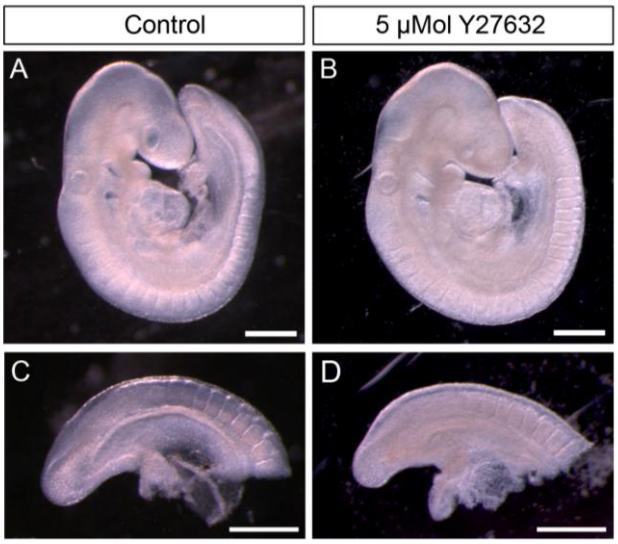

E

Treatment	Number of somite pairs		Crown-rump length (mm)	
Control	21.7 ± 0.5	p = 1.0 (Mann Whitney Rank Sum test)	2.3 ± 0.1	p = 0.738 (t-test)
5 µM Y27632	21.3 ± 0.8		2.4 ± 0.1	

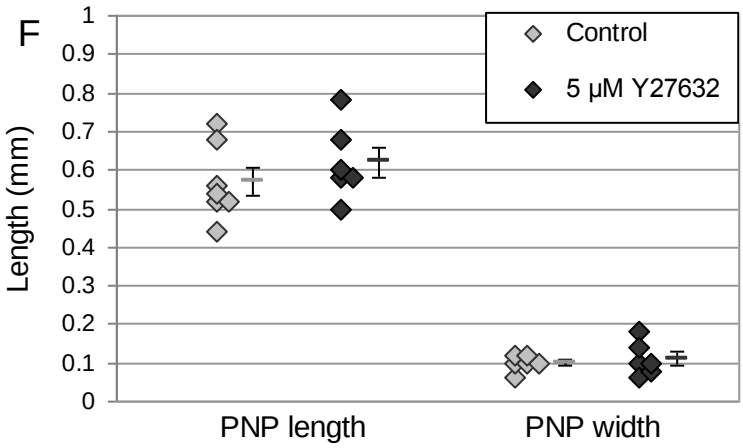

Figure 5.13 Viability of embryos after culture with 5 µM ROCK inhibitor

Data shown are for wild type embryos with 19-23 somite pairs after seven hours in culture. Culture serum was supplemented with H_2O (vehicle; control) or 5 µM Y27632. (**A, B**) Control and inhibitor-treated embryos displayed comparable morphology after culture. C and D are higher magnification views of the embryonic caudal regions in A and B, respectively. Scale bars: 500 µm. (**E**) Viability of cultured embryos: inhibitor treatment did not affect somite number or embryonic C-R length. (**F**) No differences in PNP length or width were observed between wild type control and inhibitor-treated embryos (t-test; p = 0.364 and p = 0.625, respectively).

Figure 5.14 Effect of ROCK inhibition on PNP size

Data shown are for embryos with 16-20 somite pairs after seven hours in culture. Each individual embryo is represented by a single data point, with the mean ± SEM shown to the right of each group. 2-Way ANOVA using genotype and treatment as factors was performed:

(**A**) PNP length varies significantly with treatment ($p = 0.026$) and with genotype ($p = 0.027$). No interaction between genotype and treatment was found ($p = 0.111$).

(**B**) PNP width varies significantly with treatment ($p < 0.001$) and with genotype ($p = 0.006$). No interaction between genotype and treatment was found ($p = 0.127$).

(**C**) Representative control and inhibitor-treated *Vangl2*$^{+/+}$;*Grhl3*$^{ct/ct}$ embryos after culture, demonstrating the effect of Y27632 on PNP width.

(**D**) Somite number does not vary with treatment ($p = 0.642$) or with genotype ($p = 0.154$). No interaction between genotype and treatment was found ($p = 0.623$).

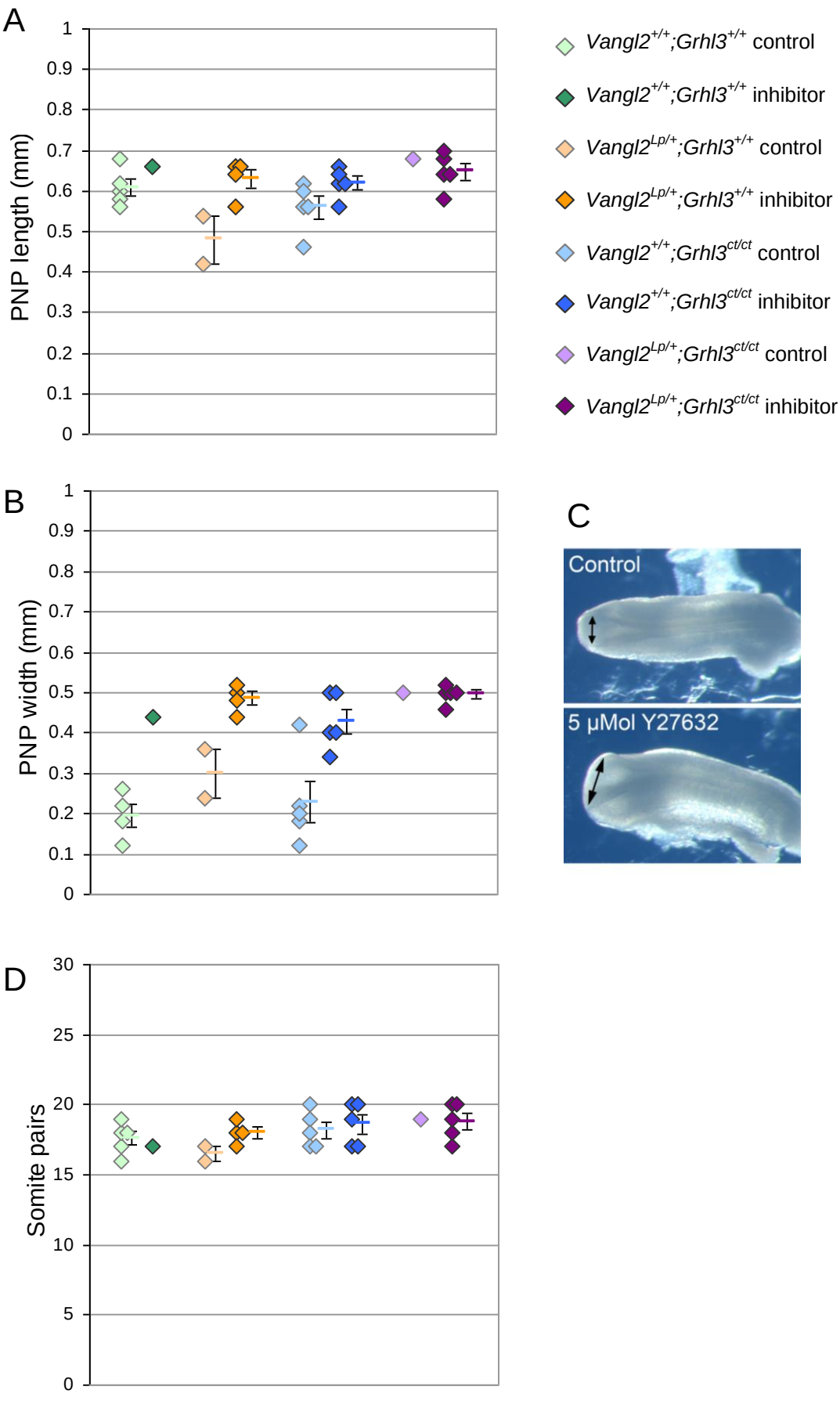
A
PNP length (mm)
1
0.9
0.8
0.7
0.6
0.5
0.4
0.3
0.2
0.1
0
Vangl2+/+;Grhl3+/+ control
Vangl2+/+;Grhl3+/+ inhibitor
Vangl2Lp/+;Grhl3+/+ control
Vangl2Lp/+;Grhl3+/+ inhibitor
Vangl2+/+;Grhl3ct/ct control
Vangl2+/+;Grhl3ct/ct inhibitor
Vangl2Lp/+;Grhl3ct/ct control
Vangl2Lp/+;Grhl3ct/ct inhibitor
B
PNP width (mm)
C
Control
5 µMol Y27632
D
Somite pairs
30
25
20
15
10
5
0

5.3 Discussion

5.3.1 Overlapping expression of *Vangl2* and *Grhl3*

The WISH data presented in Figure 5.2 and Figure 5.3 show that *Vangl2* and *Grhl3* occupy overlapping expression domains during spinal neurulation, potentially allowing a molecular interaction between the two genes to occur within the same cells. In particular, they are both strongly expressed in the caudal neuroepithelium and more weakly in the hindgut. This apparent co-expression corresponds to the time when delayed neurulation in *Lp/ct* embryos first becomes apparent (see Chapter 4). Aside from their overlapping expression at the level of PNP closure, the distribution of *Vangl2* and *Grhl3* transcripts appears to be somewhat complementary along the neuraxis. Indeed, at E9.5, *Grhl3* transcripts in the neuroepithelium are most abundant caudally in the open neural folds, the level at which *Vangl2* expression diminishes (compare A and F in Figure 5.3). A lack of suitable antibodies precluded a detailed immunohistochemical analysis of Vangl2 and Grhl3 expression in the caudal region. However, other studies have shown their mRNA and protein distributions to be closely similar during development. The expression of *Vangl2* transcripts throughout the neuroepithelium, as shown here and previously (Kibar et al., 2001b; Murdoch et al., 2001a), is comparable to the pattern of protein expression (Torban et al., 2007; Torban et al., 2008). Similarly, *in situ* hybridisation and immunofluoresence both reveal strong *Grhl3* expression in the leading edge of the E15.5 developing eyelid (Hislop et al., 2008; Yu et al., 2008).

5.3.2 Effect of *Lp* and *ct* on *Grhl3* expression

The overlapping expression of *Vangl2* and *Grhl3* raises the question of whether each gene's expression might be altered when the other gene is mutated. Unlike in *Drosophila*, where the level of *stan* (homologous to vertebrate *Celsr1*) was found to

be related to *grh* gene dosage (Lee and Adler, 2004), no evidence of perturbed core PCP gene expression was found in the epidermis of E18.5 *Grhl3*$^{-/-}$ mutant mice (Caddy et al., 2010). This study also found normal levels of *Grhl3* mRNA in *Vangl2*$^{Lp/Lp}$, *Celsr1*$^{Crsh/Crsh}$, *Ptk7*$^{-/-}$ and *Scribble*$^{Crc/Crc}$ mutant epidermis at the same stage.

Further characterisation of *Grhl3* expression dynamics in *curly tail* embryos is needed, as fundamental questions remain to be answered. For example, it is not known whether the *ct* mutation, predicted to lie upstream of the *Grhl3* start codon in a putative enhancer region (Gustavsson et al., 2007), causes a reduction in *Grhl3* at each of its different sites of embryonic expression. Alternatively there could be other, tissue-specific enhancers or upstream regulators of *Grhl3* so that, in *curly tail* embryos, expression is specifically reduced in the hindgut at E10-10.5. In this thesis, an overall 20% reduction in *Grhl3* expression was found in the caudal region of 19-20 somite stage *Vangl2*$^{+/+}$*;Grhl3*$^{ct/ct}$ and *Vangl2*$^{Lp/+}$*;Grhl3*$^{ct/ct}$ embryos (see Figure 5.4). WISH analysis suggested that this predominantly reflects a reduction of *Grhl3* in the neuroepithelium at this stage. Compared with wild type, *Grhl3* was also reduced in the *Vangl2*$^{+/+}$*;Grhl3*$^{ct/ct}$ and *Vangl2*$^{Lp/+}$*;Grhl3*$^{ct/ct}$ ventral forebrain by WISH, although this observation was not quantified by qRT-PCR. These results show that *ct* causes a reduction in *Grhl3* expression earlier than has previously been described (Gustavsson et al., 2007) and does affect tissues other than the hindgut.

Using WISH, changes in the intensity or location of *Grhl3* expression in the CNH were not obsrved in *Vangl2*$^{+/+}$*;Grhl3*$^{ct/ct}$ or *Vangl2*$^{Lp/+}$*;Grhl3*$^{ct/ct}$ embryos (see Figure 5.5). This was somewhat surprising in light of the reduced rate of proliferation observed in this region of embryos carrying the *Grhl3*$^{ct/ct}$ genotype (Chapter 4). However, this result could reflect the non-quantitative nature of the WISH technique or be due to the orientation of the sections (for example, sagittal sections may show

that expression is not expanded as far in the A-P direction). It would be useful to examine the expression in this region more precisely, for example by isolating precisely-dissected wild type and *curly tail* caudal regions for *Grhl3* qRT-PCR, and by immunohistochemistry.

The experiments in Figure 5.4 and Figure 5.5 show that the *Vangl2*$^{Lp/+}$;*Grhl3*$^{ct/ct}$ genotype is not associated with a further reduction of *Grhl3* compared to *Vangl2*$^{+/+}$;*Grhl3*$^{ct/ct}$, suggesting that such an effect does not contribute to the *Lp/ct* interaction. However, the apparent increased level of *Grhl3* in *Vangl2*$^{Lp/+}$ single heterozygous mutants is intriguing (see Figure 5.4 and Figure 5.5). This effect was rather pronounced using WISH, and continued to be seen when embryos of each genotype were allowed to continue their colorimetric development beyond the desired stage (data not shown). As the increase was observed in numerous tissues, it is unlikely that it simply reflects changes in tissue architecture; indeed, the gross morphology of the *Vangl2*$^{Lp/+}$;*Grhl3*$^{+/+}$ caudal region is relatively normal at this stage. The reason for the absence of a similar increase in *Vangl2*$^{Lp/+}$;*Grhl3*$^{ct/ct}$ remains unclear but could perhaps be explained by an epistatic effect: that is, if the *Lp*-related increase in *Grhl3* expression requires the aforementioned enhancer, then such a rise might be prevented by the presence of *ct* mutations in *Vangl2*$^{Lp/+}$;*Grhl3*$^{ct/ct}$ embryos.

5.3.3 PCP gene expression in mutant embryos

In agreement with the normal levels of *Vangl2* expression observed in E18.5 *Grhl3* null mouse embryos (Caddy et al., 2010), *Vangl2* mRNA was not found to be differentially expressed in *Vangl2*$^{+/+}$;*Grhl3*$^{ct/ct}$ at E9.5, suggesting that its expression is not transcriptionally regulated by *Grhl3*. Similarly, and in contrast to a previous report (Gofflot et al., 1998), no alterations in the level of *Wnt5a* mRNA were detected in *Vangl2*$^{+/+}$;*Grhl3*$^{ct/ct}$ (or *Vangl2*$^{Lp/+}$;*Grhl3*$^{ct/ct}$) embryos. All of the mutants

included in the current analysis were ‘affected’ embryos; that is, they displayed an enlarged PNP indicative of a future delay or failure of spinal neurulation. A reduction in *Wnt5a* expression downstream of *Grhl3*$^{ct/ct}$ is therefore unlikely to contribute to the severe spina bifida in *Vangl2*$^{Lp/+}$*;Grhl3*$^{ct/ct}$ embryos. If a reduction had been found, this hypothesis could have been pursued further. The next step would have been to examine the level of Vangl2 activation in mutant embryos, for example using antibodies against specific phosphorylated sites as previously described (Gao et al., 2011). Moreover, the expression of other PCP proteins could be examined in *curly tail* embryos. Celsr1 would be an interesting candidate, based on the finding in *Drosophila* that the level of stan protein correlates with *grh* gene dosage (Lee and Adler, 2004).

5.3.4 A downstream effect on RhoA signalling?

The Rho family of GTPases act as molecular switches, which cycle between an active (GTP-bound) and an inactive (GDP-bound) conformation. These two states are tightly regulated by three classes of conserved proteins; 1) Guanine nucleotide exchange factors (GEFs) which convert the GTPase into its active form by catalysing the exchange of GDP for GTP; 2) GTPase activating proteins (GAPs) which convert the GTPase back into its inactive form by accelerating its intrinsic GTPase activity; 3) Guanine nucleotide dissociation inhibitors (GDIs) which sequester inactive GTPases in the cytoplasm (Mulinari and Hacker, 2010). Downstream of active Rho, the ROCK family of serine/threonine kinases are a major group of effector proteins. Following their activation by Rho binding, ROCKs phosphorylate numerous downstream substrates, ultimately affecting many aspects of cell behaviour (Mulinari and Hacker, 2010).

Increased expression of three genes involved in Rho-GTPase signalling, *RhoGEF19*, *ArhGEF3* and *ROCK1*, was observed in the *curly tail* caudal region

(see Figure 5.11). The upregulation of *RhoGEF19* was surprising, given the diminished expression in *Grhl3*$^{-/-}$ mice (Caddy et al., 2010). However this study only examined the expression of *RhoGEF19 in vivo* in the E18.5 skin, much later then the neurulation stage embryos studied here. The contradictory findings could therefore reflect differences in tissue- and stage-specific roles of *Grhl3.* Indeed, in our laboratory, *RhoGEF19* was recently found to be unaltered in neurulation-stage *Grhl3*$^{-/-}$ embryos (Dr Nick Green, personal communication). On the other hand, the increased levels of *ArhGEF3* and *ROCK1* in *curly tail* are consistent with findings from a previous microarray (Nick Greene, unpublished data) and the literature (Yu et al., 2006), respectively. As mentioned earlier, there is evidence that RhoGEF19 and ArhGEF3 are capable of activating RhoA (Caddy et al., 2010; Thiesen et al., 2000). Interestingly, a feedback mechanism whereby ROCK1 indirectly mediates RhoA activity was recently described (Tang et al., 2012) so it is plausible that ROCK1, in addition to its function downstream of RhoA, could also regulate its activity upstream during neurulation.

Given the information above, the altered expression of *RhoGEF19*, *ArhGEF3* and *ROCK1* in *curly tail* might be predicted to augment RhoA activity. However, when samples were assayed for levels of GTP-RhoA: this showed a reduction downstream of both *Lp/+* and *ct/ct* (compared to wild type) and a cumulative effect in *Vangl2*$^{Lp/+}$*;Grhl3*$^{ct/ct}$. Although this experiment should be repeated with further samples, it does indicate that a decline in RhoGTPase signalling may contribute to the *Vangl2*$^{Lp/+}$*;Grhl3*$^{ct/ct}$ phenotype. The deleterious effect of ROCK inhibition on PNP closure in both of the single mutants also supports this conclusion (see Figure 5.14). Whether the reduction in GTP-RhoA reflects diminished activation by upstream regulators, or a reduction in the total abundance of available RhoA protein, warrants further investigation. How then, can the increased levels of *GEF* and *ROCK1* expression be explained? Perhaps a compensatory feedback

mechanism activates transcription of these genes in response to a decline in RhoA activity. Another possible explanation is that the level of other GEF, GAPs or GDIs is also affected in *curly tail*, so that overall the balance of their activity causes a reduction in GTP-RhoA, rather than an increase. If this is the case then examining only a few family members, as was performed here, could yield results which do not accurately represent the ultimate outcome downstream.

5.3.5 Which tissues are involved?

As the expression analyses and G-LISA assay used samples extracted from the entire caudal region (see Chapter 2 for details of dissections), is it not clear which tissue(s) is involved in a possible molecular interaction between *Vangl2* and *Grhl3*. In the following chapter, a requirement for the two genes in the same cells during neurulation is demonstrated genetically by crossing $Vangl2^{flox}$ and $Grhl3^{Cre}$ mice (see Chapter 6). Given their strong, overlapping expression in the neuroepithelium, it is tempting to speculate that this is where the two genes interact molecularly. This theory could be tested by examining embryos in which both genes have been conditionally ablated; this could be achieved by generating mice carrying both the $Grhl3^{flox}$ and $Vangl2^{flox}$ alleles and crossing these to *Sax1*-Cre animals, which have recently been generated (Professor Kate Storey, personal communication). Using embryos of each genotype, the abundance and spatial distributions of RhoA and ROCK1, along with the expression of ROCK targets such as myosin II regulatory light chain (MLC) and LIM-kinase (LIMK), could also be studied. This would hopefully reveal the precise regions or cells affected by the *Lp/ct* interaction.

In summary, the results described here show that the domains of *Vangl2* and *Grhl3* expression overlap during spinal neurulation and that they may interact at the level of RhoA-ROCK signalling. However, until the co-expression of *Vangl2* and *Grhl3* in the caudal region is confirmed at the protein level and on a single cell basis, I

cannot rule out the possibility that similar downstream effects occur independently in different cells of the same tissue, but summate mechanistically. In other words there could, in reality, be reduced signalling downstream of *Vangl2*^{Lp} in some (*Vangl2*-expressing) cells, and a deleterious effect of *Grhl3*^{ct} on Rho-GTPase signalling in others (*Grhl3*-positive cells).

6. A conditional genetic approach to investigate the interaction between *Vangl2* and *Grhl3*

6.1 Introduction

The developmental mechanisms underlying the severe spina bifida in *Vangl2*$^{Lp/+}$;*Grhl3*$^{ct/ct}$ embryos are investigated in the previous two chapters. The findings of Chapter 4 support the hypothesis that *Vangl2*^{Lp} and *Grhl3*^{ct} aberrantly affect the development of different tissues, and that these defects summate to cause failure of neurulation. The data in Chapter five additionally provide evidence for the involvement of a second effect; a molecular interaction between *Vangl2* and *Grhl3* within the caudal region. In this chapter, a cell-autonomous requirement for *Vangl2* and *Grhl3,* within the same tissue of the embryo during neurulation, was simultaneously investigated using a conditional genetic approach.

Cre-loxP recombination has provided a powerful tool to precisely manipulate the mouse genome, and has allowed the production of many knockouts, conditional knockouts and reporter strains. Importantly, the technology provides the means to inactivate genes in a spatial and temporal manner, overcoming problems of embryonic and early postnatal lethality caused by genes which are indispensible for development, and allowing cell lineage or tissue-specific gene functions to be investigated. The system relies on the activity of the 38-kDa site-specific Cre recombinase, encoded by the P1 bacteriophage *Cre* gene, which recognises 34-base pair loxP sites (Hamilton and Abremski, 1984). Cre efficiently catalyses recombination between two loxP sites that are oriented in the same direction to excise the intervening DNA sequence (leaving one loxP site at the site of excision). Therefore, mice carrying conditional knockout alleles of genes, which contain loxP-flanked ('floxed') critical regions, can be crossed with mice carrying Cre under the control of a particular promoter to achieve targeted gene deletion.

For this study *Vangl2*$^{flox/flox}$ mice (a gift from Prof. Deborah Henderson) were bred with *Grhl3*$^{Cre/+}$ mice, which have a Cre-IRES-NLSlacZ cassette inserted into the *Grhl3* locus, making them effectively *Grhl3* heterozygous loss-of-function (Camerer et al., 2010). The breeding strategies described below were used to generate *Grhl3*$^{Cre/+}$*;Vangl2*$^{flox/+}$ conditional embryos, which were *Grhl3* heterozygous due to the presence of the Cre, and mosaically heterozygous for *Vangl2* (*Vangl2*$^{+/-}$ in *Grhl3*-expressing cells but *Vangl2*$^{flox/+}$ elsewhere). It was hypothesised that, if a molecular interaction between the two genes does indeed occur, the conditional embryos would exhibit defects of neural tube closure.

6.2 Results

6.2.1 Generation of conditional *Grhl3$^{Cre/+}$;Vangl2$^{flox/+}$* embryos and negative controls

6.2.1.1 *Grhl3$^{cre/+}$;R26$^{YFP/+}$* X *Vangl2$^{flox/flox}$*

Initially, *Grhl3$^{Cre/+}$* mice were bred with *Rosa26^{YFP}* reporter mice (Srinivas et al., 2001) before being crossed to *Vangl2$^{flox/flox}$* mice, to allow fluorescent labelling of *Grhl3*-expressing cells and their descendents. The breeding strategy and embryonic genotypes are shown in Figure 6.1. Litters were collected at E9-E9.5 and E12.5, embryos were visualised for YFP expression and their phenotype was assessed. Embryos were obtained in the expected Mendelian ratios at both stages collected (Table 6.1).

When characterising the *Grhl3^{Cre}* allele, Camerer et al. described its tissue-specific expression in neurulation-stage embryos carrying a *lacZ* or *Rosa26^{YFP}* reporter allele (Camerer et al., 2010). However when embryos from our *Grhl3$^{cre/+}$;R26$^{YFP/+}$* X *Vangl2$^{flox/flox}$* matings were collected, an unexpected pattern of YFP inheritance was observed. While some embryos did indeed display YFP fluorescence specifically in tissues such as the ventral forebrain, otic vesicles and tail (Figure 6.2C), around half of them instead displayed strong ubiquitous fluorescence (Figure 6.2B). Surprisingly, genotyping assays also revealed that a third of the ubiquitously-labelled embryos were in fact *Cre*-negative (see the summary in Figure 6.2). The phenomenon did not appear to be associated with the sex of the embryo as males and females displayed both types of fluorescence. It also occurred irrespective of which parent had the *Grhl3$^{Cre/+}$;R26$^{YFP/+}$* genotype, thereby ruling out genetic imprinting effects (Figure 6.2).

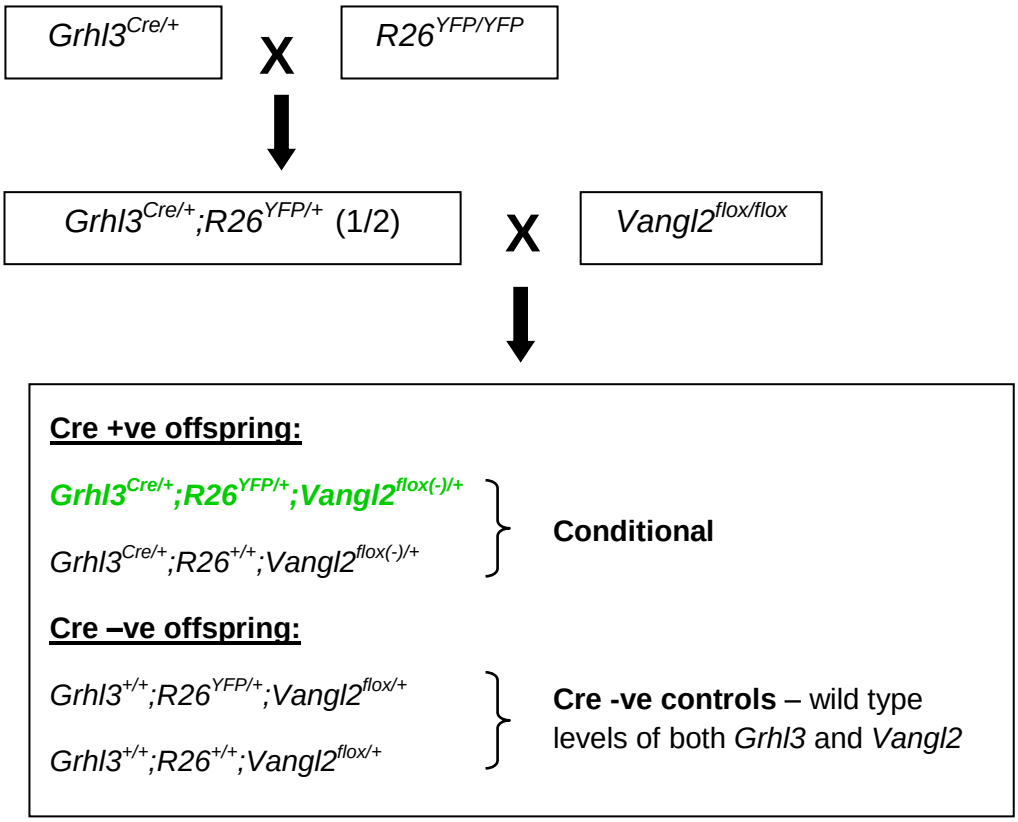

Figure 6.1 Breeding scheme to generate conditional *Grhl3*$^{Cre/+}$;*Vangl2*$^{flox/+}$ embryos

Matings between *Grhl3*$^{Cre/+}$;*R26*$^{YFP/+}$ and *Vangl2*$^{flox/flox}$ mice produce embryos with one of 4 possible genotypes. However, offspring were not genotyped for the presence of the *R26*^{YFP} allele, meaning that embryos were actually assigned to one of the following 3 categories: Fluorescent conditional (green text), non-fluorescent conditional and *Cre*-negative. Numbers in brackets indicate the expected proportion of offspring for each genotype. The 'flox(-)' notation indicates a floxed allele which has been recombined to produce a null allele due to the presence of Cre.

Interestingly, embryos with ubiquitous YFP expression were not obtained from *Grhl3*$^{Cre/+}$ X *R26*$^{YFP/YFP}$ matings (Dawn Savery, personal communication), suggesting that the phenomenon only occurs when the *Grhl3*^{Cre} and *R26*^{YFP} alleles are present in the same parent animal. It also transpired that the *Grhl3*$^{Cre/+}$;*R26*$^{YFP/+}$ animals used to produce experimental litters were in fact the offspring of a further backcross between *Grhl3*$^{Cre/+}$;*R26*$^{YFP/+}$ and *R26*$^{YFP/YFP}$, leading us to hypothesise that we were

observing a multi-generational effect. It was postulated that *Grhl3* is variably expressed in the primordial germ cells (PGCs) and/or gametes, leading to recombination events when *Grhl3*^{Cre} and *R26*^{YFP} are both present. This could ultimately produce experimental embryos with the observed Cre and YFP inheritance patterns (see schematic in Figure 6.3). For the hypothesis to be true, *Grhl3* would have to be expressed at some point during germ cell development or gametogenesis. Although this was not investigated further here, gonads from first generation *Grhl3*$^{Cre/+}$*;R26*$^{YFP/+}$ adult mice (Figure 6.4) and embryos (Nick Greene, personal communication) were indeed found to contain fluorescent tissue.

Genotype Category	E9 - E9.5				E12.5			
	Expected		Observed		Expected		Observed	
	%	Freq.	%	Freq.	%	Freq.	%	Freq.
Conditional **(fluorescent)**	25.00	5/18	44.44	8/18	25.00	7/26	30.77	8/26
Conditional (non-fluor.)	25.00	5/18	16.67	3/18	25.00	7/26	19.23	5/26
Cre -ve controls	50.00	9/18	38.89	7/18	50.00	13/26	50.00	13/26
Deviation from Mendelian ratios:	χ^2=1.416 with 2 degrees of freedom (p = 0.493)				χ^2=0.381 with 2 degrees of freedom (p = 0.826)			

Table 6.1 Genotype frequencies of offspring from *Grhl3*$^{Cre/+}$*;R26*$^{YFP/+}$ X *Vangl2*$^{flox/flox}$ matings

Embryos were collected at E9-E9.5 and E12.5 and genotypes were obtained in the expected Mendelian ratios at both stages (p > 0.49, Chi-square test).

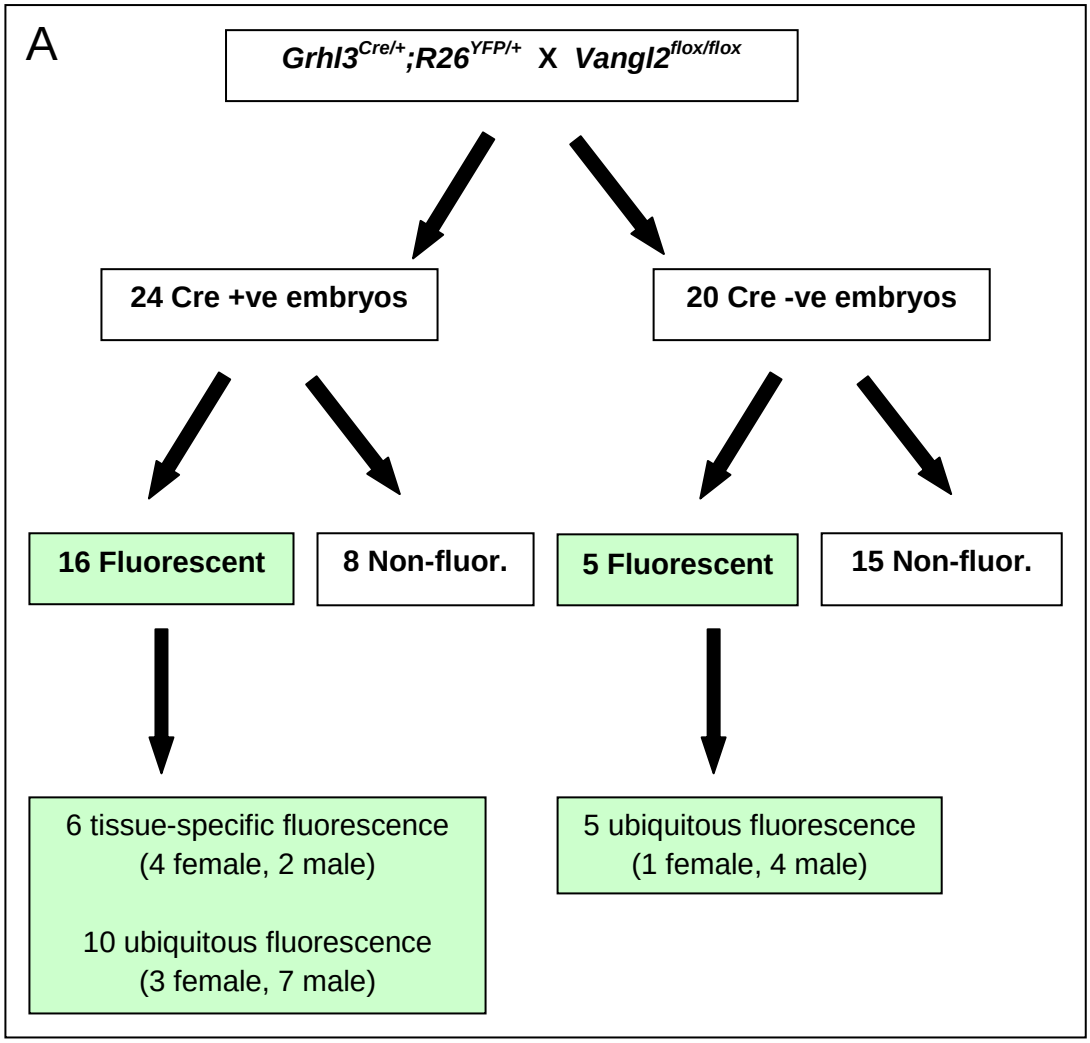

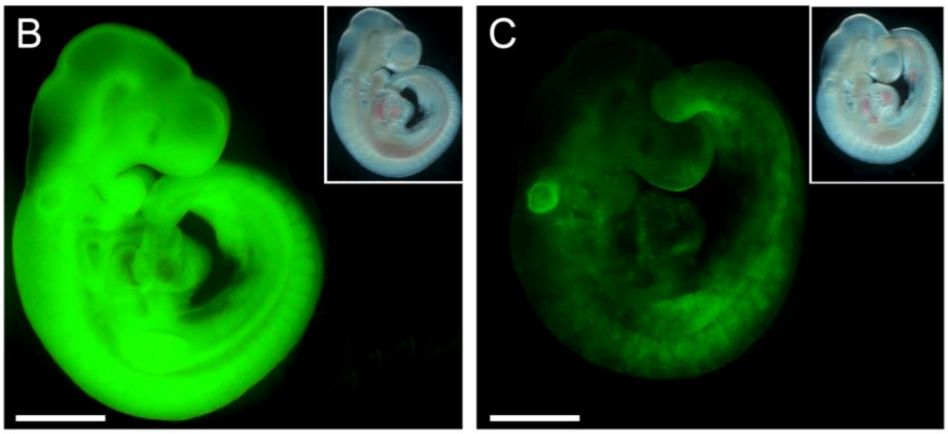

Figure 6.2 Pattern of Cre and YFP inheritance in embryos from *Grhl3*$^{Cre/+}$;*R26*$^{YFP/+}$ X *Vangl2*$^{flox/flox}$ matings

(**A**) Summary of embryos collected (E9-9.5 and E12.5 pooled). (**B, C**) Examples of embryos (with bright field inset) displaying ubiquitous (B) and tissue-specific (C) YFP fluorescence. Scale bars: 500 µm.

Figure 6.3 Multi-generational hypothesis

Schematic to explain the hypothesised multi-generational effect causing the observed YFP distribution in embryos from *Grhl3*$^{Cre/+}$;*R26*$^{YFP/+}$ X *Vangl2*$^{flox/flox}$ matings. Hatched regions indicate Cre expression and green regions indicate YFP expression.

(Generation 1; G1) If *Grhl3* is variably expressed in the PGCs or gametes, then recombination events will occur here in *Grhl3*$^{Cre/+}$;*R26*$^{YFP/+}$ animals, leading to expression of YFP.

(Generation 2; G2) Offspring generated from gametes in which recombination has already occurred will be *Grhl3*$^{Cre/+}$;*R26*$^{YFP/YFP}$ (green text indicates an *R26*^{YFP} allele from which the STOP sequence has been removed in the previous generation).

(Generation 3; G3) Embryos for analysis could therefore display one of five patterns of Cre and YFP inheritance (left to right): 1) Cre-positive, YFP-negative; 2) Cre-positive, tissue-specific YFP; 3) Cre-positive, ubiquitous YFP; 4) Cre-negative, ubiquitous YFP and 5) Cre-negative, YFP-negative.

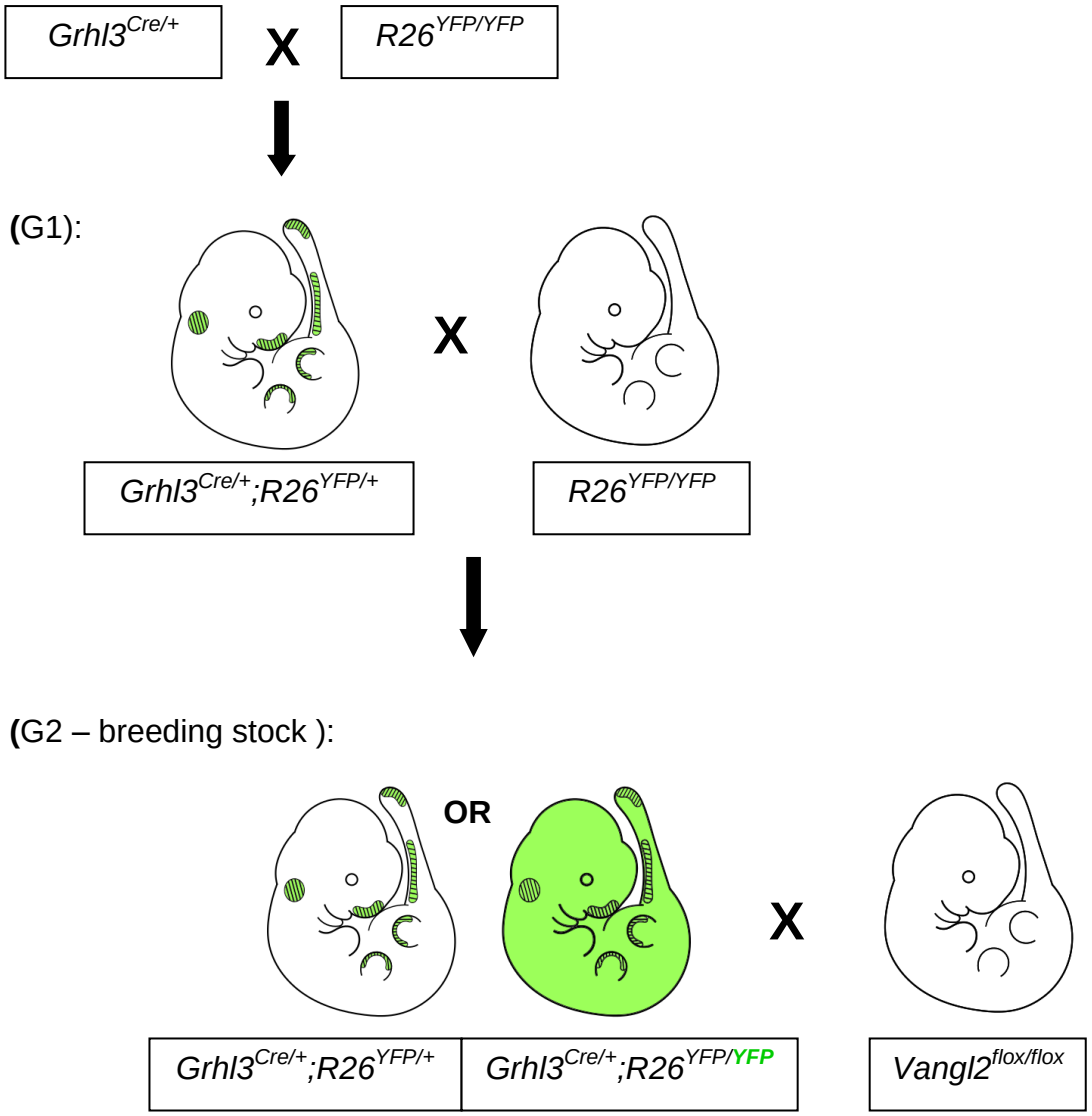
Grhl3Cre/+
X
R26YFP/YFP
(G1):
X
Grhl3Cre/+;R26YFP/+
R26YFP/YFP
(G2 – breeding stock):
OR
X
Grhl3Cre/+;R26YFP/+
Grhl3Cre/+;R26YFP/YFP
Vangl2flox/flox
(G3 – experimental embryos):
Cre-positive
Cre-negative

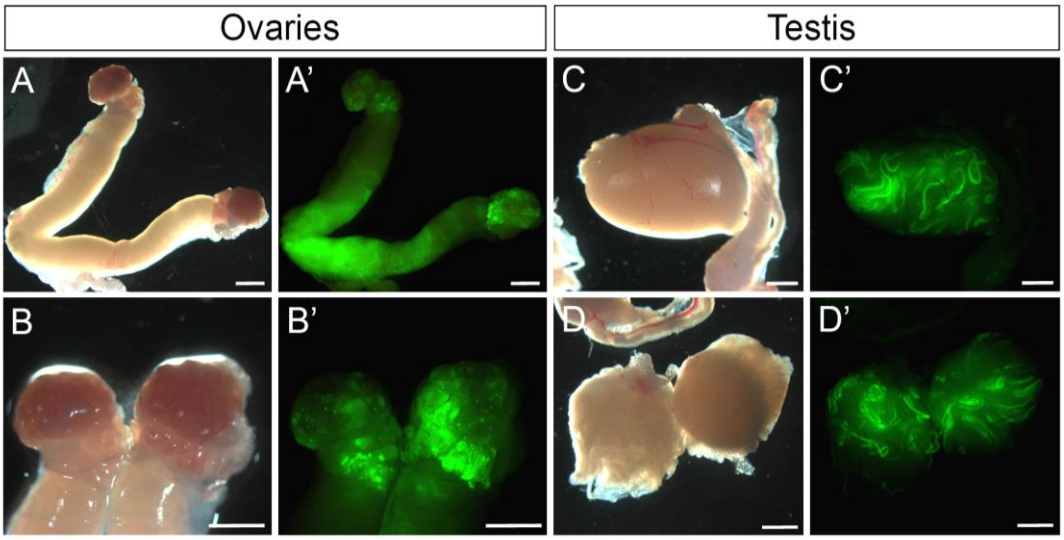

Figure 6.4 Gonads from *Grhl3*$^{Cre/+}$;*R26*$^{YFP/+}$adult mice

(**A-B**) Bright field (A) and fluorescent (A') images of the uterus and ovaries taken from a *Grhl3*$^{Cre/+}$;*R26*$^{YFP/+}$ adult female. YFP-positive tissue can be seen at the base of the uterine horns and within the ovaries (A'). Higher magnification views of the ovaries are shown in B and B'. (**C-D**) Bright field (C) and fluorescent (C') images of a testis taken from a *Grhl3*$^{Cre/+}$;*R26*$^{YFP/+}$ adult male, showing apparent YFP expression within the seminiferous tubules (C). A cross section through the testis is shown in D-D'. Scale bars: 500 µm.

6.2.1.2 *Grhl3*$^{cre/+}$ X *Vangl2*$^{fl/+}$;*R26*$^{YFP/+}$

As an alternative approach, *Grhl3*$^{cre/+}$ X *Vangl2*$^{fl/+}$;*R26*$^{YFP/+}$ matings were also set up (see breeding scheme in Figure 6.5). As the *Grhl3*^{Cre} and *R26*^{YFP} alleles were kept apart in this cross, it was hypothesised that only tissue-specific YFP distribution would be observed in the offspring. This was indeed the case; all fluorescent embryos displayed tissue-specific expression of YFP and no Cre-negative, YFP-positive embryos were obtained, supporting the multigenerational hypothesis. Embryos were collected at E9.5 and E11.5-E12.5 and genotypes were obtained in the expected Mendelian ratios at both stages (Table 6.2).

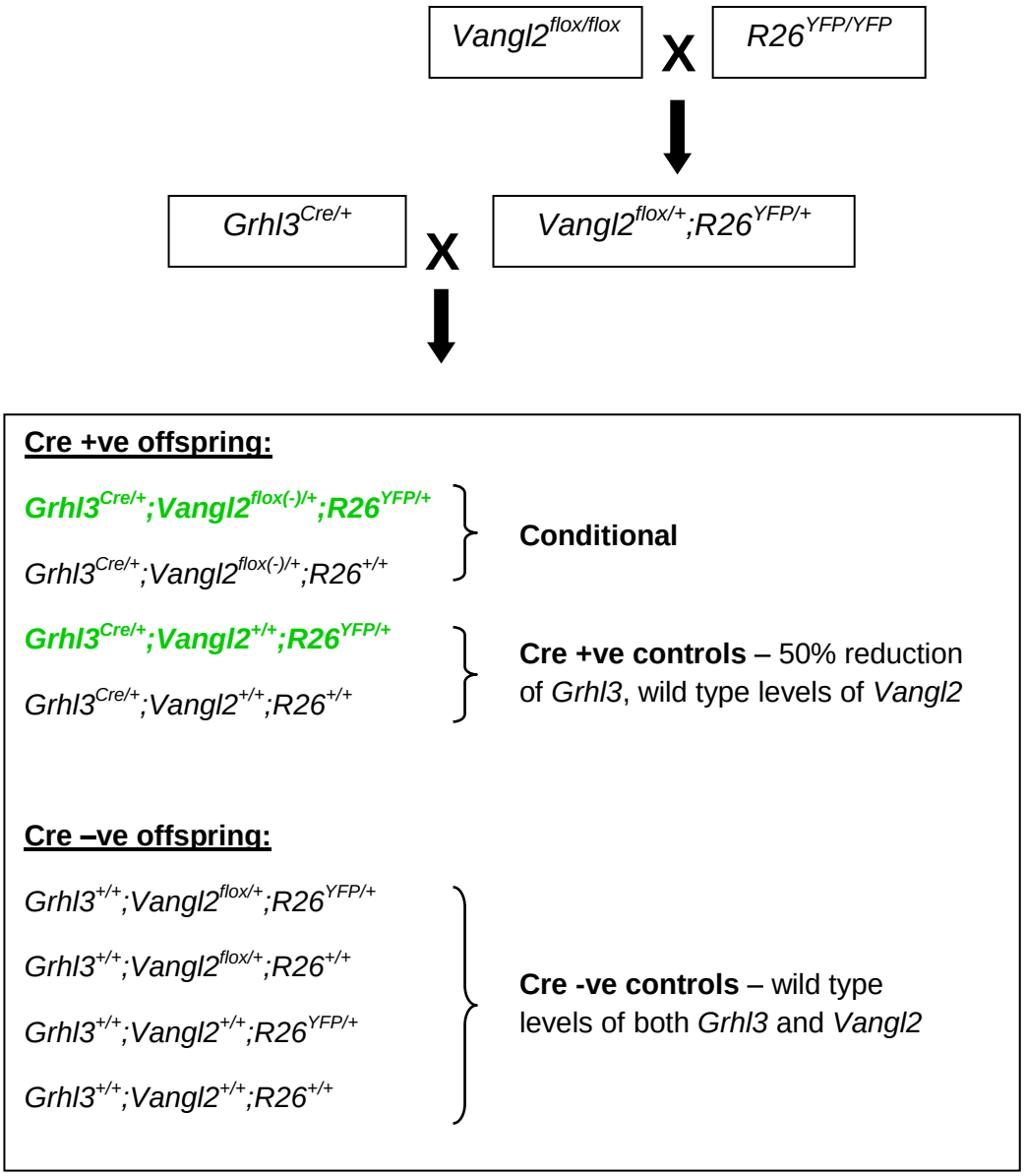

Figure 6.5 Alternative breeding scheme for the generation of *Grhl3$^{Cre/+}$;Vangl2$^{flox/+}$* embryos

Matings between *Grhl3$^{Cre/+}$* and *Vangl2^{flox};R26$^{YFP/+}$* mice produce embryos with one of 8 possible genotypes. However, embryos were not genotyped for the presence of the *R26^{YFP}* allele and *Vangl2* genotyping assays were only performed for Cre-positive offspring, meaning that embryos were actually assigned to one of the following 5 categories: fluorescent conditional (green text), non-fluorescent conditional, fluorescent Cre-positive controls (green text), non-fluorescent Cre-positive controls and Cre-negative controls.

Genotype Category	E9.5				E11.5 - E12.5			
	Expected		Observed		Expected		Observed	
	%	Freq.	%	Freq.	%	Freq.	%	Freq.
Conditional **(fluorescent)**	12.50	4/29	13.79	4/29	12.50	12/97	10.31	10/97
Conditional (non-fluor.)	12.50	4/29	24.14	7/29	12.50	12/97	11.34	11/97
Cre +ve controls **(fluorescent)**	12.50	4/29	10.34	3/29	12.50	12/97	13.31	10/97
Cre +ve controls (non-fluor.)	12.50	4/29	0.00	0/29	12.50	12/97	18.56	18/97
Cre -ve controls	50.00	15/29	51.72	15/29	50.00	49/97	49.48	48/97
Deviation from Mendelian ratios:	χ^2=4.900 with 4 degrees of freedom (p = 0.298)				χ^2=1.617 with 4 degrees of freedom (p = 0.806)			

Table 6.2 Genotype frequencies of offspring from *Grhl3*$^{Cre/+}$ X *Vangl2*$^{flox/+}$;*R26*$^{YFP/+}$ matings

Embryos were collected at E9.5 and E11.5-E12.5 and genotypes were obtained in the expected Mendelian ratios at both stages (p > 0.29, Chi-square test).

Whole *Grhl3*$^{Cre/+}$;*Vangl2*$^{flox(-)/+}$;*R26*$^{YFP/+}$ (conditional) and *Grhl3*$^{Cre/+}$;*Vangl2*$^{+/+}$;*R26*$^{YFP/+}$ (Cre-positive control) embryos were examined for the YFP lineage tracer, to examine the distribution of *Grhl3*-expressing cells and their descendants. No overt difference in the pattern of YFP expression was observed between the two genotypes. Representative examples of fluorescent embryos are shown in Figure 6.6. At E9.5, YFP-positive cells were observed at numerous sites, most notably the ventral forebrain, otic vesicles, limb buds and caudal region. Labelled cells were also distributed more widely throughout the embryo, giving a speckled appearance (Figure 6.6A). Closer examination of the caudal region revealed fluorescent cells ventrally, and extending around the caudal tip (Figure 6.6B), as well as in the neuroepithelium and surface ectoderm more dorsally (Figure 6.6C).

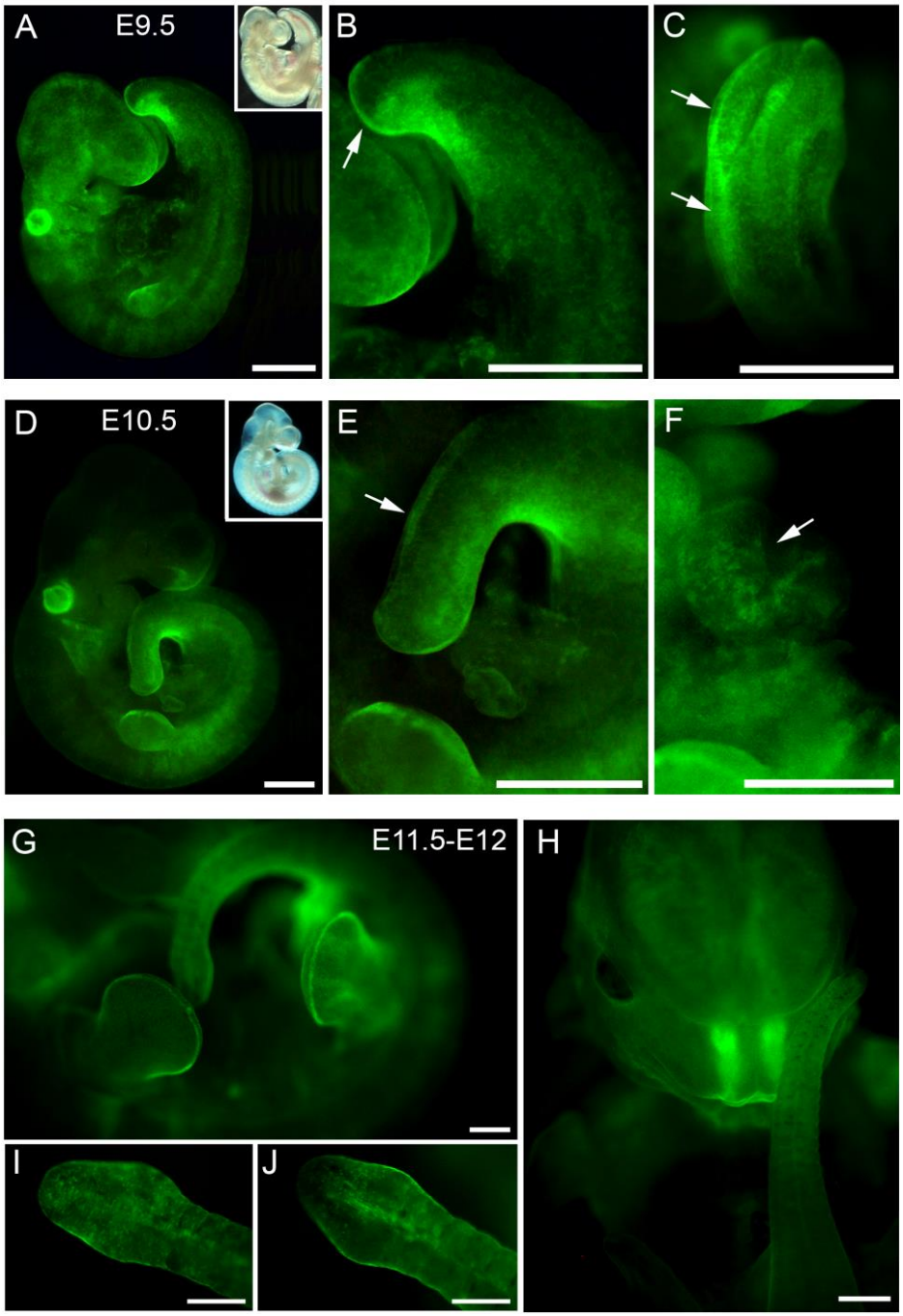

Figure 6.6 YFP expression in embryos from *Grhl3*$^{Cre/+}$ x *Vangl2*$^{flox/+}$;*R26*$^{YFP/+}$ matings

(A-C) At E9.5 strong YFP expression is observed in the forebrain, otic vesicles and limb buds (A). In the caudal region, fluorescent cells are seen ventrally (arrow in B) and dorsally at the level of the PNP (arrows in C). **(D-F)** At E10.5 a similar tissue-specific distribution of YFP-positive cells is observed. A line of fluorescent cells can be seen along the dorsal region of the tail (arrow in E) and a speckled distribution of cells is apparent within the heart (F). **(G-J)** At E11.5-E12 Strong YFP-labelling is seen in the allantois and limb buds (G), the nasal region (H) and within the distal tail (I, J). Scale bars: 500 µm.

At E10.5 expression was also observed within the developing heart (Figure 6.6F). By E11.5-E12, YFP-positive cells could be seen in the allantois and the apical ectodermal ridge (AER) of the limb buds (Figure 6.6G) and in the frontonasal prominence (Figure 6.6H). A speckled distribution was observed in the tailbud at this stage, with labelled cells appearing as a midline streak in some embryos (Figure 6.6I, J).

6.2.1.3 *Grhl3$^{cre/+}$* X *Vangl2$^{fl/fl}$*

In a third cross, conditional embryos (*Grhl3* heterozygote/*Vangl2* conditional heterozygote) were also obtained from matings between *Grhl3$^{Cre/+}$* and *Vangl2$^{flox/flox}$* mice, without the introduction of the *R26^{YFP}* allele (Figure 6.7). Embryos from this cross were harvested at E12-E12.5 and genotypes were obtained in the expected Mendelian ratios (Table 6.3).

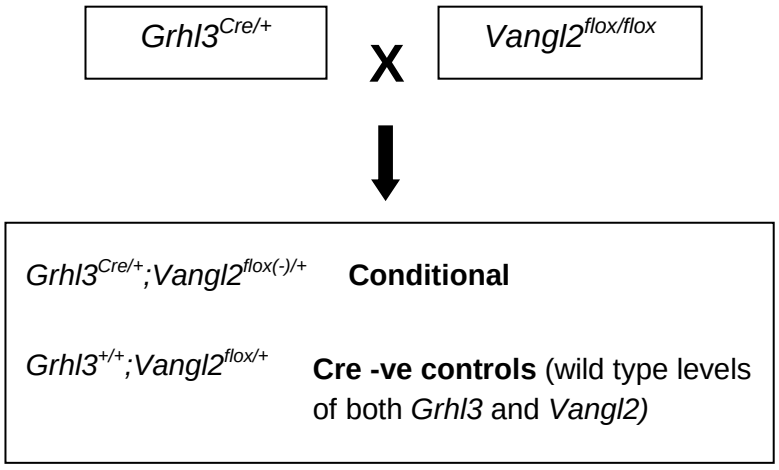

Figure 6.7 Third breeding scheme for the generation of *Grhl3$^{Cre/+}$;Vangl2$^{flox/+}$* embryos

Matings between *Grhl3$^{Cre/+}$* and *Vangl2$^{flox/flox}$* mice produce embryos with one of 2 possible genotypes: conditional and Cre-negative controls.

Genotype	Expected		Observed	
	%	Freq.	%	Freq.
Grhl3$^{Cre/+}$;*Vangl2*$^{flox(-)/+}$	50.00	34/67	46.27	31/67
Grhl3$^{+/+}$;*Vangl2*$^{flox/+}$	50.00	34/67	53.73	36/67
Deviation from Mendelian ratios:	χ^2=0.0684 with 1 degree of freedom (p = 0.794)			

Table 6.3 Genotype frequencies of offspring from *Grhl3*$^{Cre/+}$ X *Vangl2*$^{flox/flox}$ matings

Embryos were collected at E12-E12.5 and genotypes were obtained in the expected Mendelian ratios (p = 0.794, Chi-square test).

6.2.2 Spinal NTDs in conditional embryos

Litters from the three breeding strategies described above were collected at E11.5-E12.5 and embryos were examined for NTDs. Cre-negative embryos (wild type levels of both genes) obtained from each of the three matings were all phenotypically normal with a fully closed neural tube and a straight tail. Similarly, no abnormalities were observed in *Grhl3*$^{Cre/+}$;*Vangl2*$^{+/+}$;*R26*$^{YFP/+}$ or *Grhl3*$^{Cre/+}$;*Vangl2*$^{+/+}$;*R26*$^{+/+}$ 'Cre-positive control' (and therefore *Grhl3* heterozygous) embryos obtained from *Grhl3*$^{Cre/+}$ X *Vangl2*$^{flox/+}$;*R26*$^{YFP/+}$ matings (Table 6.4).

In contrast, a small proportion of conditional *Grhl3*$^{Cre/+}$;*Vangl2*$^{flox/+}$ embryos from each of the three breeding strategies displayed defects of spinal neurulation (Figure 6.8). While the majority (87-95%) were phenotypically normal, tail flexion defects or spina bifida were observed in the remaining embryos. Interestingly, those with tail defects exhibited a 'bent' tail, rather than a 'curly' tail as described in Chapter 3, and of the two cases of spina bifida, one was accompanied by a bent tail and one by a straight tail. Examples of the different caudal phenotypes observed are shown in

Figure 6.8. The frequency of spinal defects in the conditional embryos did not differ significantly between the three breeding strategies used (Table 6.4; p = 0.535, Chi-square test).

Genotype category	Caudal phenotype		
	Straight tail **%** (freq.)	**Tail flexion defects alone** **%** (freq.)	**Spina bifida** **%** (freq.)
1) *Grhl3*$^{Cre/+}$;*R26*$^{YFP/+}$ X *Vangl2*$^{flox/flox}$			
Conditional	**92.31** (12/13)	**0** (0/13)	**7.69** (1/13) (ST)
Cre –ve controls	**100** (13/13)	**0** (0/13)	**0** (0/13)
2) *Grhl3*$^{Cre/+}$ X *Vangl2*$^{flox/+}$; *R26*$^{YFP/+}$			
Conditional	**95.24** (20/21)	**4.76** (1/21) (BT)	**0** (0/21)
Cre +ve controls	**100** (28/28)	**0** (0/28)	**0** (0/28)
Cre -ve controls	**100** (48/48)	**0** (0/48)	**0** (0/48)
3) *Grhl3*$^{Cre/+}$ X *Vangl2*$^{flox/flox}$			
Conditional	**87.10** (27/31)	**9.68** (3/31) (BT)	**3.23** (1/31) (BT)
Cre –ve controls	**100** (36/36)	**0** (0/36)	**0** (0/36)

Table 6.4 Spinal phenotypes observed in E11-E12.5 conditional and control embryos

The percentage and frequency of each phenotype is shown for embryos from each of the three breeding strategies used (numbered 1-3). The proportion of conditional embryos with tail defects and spina bifida does not vary significantly between the three matings (Chi-square test; χ^2=3.136 with 4 degrees of freedom; p = 0.535). Abbreviations: ST = straight tail, BT = bent tail.

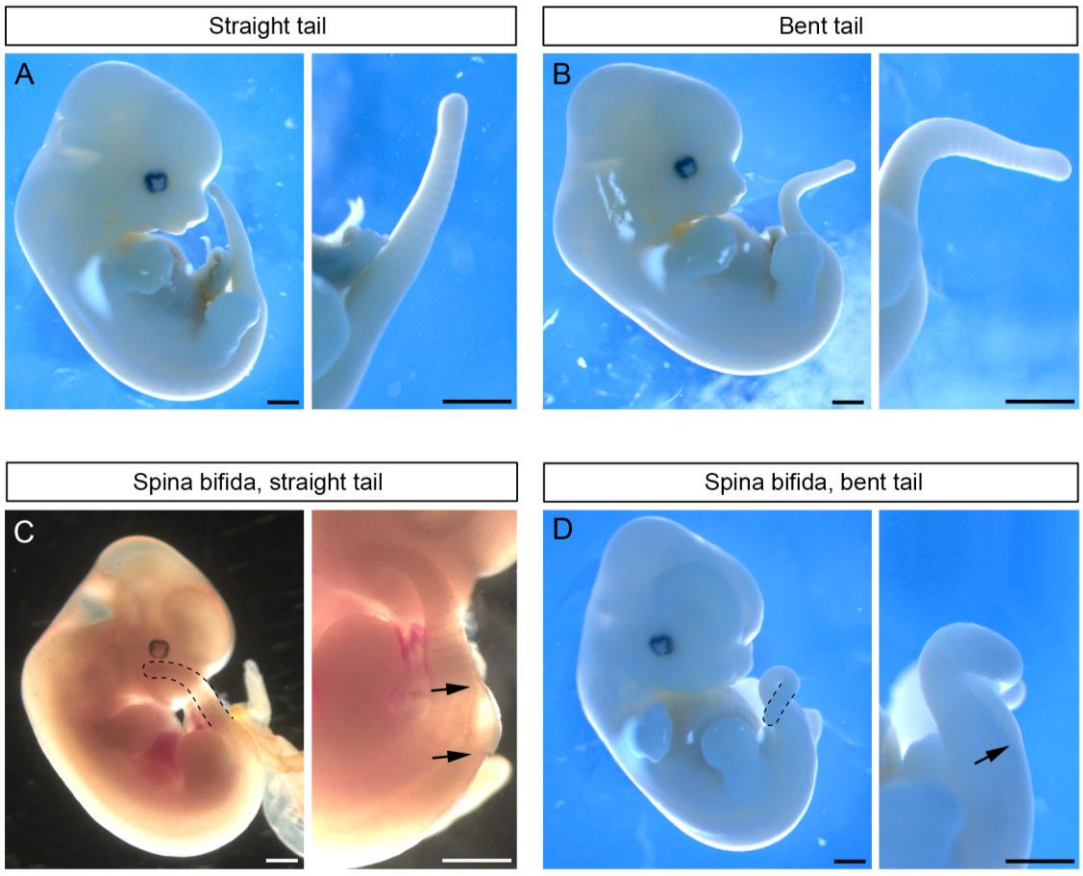

Figure 6.8 *Grhl3*$^{Cre/+}$*;Vangl2*$^{flox/+}$ phenotypes

Examples of the different phenotypes observed in conditional embryos at E11-E12.5. (**A**) Phenotypically normal embryo with a straight tail. (**B-D**) Spectrum of spinal defects observed. Higher magnification views are shown in the right hand panels. Arrows indicate the axial level of the open neural tube. Scale bars: 200 µm.

6.2.3 Generation of *Vangl2*$^{+/-}$*;Grhl3*$^{+/-}$ 'positive controls'

The finding that conditional *Grhl3*$^{Cre/+}$*;Vangl2*$^{flox/+}$ embryos display partially penetrant spinal NTDs indicates that *Grhl3* and *Vangl2* do interact within cells in which they are co-expressed, to affect the outcome of spinal neurulation. To test whether such a mechanism can fully explain the gene interaction (such as that observed in *Vangl2*$^{Lp/+}$*;Grhl3*$^{ct/ct}$ embryos; Chapter 3), compound heterozygous *Grhl3*$^{+/-}$*;Vangl2*$^{+/-}$ embryos, in which one allele of *Vangl2* and *Grhl3* has been lost in all cells, were also generated for analysis.

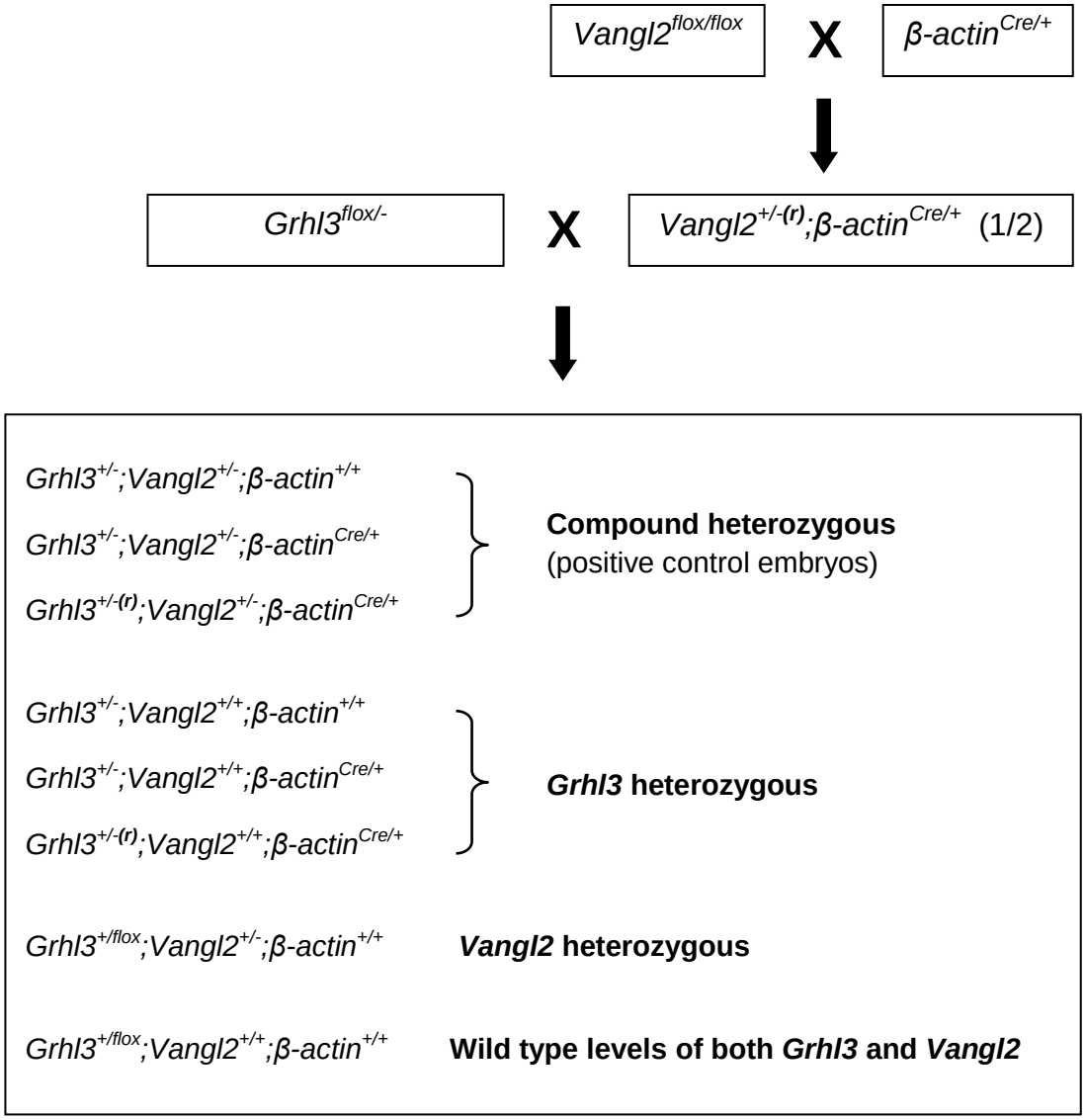

Figure 6.9 Breeding scheme to generate compound heterozygous control embryos

Vangl2$^{flox/flox}$ mice were initially bred with *β-actin*$^{Cre/+}$ mice to produce the null (*Vangl2*$^{-}$) allele. Numbers in brackets indicate the expected proportion of offspring for each genotype. Matings between *Grhl3*$^{flox/-}$ and *Vangl2*$^{+/-}$*;β-actin*$^{Cre/+}$ mice produce embryos with one of 8 possible genotypes. (r) indicates a null allele produced by recombination. Genotyping did not distinguish between the *Grhl3*$^{-}$ and *Grhl*$^{-(r)}$ alleles, meaning that embryos were actually assigned to one of 6 categories (see Table 6.5).

Genotype	E12.5	
	Expected **%** (freq.)	**Observed** **%** (freq.)
Grhl3$^{+/-}$;*Vangl2*$^{+/-}$;*β-actin*$^{+/+}$	**12.50** (19/151)	**15.89** (24/151)
Grhl3$^{+/-}$;*Vangl2*$^{+/-}$;*β-actin*$^{cre/+}$	**25.00** (38/151)	**25.83** (39/151)
Grhl3$^{+/-}$;*Vangl2*$^{+/+}$;*β-actin*$^{+/+}$	**12.50** (19/151)	**10.60** (16/151)
Grhl3$^{+/-}$;*Vangl2*$^{+/+}$;*β-actin*$^{cre/+}$	**25.00** (38/151)	**26.49** (40/151)
Grhl3$^{+/flox}$;*Vangl2*$^{+/-}$;*β-actin*$^{+/+}$	**12.50** (19/151)	**9.93** (15/151)
Grhl3$^{+/flox}$;*Vangl2*$^{+/+}$;*β-actin*$^{+/+}$	**12.50** (19/151)	**11.26** (17/151)
Deviation from Mendelian ratios:	χ^2=1.481 with 5 degrees of freedom (p = 0.915)	

Table 6.5 Genotype frequencies of offspring from *Grhl3*$^{flox/-}$ x *Vangl2*$^{+/-}$;*β-actin*$^{Cre/+}$ matings

Genotypes were obtained in the expected Mendelian ratios (Chi-square test).

It was reasoned that, if the incidence of NTDs in *Grhl3*$^{+/-}$;*Vangl2*$^{+/-}$ embryos was found to be no higher than in *Grhl3*$^{Cre/+}$;*Vangl2*$^{flox/+}$, it would suggest that an interaction between *Grhl3* and *Vangl2* during neurulation can be fully explained by a cellular/molecular interaction within the same tissue(s). On the other hand, if *Grhl3*$^{+/-}$;*Vangl2*$^{+/-}$ embryos develop NTDs at a significantly higher frequency it would point to an additional contribution from another mechanism, such as the summation of distinct effects in more than one tissue. The breeding strategy described in Figure 6.9 was used to generate *Grhl3*$^{+/-}$;*Vangl2*$^{+/-}$ embryos for analysis. Litters were collected at E12.5 and genotypes were obtained in the expected Mendelian ratios (Table 6.5).

6.2.4 Spinal NTDs in *Grhl3*$^{+/-}$;*Vangl2*$^{+/-}$ embryos

As expected, spinal abnormalities were observed in a proportion of compound heterozygous embryos. The presence of the *β-actin*^{Cre} allele, which was not bred out due to time constraints, did not affect the incidence of NTDs: both *Grhl3*$^{+/-}$;*Vangl2*$^{+/-}$;*β-actin*$^{+/+}$ and *Grhl3*$^{+/-}$;*Vangl2*$^{+/-}$;*β-actin*$^{Cre/+}$ embryos developed normally in 69-75% of cases, while the remaining proportion displayed tail flexion defects alone or with spina bifida (Table 6.6). Among the embryos affected by spina bifida, 4/7 had a bent tail while 3/7 developed a more tightly curled tail similar to that seen in *Vangl2*$^{Lp/+}$;*Grhl3*$^{ct/ct}$ embryos (Chapter 3). Embryos of all other genotypes (*Grhl3* heterozygous, *Vangl2* heterozygous and those with wild type levels of both genes) developed normally (Table 6.6).

Genotype	Caudal phenotype		
	Straight tail **%** (freq.)	**Tail flexion defects alone** **%** (freq.)	**Spina bifida** **%** (freq.)
Grhl3$^{+/-}$;*Vangl2*$^{+/-}$;*β-actin*$^{+/+}$	**75.00** (18/24)	**16.67** (4/24)	**8.33** (2/24) (1BT, 1CT)
Grhl3$^{+/-}$;*Vangl2*$^{+/-}$;*β-actin*$^{cre/+}$	**69.23** (27/39)	**17.95** (7/39)	**12.82** (5/39) (3BT, 2CT)
Grhl3$^{+/-}$;*Vangl2*$^{+/+}$;*β-actin*$^{+/+}$	**100** (16/16)	**0** (0/16)	**0** (0/16)
Grhl3$^{+/-}$;*Vangl2*$^{+/+}$;*β-actin*$^{cre/+}$	**100** (40/40)	**0** (0/40)	**0** (0/40)
Grhl3$^{+/flox}$;*Vangl2*$^{+/-}$;*β-actin*$^{+/+}$	**100** (15/15)	**0** (0/15)	**0** (0/15)
Grhl3$^{+/flox}$;*Vangl2*$^{+/+}$;*β-actin*$^{+/+}$	**100** (17/17)	**0** (0/17)	**0** (0/17)

Table 6.6 Spinal phenotypes observed in E12.5 compound heterozygous and control embryos

The presence of the *β-actin*^{Cre} allele does not affect the frequency of defects in compound heterozygous embryos, shown in rows 1 and 2 (Chi-square test; χ^2=0.352 with 2 degrees of freedom; p = 0.838). Abbreviations: BT = bent tail, CT = curly tail.

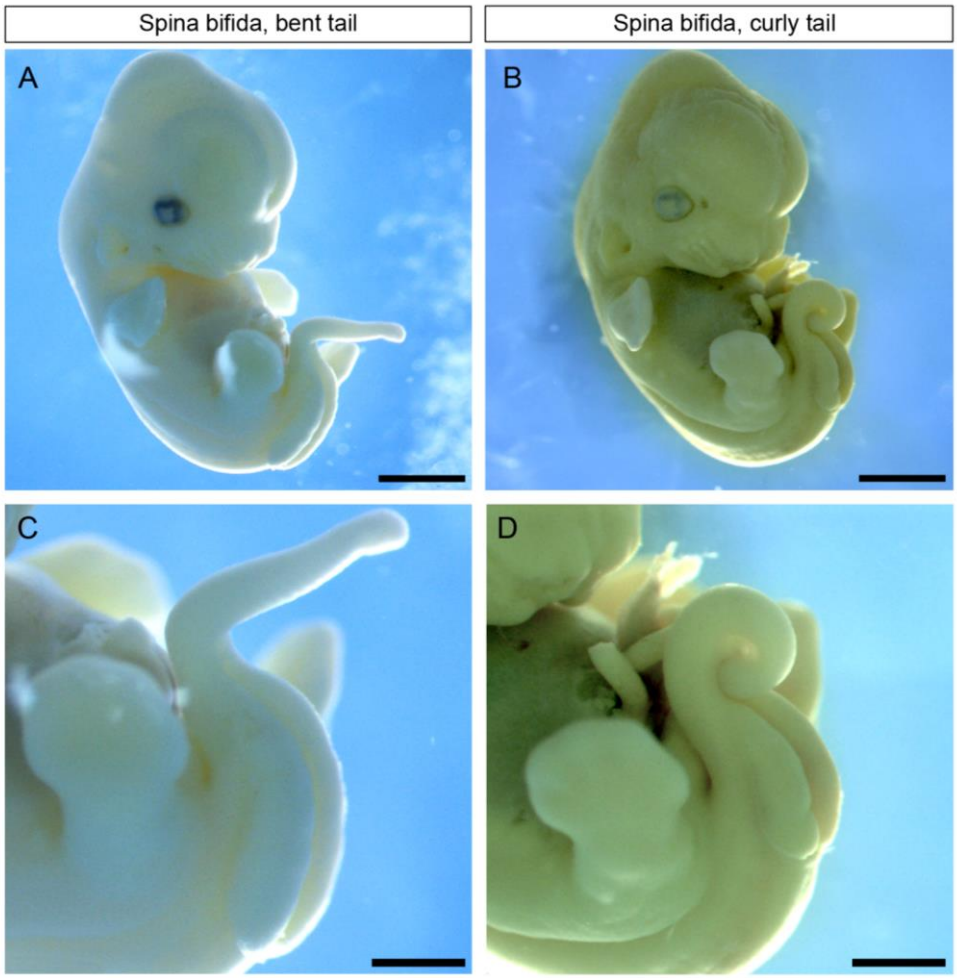

Figure 6.10 Spina bifida in *Grhl3*$^{+/-}$;*Vangl2*$^{+/-}$ embryos

Examples of the different phenotypes observed in compound heterozygous embryos at E12.5. **(A)** Embryo with spina bifida and a bent tail. **(B)** Embryo with spina bifida and a curled tail. Higher magnification views are shown in C and D. Scale bars: 500 µm (A-B) and 250 µm (C-D).

6.2.5 Summary of spinal NTD data

Having established that the NTD prevalence in *Grhl3*$^{Cre/+}$;*Vangl2*$^{flox/+}$ was not affected by the breeding strategy used (Table 6.4), and that the incidence of defects in *Grhl3*$^{+/-}$;*Vangl2*$^{+/-}$ was not affected by the presence of the *β-actin*^{cre} allele (Table 6.6), data from embryos of the same genotype were pooled. As in Chapter 3, spina bifida cases were also categorised by severity according to the axial level of the open region.

Genotype	Caudal phenotype			
	Straight tail **%** (freq.)	**Tail flexion defects alone** **%** (freq.)	**Small spina bifida** **%** (freq.)	**Large spina bifida** **%** (freq.)
Negative control pooled (*Grhl3*$^{+/+}$;*Vangl2*$^{flox/+}$ or *Grhl3*$^{+/+}$;*Vangl2*$^{+/+}$)	**100** (97/97)	**0** (0/97)	**0** (0/97)	**0** (0/97)
Conditional pooled (*Grhl3*$^{Cre/+}$;*Vangl2*$^{flox/+}$)	**90.77** (59/65)	**6.15** (4/65)	**3.08** (2/65)	**0.00** (0/65)
Compound heterozygous pooled (*Grhl3*$^{+/-}$;*Vangl2*$^{+/-}$)	**71.43** (45/63)	**17.46** (11/63)	**0.00** (0/63)	**11.11** (7/63)

Table 6.7 Summary of NTD frequencies

The phenotypic proportions observed in *Grhl3*$^{Cre/+}$;*Vangl2*$^{flox/+}$ differ significantly from those in *Grhl3*$^{+/-}$;*Vangl2*$^{+/-}$ (Chi-square test; χ^2=14.123 with 3 degrees of freedom; p = 0.003).

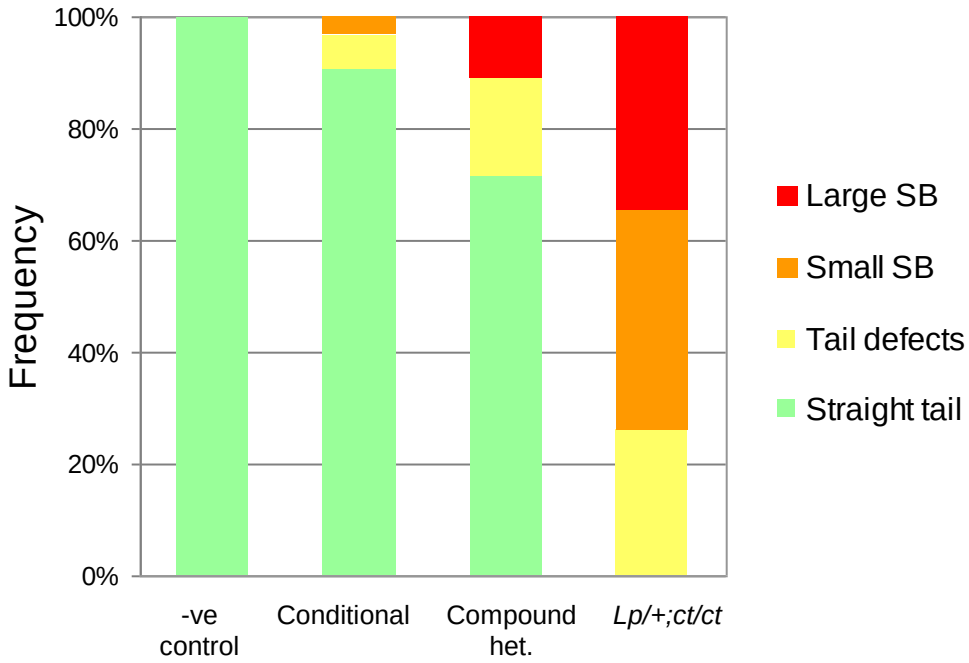

Figure 6.11 Graphical summary of NTD frequencies at E11-E12.5

Graph illustrating a significantly more severe phenotype in *Grhl3*$^{+/-}$;*Vangl2*$^{+/-}$ (compound het.) embryos than in *Grhl3*$^{Cre/+}$;*Vangl2*$^{flox/+}$ (conditional). The NTD frequency in *Vangl2*$^{Lp/+}$;*Grhl3*$^{ct/ct}$ (Chapter 3) is also included for comparison.

Overall, 28% of compound heterozygous *Grhl3*$^{+/-}$;*Vangl2*$^{+/-}$ embryos displayed a spinal neurulation defect, compared with only 9% of conditional *Grhl3*$^{Cre/+}$;*Vangl2*$^{flox/+}$ embryos. Hence, there was a three-fold increase in defect frequency in compound heterozygotes compared with conditional embryos (Table 6.7). Of the spina bifida cases recorded, *Grhl3*$^{+/-}$;*Vangl2*$^{+/-}$ displayed increased axial severity compared to *Grhl3*$^{Cre/+}$;*Vangl2*$^{flox/+}$ (Figure 6.11).

6.2.6 Cranial NTDs

One exencephalic *Grhl3*$^{+/-}$;*Vangl2*$^{+/-}$ embryo was recorded (1.59%), while no cranial defects were observed in conditional *Grhl3*$^{Cre/+}$;*Vangl2*$^{flox/+}$ embryos or in any other control genotypes.

6.3 Discussion

This chapter aims to investigate the interaction between *Vangl2* and *Grhl3* during neurulation using a conditional genetic approach. Spinal defects (tail defects and/or spina bifida) were observed in nearly 10% of conditional *Grhl3*$^{Cre/+}$;*Vangl2*$^{flox/+}$ embryos, demonstrating that when embryos are heterozygous for *Grhl3* with the additional loss of one *Vangl2* allele in *Grhl3*-expressing cells, neurulation is compromised. Compound heterozygous *Grhl3*$^{+/-}$;*Vangl2*$^{+/-}$ embryos were more severely affected, developing abnormalities in around 30% of cases. These experiments suggest that a molecular interaction in the same population of cells only partially accounts for the phenotype observed when both genes are mutated.

Defects were not observed in *Vangl2* heterozygotes (*Vangl2*$^{+/-}$; Table 6.6), consistent with a report by Song et al., in which embryos heterozygous for a *Vangl2* null allele (*Vangl2*$^{\Delta/+}$) have normal, straight tails (Song et al., 2010). However, a more recent study found that 11% of mice carrying one copy of another null allele (*Vangl2*$^{\Delta TMs/+}$) display a looped or kinked tail (Yin et al., 2012). *Grhl3* heterozygotes were found to be normal here (Table 6.6), as previously reported (Caddy et al., 2010). Importantly, Cre-positive control embryos were also phenotypically normal, confirming the finding by Camerer et al. that the *Grhl3*^{Cre} allele has no deleterious effect on neurulation in the absence of a relevant floxed allele (Camerer et al., 2010). No NTDs were observed in embryos with wild type levels of both *Vangl2* and *Grhl3*.

The data in this Chapter support the findings in Chapters 4 and 5, which suggest that in *Vangl2*$^{Lp/+}$;*Grhl3*$^{ct/ct}$ embryos there are two different effects underlying the NTD phenotype: (1) cell autonomous effects of the mutated forms of *Vangl2* and *Grhl3* in the same cells and (2) non-cell autonomous effects due to the activities of

Vangl2 and *Grhl3* in different tissues. As discussed in Chapter 5, it will be important to accurately determine the spatiotemporal co-expression of the two proteins within the caudal tissues of the embryo. The dynamic nature of *Grhl3* expression also suggests that the *Vangl2*^{flox} allele could be recombined in descendants of *Grhl3*-expressing cells prior to neurulation, and/or in regions where *Grhl3* is no longer being transcribed. A thorough analysis of *Grhl3* and *Vangl2* expression at earlier embryonic stages would help to explore this further.

6.3.1 Why the variable effects of different *Vangl2* and *Grhl3* mutant alleles?

The frequencies of NTDs in conditional *Grhl3*$^{Cre/+}$;*Vangl2*$^{flox/+}$ and compound heterozygous *Grhl3*$^{+/-}$;*Vangl2*$^{+/-}$ embryos are both considerably lower than in *Vangl2*$^{Lp/+}$;*Grhl3*$^{ct/ct}$ (Figure 6.11) or indeed than in *Vangl2*$^{Lp/+}$;*Grhl3*$^{ct/+}$ (see Chapter 3). When designing the current breeding schemes, a partially penetrant NTD phenotype was predicted in *Grhl3*$^{+/-}$;*Vangl2*$^{+/-}$ embryos, based on the observation that *Vangl2*$^{Lp/+}$;*Grhl3*$^{+/-}$ embryos display spina bifida at a frequency of 67% (Caddy et al., 2010). However, the incidence of spina bifida observed here (11%) is mild in comparison. These observations raise the question of why mice carrying the *Vangl2*^{Lp} allele are more predisposed to NTDs than those with a *Vangl2*$^{-}$ (null) allele.

6.3.1.1 Does *Vangl2*^{Lp} exert a dominant negative effect?

Recent comparisons between the phenotypes of *loop-tail* mutants and *Vangl2* knockout embryos have demonstrated that *loop-tail* is, in fact, a dominant negative allele. A *Vangl2* null allele (*Vangl2*$^{\Delta}$) was previously generated by deleting exons four and five, a region which includes the four Vangl2 transmembrane domains. The authors of this study found that, compared with *Vangl2*^{Lp}, the *Vangl2*$^{\Delta}$ allele had a weaker phenotypic impact: all *Vangl2*$^{Lp/+}$ mice developed tail defects while 99% of

Vangl2$^{\Delta/+}$ mice were normal and, while many *Vangl2*$^{Lp/+}$ females were infertile due to an imperforate vagina, all *Vangl2*$^{\Delta/+}$ were fertile. *Vangl2*^{Lp} also had a stronger effect in combination with a *Vangl1* gene-trap allele, with an exacerbation of cochlea polarity defects observed in *Vangl2*$^{Lp/Lp}$ and *Vangl2*$^{Lp/+}$;*Vangl1*$^{gt/gt}$, compared to *Vangl2*$^{\Delta/\Delta}$ and *Vangl2*$^{\Delta/+}$;*Vangl1*$^{gt/gt}$, respectively (Song et al., 2010). *Vangl2*$^{\Delta/+}$;*Vangl1*$^{gt/+}$ were otherwise morphologically normal, which contrasts with the craniorachischisis reported in a proportion of *Vangl2*$^{Lp/+}$;*Vangl1*$^{gt/+}$ embryos (Torban et al., 2008).

A similar effect was recently reported in embryos carrying an independent *Vangl2* null allele (*Vangl2*$^{\Delta TMs}$) (Yin et al., 2012). While *Vangl2*$^{Lp/Lp}$ mutants develop craniorachischisis with 100% penetrance, only 74% of *Vangl2*$^{\Delta TMs/\Delta TMs}$ animals exhibited this severe neural tube defect, with the remaining 26% displaying a milder spina bifida phenotype. Similarly, only 11% of *Vangl2*$^{\Delta TMs/+}$ mice showed tail defects, a characteristic feature of the majority of *Vangl2*$^{Lp/+}$ animals. When the polarity of hair cells in the developing inner ear was examined, more severe phenotypes were observed in *Vangl2*$^{\Delta TMs/Lp}$ compound mutants than in *Vangl2*$^{\Delta TMs/\Delta TMs}$ embryos. Together, these findings indicate that the presence of the *Lp* mutant protein has a greater effect than the loss of wild-type Vangl2.

The *Lp* mutation has previously been shown to disrupt Vangl2 protein trafficking from the endoplasmic reticulum to the plasma membrane (Merte et al., 2010). One possible molecular explanation for the *loop-tail* dominant effect is that disrupted Vangl2^{Lp} protein trafficking also affects the cellular distribution of other PCP proteins, leading to an overall reduction in planar polarity. Indeed, both *in vitro* and *in vivo* experiments indicate that the presence of the Vangl2^{Lp} protein alters the normal localisation of wild type Vangl2, Vangl1 and the putative Vangl2-interacting protein, Prickle-like2 (Yin et al., 2012). Moreover, phosphorylation of wild type

Vangl2, which is required for its function, was reduced when it was co-expressed with Vangl2^{Lp} *in vitro* (Gao et al., 2011). Hence, the *loop-tail* mutation may disturb PCP signalling through an adverse effect on wild type Vangl2 and several key interacting proteins, producing a more profound disturbance than loss of Vangl2 alone.

6.3.1.2 *Grhl3^{ct}* versus *Grhl3^{-}*

Conversely, the low-frequency NTDs in homozygous *curly tail* (*Grhl3$^{ct/ct}$*) embryos represent a milder phenotype than the fully penetrant spina bifida observed in homozygous *Grhl3* null mice (Ting et al., 2003a; Van Straaten and Copp, 2001; Yu et al., 2006). Genetic complementation studies have also shown the incidence of spina bifida to be 31% in *Grhl3$^{-/ct}$* embryos, compared to 12% in *Grhl3$^{ct/ct}$* (Ting et al., 2003a; Van Straaten and Copp, 2001). These alleles result in different levels of gene expression; *Grhl3* mRNA is reportedly absent in null (-/-) mice (Ting et al., 2003a; Yu et al., 2006), which contrasts with the hypomorphic nature of the *Grhl3^{ct}* allele (see Chapter 5) (Gustavsson et al., 2007; Ting et al., 2003a).

As described in Chapter 1, genetic modifier loci are present within the background of the *curly tail* strain. However, non-specific modifier effects are unlikely to account for the variation in NTD prevalence observed between *Grhl3$^{Cre/+}$;Vangl2$^{flox/+}$* and *Grhl3$^{+/-}$;Vangl2$^{+/-}$* embryos as, here, the differences in genetic background are predicted to be minimal: The *Grhl3$^{Cre/+}$*, *R26$^{YFP/YFP}$* and *Vangl2$^{flox/flox}$* mouse strains were all maintained on a C57BL/6J background for generation of conditional embryos, as were the *β-actin$^{Cre/+}$ and Grhl3$^{flox/-}$* animals used to produce compound heterozygotes.

6.3.2 Development of tail defects

Although it has been established that spina bifida and tail flexion defects are alternative outcomes of delayed PNP closure, the mechanism by which the tail curls or bends dorsally is not well understood. An early study showed that, although the neural tube is fully closed in embryos with tail flexion defects alone, this region is morphologically abnormal: the neural tube is positioned above the somites rather than lying between them, possibly due to mechanical stress imposed by the persistently open neural folds (Copp et al., 1982). Interestingly, the curled region of the tail is actually formed during secondary neurulation, suggesting that there could be defects in the transition from primary to secondary neurulation. In *curly tail* embryos tail defects are strongly, but not absolutely, associated with spina bifida, demonstrating that the two phenotypes are occasionally uncoupled (Van Straaten and Copp, 2001). It would be interesting to investigate whether the development of tail defects in *curly tail* embryos is linked to the expression of *Grhl3* in the tailbud.

The relationship between spina bifida and tail defects appears to differ between the strains examined here: in *Vangl2*$^{Lp/+}$*;Grhl3*$^{ct/ct}$ embryos spina bifida was always accompanied by a curled tail (Chapter 3), while the *Grhl3*$^{Cre/+}$*;Vangl2*$^{flox/+}$ and *Grhl3*$^{+/-}$*;Vangl2*$^{+/-}$ embryos with spina bifida exhibited either a straight, curled or more sharply bent tail (Figure 6.8, Figure 6.10). These findings are reminiscent of previous observations that a proportion of transgenic *curly tail* embryos, which over-express *Grhl3* from a BAC (*ct*^{TgGrhl3}/*ct*^{TgGrhl3}), display spina bifida with a straight rather than a curled tail (Sandra C.P. de Castro, unpublished data). Together these data suggest that there may be different mechanisms underlying the NTDs in different *Grhl3*-mutant strains.

6.3.3 Additional roles of *Grhl3*?

As described in Chapter 5, *Grhl3* transcripts are present at various embryonic sites during neurulation, including the forebrain, caudal neural plate, tail bud and hindgut. In *Grhl3*$^{Cre/+}$;*R26*$^{YFP/+}$ embryos, YFP-positive cells are also observed in regions such as the otic vesicles and limb-buds, and they appear to be more widely distributed throughout the embryo, giving a overall speckled appearance. This pattern of labelled cells suggests that there could be, or have previously been, low level expression of *Grhl3* at additional sites during development, perhaps below the level that would be detected by WISH. Alternatively, the speckled distribution could reflect a very early recombination event, for example in a few cells of the inner cell mass (ICM), which could lead to the observed mosaic pattern of fluorescence. To address these possibilities, it would be interesting to examine YFP expression in early *Grhl3*$^{Cre/+}$;*R26*$^{YFP/+}$ embryos, in combination with detailed WISH or IHC studies of *Grhl3* expression dynamics.

Additionally, the multigenerational pattern of YFP inheritance (see Figure 6.3) and the expression of YFP in the gonads of *Grhl3*$^{Cre/+}$;*R26*$^{YFP/+}$ adult mice (Figure 6.4) suggest that *Grhl3* is activated in the germ cell precursors (PGCs) and/or gametes. In the mouse embryo, PGCs arise in the posterior primitive streak at E7.5, from where they migrate into the adjacent endoderm (future hindgut). By E8.5 they are highly motile and migrate along the hindgut as it extends anteriorly. Between E9.5-E10.5 germ cells exit the hindgut tissue and migrate dorsally, then bilaterally towards the genital ridges, the mesodermal precursors to the gonads. By E11.5, the majority of PGCs have reached the genital ridges where they undergo extensive reprogramming and associate with somatic cells during gonad formation (Molyneaux et al., 2001; Richardson and Lehmann, 2010).

A potential role for *Grhl3* in germ cell development is interesting and warrants further investigation. Although this was beyond the scope of the current project, our group is currently examining *Grhl3* expression during gonad development in collaboration with members of Dr Andrew Greenfield's laboratory (MRC Harwell). So far, YFP-positive cells have been identified in the developing gonads of both male and female *Grhl3*$^{Cre/+}$*;R26*$^{YFP/+}$ adult mice (Figure 6.4) and in embryos at E14.5 (Nick Greene, personal communication). Whether *Grhl3* is required for PGC migration, differentiation, or later during oogenesis and spermatogenesis, remains to be determined.

7. PCP and neural crest cell migration

7.1 Introduction

The signals and pathways known to regulate neural crest (NC) cell migration are described in Chapter 1. Most of these molecules act as inhibitory cues, preventing the NC from entering prohibited areas while allowing them to populate permissive zones. However, while such factors can explain how the segmented pattern of NC migration is achieved, they do not explain how the persistent directionality of their migration is controlled. In recent years, studies of the molecular mechanisms that control this directional migration in *Xenopus* and zebrafish embryos have demonstrated an essential role for the non-canonical Wnt/PCP signalling pathway.

7.1.1 PCP signalling regulates *Xenopus* and zebrafish neural crest migration

In *Xenopus* embryos, the expression of mutant PCP pathway components has been shown to 'dramatically' inhibit the migration of cranial NC cells (De Calisto et al., 2005). De Calisto et al. injected two-cell-stage embryos with mutated *Dishevelled* constructs (*Dsh-DEP*+ or *Dsh-*Δ*N*) that specifically interfere with Wnt/PCP signalling, without affecting the canonical pathway (Tada and Smith, 2000). Injected embryos displayed greatly reduced cranial NC migration, while NC induction appeared normal. The same effect on migration was seen when *Dsh-DEP*+ expressing NC cells were transplanted to an uninjected host embryo, suggesting that the PCP pathway works in a cell-autonomous manner (Figure 7.1A, B). This phenotype was also observed after disrupting the activity of the PCP ligand *Wnt11*, by injecting either *Wnt11* itself, or its dominant negative mRNA (*dnWnt11*). *Xenopus Wnt11* is expressed just ahead of the laterally migrating NC cells, while the *Frizzled7* (*Fz7*) receptor is expressed in the pre-migratory and migrating NC themselves. It was observed that early NC cells move beneath the *Wnt11*-expressing cells as they migrate, leading the authors of this study to propose that NC cells are attracted to regions with high *Wnt11* activity, before

making way for later-migrating cells (De Calisto et al., 2005). In zebrafish embryos, similar NC migration defects have been reported in the trunk after injection of mutant *Dishevelled* (*Dsh-DEP+)* or *Wnt5* morpholino, and in the *trilobite* (*Stbm/Vangl2*) mutant (Figure 7.1E-H) (Matthews et al., 2008).

7.1.2 Mechanism of PCP signalling in the neural crest

When *Xenopus* NC cells are cultured *in vitro*, the migration of those explanted from PCP-mutant embryos is strongly inhibited (Figure 7.1C, D), as *in vivo*. At a cellular level, PCP signalling is required to stabilise the production of polarised cell protrusions in leading edge NC cells; control cells extend large lamellipodia towards the front, while PCP-mutant cells display fewer, less stable, protrusions (De Calisto et al., 2005).

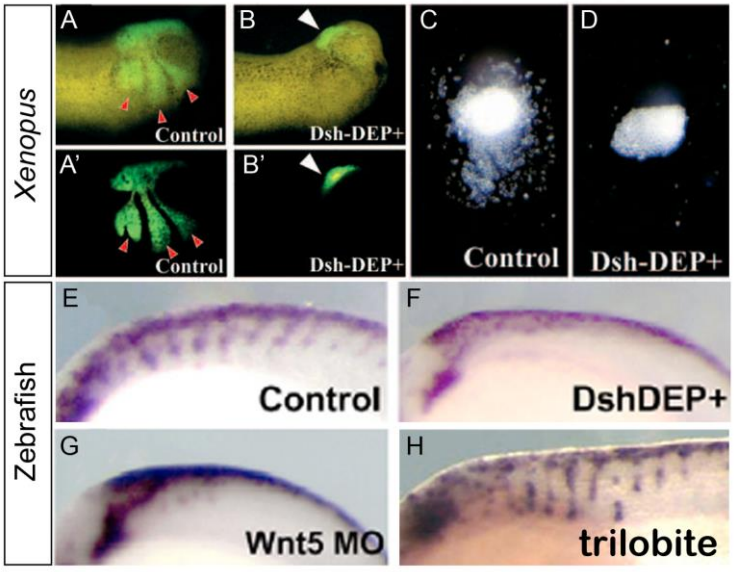

Figure 7.1 PCP signalling is required for neural crest migration in *Xenopus* and zebrafish

(**A**) Control *Xenopus* embryo following transplantation of fluorescein dextran (FDX)-labelled cranial NC cells. (**B**) Embryo grafted with NC from an embryo expressing Dsh-DEP+. (**C,D**) Culture of NC explants taken from control (C) and Dsh-DEP+ injected (D) embryos. (**E-H**) Zebrafish trunk NC migration in control and PCP-mutant embryos. Images taken from (De Calisto et al., 2005) (A-D) and (Matthews et al., 2008) (E-H).

More recently it was reported that *Xenopus* and zebrafish NC cells achieve directional migration via contact inhibition of locomotion (CIL) (Carmona-Fontaine et al., 2008b), a phenomenon that was originally discovered around 60 years ago and describes how fibroblast cells *in vitro* 'cease to continue moving in the same direction after contact with another cell' (Abercrombie and Heaysman, 1953; Abercrombie and Heaysman, 1954). Carmona-Fontaine and colleagues studied the interactions between neighbouring NC cells and found that migratory cells exhibit CIL, both *in vitro* and *in vivo*. This behaviour requires intact non-canonical Wnt signalling; while control NC cells retract their lamellipodia and change direction on contact with one another, those lacking PCP components (cells from *Dsh-DEP+, dnWnt11*, *Stbm* MO or *Pk* MO-treated embryos) fail to do so. Instead, these cells extend protrusions between their neighbours and migrate on top of one other (Carmona-Fontaine et al., 2008b).

Together these studies propose a model whereby the collision of two NC cells leads to an accumulation of PCP components (*Dsh, Wnt11* and *Fz7*) at the points of contact between adjacent cells. Analysis of Rho GTPase activity revealed that an increase in PCP signalling results in a local increase in RhoA activity, which inhibits Rac. Rac is also inhibited by the proteoglycan *Syndecan-4* (*Syn4*), which is expressed in the migrating NC of *Xenopus* and zebrafish embryos and is required for their directionality. The NC phenotype produced by inhibition of *Syn4* is reminiscent of that caused by PCP inhibition, and convergence of the two pathways has been found to occur via the regulation of the small GTPases. Thus, the model postulates that a decrease in Rac activity at cell-cell contacts directs the collapse of cell protrusions at the back of the NC cell, while an enrichment of Rac at the leading edge promotes actin polymerisation and lamellipodia. This brings about a change in polarity and the direction of migration (Carmona-Fontaine et al., 2008a; Matthews et al., 2008). This chapter aims to investigate whether there is a comparable role for PCP signalling during mammalian NC cell migration.

7.2 Results

To investigate whether PCP plays an essential role in mammalian NC migration the *loop-tail* (*Vangl2*^{Lp}) mouse, which carries a likely dominant negative allele of the core PCP gene *Vangl2* (Kibar et al., 2001b; Murdoch et al., 2001a; Song et al., 2010; Yin et al., 2012), was studied.

7.2.1 Neural crest specification and migration are normal in *Vangl2*$^{Lp/Lp}$ embryos

The specification of NC cells in wild-type and *loop-tail* embryos was examined using WISH for markers of pre-migratory and early migrating NC cells. The forkhead transcription factor *FoxD3* is one of the earliest markers of the NC lineage (Sauka-Spengler and Bronner-Fraser, 2008) and in E8.5 wild type embryos, *FoxD3* labelled NC cells along the edges of the dorsal neural folds in the cranial region and as far caudally as the closed neural tube adjacent to the fourth somite pair (Figure 7.2A). In *Vangl2*$^{Lp/Lp}$ embryos a similar pattern of expression was observed, despite the failure of closure 1 in these mutants (Figure 7.2B). In both genotypes, *FoxD3* expression was absent at the level of rhombomeres 3 and 5, the so-called 'neural crest-free' zones (Trainor et al., 2002).

WISH for the transcription factor *Sox9*, another NC specifier, was also performed. At E9.5 a dorsal line of *Sox9*-positive NC cells was visible along the neural tube of wild-type embryos, with a caudal limit at the level of the most recently formed somites (Figure 7.3A). A similar pattern of *Sox9* staining was observed in the equivalent rostro-caudal region on the tips of the open neural folds in *Vangl2*$^{Lp/Lp}$ embryos (Figure 7.3B). Together, these data suggest that NC cells are specified similarly in both genotypes, despite the failed neural tube closure in *Lp* homozygotes.

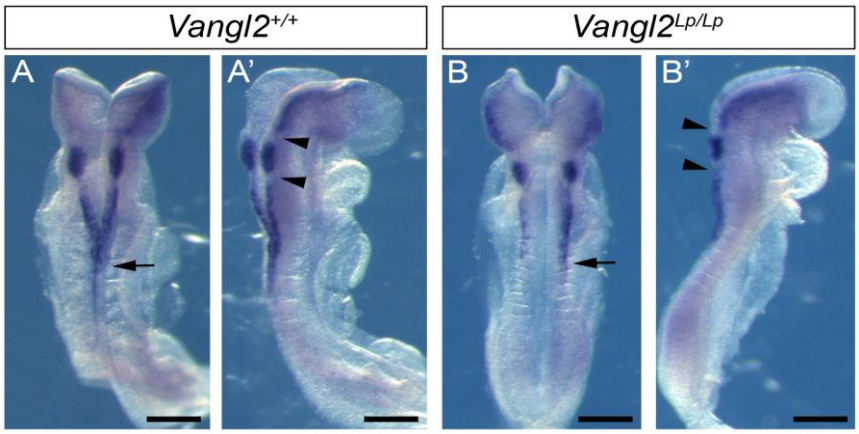

Figure 7.2 *Vangl2*$^{Lp/Lp}$ embryos display normal neural crest specification at E8.5.

Whole-mount *in situ* hybridisation for *FoxD3* in wild-type (*Vangl2*$^{+/+}$; A) and *Vangl2*$^{Lp/Lp}$ (B) embryos. (**A, B**) Dorsal views showing *FoxD3* labelling of pre-migratory NC cells in the dorsal neuroepithelium. In both genotypes the rostro-caudal wave of NC specification has reached as far caudally as somite 4 (arrows). (**A', B'**) Lateral views of the embryos shown in A and B. In both genotypes *FoxD3*-positive NC cells are absent at the level of rhombomeres 3 and 5 (arrowheads). n = minimum of 4 embryos per genotype. Scale bars: 200 µm.

Next the spatiotemporal pattern of NC migration was compared in wild-type and *Vangl2*$^{Lp/Lp}$ embryos by WISH for *Erbb3*, a member of the neuregulin receptor tyrosine kinase family which is expressed by NC cells during their migration (Meyer and Birchmeier, 1995) In wild-type embryos at the 13-somite stage, characteristic streams of cranial NC cells were observed migrating from the hindbrain towards the first and second branchial arches and around the optic vesicles (Figure 7.4A, B). More caudal sections also revealed *Erbb3*-positive trunk NC cells delaminating from the neuroepithelium and migrating ventrally (Figure 7.4C). When stage-matched *Vangl2*$^{Lp/Lp}$ embryos were examined, no differences in the pattern of NC migration were detected, despite the widely open neural folds (Figure 7.4D-F). By 20-22 somites, *Erbb3*-labelled trunk NC cells could be seen migrating from the dorsal neural tube of wild-type embryos (Figure 7.5A-F) and from the equivalent (lateral) region of the neuroepithelium in *Vangl2*$^{Lp/Lp}$ embryos (Figure 7.5G-L). By the 25-somite stage,

distinct migratory streams were observed in embryos of both genotypes (Figure 7.5M-N). Notably, the axial level and rostro-caudal progression of NC migration in *Vangl2*$^{Lp/Lp}$ was comparable to wild-type at all stages analysed, despite the failure of body axis extension and neural tube closure in the mutants.

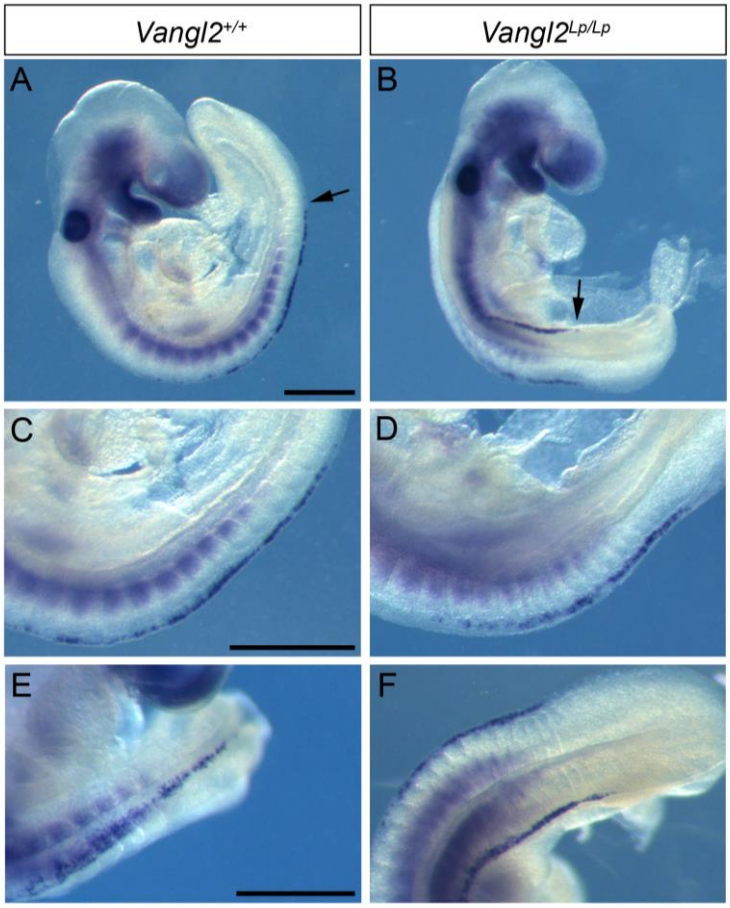

Figure 7.3 *Vangl2*$^{Lp/Lp}$ embryos display normal neural crest specification at E9.5.

Whole-mount *in situ* hybridisation for *Sox9* in wild-type (*Vangl2*$^{+/+}$; A, C, E) and *Vangl2*$^{Lp/Lp}$ (B, D, F) embryos. **(A, B)** Lateral views of wild-type and *Vangl2*$^{Lp/Lp}$ embryos showing *Sox9* labelling of pre-migratory NC cells in the dorsal neural tube and tips of the open neural folds, respectively. *Sox9* labels NC cells as far caudally as the most recently formed somites in both genotypes (arrows). **(C, D)** Higher magnification images of the trunk region of embryos shown in A and B. **(E, F)** Dorsal views of *Sox9*-positive NC cells in the dorsal midline of the wild-type neural tube (E) and at the tips of the persistently open neural folds of *Vangl2*$^{Lp/Lp}$ (F). n = 3 embryos per genotype. Scale bars: 500 µm.

As an alternative, genetic approach to identifying NC cells, transgenic mice expressing Cre recombinase under the control of the *Wnt1* promotor (Jiang et al., 2000) and *Rosa26*^{YFP} reporter mice (Srinivas et al., 2001) were used to generate wild-type and *Vangl2*$^{Lp/Lp}$ embryos in which the NC and their derivatives were fluorescently labelled. The breeding strategy outlined in Figure 7.6 was used to produce *Vangl2*$^{+/+}$*;Wnt1-Cre/YFP* and *Vangl2*$^{Lp/Lp}$*;Wnt1-Cre/YFP* embryos for analysis. As expected, *loop-tail* homozygous mutants (*Vangl2*$^{Lp/Lp}$) displayed craniorachischisis with 100% penetrance, while all *Vangl2*$^{Lp/+}$ and *Vangl2*$^{+/+}$ embryos had successfully completed closure 1 and were undergoing low spinal neurulation.

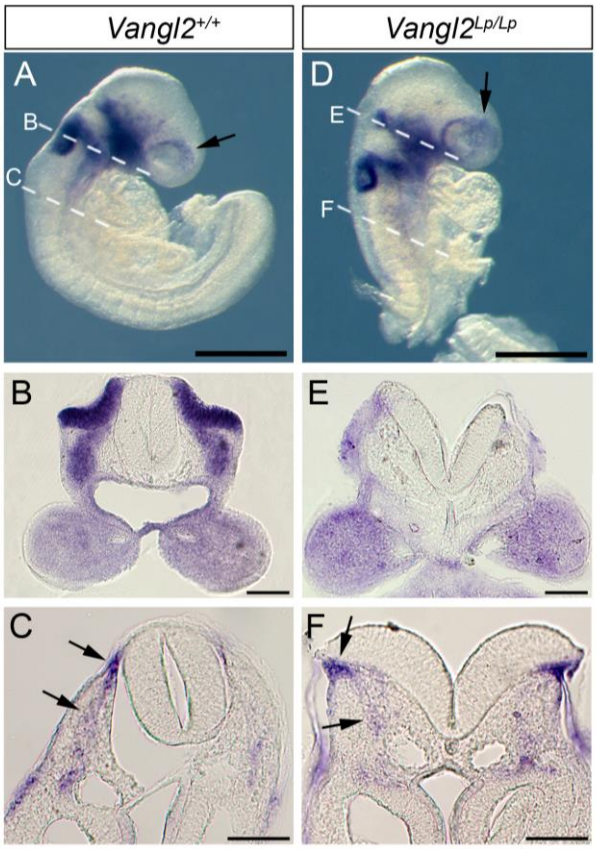

Figure 7.4 *Erbb3* expression in *Vangl2*$^{+/+}$ and *Vangl2*$^{Lp/Lp}$ at E9.0

WISH *Erbb3* in wild-type (A-C) and *loop-tail* (D-F) embryos. Cranial NC cells can be seen migrating in two distinct streams towards the first and second branchial arches and to surround the optic vesicles, in both *Vangl2*$^{+/+}$ and *Vangl2*$^{Lp/Lp}$ embryos (arrows in A, D). Transverse sections reveal colonisation of the branchial arches (B, E) and migrating NC cells (arrows in C, F) in both genotypes. Scale bars: 500 µm (A, D) and 100 µm (B, C, E, F).

Figure 7.5 *Erbb3* expression in *Vangl2*$^{+/+}$ and *Vangl2*$^{Lp/Lp}$ at E9.5

WISH for the NC marker *Erbb3* in wild-type (A-F, M) and *loop-tail* (G-L, N) embryos.

(A-L) By 20-22 somites, *Erbb3* marks the rostral-caudal progression of trunk NC cells emigrating from the dorsal neural tube. A similar pattern of emigration is observed in *Vangl2*$^{+/+}$ and *Vangl2*$^{Lp/Lp}$, despite the widely open neural folds and failure of body axis elongation in the latter. Transverse sections confirm closely similar NC migration in both genotypes (B-F, G-L).

(M, N) At the 25 somite stage, streams of NC cells can be seen migrating in the trunk of both *Vangl2*$^{+/+}$ (M) and *Vangl2*$^{Lp/Lp}$ (N) embryos. Higher magnification views of the boxed areas in M and N reveal comparable NC migration in both genotypes (M', N'). Abbreviations: ba = branchial arch, da = dorsal aorta, f = facial NC, ov = optic vesicle. n = minimum of 3 embryos per genotype. Scale bars: 500 µm (A, G, M, N) and 200 µm (B-F, H-L, M', N').

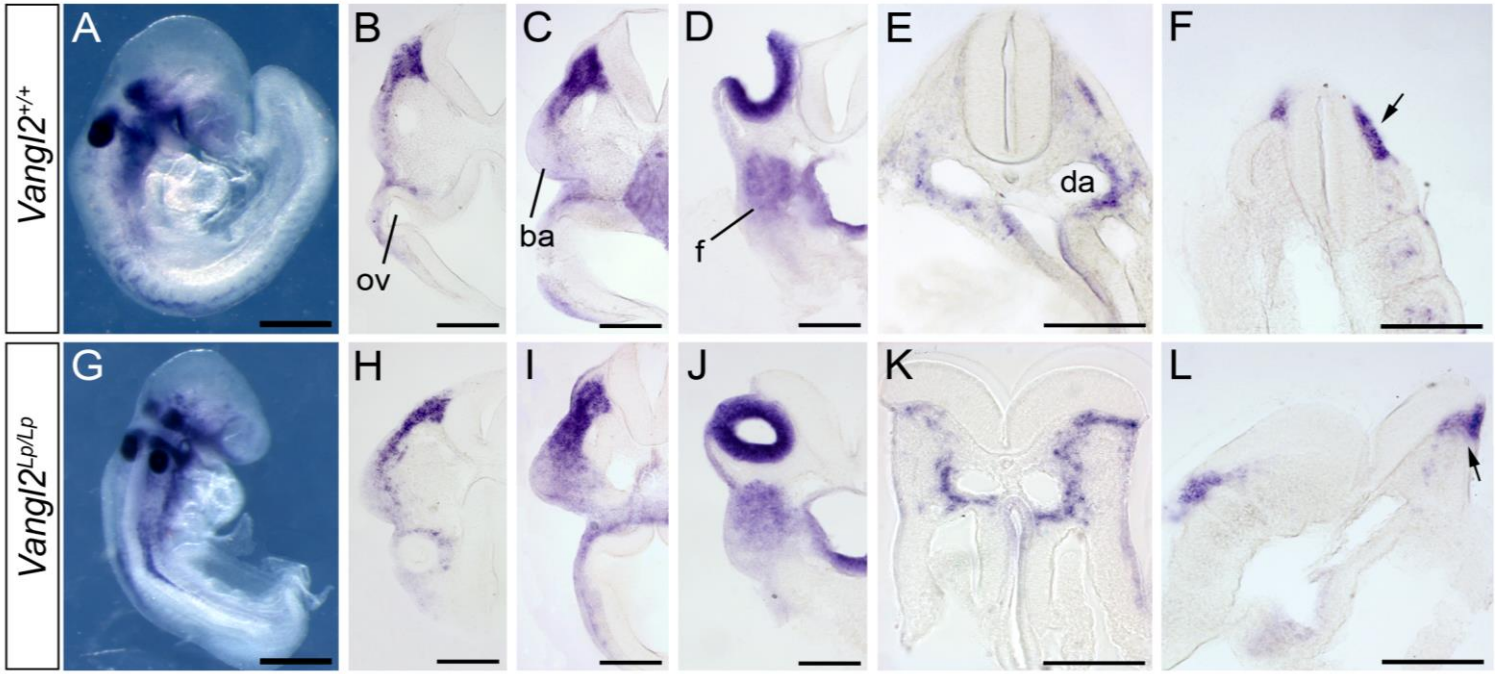
Vangl2+/+
Vangl2Lp/Lp
A
B
C
D
E
F
G
H
I
J
K
L
ov
ba
f
da

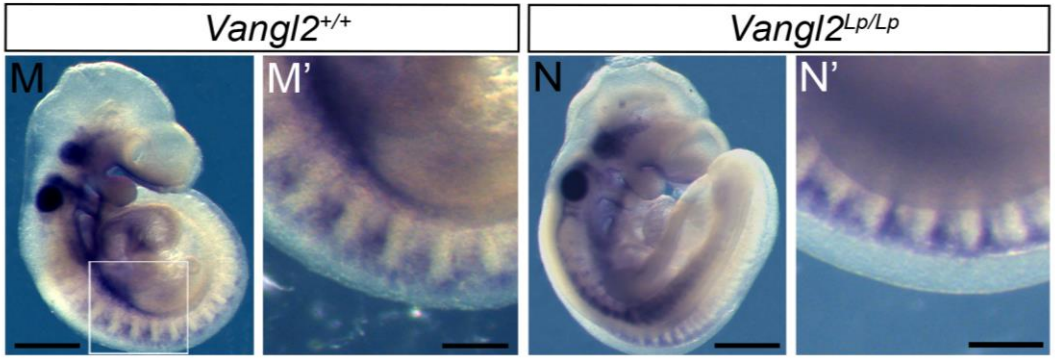
Vangl2+/+
Vangl2Lp/Lp
M
M'
N
N'

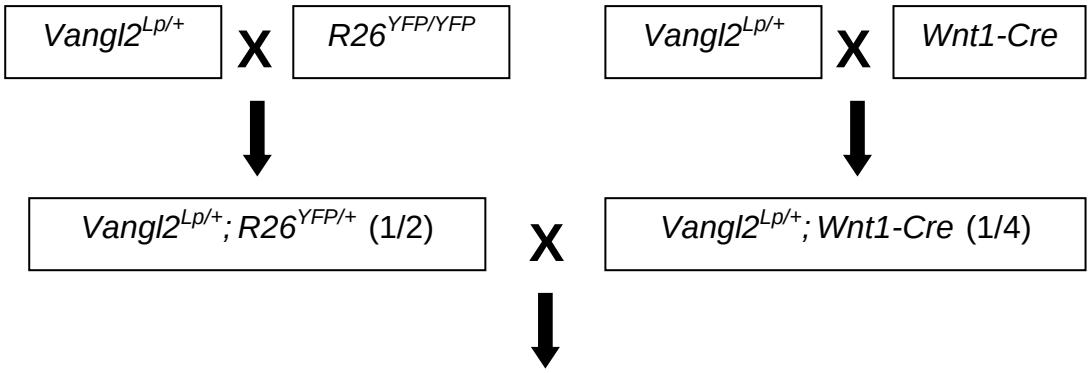

Offspring Genotype Category	Genotype(s)
1	***Vangl2$^{+/+}$; Wnt1-Cre; R26$^{YFP/+}$ (1/16)***
2	***Vangl2$^{Lp/+}$; Wnt1-Cre; R26$^{YFP/+}$ (2/16)***
3	***Vangl2$^{Lp/Lp}$; Wnt1-Cre; R26$^{YFP/+}$ (1/16)***
4	*Vangl2$^{+/+}$; Wnt1$^{+/+}$; R26$^{+/+}$* (1/16) *Vangl2$^{+/+}$; Wnt1$^{+/+}$; R26$^{YFP/+}$* (1/16) *Vangl2$^{+/+}$; Wnt1-Cre; R26$^{+/+}$* (1/16)
5	*Vangl2$^{Lp/+}$; Wnt1$^{+/+}$; R26$^{+/+}$* (2/16) *Vangl2$^{Lp/+}$; Wnt1$^{+/+}$; R26$^{YFP/+}$* (2/16) *Vangl2$^{Lp/+}$; Wnt1-Cre; R26$^{+/+}$* (2/16)
6	*Vangl2$^{Lp/Lp}$; Wnt1$^{+/+}$; R26$^{+/+}$* (1/16) *Vangl2$^{Lp/Lp}$; Wnt1$^{+/+}$; R26$^{YFP/+}$* (1/16) *Vangl2$^{Lp/Lp}$; Wnt1-Cre; R26$^{+/+}$* (1/16)

Figure 7.6 Breeding scheme used to generate *Vangl2$^{+/+}$; Wnt1-Cre/YFP* and *Vangl2$^{Lp/Lp}$; Wnt1-Cre/YFP* embryos for analysis.

Matings between *Vangl2$^{Lp/+}$; R26$^{YFP/+}$* and *Vangl2$^{Lp/+}$; Wnt1-Cre* mice produces embryos with one of 16 possible genotypes. However, offspring were only examined for YFP expression and genotyped for the presence of the *Vangl2^{Lp}* allele, meaning that embryos were actually assigned to one of the following 6 categories: (1) fluorescent *Vangl2$^{+/+}$*, (2) fluorescent *Vangl2$^{Lp/+}$*, (3) fluorescent *Vangl2$^{Lp/Lp}$*, (4) non-fluorescent *Vangl2$^{+/+}$*, (5) non-fluorescent *Vangl2$^{Lp/+}$* and (6) non-fluorescent *Vangl2$^{Lp/Lp}$*. Numbers in brackets indicate the expected proportion of offspring for each genotype. Green text indicates fluorescent embryos.

Whole-mount embryos were examined by direct visualisation of the YFP fluorescence, and anti-GFP/YFP immunostaining was performed on transverse sections. Both analyses revealed a similar NC migration pattern in *Vangl2*$^{+/+}$*;Wnt1-Cre/YFP* and *Vangl2*$^{Lp/Lp}$*;Wnt1-Cre/YFP* embryos (Figure 7.7), consistent with the WISH data. At 13-14 somites migrating, YFP-positive NC cells were visible within the forebrain, peri-ocular region and branchial arch 1 (also entering arch 2) in both *Vangl2*$^{+/+}$*;Wnt1-Cre/YFP* and *Vangl2*$^{Lp/Lp}$*;Wnt1-Cre/YFP* embryos (Figure 7.7A-C, E-G). At the level of the heart, migrating NC could be seen in both genotypes (Figure 7.7D, H). By 22-23 somites, branchial arches 1 and 2 were colonised by NC, and cells were also entering the lower arches, similarly in both *Vangl2*$^{+/+}$*;Wnt1-Cre/YFP* and *Vangl2*$^{Lp/Lp}$*;Wnt1-Cre/YFP* embryos (Figure 7.7I, M). Sections again revealed closely comparable patterns of NC cell distribution at different axial levels. Thus, WISH and fluorescent labelling of the neural crest and its descendants reveal normal migration in *Vangl2*$^{Lp/Lp}$ embryos at E9-E9.5.

I also quantified the numbers of migrating NC cells in *Vangl2*$^{+/+}$*;Wnt1-Cre/YFP* and *Vangl2*$^{Lp/Lp}$*;Wnt1-Cre/YFP* embryos between E9 and E10.5. When migrating YFP-positive cells at three different embryonic regions were counted, no significant differences in cell number were found between genotypes (Figure 7.8). These data indicate that the numbers of NC cells emigrating from the neural tube of *Vangl2*$^{Lp/Lp}$ embryos are comparable to wild-type.

Figure 7.7 Fluorescent labelling of the neural crest lineage at E9-9.5

Neural crest cell migration in *Vangl2*$^{+/+}$*;Wnt1-Cre/YFP* (Hereafter denoted +/+; A-D, I-L) and *Vangl2*$^{Lp/Lp}$*;Wnt1-Cre/YFP* (Hereafter denoted *Lp/Lp*; E-H, M-P) embryos. Whole mount embryos (A,E,I,M) show directly visualised YFP. Transverse sections (B-D, F-H, J-L, N-P; at the level of the dashed lines in bright field inset images) are immunostained with anti-GFP/YFP.

(A-H) At 13-14 somites, YFP-positive NC cells have colonised the forebrain, peri-ocular region and first branchial arch, and are entering the second branchial arch, with similar appearance in both +/+ (A) and *Lp/Lp* (E) embryos. Transverse sections show forebrain and branchial arch colonisation (B, C, F, G) and active NC migration at the level of the heart (arrows in D, H).

(I-P) At 22-23 somites, fluorescently labelled cells are observed in the lower branchial arches of both +/+ and *Lp/Lp* embryos (arrows in I and M). Transverse sections show extensive NC colonisation of forebrain and hindbrain in both genotypes (J, N). Neural crest emigration from the neural tube (arrows in K,L,O,P) and NC colonisation of the region lateral to the foregut (arrowheads in K,O) and adjacent to the paired aortae (arrowheads in L,P) appear closely similar in +/+ and *Lp/Lp*. Scale bars: 100 µm.

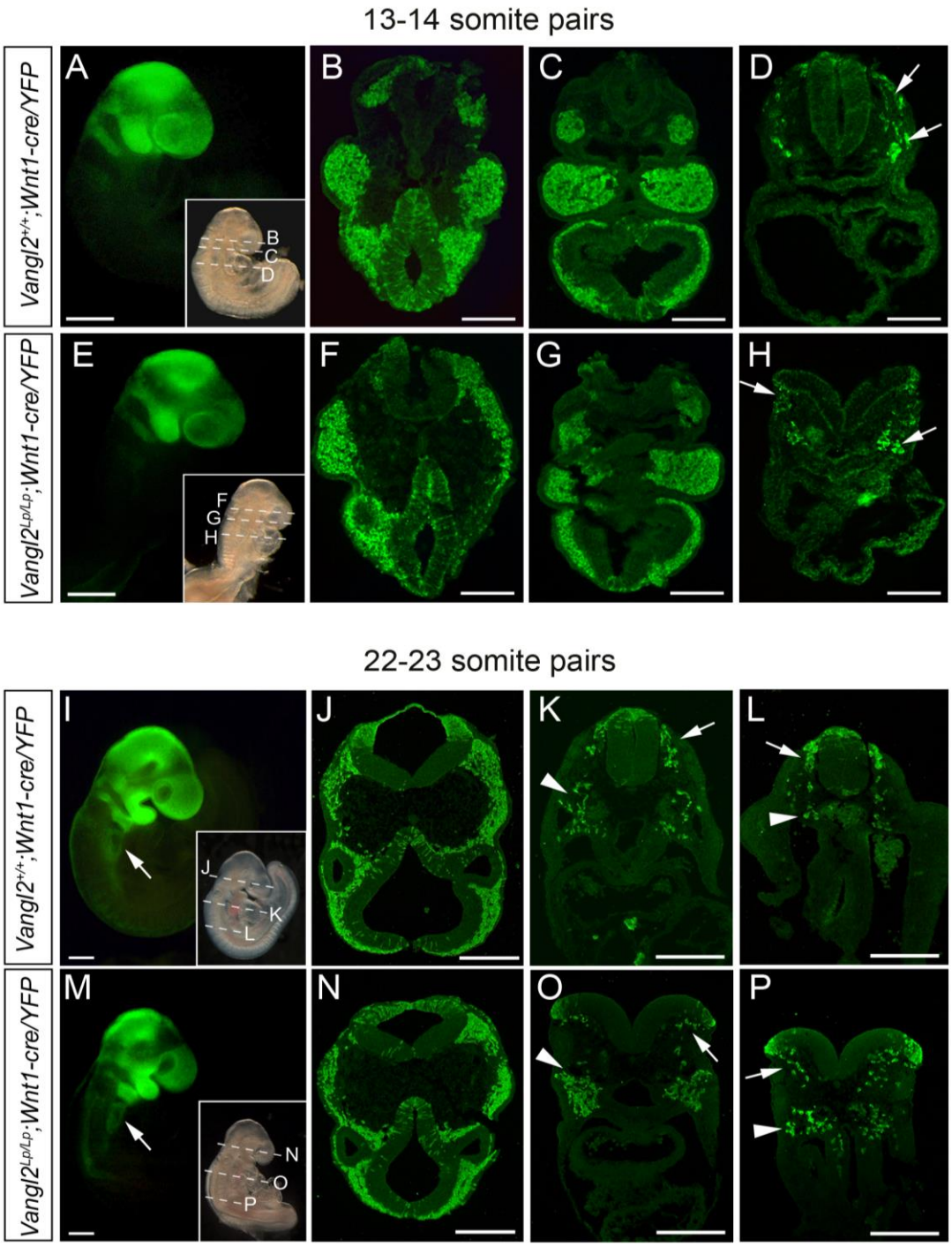
13-14 somite pairs
Vangl2+/+;Wnt1-cre/YFP
Vangl2Lp/Lp;Wnt1-cre/YFP
A
B
C
D
E
F
G
H
22-23 somite pairs
I
J
K
L
M
N
O
P

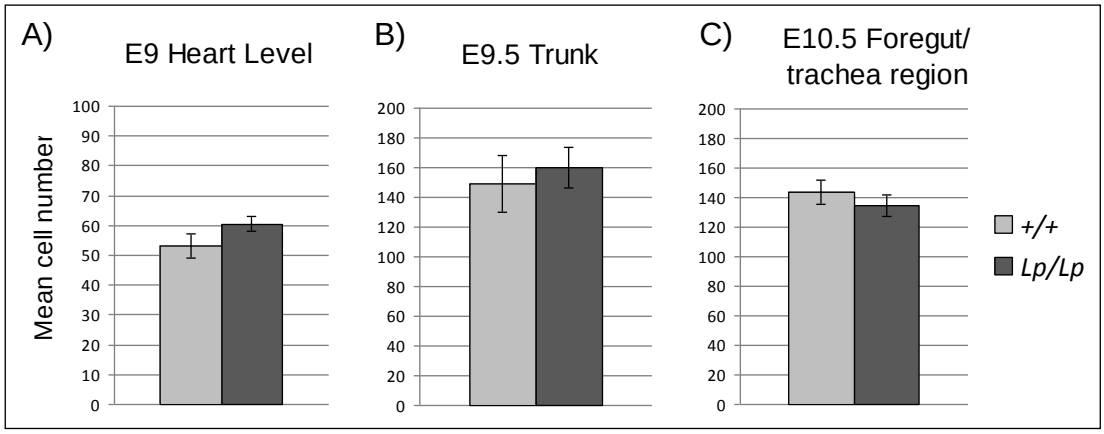

Figure 7.8 Quantification of migrating neural crest cells in *Vangl2$^{+/+}$; Wnt1-Cre/YFP* and *Vangl2$^{Lp/Lp}$; Wnt1-Cre/YFP* embryos.

Mean numbers of migrating, YFP-positive neural crest cells at different regions of E9-10.5 embryos. (**A**) Sections at the level of the developing heart as shown in Figure 7.7D and H (p = 0.183, t-test; n = at least 4 sections per genotype). (**B**) Trunk sections as shown in Figure 7.7L and P (p = 0.446, t-test; n = 3 sections per genotype). (**C**) Sections at the level of the foregut/trachea as shown in Figure 7.10L and Q (p = 0.664, t-test; n = 5 sections per genotype).

7.2.2 Neural crest derivatives are patterned normally in *Vangl2$^{Lp/Lp}$* embryos

We next investigated whether *loop-tail* embryos display any abnormalities in NC cell distribution or the patterning of NC-derived structures at E10.5, which could be indicative of earlier defective migration. WISH for *Erbb3* revealed the cranial ganglia to be appropriately sized and patterned in *Vangl2$^{Lp/Lp}$* compared to stage-matched wild-type embryos (Figure 7.9A, D). The dorsal root ganglia (DRG), which come to lie either side of the closed spinal neural tube in wild-type embryos (Figure 7.9B), appeared normal in *Vangl2$^{Lp/Lp}$* embryos. Despite the grossly abnormal morphology of *loop-tail* mutants, distinct ganglia were seen along the trunk adjacent to the equivalent region of open neural folds (Figure 7.9E). More caudally, at the level of the hindlimb buds, NC cells were beginning to delaminate as 'segmental' streams from the neuroepithelium in both wild-type and *Vangl2$^{Lp/Lp}$* embryos (Figure 7.9C and F).

Examination of the distribution of NC cells and their derivatives in *Vangl2*$^{+/+}$;*Wnt1-Cre/YFP* and *Vangl2*$^{Lp/Lp}$;*Wnt1-Cre/YFP* embryos at E10.5 revealed no differences in the pattern of YFP-labelled cells between genotypes (Figure 7.10A, F). NC derivatives were similarly distributed throughout the cranial and pharyngeal regions of *Vangl2*$^{+/+}$;*Wnt1-Cre/YFP* and *Vangl2*$^{Lp/Lp}$;*Wnt1-Cre/YFP* embryos (Figure 7.10B-E, G-J) and the DRG were similarly sized in both genotypes (Figure 7.10M-N, R-S). NC cells were also seen migrating towards the heart and around the foregut in embryos of both genotypes (Figure 7.10K-L, P-Q). More caudal sections revealed no difference in the ventral migration of NC cells from the neuroepithelium (Figure 7.10O,T). Hence, these data show that the colonisation of numerous tissues by NC cells occurs normally in *Vangl2*$^{Lp/Lp}$ mutants, further indicating that NC migration is not impaired by the disruption of PCP signalling.

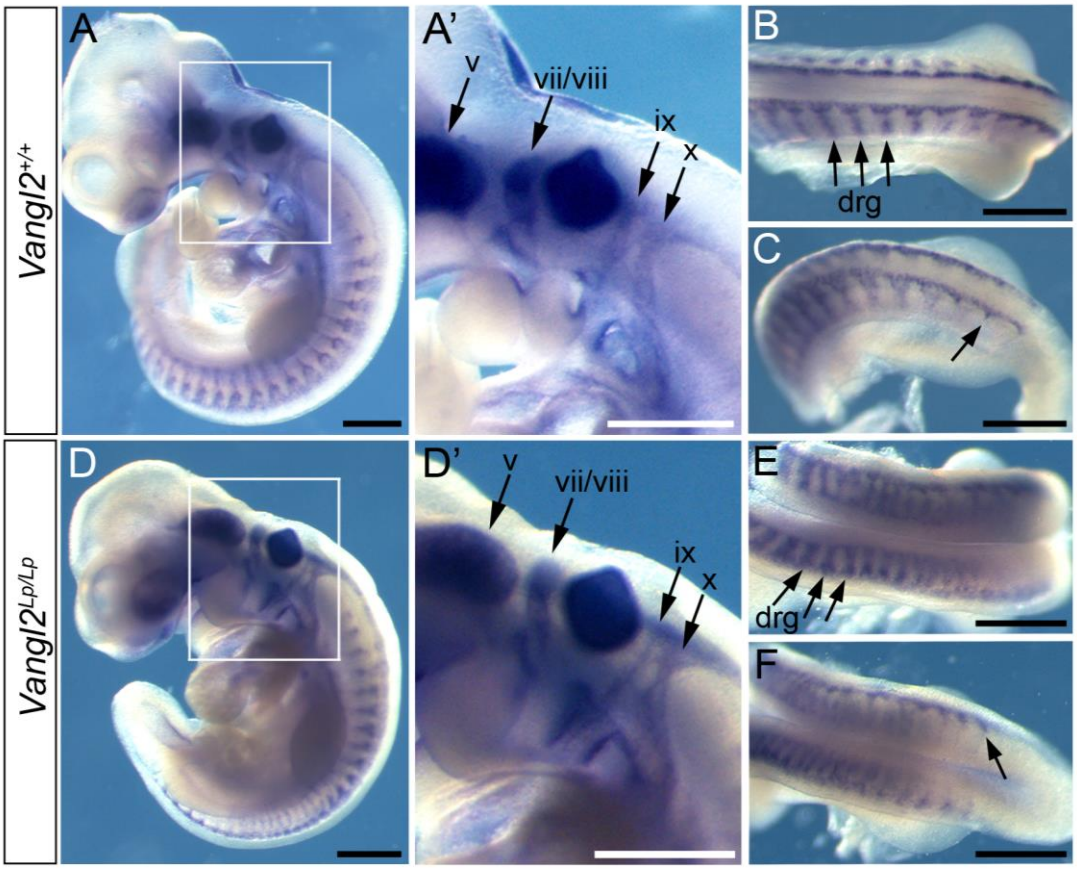

Figure 7.9 *Erbb3* expression in *Vangl2*$^{+/+}$ and *Vangl2*$^{Lp/Lp}$ at E10.5

WISH for the NC marker *Erbb3* in wild-type (*Vangl2*$^{+/+}$; A-C) and *loop-tail* (*Vangl2*$^{Lp/Lp}$; D-F) embryos. *Erbb3* expression is seen in the trigeminal (v), facio-acoustic (vii/viii), glossopharyngeal (ix), and vagal (x) cranial ganglia in both *Vangl2*$^{+/+}$ and *Vangl2*$^{Lp/Lp}$ embryos (A and D; higher magnification views of the boxed areas are shown in A' and D'). A dorsal view shows *Erbb3* expression in developing dorsal root ganglia (DRG) throughout the trunk of wild-type embryos (arrows in B). Despite the widely open neural folds in *Vangl2*$^{Lp/Lp}$ embryos, the DRG appear normally sized and patterned (arrows in E). Further caudally, segregated streams of NC cells can be seen migrating from the dorsal neural tube in both *Vangl2*$^{+/+}$ (arrow in C) and *Vangl2*$^{Lp/Lp}$ (arrow in F). Scale bars: 500 µm. n = minimum of 3 embryos per genotype.

Figure 7.10 Fluorescent labelling of the neural crest lineage at E10.5

Whole mounts (A, F) and sections (B-E,G-J, K-O and P-T) through E10.5 *Vangl2*$^{+/+}$*; Wnt1-Cre/YFP* (Hereafter denoted +/+) and *Vangl2*$^{Lp/Lp}$*; Wnt1-Cre/YFP* (Hereafter denoted *Lp/Lp*) embryos showing YFP-positive NC cells and their derivatives.

(**A, F**) Fluorescent images (with bright field inset) show labelled cells within the nasal process, branchial arches and branchial pouches (arrowheads) with closely similar appearance in +/+ (A) and *Lp/Lp* (F). YFP positive cells are also seen in the dorsal root ganglia of both genotypes (arrows).

(**B-E, G-J**) Sections through the embryos in A and F, immunostained with anti-GFP/YFP. Auto-fluorescent cells appear yellow (by overlay with the red channel). Despite the widely open neural folds and overall abnormal morphology in *Lp/Lp*, no differences in the distribution of YFP-expressing NC cells are observed between genotypes. Neural crest derivatives are detected sub-epidermally (B, G), around the developing eye (C, H), in the branchial pouches (D, I), and in the pharyngeal region and aortic sac (E, J).

(**K-O, P-T**) Labelled cells can be seen migrating towards the developing heart (arrows in F and P) and around the foregut (asterisks in G and Q). YFP-positive dorsal root ganglia appear normally sized in *Lp/Lp* despite the open neural folds (M, N, R, S; arrows). Caudally, at the level of the hindgut (O, T), ventrally migrating neural crest cells can be seen in both +/+ and *Lp/Lp* embryos (arrows). Scale bars: 500 µm (A, K) and 100 µm (B-E, G-J, K-O, P-T).

.

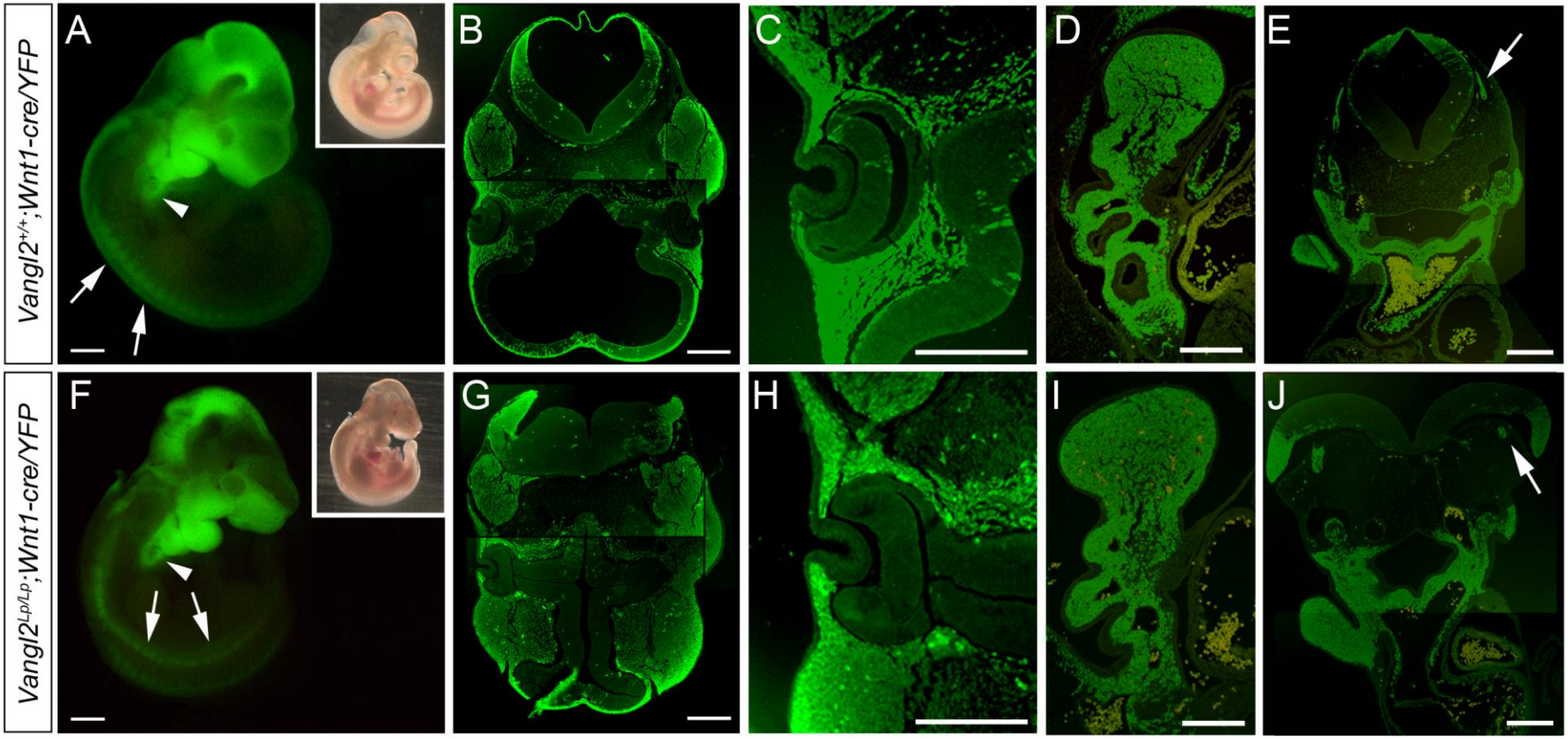
Vangl2+/+;Wnt1-cre/YFP
Vangl2Lp/Lp;Wnt1-cre/YFP
A
B
C
D
E
F
G
H
I
J

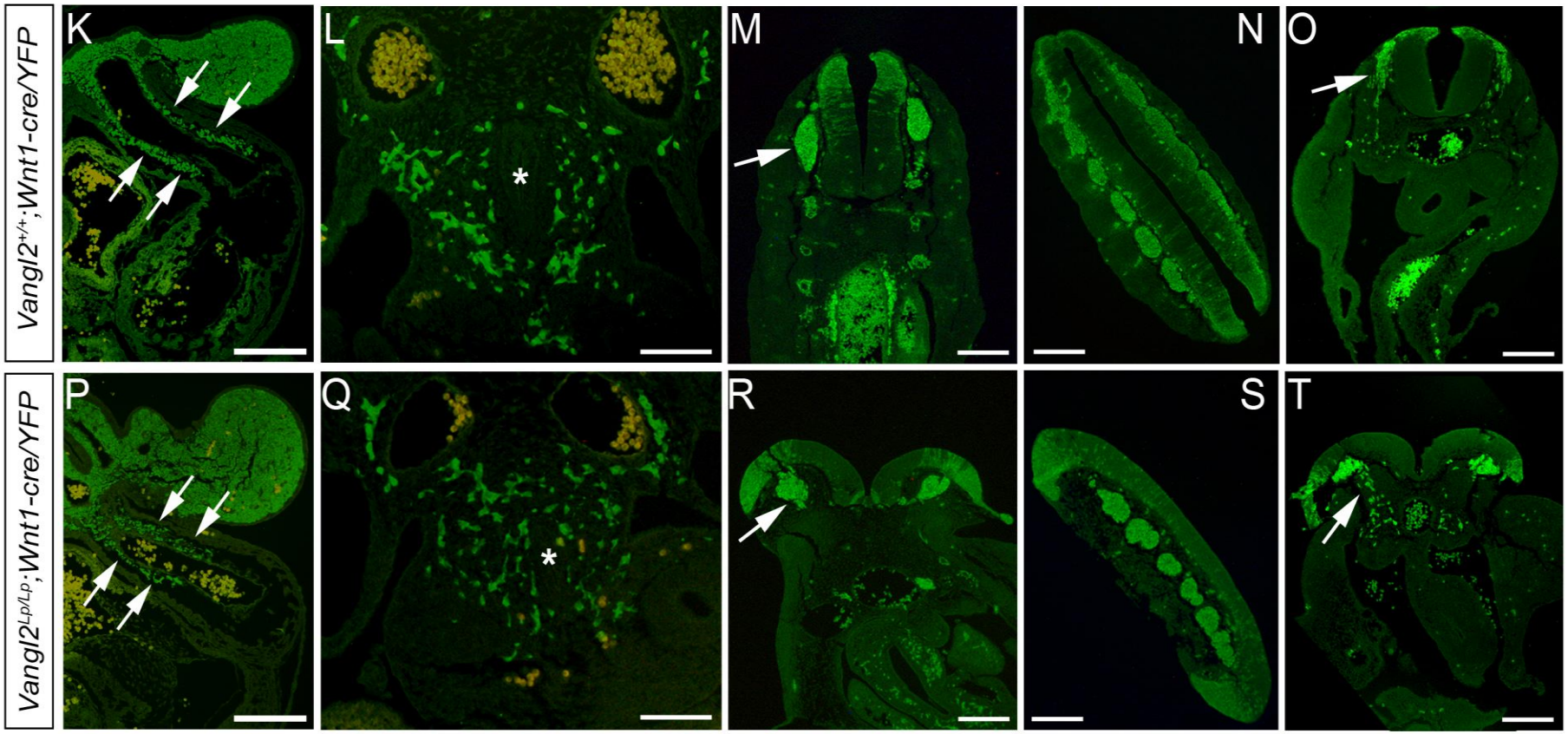

Figure 7.10 (continued)

7.2.3 *Vangl1* does not compensate for the loss of *Vangl2* during neural crest migration

Although *loop-tail* is a well-established, severe PCP mutant that displays a wide spectrum of related defects, the possibility that the *Vangl1* might compensate for the loss of *Vangl2* during NC migration was considered. As described in Chapter 1, *Vangl1* is a highly conserved, structurally similar paralogue of *Vangl2* (Torban et al., 2004) and is the only other known mammalian orthologue of *Drosophila Strabismus/Van gogh*. Like Vangl2, the Vangl1 protein has been shown to interact physically with mammalian Dishevelled (Dvl) proteins (Torban et al., 2004). Moreover, *Vangl1* interacts genetically with *Vangl2* during neurulation, although homozygous loss of *Vangl1* alone does not disturb neural tube closure (Torban et al., 2008).

The expression of *Vangl1* was studied in wild-type and *Vangl2*$^{Lp/Lp}$ embryos by WISH. At E8.5, *Vangl1* was expressed along a narrow region of the ventral neuroepithelium in wild-type embryos, from the level of the hindbrain to the PNP (Figure 7.11A-D), consistent with previous reports (Doudney et al., 2005; Liu et al., 2008). In *Vangl2*$^{Lp/Lp}$ embryos, the expression pattern appeared unaltered and *Vangl1* was not expressed ectopically in other regions of the neuroepithelium (Figure 7.11E-H). Importantly, *Vangl1* transcripts were absent from the upper hindbrain and midbrain regions of both wild-type and *Vangl2*$^{Lp/Lp}$ embryos which, at E8.5, is the level from which NC cells are migrating (compare with *Erbb3* expression marking NC cells in Figure 7.11I-J). Furthermore, *Vangl1* expression was not seen at the edges of the trunk neural folds, the site of NC induction and subsequent delamination, in either wild-type (Figure 7.11C,D) or *Vangl2*$^{Lp/Lp}$ (Figure 7.11G,H). The highly restricted pattern of *Vangl1* expression at E8.5, in the neuroepithelial midline, contrasts with the more generalised nervous system expression of *Vangl2* at this stage (Figure 7.11M-P).

By E9.5, *Vangl1* expression could be seen extending further along the embryonic axis of both wild-type and *Vangl2*$^{Lp/Lp}$ embryos, from midbrain to low spine (Figure 7.12A, D), although this was difficult to visualise in whole mutant embryos due to their abnormal morphology. Transverse sections at the level of the migrating trunk NC revealed *Vangl1* expression only in the ventral half of the neural tube in wild-type embryos, and in an equivalent region of the open neuroepithelium of *Vangl2*$^{Lp/Lp}$ embryos (Figure 7.12B-C, E-F). This *Vangl1* expression domain was clearly distinct from, and non-overlapping with, the more dorsal NC progenitor domain (compare with *Erbb3* expression in Figure 7.12G-I). In contrast, *Vangl2* is expressed throughout the neuroepithelium at all axial levels at this stage (Figure 7.12J-L). These results show that, in wild-type embryos, *Vangl1* is neither expressed by NC, nor by neighbouring cells, prior to or during NC cell emigration from the dorsal neuroepithelium. Moreover, *Vangl1* expression was not detected ectopically in the NC region *of loop-tail* embryos. These data therefore argue against the idea that *Vangl1* acts redundantly with *Vangl2* during NC migration.

Figure 7.11 *Vangl1* is not ectopically activated at E8.5

(**A-H**) WISH for *Vangl1* in wild-type (*Vangl2*$^{+/+}$; A-D) and *loop-tail* (*Vangl2*$^{Lp/Lp}$*;* E-H) embryos. Dorsal (A) and lateral (A') views show that *Vangl1* expression is confined to a narrow region of the ventral neuroepithelium in *Vangl2*$^{+/+}$, with a rostral limit at the level of the hindbrain (arrows in A'). Transverse sections (B-D; at the level of the dotted lines in A) confirm midline neuroepithelial expression. *Vangl2*$^{Lp/Lp}$ embryos exhibit a closely similar *Vangl1* expression domain to that seen in wild-type, both in whole mount (E,E') and sections (F-H). n = minimum of 3 embryos per genotype.

(**I-L**) WISH for the NC marker *Erbb3* at E8.5 for comparison with *Vangl1*. The wild-type embryo in I and I' shows expression in the migrating cranial NC, and this is confirmed in sections (J-L). There is no overlap in expression of *Erbb3* and *Vangl1*.

(**M-P**) WISH for *Vangl2* at E8.5 showing expression within the neuroepithelium at all levels of the body axis. Co-expression of *Vangl1* and *Vangl2* occurs only in ventral midline neural tube cells. Scale bars: 200 µm (A, E, I, M) and 50 µm (B-D, F-H, J-L, N-P).

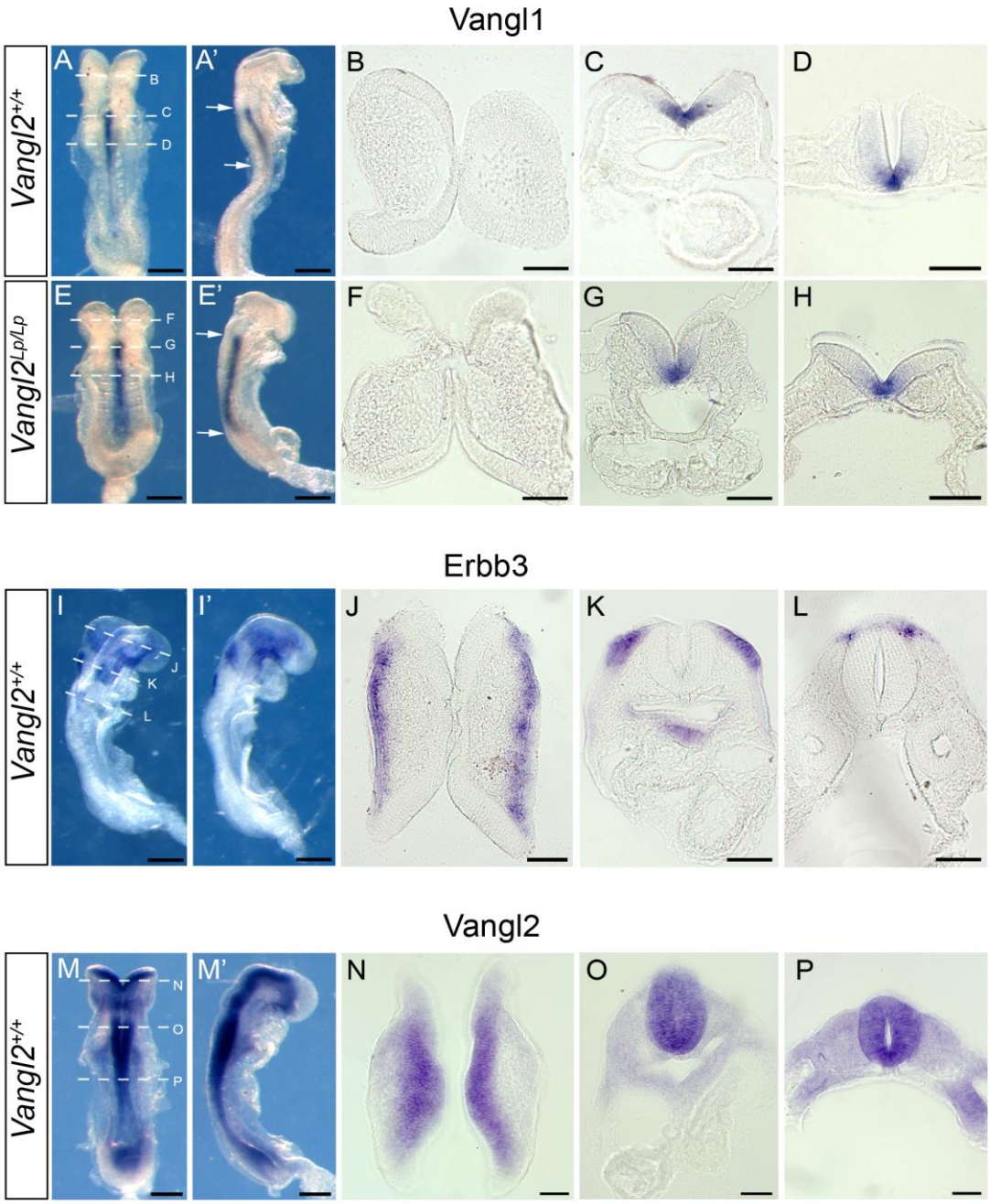
Vangl1
Vangl2+/+
Vangl2Lp/Lp
A
A'
B
C
D
E
E'
F
G
H
Erbb3
Vangl2+/+
I
I'
J
K
L
Vangl2
Vangl2+/+
M
M'
N
O
P

Figure 7.12 *Vangl1* is not ectopically activated at E9.5

(**A-F**) Whole-mount *in situ* hybridisation for *Vangl1* in wild-type (*Vangl2*$^{+/+}$; A-C) and *loop-tail* (*Vangl2*$^{Lp/Lp}$*;* D-F) embryos*.* Transcripts are detected in the ventral half of the neural tube from midbrain to level of the posterior neuropore in *Vangl2*$^{+/+}$ (A, asterisk indicates probe trapped within the hindgut). This expression pattern is confirmed in transverse sections (B,C; at level indicated by dotted lines in A). The pattern of *Vangl1* expression in *Vangl2*$^{Lp/Lp}$ appears unaltered compared with wild-type (D-F)*.* While staining appears marginally more intense in *Vangl2*$^{Lp/Lp}$ (D), this is likely an experimental artefact due to the widely open neural folds. Indeed, transverse sections (E-F) reveal *Vangl1* expression confined to the ventral neuroepithelium at a similar intensity as wild-type. n = minimum of 3 embryos per genotype.

(**G-I**) *Erbb3* mRNA expression is confined to migrated NC in the cranio-facial region (G) and actively migrating NC cells in the trunk (H,I). There is no overlap between *Vangl1* and *Erbb3* expression in either wild-type or *Vangl2*$^{Lp/Lp}$ embryos.

(**J-L**) *Vangl2* mRNA expression at E9.5 is present at greatest intensity throughout the neuroepithelium, and at low intensity in mesoderm and gut endoderm (asterisk in J indicates probe trapped within the hindgut). As at E8.5, co-expression of *Vangl1* and *Vangl2* occurs only in ventral midline neural tube cells. Scale bars: 500 µm (A, D, G, J), 200 µm (all sections).

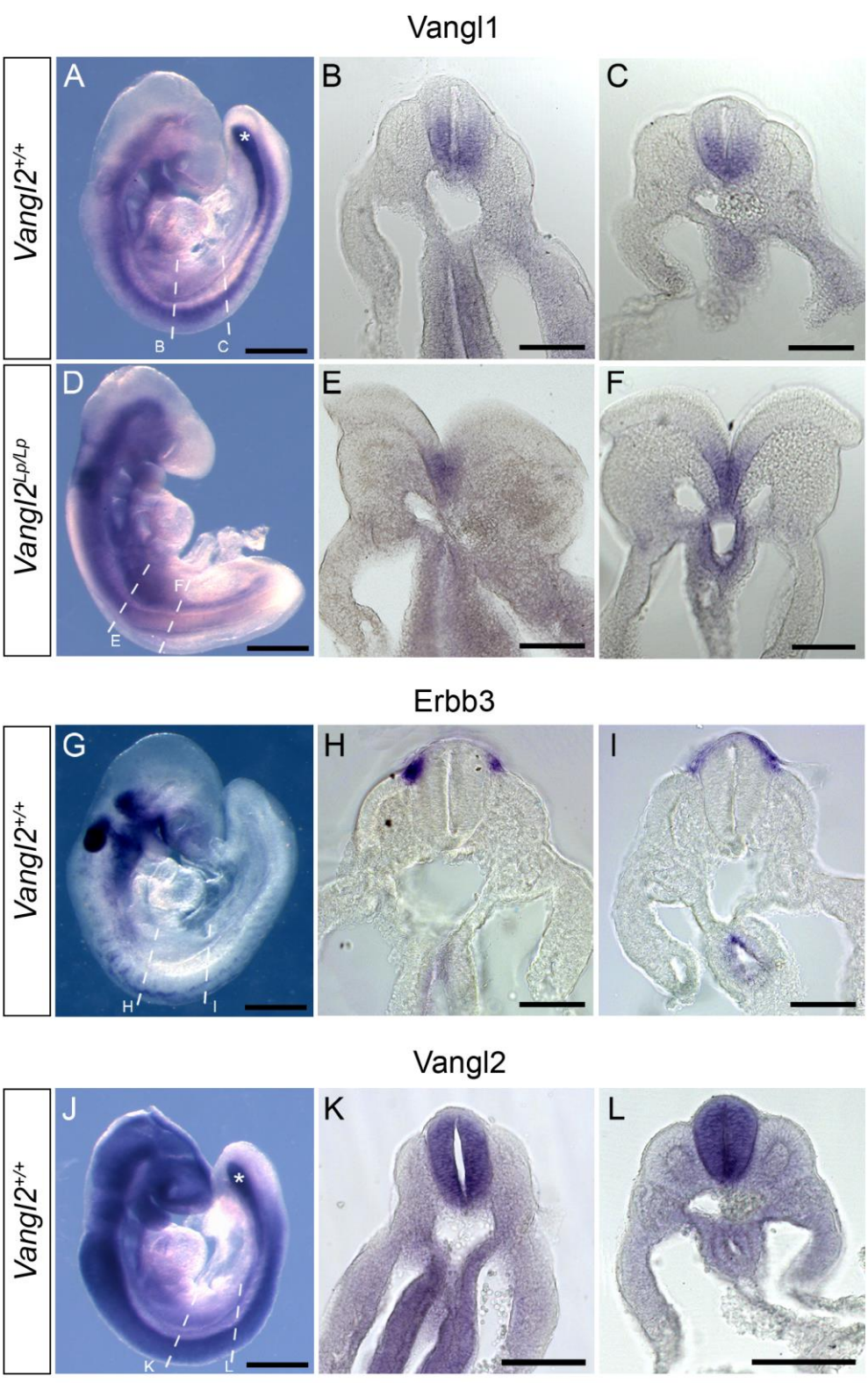
Vangl1
Vangl2+/+
Vangl2Lp/Lp
A
B
C
D
E
F
Erbb3
Vangl2+/+
G
H
I
Vangl2
Vangl2+/+
J
K
L

7.2.4 Analysis of neural crest migration *in vitro*

The migration of *Xenopus* and zebrafish NC cells *in vitro* is strongly inhibited when components of the PCP pathway are mutated, and PCP signalling is required to restrict lamellipodial protrusions to the leading edge of migratory cells (Carmona-Fontaine et al., 2008a; Carmona-Fontaine et al., 2008b; De Calisto et al., 2005; Matthews et al., 2008). Therefore, to extend the analysis of NC migration in mammalian PCP mutants, neural tube explants from wild-type and *Vangl2*$^{Lp/Lp}$ embryos were dissected and cultured over a 2 day period. After 24 and 48 hours, comparable outgrowth of migratory cells from both wild-type and *Vangl2*$^{Lp/Lp}$ explants was observed, with cells spreading radially from the central explant (Figure 7.13A). In all cultures, cells at the leading edge of the migratory population displayed various morphologies: some appeared to be polarised in the direction of migration, while others did not display any obvious polarity (Figure 7.13B).

To confirm the identity of NC cells in this assay, explants from E9.5 *Vangl2*$^{+/+}$*;Wnt1-Cre/YFP* and *Vangl2*$^{Lp/Lp}$*;Wnt1-Cre/YFP* embryos were cultured. Immediately after explantation, YFP-positive pre-migratory NC cells could be seen along the dorsal margin of *Vangl2*$^{+/+}$*;Wnt1-Cre/YFP* neural tube explants, and in the equivalent dorsolateral regions of the open *Vangl2*$^{Lp/Lp}$*; Wnt1-Cre/YFP* explant tissue (Figure 7.14; 0 hours). After 24 hours, similar numbers of YFP-positive migratory cells had emerged from the explants of both genotypes (Figure 7.14; 24 hours). The rate of outgrowth was measured as the percentage increase in outgrowth area (see Chapter 2); the increase in explant culture area did not differ between genotypes at either 24 or 48 hours (Figure 7.15), arguing for a closely similar rate of NC migration in wild-type and mutant explants. Further analysis of the *Wnt1-Cre/YFP* neural tube explant cultures revealed that, whilst the majority of migratory cells were YFP-labelled NC cells, non-NC cells were also present (Figure 7.16). This suggests that other mammalian neuroepithelial

cells display migratory potential when cultured *in vitro*, consistent with previous findings for the avian neural tube (Duband et al., 2009). Double immunostaining of cells *in vitro* confirmed that the majority of YFP-positive NC cells also expressed the NC cell marker P75 (Figure 7.17).

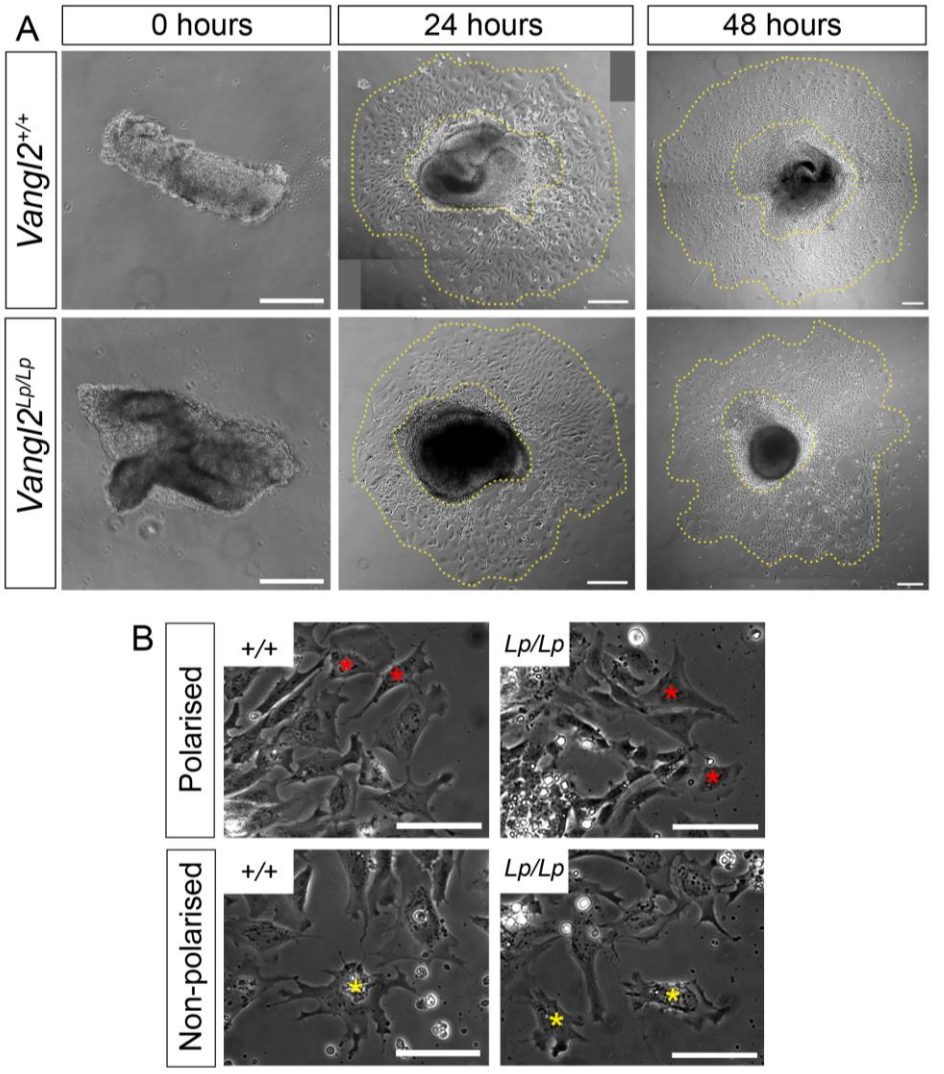

Figure 7.13 *In vitro* culture of neural tube explants

(**A**) *Vangl2*$^{+/+}$ and *Vangl2*$^{Lp/Lp}$ neural tube explants cultured for 24 and 48 hours. Inner yellow dotted lines indicate the area covered by the central mass of neuroepithelial tissue; outer dotted lines indicate the leading edge of the migratory population. (**B**) Examples of the variable morphology of leading edge cells. Red asterisks: *Vangl2*$^{+/+}$ and *Vangl2*$^{Lp/Lp}$ cells which appear polarised. Yellow asterisks: cells which extend protrusions in all directions. Scale bars: 200 µm (A) and 50 µm (B).

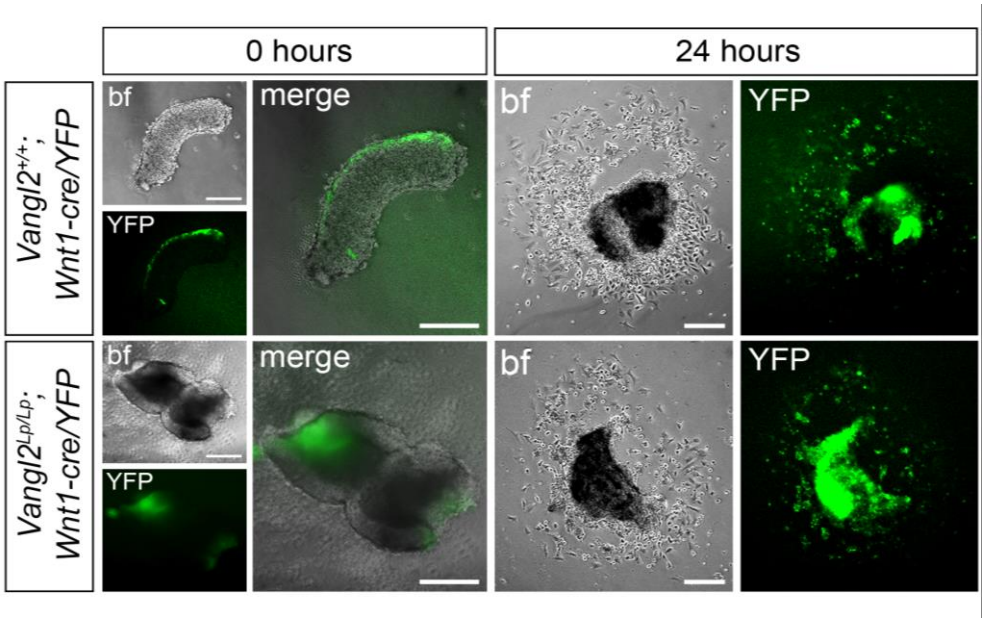

Figure 7.14 *Wnt1-cre/YFP* explants in culture

Vangl2$^{+/+}$*; Wnt1-Cre/YFP* and *Vangl2*$^{Lp/Lp}$*; Wnt1-Cre/YFP* neural tube explant cultures. At 0 hours, YFP expression can be seen along the dorsal margin of the +/+ explant, and at the equivalent dorsolateral regions of the persistently open neural folds in the *Lp/Lp* explant. After 24 hours, similar numbers of YFP-positive migratory cells have emerged from the explants of both genotypes. Abbreviations: bf = bright field image. Scale bars: 100 µm.

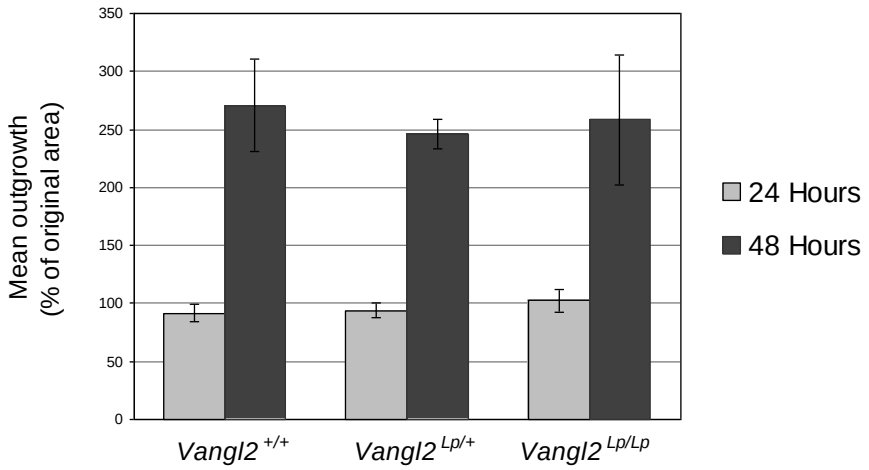

Figure 7.15 Outgrowth of neural tube explant cultures

Explant outgrowth over two days measured as the percentage increase in area. There is no significant difference in rate of NC emigration between genotypes (p = 0.91, Kruskal-Wallis 1-way ANOVA on ranks; n = at least 5 explants per genotype for 24 hours and 3 explants per genotype for 48 hours). Explants from both fluorescent and non-fluorescent embryos were included for this analysis.

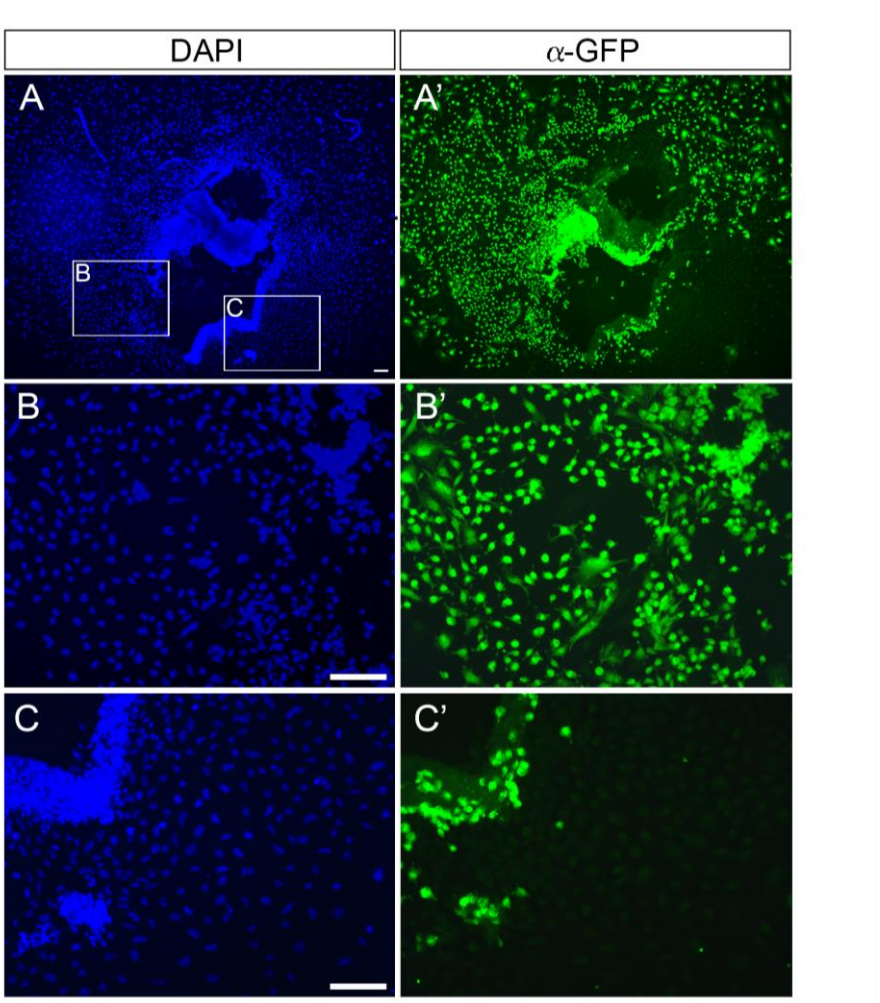

Figure 7.16 Anti-GFP/YFP immunostaining of neural tube explant cultures

Representative *Vangl2*$^{+/+}$*;Wnt1-Cre/YFP* neural tube explant culture immunostained with anti-GFP/YFP (A, A'). Higher magnification views of the boxed regions are shown in B and C. While the majority of migratory cells are YFP-positive NC cells (B, B'), other cell types, which do not express YFP, are also present (C, C'). Nuclei are stained with DAPI. Scale bars: 100 µm.

Control *Xenopus* NC cells at the leading edge of an *in vitro* migratory population extend large, polarised lamellipodia in the direction of migration, while those expressing mutant forms of PCP proteins are not polarised and extend a higher proportion of filopodia in all directions (Carmona-Fontaine et al., 2008b; De Calisto et al., 2005). In our explant cultures, YFP-positive NC cells at the leading edge exhibited a variety of morphologies: some extended large sheet-like lamellipodia at the front of

the cell, while others extended numerous protrusions around their periphery and did not appear to be polarised in any particular direction. No difference was observed in this cell behaviour between *Vangl2*$^{+/+}$*;Wnt1-Cre/YFP* and *Vangl2*$^{Lp/Lp}$*;Wnt1-Cre/YFP* explants (Figure 7.18A). The polarity of leading edge NC cells was assessed by measuring the distribution of cell area relative to the direction of migration (Figure 7.18B and see Chapter 2). The proportion of cells polarised in the direction of migration did not differ significantly between genotypes (Figure 7.18C) although the tendency was for *Vangl2*$^{Lp/Lp}$ cells to show enhanced polarity compared with wild-type. The distance migrated by leading edge NC cells from the central explant tissue was also measured. Distance did not differ significantly between genotypes (Figure 7.19). Together, these data demonstrate that loss of function of the core PCP gene *Vangl2* does not impair NC cell migration *in vitro*.

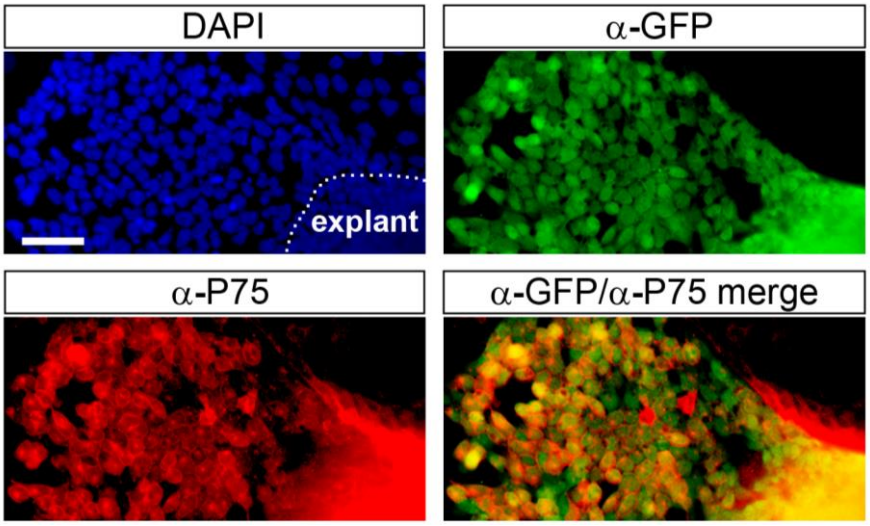

Figure 7.17 Identification of neural crest cells *in vitro*

Representative *Vangl2*$^{+/+}$*;Wnt1-Cre/YFP* neural tube explant culture immunostained with anti-GFP/YFP and anti-P75 (nuclei stained with DAPI). Most YFP-positive cells also express the NC marker P75 in vitro. Scale bars: 100 µm.

Figure 7.18 Neural crest cell polarity *in vitro*

(**A**) Examples of the variable morphology of *Vangl2*$^{+/+}$ and *Vangl2*$^{Lp/Lp}$ NC cells at the leading edge of the migratory population after 24 hours in culture (immunostained with anti-GFP/YFP, nuclei stained with DAPI). For both genotypes, some cells appear highly polarised in the direction of migration while others do not.

(**B**) Analysis of NC cell polarity in leading edge cells (e.g. boxed area). Forward is defined as the direction away from the central mass of explant tissue (arrows). Distribution of cell area was compared between six circular sectors, centred on the nucleus. Most of this cell occurs in sectors 1 (yellow dotted line) and 2, indicating a highly polarised cell that is migrating.

(**C**) The proportion of leading edge cells polarised in the direction of migration does not differ significantly between genotypes (p = 0.09, Chi-square test; n = at least 64 cells from 3 explants for each genotype). Scale bars: 20 µm (A).

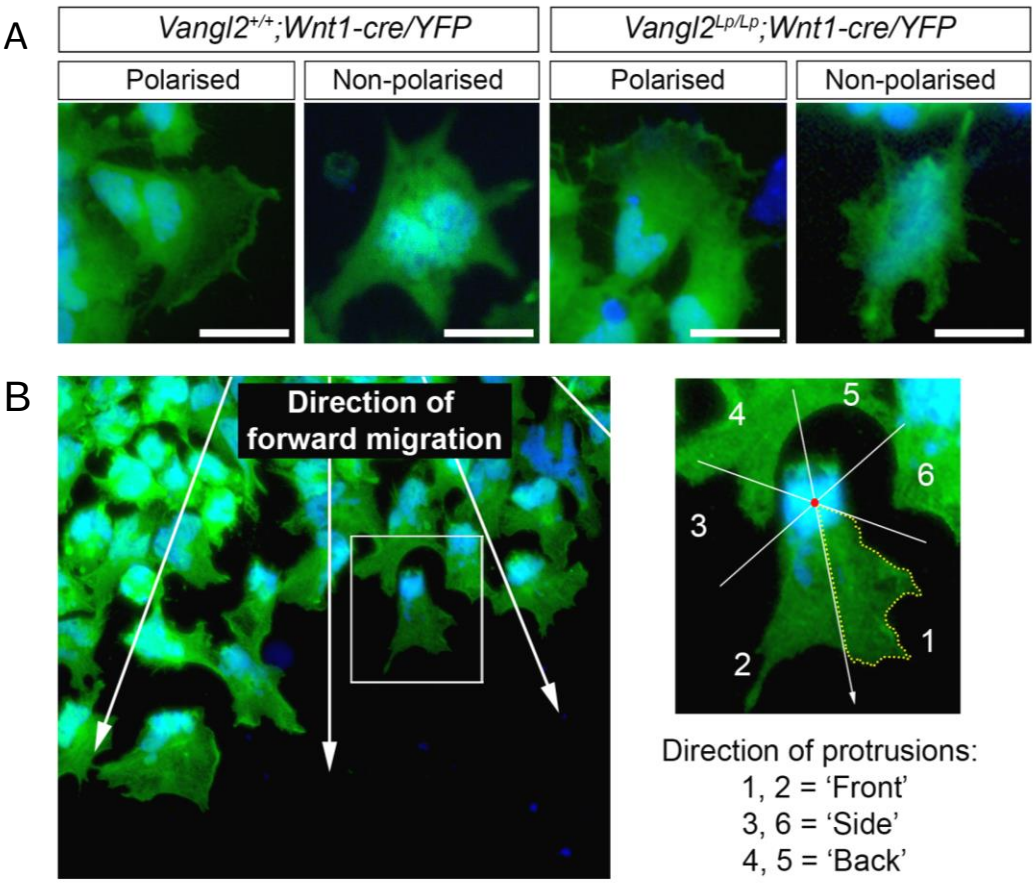
A
Vangl2+/+;Wnt1-cre/YFP
Vangl2Lp/Lp;Wnt1-cre/YFP
Polarised
Non-polarised
Polarised
Non-polarised
B
Direction of forward migration
4
5
6
3
1
2
Direction of protrusions:
1, 2 = 'Front'
3, 6 = 'Side'
4, 5 = 'Back'

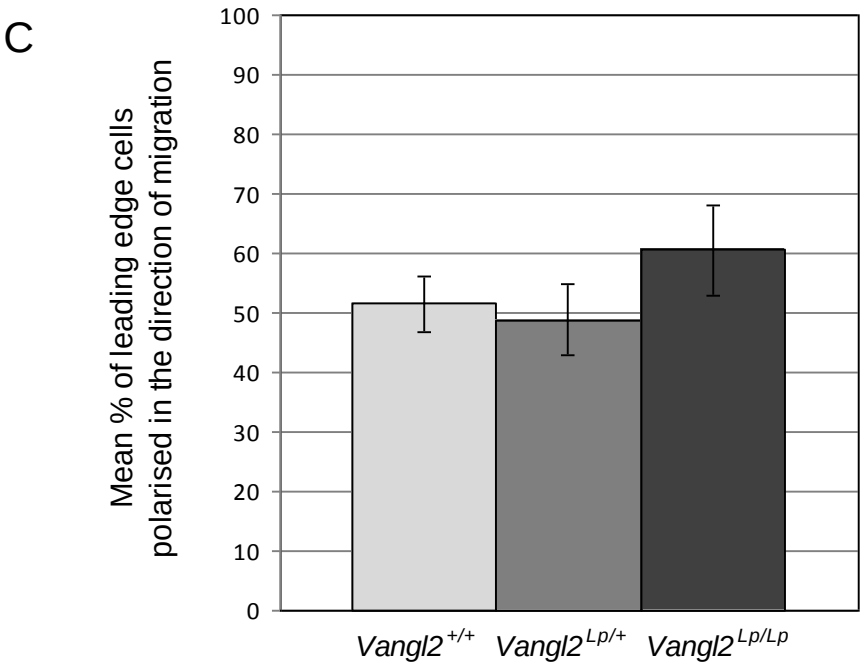
C
Mean % of leading edge cells polarised in the direction of migration
100
90
80
70
60
50
40
30
20
10
0
Vangl2+/+
Vangl2Lp/+
Vangl2Lp/Lp

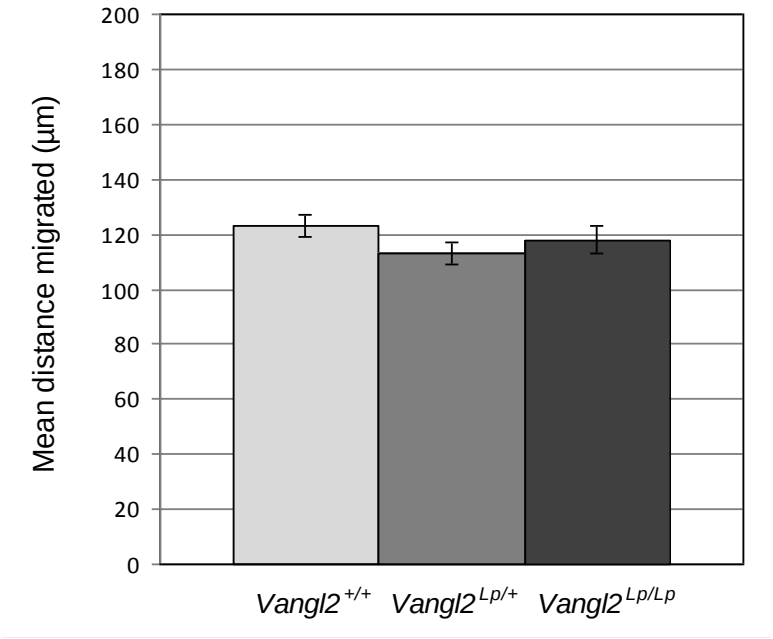

Figure 7.19 Distance migrated by neural crest cells in culture

The mean distance migrated by leading edge NC cells does not differ between genotypes (p = 0.21, Kruskal Wallis 1-way ANOVA on ranks; n = at least 64 cells from 3 explants for each genotype).

7.2.5 Acute ablation of *Vangl2* function in the neural crest lineage

Finally, we considered the possibility that absence of PCP signalling from *Vangl2*$^{Lp/Lp}$ embryos, throughout their development, might allow a compensatory mechanism such as the activation of a non-*Vangl2*-dependent pathway to arise in the NC or surrounding tissue, allowing normal NC migration (Figure 7.20A). This was addressed by crossing *Vangl2*$^{Lp/+}$*;Wnt1-Cre/YFP* (obtained from the breeding scheme shown in Figure 7.6) with *Vangl2*$^{flox/flox}$ mice, to produce *Vangl2*$^{Lp/flox}$*;Wnt1-Cre* and *Vangl2*$^{Lp/flox}$*;Wnt1-Cre/YFP* offspring in which *Vangl2* expression was acutely ablated specifically in the NC lineage. That is, in non-*Wnt1*-expressing tissues, such embryos were heterozygous for the *Vangl2*^{Lp} allele, whereas in the *Wnt1*-positive NC cells they were *Vangl2*$^{Lp/-}$ (See Figure 7.21 for breeding strategy). It was hypothesised that acute ablation of *Vangl2*

would prevent the 'compensatory mechanism' that putatively results from constitutional abrogation of *Vangl2* function. Hence, if NC migration is, in fact, PCP-dependent, the conditional *Vangl2*$^{Lp/flox}$*; Wnt1-Cre/YFP* embryos should exhibit NC defects (Figure 7.20B).

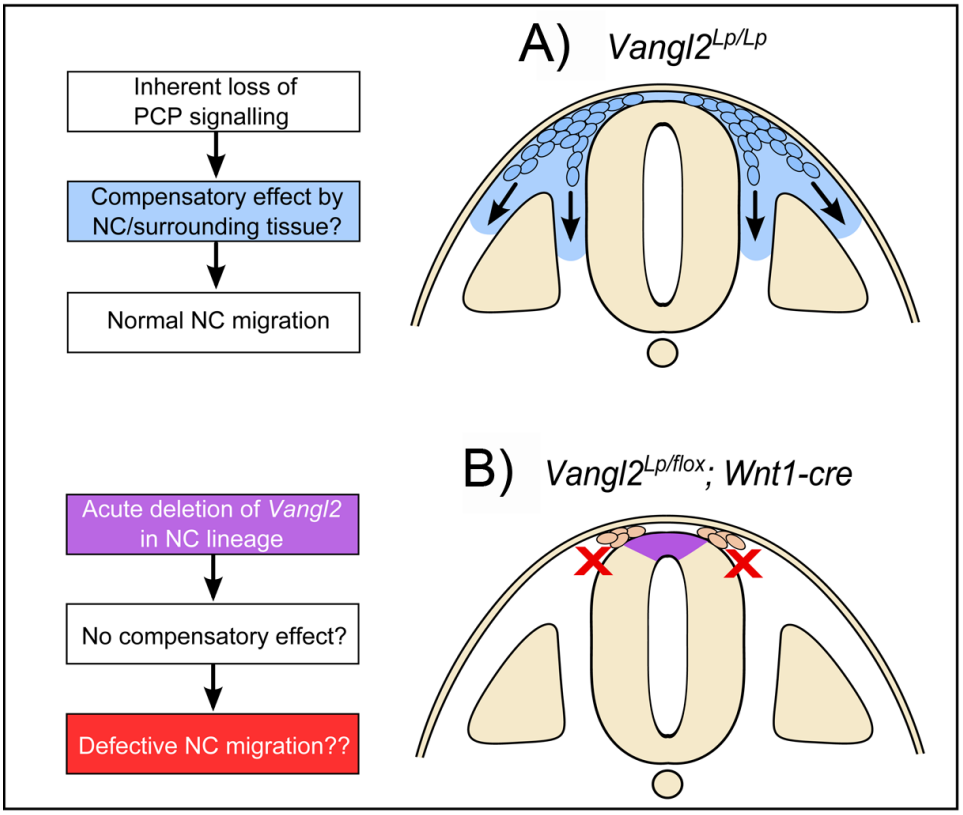

Figure 7.20 Hypothesis being tested by acutely ablating *Vangl2* in the neural crest

Schematic diagram of the hypothesis being tested. (A) Could the constitutional ablation of PCP signalling in *Vangl2*$^{Lp/Lp}$ embryos lead to a compensatory mechanism (blue) by the NC or surrounding tissue, resulting in normal NC migration? (B) Predicted effect on NC migration in *Vangl2*$^{Lp/flox}$*;Wnt1-Cre* embryos if such a mechanism exists. Would acute ablation of *Vangl2* in the NC (*Vangl2*$^{Lp/-}$; purple region) prevent the compensatory effect, resulting in defective NC migration?

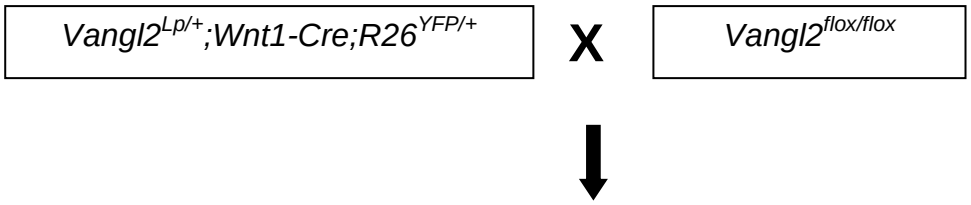

Cre +ve offspring:

Vangl2$^{+/flox(-)}$*;R26*$^{+/+}$

***Vangl2*$^{+/flox(-)}$*;R26*$^{YFP/+}$**

'Type 1 controls' – deletion of one copy of *Vangl2* in the NCC

Vangl2$^{Lp/flox(-)}$*;R26*$^{+/+}$

***Vangl2*$^{Lp/flox(-)}$*;R26*$^{YFP/+}$**

'Experimental' – *Lp* heterozygous plus deletion of other *Vangl2* allele in the NCC

Cre -ve offspring:

Vangl2$^{+/flox}$*;R26*$^{+/+}$

Vangl2$^{+/flox}$*;R26*$^{YFP/+}$

'Type 2 controls' – wild type levels of *Vangl2*

Vangl2$^{Lp/flox}$*;R26*$^{+/+}$

Vangl2$^{Lp/flox}$*;R26*$^{YFP/+}$

'Type 3 controls' – *Lp* heterozygous

Figure 7.21 Breeding scheme used to generate *Vangl2*$^{Lp/flox}$*;Wnt1-cre* embryos

Matings between *Vangl2*$^{Lp/+}$*;Wnt1-Cre;R26*$^{YFP/+}$ and *Vangl2*$^{flox/flox}$ mice produces embryos with one of 8 possible genotypes. However, Cre-negative offspring were not genotyped for the presence of the *R26*^{YFP} allele, meaning that embryos were actually assigned to one of the following 6 categories: non-fluorescent type 1 control, fluorescent type 1 control, non-fluorescent experimental, fluorescent experimental, Type 2 control or Type 3 control. Green text indicates fluorescent embryos.

Embryos from *Vangl2*$^{Lp/+}$*;Wnt1-cre;R26*$^{YFP/+}$ X *Vangl2*$^{flox/flox}$ matings were collected at E9.5 for analysis and genotypes were obtained in the expected Mendelian ratios (Table 7.1). Unlike in *loop-tail* litters, craniorachischisis was never seen; all embryos had successfully completed closure 1 and were undergoing PNP closure. Whole-mount analysis of *Vangl2*$^{Lp/flox}$*;Wnt1-Cre/YFP* embryos revealed a pattern of fluorescently-labelled NC cells that was indistinguishable from *Vangl2*$^{+/flox}$*;Wnt1-Cre/YFP* controls (Figure 7.22). YFP-positive NC cells appeared normally distributed within the pharyngeal region (Figure 7.22D) and could be seen migrating in organised streams within the trunk (Figure 7.22E, arrows). Further caudally, NC cells were observed beginning to migrate from the neuroepithelium in both genotypes (Figure 7.22C and F). Similarly, WISH for *Erbb3* at E9.5 revealed no difference between *Vangl2*$^{Lp/flox}$*; Wnt1-Cre* embryos and controls (Figure 7.23). Together these findings show that acute ablation of *Vangl2* in the NC does not lead to migratory defects, indicating that the normal pattern of NC migration observed in *Vangl2*$^{Lp/Lp}$ embryos is not due to a compensatory mechanism masking a role for the *Vangl2* protein.

Offspring Category	Expected		Observed	
	%	Freq.	%	Freq.
Type 1 controls (non-fluorescent)	12.50	3/23	26.09	6/23
Type 1 controls **(fluorescent)**	12.50	3/23	8.70	2/23
Experimental (non-fluorescent)	12.50	3/23	8.70	2/23
Experimental **(fluorescent)**	12.50	3/23	13.04	3/23
Type 2 controls	25.00	6/23	21.74	5/23
Type 3 controls	25.00	6/23	21.74	5/23
Deviation from Mendelian ratios:	χ^2=1.561 with 5 degrees of freedom (p = 0.906)			

Table 7.1 Genotype frequencies of E9.5 offspring from *Vangl2*$^{Lp/+}$*;Wnt1-Cre;R26*$^{YFP/+}$ X *Vangl2*$^{flox/flox}$ matings

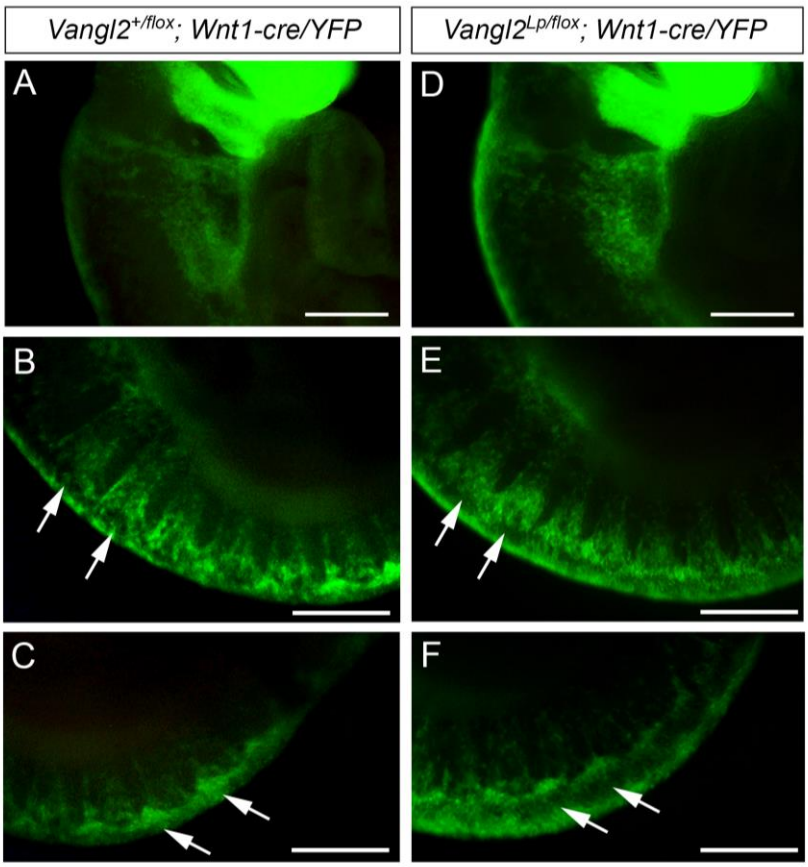

Figure 7.22 Neural crest cells migrate normally following acute ablation of *Vangl2*.

Control *Vangl2*$^{+/flox}$*; Wnt1-Cre/YFP* and experimental *Vangl2*$^{Lp/flox}$*; Wnt1-Cre/YFP* E9.5 embryos showing directly visualised YFP-positive NC cells, which have colonised branchial arches 1 and 2, with similar appearance in both genotypes (A and D). Comparable streams of NC cells can be seen migrating from the dorsal neural tube in the trunk (arrows in B and E), and beginning to delaminate more caudally (arrows in C and F). n = minimum of 2 embryos per genotype. Scale bars: 100 µm.

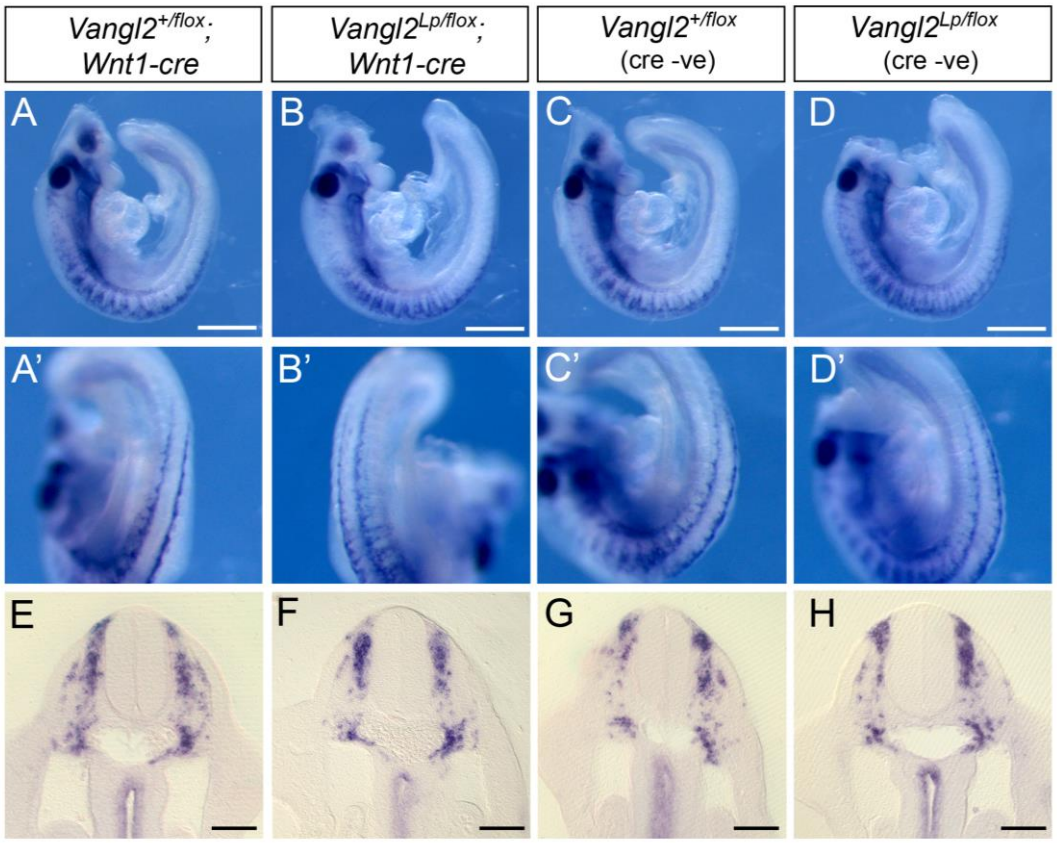

Figure 7.23 *Erbb3* WISH reveals normal NC migration in *Vangl2$^{Lp/flox}$; Wnt1-Cre* embryos.

Whole-mount *in situ* hybridisation for the NC marker *Erbb3* in E9.5 *Vangl2$^{Lp/flox}$; Wnt1-Cre* (B) and control (A, C, D) embryos. No difference in the pattern of NC migration was observed between genotypes (A-D show dorsal views, A'-D' show lateral views of the same embryos). Transverse sections through the embryos in A-D show a closely similar pattern of NC emigration from the neural tube and colonisation of the region adjacent to the paired aortae in *Vangl2$^{Lp/flox}$; Wnt1-Cre* (F) and controls (E, G, H). n = 3 embryos per genotype.

7.3 Discussion

The data described in this chapter demonstrate that *Vangl2*, a highly conserved, core component of the PCP signalling pathway, is not required for NC migration in mouse embryos. These findings indicate that PCP signalling is not essential for this process during mammalian development and, therefore, that PCP-dependence of NC migration is not a universal phenomenon among vertebrate species.

NC cell distribution in *Vangl2*$^{Lp/Lp}$ embryos was examined using both gene expression markers and YFP lineage tracing. Despite the many severe developmental defects in *loop-tail*, including complete failure of neural tube closure, NC specification and migration were found to proceed normally. No differences in the spatiotemporal patterns of cranial and trunk NC migration were identified between *loop-tail* and wild type embryos, and *Vangl2*$^{Lp/Lp}$ NC-derived structures appeared to be appropriately sized and patterned. Normal NC development was also observed when *Vangl2* was diminished specifically in the NC lineage, arguing against the possibility that constitutional absence of PCP signalling, as in *loop-tail*, results in a compensatory mechanism masking PCP-dependence of NC migration. *In vitro*, the migration of cells from *loop-tail* neural tube explants was found to be indistinguishable from controls.

7.3.1 Support from previous studies

The data presented here are consistent with previous reports which allude to species differences in the role of PCP signalling during NC migration. Evidence against an essential role in mammals comes from a study examining cardiovascular development in *loop-tail* mutant mice. Henderson and colleagues (Henderson et al., 2001) identified outflow tract and aortic arch abnormalities in *Vangl2*$^{Lp/Lp}$ embryos, problems which are often related to defects in the cardiac NC. However an examination of NC markers at E10.5, when NC cells are migrating towards the developing outflow tract, did not reveal

any migratory defects in these mice. Histological analysis also showed that NC-derived structures such as cranial and dorsal root ganglia appear to form normally. However, this study did not provide a detailed examination of NC migration in PCP mutants at earlier stages, or in other regions of the developing embryo.

Support for our data is also provided by studies of *Ptk7*, a regulator of PCP signalling during convergent extension, neural tube closure, heart morphogenesis, lung development and inner ear hair cell formation in mice, and neural convergent extension in *Xenopus* (Lu et al., 2004; Paudyal et al., 2010; Yen et al., 2009). In *Xenopus Ptk7* has also been found to regulate NC migration (Shnitsar and Borchers, 2008), with its disruption causing a NC phenotype similar to that of the PCP morphants described earlier (De Calisto et al., 2005). *Xenopus Ptk7* is thought to promote PCP signalling by forming part of a protein complex with Dsh and Fz7 that localises Dsh to the plasma membrane (Shnitsar and Borchers, 2008). However, the *Ptk7* mutant mouse, *chuzhoi*, does not exhibit overt NC migration defects and has normally patterned NC derivatives (Paudyal et al., 2010).

Downstream of the core PCP genes, the small GTPase *Rac1* is involved in the directional migration of *Xenopus* NC cells (Matthews et al., 2008). In mouse embryos the proliferation and cell cycle control of post-migratory NC is *Rac1* dependent (Fuchs et al., 2009). However *Rac1* is not required for the migration of mouse NC cells from the neural tube to their initial target structures and, *in vitro,* migration from *Rac1* knock-out NT explants is not impaired (Fuchs et al., 2009; Thomas et al., 2010).

7.3.2 Is PCP signalling completely abolished in *loop-tail* embryos?

Vangl2 is widely accepted to be a core component of the PCP pathway and is highly conserved from *Drosophila* to vertebrates. *Loop-tail* homozygous embryos are among the most severe mouse PCP mutants, displaying a broad spectrum of developmental abnormalities (see Chapter 1) All of the affected tissues have been identified as sites of *Vangl2* expression during embryogenesis (Montcouquiol et al., 2003; Torban et al., 2007; Vandenberg and Sassoon, 2009; Yates et al., 2010a; Yates et al., 2010b). In mammals Vangl2 interacts directly with all three Dishevelled family members, leading to their recruitment to the membrane. These associations appear to be crucial in establishing the asymmetric localisation of PCP protein complexes needed for signal transduction, and are abrogated or severely impaired when *Lp*-associated mutations are introduced (Torban et al., 2004). Furthermore, in *loop-tail* embryos the normal membrane localisation of Vangl2 protein is lost (Torban et al., 2007). As discussed in Chapter 6 there is now emerging evidence that *Vangl2*^{Lp} is, in fact, a dominant negative allele (Song et al., 2010; Yin et al., 2012). These findings indicate that the presence of the *Lp* mutant protein has an adverse effect on several of the key interacting proteins, hence producing a more profound disturbance of PCP function than the loss of wild-type Vangl2 alone.

7.3.3 Possible functional redundancy between *Vangl1* and *Vangl2*

Although not expressed by migrating NC cells themselves, *Vangl2* transcripts are present throughout the dorso-ventral axis of the neuroepithelium before, and at the stage of, NC migration (see Figure 7.11 and Figure 7.12), as has been reported previously (Kibar et al., 2001b; Torban et al., 2007). It is likely, therefore, that *Vangl2* is expressed by NC progenitors prior to their emigration from the neural tube. It was

therefore asked whether the closely-related gene *Vangl1* might compensate for the loss of *Vangl2* in pre-migratory *loop-tail* NC cells, masking an essential role for *Vangl2*. However in *loop-tail,* as in wild-type embryos, *Vangl1* transcripts are restricted to the ventral neuroepithelium and are not detected in either dorsal neuroepithelial cells or migratory NC cells. These data suggest that the *loop-tail* mouse model represents a complete abrogation of PCP signalling, without functional redundancy with *Vangl1*. However, the pattern of expression observed here differs slightly to that described previously using LacZ staining (Song et al., 2010), a more sensitive method than WISH. We are currently analysing NC migration in Vangl1/2 double mutant embryos, in collaboration with Dr Yingzi Yang.

7.3.4 How can the species difference be explained?

Despite the high level of similarity in NC migration among different vertebrate groups, some fundamental differences do exist, possibly reflecting variations in the signalling pathways and molecular mechanisms involved. For example, the timing of onset of migration varies between species (see Chapter 1). Indeed, while members of the core PCP pathway are expressed in migrating *Xenopus* NC cells, we did not detect expression of *Vangl2* at any stage of mouse NC migration, and there is published evidence that other core PCP components are also not expressed in mouse migratory NC cells. For example, *Celsr1*, whose homozygous mutants display craniorachischisis and cochlear disorganisation (Curtin et al., 2003), is expressed in a similar pattern to *Vangl2*; that is, within the neuroepithelium but not in the migrating NC cells (Formstone and Little, 2001; Shima et al., 2002).

Similarly the non-canonical Wnt ligand, *Wnt5a*, is not expressed in the NC cells in mouse ambryos; rather, transcripts are found in outgrowing areas of the embryo such as the facial primordial, limb buds and tail (Yamaguchi et al., 1999). Moreover, mouse

and frog *Dvl* homologues display very different expression patterns during development. *Xenopus Dvl1* and *Dvl2* exhibit strong tissue-specific expression in migrating NC cells and otic placodes, whereas no NC-specific expression has been described for any of the mouse *Dvl* genes (Gray et al., 2009b). Hence, it appears unlikely that an alternative, *Vangl2*-independent PCP pathway is activated in mammalian NC cells.

While non canonical Wnt/PCP signalling may regulate directional NC migration in *Xenopus* and zebrafish, our data suggest that other mechanisms are involved in the mouse. As described in Chapter 1, there is some evidence that positive cues such as chemoattractants have a role to play, with members of the VEGF, PDGF and FGF families of growth factors among the candidate molecules described (Theveneau and Mayor, 2012). Perhaps the best candidate for a NC chemoattractant is the chemokine *stromal cell-derived factor 1* (*Sdf1*) (Theveneau and Mayor, 2012), which is required for cranial NC migration in *Xenopus* and zebrafish (Olesnicky Killian et al., 2009; Theveneau et al., 2010). Theveneau and colleagues (Theveneau et al., 2010) demonstrated that NC cells in culture actively track moving Sdf1-soaked beads and that this chemotactic behaviour requires interactions with other neighbouring cells (termed 'collective chemotaxis'). While not required for the initial cell polarisation, *Sdf1* was found to stabilise the polarised protrusions promoted by cell-cell interactions. N-cadherin is also required for the response to Sdf1, with disruption of N-cadherin impairing cells' ability to 'sense' each other and exhibit contact inhibition of locomotion. Interestingly, N-cadherin blocking antibody (NCD2) treatment significantly reduced polarised Rac1 activity in the migrating cells, although the authors do not speculate about how N-cadherin and non canonical Wnt/PCP signalling might interact mechanistically (Theveneau et al., 2010).

In mice *Sdf1* is thought to play a role in the migration of various cell types, including melanoblasts and sensory neuron progenitors (Belmadani et al., 2005; Belmadani et al., 2009), suggesting that similar or unknown chemoattractants contribute to the directionality of NC migration in mammals, perhaps in combination with cell adhesion molecules and the RhoGTPases. It would appear, therefore, that the factors regulating cell-cell interactions, CIL, chemotaxis, and the restrictive signals which pattern the NC streams, must all be integrated in order for the NC to migrate with persistence and directionality.

8. General Discussion

8.1 PCP and low spinal neurulation

8.1.1 Summary of findings

The crucial role of PCP signalling in regulating CE prior to the initiation of neural tube closure has been well established in mice (see Chapter 1). One of the initial aims of this project was to investigate the requirement for PCP genes during a later event of spinal neurulation, closure of the posterior neuropore. To this end, the *loop-tail/curly tail* (*Vangl2*$^{Lp/+}$;*Grhl3*$^{ct/ct}$) mouse mutant provides a valuable model, not only to analyse the specific requirement for core PCP components, but also to unravel the nature of genetic interactions between *Vangl2* and *Grhl3*, two genes with important roles in neurulation. The *Vangl2*$^{Lp/+}$;*Grhl3*$^{ct/ct}$ spina bifida phenotype was found to be severe, both in terms of its frequency (>70% penetrance) and the axial level from which neural tube closure fails (Chapter 3). Initial analyses revealed that the defect arises due to primary failure of neural tube closure, but is not caused by a disruption of the dorsolateral bending that occurs in the neuroepithelium at this level. The phenotype is also not the result of an exacerbation, by *Vangl2*^{Lp}, of the known *curly tail* developmental defect (reduced hindgut proliferation and increased ventral body curvature).

Morphometric analyses showed that the *Vangl2*^{Lp} allele causes reduced CE in the midline of the caudal region (Chapters 3 and 4), evidence that this process is indeed an important aspect of neurulation at low spinal levels. When compared to wild type embryos, both *Vangl2*$^{Lp/+}$;*Grhl3*$^{+/+}$ and *Vangl2*$^{Lp/+}$;*Grhl3*$^{ct/ct}$ embryos display a shorter caudal embryonic axis and an increase in width of the ventral neuroepithelium and notochord, with the latter also accompanied by wider domains of marker gene expression. The effect of *Vangl2*^{Lp} on CE was confirmed by DiI labelling and whole embryo culture; these experiments demonstrated that the presence of the *Vangl2*^{Lp} allele is associated with a significant reduction in caudal axis extension.

However, with regards to the *Lp/ct* interaction, the severe spina bifida in *Vangl2*$^{Lp/+}$;*Grhl3*$^{ct/ct}$ is not solely explained by a 'PCP effect'. *Grhl3*^{ct} mutations were not found to influence the CE phenotype, raising the question of whether *Grhl3* is required for a different aspect of caudal development at E9-E9.5 (in addition to regulating hindgut and notochord proliferation at E10.5). Analysis of cell proliferation in the chordo-neural-hinge (CNH), one of several sites of *Grhl3* expression, revealed an abnormally low mitotic index in embryos carrying *ct* mutations, suggesting that *Grhl3* regulates cell cycle dynamics within the axial stem cell population of the tail bud. Thus, two distinct, tissue-specific effects appear to summate and contribute to the phenotype of *Vangl2*$^{Lp/+}$;*Grhl3*$^{ct/ct}$ mice; defective midline CE downstream of *Vangl2*^{Lp} and altered cell cycle dynamics in the tail bud downstream of *Grhl3*^{ct}. This 'tissue-tissue interaction' hypothesis is supported by the results of genetic experiments (Chapter 6). Here, the frequency of spinal neurulation defects is shown to be three-fold lower in conditional *Grhl3*$^{Cre/+}$;*Vangl2*$^{flox/+}$ embryos (9%) than in compound heterozygous *Grhl3*$^{+/-}$;*Vangl2*$^{+/-}$ embryos (29%) where one allele of *Vangl2* and *Grhl3* has been lost in all cells. This shows that a requirement for the two genes within the same cells of the embryo only partially accounts for the phenotype observed when they are both mutated.

The association between the presence of *Grhl3*^{ct} alleles and a reduced rate of cell proliferation in the CNH (and also in the neuroepithelium; see Chapter 4) corresponds to the timing and site of normal *Grhl3* expression. These data are consistent with the reduced proliferation seen in the hindgut of E10.5 *curly tail* embryos and with the finding that reinstating *Grhl3* function in this tissue via BAC transgenesis restores cell proliferation (Copp et al., 1988a; Gustavsson et al., 2007). However, the mechanism by which *Grhl3* regulates the cell cycle is not understood. As it is a transcription factor, the effects of reduced expression levels in *curly tail* are presumably exerted via the mis-regulation of downstream target genes, with *Grhl3* likely able to act as both a transcriptional activator and repressor (Kudryavtseva et al., 2003). Very few *Grhl3*

targets have been identified to date. Indeed, as described earlier in this thesis, the only known direct targets are *transglutaminase 1* (*TGase1*) and *RhoGEF19*, both of which were identified from analyses of expression levels in the skin at late gestation. It is possible, therefore, that these downstream genes are specific to the function of *Grhl3* during epidermal development and wound repair (Caddy et al., 2010; Ting et al., 2005). Work in our group is currently focused on trying to identify genes that are activated or suppressed by *Grhl3* during neural tube closure, and are mis-regulated in embryos that develop NTDs.

In addition to a tissue-tissue interaction, the finding that conditional *Grhl3*$^{Cre/+}$*;Vangl2*$^{flox/+}$ embryos develop low frequency spinal defects (Chapter 6) does also show that there is some interaction between *Grhl3* and *Vangl2* within cells in which they are co-expressed, and that this affects neurulation. This indicates that a second, cell-autonomous effect also makes a minor contribution to the *Lp/ct* phenotype. Possible mechanisms underlying this interaction were investigated in Chapter 5. The expression domains of *Vangl2* and *Grhl3* were found to overlap at E9-E9.5, most notably in the neuroepithelium, consistent with a possible interaction at a molecular level. The expression level of each gene was found to be unaltered when the other gene was mutated, and expression of the PCP ligand *Wnt5a* was not diminished in *curly tail* (or *Vangl2*$^{Lp/+}$*;Grhl3*$^{ct/ct}$) embryos, contrary to a previous study (Gofflot et al., 1998). However, a possible transcriptional effect of *Grhl3* at the level of RhoGTPase signalling was identified; in the *curly tail* (and to a lesser extent in the *Vangl2*$^{Lp/+}$*;Grhl3*$^{ct/ct}$) caudal region an increase in the RhoA activators, *RhoGEF19* and *ArhGEF3*, as well as an increase in *ROCK1*, was identified. Interestingly, the level of active RhoA was reduced in both *Vangl2*$^{Lp/+}$*;Grhl3*$^{+/+}$ and *Vangl2*$^{+/+}$*;Grhl3*$^{ct/ct}$ embryos and a cumulative reduction was observed in *Vangl2*$^{Lp/+}$*;Grhl3*$^{ct/ct}$, although whether this represents decreased RhoA activation or diminished levels of total RhoA protein remains to be determined. In support of this result, pharmacological inhibition of the

pathway by ROCK inhibition in whole embryo culture summates with the *Vangl2*$^{Lp/+}$;*Grhl3*$^{+/+}$ and *Vangl2*$^{+/+}$;*Grhl3*$^{ct/ct}$ genotypes to delay PNP closure.

These data point towards a requirement for RhoA-ROCK signalling downstream of PCP genes during low spinal neurulation, as has been shown previously for closure 1 (Ybot-Gonzalez et al., 2007b). However, how this pathway ultimately affects caudal development is unclear. If *Vangl2* and *Grhl3* do interact in the neuroepithelium at the level of RhoA-ROCK signalling to regulate midline CE, then a more severe axis elongation phenotype might be expected in *Vangl2*$^{Lp/+}$;*Grhl3*$^{ct/ct}$ embryos compared to *Vangl2*$^{Lp/+}$;*Grhl3*$^{+/+}$. This is not the case and, moreover, *curly tail* embryos do not display defective CE. Alternatively, the requirement for RhoA-ROCK might again reflect tissue-specific roles downstream of *Vangl2* and *Grhl3* during midline CE and tail bud proliferation, respectively. It would be interesting to determine whether ROCK inhibition adversely affects these processes.

8.1.2 PCP and NTD spectrum in mice

When considering the relationship between PCP gene mutations and NTDs in mice, several interesting patterns emerge (Juriloff and Harris, 2012a). For example, genetic redundancy between both homologous and non-homologous genes is common, as is the appearance of multiple phenotypic traits (such as neural tube, cochlea and heart defects) when a single gene is mutated, a phenomenon known as ‘pleiotropy’. Another theme is that, among the mutants with a craniorachischisis phenotype, the penetrance is usually high, often 100%. The work in this thesis is particularly relevant with regards to the link between PCP mutations and the types of NTD phenotypes that are produced. As described in Chapter 1, craniorachischisis in the mouse is caused almost exclusively by mutations in PCP genes or genes that affect the function of this pathway. However, this is not the only NTD associated with disturbed PCP signalling;

the *Vangl2* genetic interactions listed in Chapter 3 are clear examples of the effects of mutant combinations on the development of spina bifida and exencephaly. These other conditions are either the sole NTD phenotype observed in such mutant strains, or they occur as an alternative phenotype to craniorachischisis (see Table 3.1 in Chapter 3). While defective CE has been found to underlie craniorachischisis in several PCP mutants, the cellular basis of spina bifida and exencephaly has not been clearly demonstrated (see below). An understanding of these mechanisms, and of the basis of the PCP 'modifier gene' effect, could also indicate how PCP signalling might increase genetic predisposition to different types of NTDs in humans.

The findings of this thesis show that PCP-dependent CE is required for successful neurulation in the low spine. It seems likely, therefore, that spina bifida in other PCP mutants, including hypomorphic *Vangl2*$^{Lpm2Jus;Lpm2Jus}$ mice (Guyot et al., 2011) and digenic models such as *Vangl2/Fzd* and *Vangl2/Ptk7* mutants (Lu et al., 2004; Paudyal et al., 2010; Yu et al., 2010), arises via a similar mechanism. For spina bifida models that comprise interactions between PCP and non-PCP genes (see Chapter 3; *Vangl2*$^{Lp/+}$*;Sec24b*$^{Y613/+}$, *Vangl2*$^{Lp/+}$*;Grhl3*$^{+/-}$, *Vangl2*$^{Lp/+}$*;Grhl3*$^{ct/ct}$ and *Vangl2*$^{Lp/+}$*;Zic2*$^{ku/+}$) there has not yet been published evidence demonstrating whether spinal neurulation fails due to molecular interactions between the genes influencing the same developmental process, or as a result of tissue-tissue interactions. While the former mechanism might be predicted to explain the interaction between *Vangl2* and the COPII vesicle gene *Sec24b* (Merte et al., 2010), the data presented here (Chapters 4-6) indicate that the *Vangl2*/*Grhl3* interaction during neurulation is largely due to distinct, tissue-specific effects.

The association between PCP and exencephaly is also interesting. Indeed, *Vangl2* interacts with a number of genes to cause this defect, with variable penetrance (see Chapter 3), and it is the only NTD phenotype produced by mutations in the PCP

effector genes *Inturned* (*Intu*) and *Fuzzy* (*Fuz*) (Gray et al., 2009a; Heydeck et al., 2009; Zeng et al., 2010). The appearance of exencephaly could reflect other functions of PCP genes at different levels of the neuraxis. In particular it has been suggested that the link between PCP signalling and cilia, a seemingly complex relationship that has emerged in recent years, is involved. On one hand PCP proteins have been found to control the polarised beating of motile cilia in several tissues while, on the other hand, there is evidence to support a role for cilia in PCP signal transduction: mice mutant for several genes associated with the ciliopathy Bardet-Biedl syndrome (BBS) display PCP-like phenotypes and several ciliopathy genes interact genetically with *Vangl2* (Wallingford and Mitchell, 2011). In mouse embryos, null mutations in *Intu* and *Fuz* cause exencephaly, defective ciliogenesis in various structures, abnormal patterning of the neural tube and limb buds and disrupted hedgehog signalling (Gray et al., 2009a; Heydeck et al., 2009; Zeng et al., 2010). However, these studies did not explore the cellular basis of the cranial NTDs in these mutants. The nature of the requirement for *Intu* and *Fuz* during neurulation remains elusive; indeed, a recent study found that they do not show genetic interactions with *Vangl2* or regulate CE in the midline (Heydeck and Liu, 2011).

8.1.3 Clinical relevance of findings

Of the over 240 mouse models of NTDs, many arise from single-gene mutations and these are often syndromic. However, several others develop NTDs as a result of digenic or oligogenic interactions (Harris and Juriloff, 2007; Harris and Juriloff, 2010) and this latter group is likely to better reflect the complex aetiology of human NTDs. To explain the pattern of NTD inheritance observed in humans, the ‘multifactorial threshold model’ has been proposed (Harris and Juriloff, 2007; Zohn, 2012). This theory predicts that multiple genetic and environmental factors, which alone do not cause NTDs, interact to influence the outcome of neurulation. These may act in a

cumulative fashion to affect a single developmental process or act synergistically, involving processes in more than one tissue (Zohn, 2012). As a result, individuals with particular combinations of genetic variants and environmental influences have an elevated risk of disturbed neurulation; if neural tube closure is compromised beyond a certain threshold it fails, resulting in NTDs.

This model seems to fit well with the known additive effects of PCP gene mutations in predisposing to failure of neurulation in mice, and with the well established modifying effect of the *Vangl2*^{Lp} mutation (see Chapter 3). It is also particularly relevant to the findings described here for genetic interactions between *Vangl2* and *Grhl3*. The heterozygous *Vangl2*$^{Lp/+}$ genotype causes defective CE during spinal neurulation, but only when combined with a 'second hit' such as the presence of *Grhl3*^{ct} alleles does it lead to a severe NTD phenotype. Similarly, the model is consistent with the effect of modifier loci on NTD phenotype, such as in the *curly tail* mouse (de Castro et al., 2012; Van Straaten and Copp, 2001). In these cases polymorphic modifier alleles vary between strains and exert little effect on their own. However, when suboptimal variants are inherited with a particular gene mutation, which already compromises neurulation, they can determine whether a cellular/developmental process falls above or below the threshold level required for successful neural tube closure.

As described in Chapter 1, several recent studies have screened the coding sequences of candidate PCP genes in human NTD cases to look for rare, non-synonymous, deleterious sequence variants that are not present in controls. The identification of such putative mutations in several PCP components suggests that variants of genes within this complex signalling network contribute to the aetiology of human NTDs and should be a focus of future studies. According to a recent review of these reports, overall, PCP mutations were detected in 44 out of over 500 cases with defects of primary neurulation. These included open NTDs as well as closed defects

such as lipomyelomeningocele, lipomyelocele and lipoma. In total, 44 mutations were identified; these were in eight PCP genes (*CELSR1*, *VANGL1*, *VANGL2*, *FZD6*, *PRICKLE1*, *SCRIB*, *FUZ* and the PCP-related gene, *DACT1*) and the majority were heterozygous, non-synonymous and affected highly conserved amino acids. For around half of them, biological assays were used to test whether the variant had a deleterious effect on the protein and, of these, 76% displayed functional abnormalities (Juriloff and Harris, 2012a). Interestingly, PCP mutations were also found in cases of defects thought to arise from aberrant secondary neurulation (such as tight filum terminale and lumbar myelocystocele) as well as cases of caudal regression and diastematomyelia, which are not NTDs but rather are gastrulation and notochord defects that were included in some NTD cohorts.

When considering the evidence for a contribution of PCP mutations to human NTD aetiology, it should be noted that the approaches used so far raise the possibility that there are additional, undetected mutations. The general strategy has been to identify rare variants that are absent in controls. However, consistent with the multifactorial threshold model, studies that had available sequence data for family members sometimes showed that the mutation was transmitted from an apparently unaffected parent. If this is the case then the variants are presumably also present in other unaffected individuals within the same population and contribute to NTDs in combination with other genetic or environmental factors. Their absence in the majority of sequenced controls is likely to be explained by their rarity (Juriloff and Harris, 2012a). It is likely, therefore, that other deleterious variants do exist and have been overlooked due to their presence in control samples. Moreover, the strategy of sequencing coding regions of PCP genes does also not detect other types of mutations, such as copy number variants and those in regulatory elements.

In contrast to PCP genes, no putative *GRHL3* mutations have been identified in human NTD cases to date. However, as described earlier in this thesis, both insufficient and excessive levels of *Grhl3* expression, as a result of either coding or regulatory mutations, cause NTDs in mice. *GRHL3* therefore represents a candidate gene that could contribute to risk of human NTDs. It will be interesting to see if rare variants are found to be associated with NTD cases and, if so, whether these are present in combination with other mutations, for example in PCP family members.

8.2 PCP and NC cell migration

In recent years, several studies have reported an essential role for the PCP signalling pathway in NC cell migration (Carmona-Fontaine et al., 2008a; Carmona-Fontaine et al., 2008b; De Calisto et al., 2005; Matthews et al., 2008). The evidence in these papers came from *Xenopus* and zebrafish embryos and was based on the effects of expressing dominant negative constructs that perturb PCP signalling. Since these findings, the question of whether a similar relationship applies to mammalian development has not been investigated. Data in this thesis demonstrates that abrogation of the core PCP component, *Vangl2*, does not cause defects of early NC cell migration, or the initial formation of NC-derived structures in mice (findings summarised in Chapter 7). This is in stark contrast to various other developmental processes, which are strongly PCP-dependent in mammals, such as neural tube closure and inner ear development (see Chapter 1). Thus, these findings indicate that PCP-dependence is not a universal feature of NC cell migration and therefore represents an important species difference in the molecular regulation of NC development.

8.2.1 Clinical significance

The biology of the NC is of considerable clinical significance as defects of their development contribute to medical conditions in humans. NC-related disorders comprise a heterogeneous group of diseases, collectively known as the 'neurocristopathies' (Bolande, 1997). The extensive range of malformations seen within this group, such as craniofacial, heart and gut innervation defects, reflects the wide variety of NC cell derivatives in the embryo. For example, neurocristopathies include: Hirschsprung's disease, a bowel motility disorder characterized by aganglionosis of the distal colon due to failure of NC colonization (Burzynski et al., 2009); Waardenberg syndrome, which is classified into subtypes depending on its symptoms, but often combines sensorineural hearing loss, pigmentation defects and craniofacial abnormalities (Pingault et al., 2010; Read and Newton, 1997); and DiGeorge syndrome, a severe form of the chromosome disorder 22q11 deletion, which can involve many symptoms, such as heart defects, cleft palate, facial dysmorphology and glandular defects (Wurdak et al., 2006). Some neurocristopathies also occur as aggressive tumours, derived from NC cells, such as neuroblastomas and melanomas (Bolande, 1997).

The NC has also attracted attention as a model of invasive cell migration, as there are several similarities between NC cell migration and tumour cell metastasis (Theveneau and Mayor, 2012). Both NC and cancer cells express a combination of transcription factors (including *Snail*, *Twist*, and *Sox* family members), which enables them to undergo EMT. Also, as described in Chapter 1, an important aspect of EMT is a change in cell-cell adhesion properties, allowing cells to delaminate from their original tissue. Similar to NC cells, switches in the expression of cadherin molecules have been observed in several tumour cell types (Wheelock et al., 2008). Like NC cells, tumour cells also express members of the MMP and ADAM metalloprotease families and this

is often associated with a high invasive potential and poor disease prognosis (Theveneau and Mayor, 2012). Thus, it appears that the mechanisms controlling the release and migration of malignant cells from a primary tumour are similar to those used during the delamination of NC cells from the neuroepithelium. Furthermore, on reaching their final destination in the embryo, NC cells cease migration and undergo differentiation. During this process, the cells often reaggregate, for example during the formation of the ganglia of the PNS. Interestingly there is evidence that metastatic cells revert to a more epithelial-like state during the formation of secondary tumours, and that this increases their survival ability (Polyak and Weinberg, 2009).

In summary, an understanding of the genes and pathways that trigger and regulate NC cell migration is essential in order to better understand neurocristopathies and tumour progression. Given the evidence for a crucial role of PCP signalling during NC cell migration in amphibia and fish, it might be predicted that PCP genes are strong candidates for the study of NC-related pathologies in humans. However, the findings of this thesis argue otherwise and suggest that attention should be focused elsewhere.

References

Abdul-Aziz,N.M., Turmaine,M., Greene,N.D., and Copp,A.J. (2009). EphrinA-EphA receptor interactions in mouse spinal neurulation: implications for neural fold fusion. *Int. J. Dev. Biol.* 53, 559-568.

ABERCROMBIE,M. and HEAYSMAN,J.E. (1953). Observations on the social behaviour of cells in tissue culture. I. Speed of movement of chick heart fibroblasts in relation to their mutual contacts. *Exp. Cell Res.* 5, 111-131.

ABERCROMBIE,M. and HEAYSMAN,J.E. (1954). Observations on the social behaviour of cells in tissue culture. II. Monolayering of fibroblasts. *Exp. Cell Res.* 6, 293-306.

Adinolfi,M., Beck,S., Embury,S., Polani,P.E., and Seller,M.J. (1976). Levels of alpha-fetoprotein in amniotic fluids of mice (curly-tail) with neural tube defects. *J. Med. Genet.* 13, 511-513.

Adzick,N.S., Thom,E.A., Spong,C.Y., Brock,J.W., III, Burrows,P.K., Johnson,M.P., Howell,L.J., Farrell,J.A., Dabrowiak,M.E., Sutton,L.N. et al. (2011). A randomized trial of prenatal versus postnatal repair of myelomeningocele. *N. Engl. J. Med.* 364, 993-1004.

Alfandari,D., Cousin,H., Gaultier,A., Smith,K., White,J.M., Darribere,T., and DeSimone,D.W. (2001). Xenopus ADAM 13 is a metalloprotease required for cranial neural crest-cell migration. *Curr. Biol.* 11, 918-930.

Allache,R., De,M.P., Merello,E., Capra,V., and Kibar,Z. (2012). Role of the planar cell polarity gene CELSR1 in neural tube defects and caudal agenesis. *Birth Defects Res. A Clin. Mol. Teratol.* 94, 176-181.

Amorim,M.R., Lima,M.A., Castilla,E.E., and Orioli,I.M. (2007). Non-Latin European descent could be a requirement for association of NTDs and MTHFR variant 677C > T: a meta-analysis. *Am. J. Med. Genet. A* 143A, 1726-1732.

Ang,S.L. and Rossant,J. (1994). HNF-3 beta is essential for node and notochord formation in mouse development. *Cell* 78, 561-574.

Attardi,L.D., Von,S.D., and Tjian,R. (1993). Ectopic expression of wild-type or a dominant-negative mutant of transcription factor NTF-1 disrupts normal Drosophila development. *Proc. Natl. Acad. Sci. U. S. A* 90, 10563-10567.

Au,K.S., Ashley-Koch,A., and Northrup,H. (2010). Epidemiologic and genetic aspects of spina bifida and other neural tube defects. *Dev. Disabil. Res. Rev.* 16, 6-15.

Auden,A., Caddy,J., Wilanowski,T., Ting,S.B., Cunningham,J.M., and Jane,S.M. (2006). Spatial and temporal expression of the Grainyhead-like transcription factor family during murine development. *Gene Expr. Patterns.* 6, 964-970.

Beier,D.R., Dushkin,H., and Telle,T. (1995). Haplotype analysis of intra-specific backcross curly-tail mice confirms the localization of ct to chromosome 4. *Mamm. Genome* 6, 269-272.

Belmadani,A., Jung,H., Ren,D., and Miller,R.J. (2009). The chemokine SDF-1/CXCL12 regulates the migration of melanocyte progenitors in mouse hair follicles. *Differentiation* 77, 395-411.

Belmadani,A., Tran,P.B., Ren,D., Assimacopoulos,S., Grove,E.A., and Miller,R.J. (2005). The chemokine stromal cell-derived factor-1 regulates the migration of sensory neuron progenitors. *J. Neurosci.* 25, 3995-4003.

Belotti,E., Puvirajesinghe,T.M., Audebert,S., Baudelet,E., Camoin,L., Pierres,M., Lasvaux,L., Ferracci,G., Montcouquiol,M., and Borg,J.P. (2012). Molecular characterisation of endogenous Vangl2/Vangl1 heteromeric protein complexes. *PLoS. One.* 7, e46213.

Berry,R.J., Li,Z., Erickson,J.D., Li,S., Moore,C.A., Wang,H., Mulinare,J., Zhao,P., Wong,L.Y., Gindler,J. et al. (1999). Prevention of neural-tube defects with folic acid in China. China-U.S. Collaborative Project for Neural Tube Defect Prevention. *N. Engl. J. Med.* 341, 1485-1490.

Bolande,R.P. (1997). Neurocristopathy: its growth and development in 20 years. *Pediatr. Pathol. Lab Med.* 17, 1-25.

Bosoi,C.M., Capra,V., Allache,R., Trinh,V.Q., De,M.P., Merello,E., Drapeau,P., Bassuk,A.G., and Kibar,Z. (2011). Identification and characterization of novel rare mutations in the planar cell polarity gene PRICKLE1 in human neural tube defects. *Hum. Mutat.* 32, 1371-1375.

Bray,S.J., Johnson,W.A., Hirsh,J., Heberlein,U., and Tjian,R. (1988). A cis-acting element and associated binding factor required for CNS expression of the Drosophila melanogaster dopa decarboxylase gene. *EMBO J.* 7, 177-188.

Bray,S.J. and Kafatos,F.C. (1991). Developmental function of Elf-1: an essential transcription factor during embryogenesis in Drosophila. *Genes Dev.* 5, 1672-1683.

Brook,F.A., Shum,A.S., Van Straaten,H.W., and Copp,A.J. (1991). Curvature of the caudal region is responsible for failure of neural tube closure in the curly tail (ct) mouse embryo. *Development* 113, 671-678.

Brouns,M.R., de Castro,S.C., Terwindt-Rouwenhorst,E.A., Massa,V., Hekking,J.W., Hirst,C.S., Savery,D., Munts,C., Partridge,D., Lamers,W. et al. (2011). Over-expression of Grhl2 causes spina bifida in the Axial defects mutant mouse. *Hum. Mol. Genet.* 20, 1536-1546.

Brouns,M.R., Matheson,S.F., Hu,K.Q., Delalle,I., Caviness,V.S., Silver,J., Bronson,R.T., and Settleman,J. (2000). The adhesion signaling molecule p190 RhoGAP is required for morphogenetic processes in neural development. *Development* 127, 4891-4903.

Brouns,M.R., Peeters,M.C., Geurts,J.M., Merckx,D.M., Engelen,J.J., Hekking,J.W., Terwindt-Rouwenhorst,E.A., Oosterbaan,M.E., Geraedts,J.P., and Van Straaten,H.W. (2005). Toward positional cloning of the curly tail gene. *Birth Defects Res. A Clin. Mol. Teratol.* 73, 154-161.

Burren,K.A., Savery,D., Massa,V., Kok,R.M., Scott,J.M., Blom,H.J., Copp,A.J., and Greene,N.D. (2008). Gene-environment interactions in the causation of neural tube defects: folate deficiency increases susceptibility conferred by loss of Pax3 function. *Hum. Mol. Genet.* 17, 3675-3685.

Burren,K.A., Scott,J.M., Copp,A.J., and Greene,N.D. (2010). The genetic background of the curly tail strain confers susceptibility to folate-deficiency-induced exencephaly. *Birth Defects Res. A Clin. Mol. Teratol.* 88, 76-83.

Burzynski,G., Shepherd,I.T., and Enomoto,H. (2009). Genetic model system studies of the development of the enteric nervous system, gut motility and Hirschsprung's disease. *Neurogastroenterol. Motil.* 21, 113-127.

Caddy,J., Wilanowski,T., Darido,C., Dworkin,S., Ting,S.B., Zhao,Q., Rank,G., Auden,A., Srivastava,S., Papenfuss,T.A. et al. (2010). Epidermal wound repair is regulated by the planar cell polarity signaling pathway. *Dev. Cell* 19, 138-147.

Cambray,N. and Wilson,V. (2002). Axial progenitors with extensive potency are localised to the mouse chordoneural hinge. *Development* 129, 4855-4866.

Cambray,N. and Wilson,V. (2007). Two distinct sources for a population of maturing axial progenitors. *Development* 134, 2829-2840.

Camerer,E., Barker,A., Duong,D.N., Ganesan,R., Kataoka,H., Cornelissen,I., Darragh,M.R., Hussain,A., Zheng,Y.W., Srinivasan,Y. et al. (2010). Local protease signaling contributes to neural tube closure in the mouse embryo. *Dev. Cell* 18, 25-38.

Cameron,M. and Moran,P. (2009). Prenatal screening and diagnosis of neural tube defects. *Prenat. Diagn.* 29, 402-411.

Cantemir,V., Cai,D.H., Reedy,M.V., and Brauer,P.R. (2004). Tissue inhibitor of metalloproteinase-2 (TIMP-2) expression during cardiac neural crest cell migration and its role in proMMP-2 activation. *Dev. Dyn.* 231, 709-719.

Carmona-Fontaine,C., Matthews,H., and Mayor,R. (2008a). Directional cell migration in vivo: Wnt at the crest. *Cell Adh. Migr.* 2, 240-242.

Carmona-Fontaine,C., Matthews,H.K., Kuriyama,S., Moreno,M., Dunn,G.A., Parsons,M., Stern,C.D., and Mayor,R. (2008b). Contact inhibition of locomotion in vivo controls neural crest directional migration. *Nature* 456, 957-961.

Carreira-Barbosa,F., Concha,M.L., Takeuchi,M., Ueno,N., Wilson,S.W., and Tada,M. (2003). Prickle 1 regulates cell movements during gastrulation and neuronal migration in zebrafish. *Development* 130, 4037-4046.

Carroll,E.A., Gerrelli,D., Gasca,S., Berg,E., Beier,D.R., Copp,A.J., and Klingensmith,J. (2003). Cordon-bleu is a conserved gene involved in neural tube formation. *Dev. Biol.* 262, 16-31.

Cavalli,P., Tedoldi,S., and Riboli,B. (2008). Inositol supplementation in pregnancies at risk of apparently folate-resistant NTDs. *Birth Defects Res. A Clin. Mol. Teratol.* 82, 540-542.

Chacon-Heszele,M.F., Ren,D., Reynolds,A.B., Chi,F., and Chen,P. (2012). Regulation of cochlear convergent extension by the vertebrate planar cell polarity pathway is dependent on p120-catenin. *Development* 139, 968-978.

Chen,B., Mao,H.H., Chen,L., Zhang,F.L., Li,K., and Xue,Z.F. (2013). Loop-tail phenotype in heterozygous mice and neural tube defects in homozygous mice result from a nonsense mutation in the Vangl2 gene. *Genet. Mol. Res.* 12.

Chiang,C., Litingtung,Y., Lee,E., Young,K.E., Corden,J.L., Westphal,H., and Beachy,P.A. (1996). Cyclopia and defective axial patterning in mice lacking Sonic hedgehog gene function. *Nature* 383, 407-413.

Ciruna,B., Jenny,A., Lee,D., Mlodzik,M., and Schier,A.F. (2006). Planar cell polarity signalling couples cell division and morphogenesis during neurulation. *Nature* 439, 220-224.

Cockroft,D.L. (1988). Changes with gestational age in the nutritional requirements of postimplantation rat embryos in culture. *Teratology* 38, 281-290.

Cockroft,D.L., Brook,F.A., and Copp,A.J. (1992). Inositol deficiency increases the susceptibility to neural tube defects of genetically predisposed (curly tail) mouse embryos in vitro. *Teratology* 45, 223-232.

Cogram,P., Hynes,A., Dunlevy,L.P., Greene,N.D., and Copp,A.J. (2004). Specific isoforms of protein kinase C are essential for prevention of folate-resistant neural tube defects by inositol. *Hum. Mol. Genet.* 13, 7-14.

Cogram,P., Tesh,S., Tesh,J., Wade,A., Allan,G., Greene,N.D., and Copp,A.J. (2002). D-chiro-inositol is more effective than myo-inositol in preventing folate-resistant mouse neural tube defects. *Hum. Reprod.* 17, 2451-2458.

Colas,J.F. and Schoenwolf,G.C. (2001). Towards a cellular and molecular understanding of neurulation. *Dev. Dyn.* 221, 117-145.

Copp,A., Cogram,P., Fleming,A., Gerrelli,D., Henderson,D., Hynes,A., Kolatsi-Joannou,M., Murdoch,J., and Ybot-Gonzalez,P. (2000). Neurulation and neural tube closure defects. *Methods Mol. Biol.* 136, 135-160.

Copp,A.J. (1985). Relationship between timing of posterior neuropore closure and development of spinal neural tube defects in mutant (curly tail) and normal mouse embryos in culture. *J. Embryol. Exp. Morphol.* 88, 39-54.

Copp,A.J., Brook,F.A., Estibeiro,J.P., Shum,A.S., and Cockroft,D.L. (1990). The embryonic development of mammalian neural tube defects. *Prog. Neurobiol.* 35, 363-403.

Copp,A.J., Brook,F.A., and Roberts,H.J. (1988a). A cell-type-specific abnormality of cell proliferation in mutant (curly tail) mouse embryos developing spinal neural tube defects. *Development* 104, 285-295.

Copp,A.J., Checiu,I., and Henson,J.N. (1994). Developmental basis of severe neural tube defects in the loop-tail (Lp) mutant mouse: use of microsatellite DNA markers to identify embryonic genotype. *Dev. Biol.* 165, 20-29.

Copp,A.J., Crolla,J.A., and Brook,F.A. (1988b). Prevention of spinal neural tube defects in the mouse embryo by growth retardation during neurulation. *Development* 104, 297-303.

Copp,A.J. and Greene,N.D. (2010). Genetics and development of neural tube defects. *J. Pathol.* 220, 217-230.

Copp,A.J. and Greene,N.D. (2012). Neural tube defects – disorders of neurulation and related embryonic processes. IREs Dev Biol 2013, 2:213–227. doi: 10.1002/wdev.71

Copp,A.J., Greene,N.D., and Murdoch,J.N. (2003). The genetic basis of mammalian neurulation. *Nat. Rev. Genet.* 4, 784-793.

Copp,A.J., Seller,M.J., and Polani,P.E. (1982). Neural tube development in mutant (curly tail) and normal mouse embryos: the timing of posterior neuropore closure in vivo and in vitro. *J. Embryol. Exp. Morphol.* 69, 151-167.

Crider,K.S., Bailey,L.B., and Berry,R.J. (2011). Folic acid food fortification-its history, effect, concerns, and future directions. *Nutrients.* 3, 370-384.

Curtin,J.A., Quint,E., Tsipouri,V., Arkell,R.M., Cattanach,B., Copp,A.J., Henderson,D.J., Spurr,N., Stanier,P., Fisher,E.M. et al. (2003). Mutation of Celsr1 disrupts planar polarity of inner ear hair cells and causes severe neural tube defects in the mouse. *Curr. Biol.* 13, 1129-1133.

Czeizel,A.E. and Dudas,I. (1992). Prevention of the first occurrence of neural-tube defects by periconceptional vitamin supplementation. *N. Engl. J. Med.* 327, 1832-1835.

Darken,R.S., Scola,A.M., Rakeman,A.S., Das,G., Mlodzik,M., and Wilson,P.A. (2002). The planar polarity gene strabismus regulates convergent extension movements in Xenopus. *EMBO J.* 21, 976-985.

Davidson,B.P., Kinder,S.J., Steiner,K., Schoenwolf,G.C., and Tam,P.P. (1999). Impact of node ablation on the morphogenesis of the body axis and the lateral asymmetry of the mouse embryo during early organogenesis. *Dev. Biol.* 211, 11-26.

De Bellard,M.E., Rao,Y., and Bronner-Fraser,M. (2003). Dual function of Slit2 in repulsion and enhanced migration of trunk, but not vagal, neural crest cells. *J. Cell Biol.* 162, 269-279.

De Calisto,J., Araya,C., Marchant,L., Riaz,C.F., and Mayor,R. (2005). Essential role of non-canonical Wnt signalling in neural crest migration. *Development* 132, 2587-2597.

de Castro,S.C., Malhas,A., Leung,K.Y., Gustavsson,P., Vaux,D.J., Copp,A.J., and Greene,N.D. (2012). Lamin b1 polymorphism influences morphology of the nuclear envelope, cell cycle progression, and risk of neural tube defects in mice. *PLoS. Genet.* 8, e1003059.

De,M.P., Merello,E., Rossi,A., Piatelli,G., Cama,A., Kibar,Z., and Capra,V. (2012). FZD6 is a novel gene for human neural tube defects. *Hum. Mutat.* 33, 384-390.

Ding,Q., Motoyama,J., Gasca,S., Mo,R., Sasaki,H., Rossant,J., and Hui,C.C. (1998). Diminished Sonic hedgehog signaling and lack of floor plate differentiation in Gli2 mutant mice. *Development* 125, 2533-2543.

Dolk,H., Loane,M., and Garne,E. (2010). The prevalence of congenital anomalies in Europe. *Adv. Exp. Med. Biol.* 686, 349-364.

Doudney,K., Ybot-Gonzalez,P., Paternotte,C., Stevenson,R.E., Greene,N.D., Moore,G.E., Copp,A.J., and Stanier,P. (2005). Analysis of the planar cell polarity gene Vangl2 and its co-expressed paralogue Vangl1 in neural tube defect patients. *Am. J. Med. Genet. A* 136, 90-92.

Duband,J.L., Blavet,C., Jarov,A., and Fournier-Thibault,C. (2009). Spatio-temporal control of neural epithelial cell migration and epithelium-to-mesenchyme transition during avian neural tube development. *Dev. Growth Differ.* 51, 25-44.

Duong,T.D. and Erickson,C.A. (2004). MMP-2 plays an essential role in producing epithelial-mesenchymal transformations in the avian embryo. *Dev. Dyn.* 229, 42-53.

Dworkin,S., Jane,S.M., and Darido,C. (2011). The planar cell polarity pathway in vertebrate epidermal development, homeostasis and repair. *Organogenesis.* 7, 202-208.

Elul,T. and Keller,R. (2000). Monopolar protrusive activity: a new morphogenic cell behavior in the neural plate dependent on vertical interactions with the mesoderm in Xenopus. *Dev. Biol.* 224, 3-19.

Essien,F.B. and Wannberg,S.L. (1993). Methionine but not folinic acid or vitamin B-12 alters the frequency of neural tube defects in Axd mutant mice. *J. Nutr.* 123, 27-34.

Estibeiro,J.P., Brook,F.A., and Copp,A.J. (1993). Interaction between splotch (Sp) and curly tail (ct) mouse mutants in the embryonic development of neural tube defects. *Development* 119, 113-121.

Etheridge,S.L., Ray,S., Li,S., Hamblet,N.S., Lijam,N., Tsang,M., Greer,J., Kardos,N., Wang,J., Sussman,D.J. et al. (2008). Murine dishevelled 3 functions in redundant pathways with dishevelled 1 and 2 in normal cardiac outflow tract, cochlea, and neural tube development. *PLoS. Genet.* 4, e1000259.

Fleming,A. and Copp,A.J. (1998). Embryonic folate metabolism and mouse neural tube defects. *Science* 280, 2107-2109.

Forlani,S., Lawson,K.A., and Deschamps,J. (2003). Acquisition of Hox codes during gastrulation and axial elongation in the mouse embryo. *Development* 130, 3807-3819.

Formstone,C.J. and Little,P.F. (2001). The flamingo-related mouse Celsr family (Celsr1-3) genes exhibit distinct patterns of expression during embryonic development. *Mech. Dev.* 109, 91-94.

Fuchs,S., Herzog,D., Sumara,G., Buchmann-Moller,S., Civenni,G., Wu,X., Chrostek-Grashoff,A., Suter,U., Ricci,R., Relvas,J.B. et al. (2009). Stage-specific control of neural crest stem cell proliferation by the small rho GTPases Cdc42 and Rac1. *Cell Stem Cell* 4, 236-247.

Gammill,L.S., Gonzalez,C., and Bronner-Fraser,M. (2007). Neuropilin 2/semaphorin 3F signaling is essential for cranial neural crest migration and trigeminal ganglion condensation. *Dev. Neurobiol.* 67, 47-56.

Gammill,L.S., Gonzalez,C., Gu,C., and Bronner-Fraser,M. (2006). Guidance of trunk neural crest migration requires neuropilin 2/semaphorin 3F signaling. *Development* 133, 99-106.

Gao,B., Song,H., Bishop,K., Elliot,G., Garrett,L., English,M.A., Andre,P., Robinson,J., Sood,R., Minami,Y. et al. (2011). Wnt signaling gradients establish planar cell polarity by inducing Vangl2 phosphorylation through Ror2. *Dev. Cell* 20, 163-176.

Geelen,J.A. and Langman,J. (1979). Ultrastructural observations on closure of the neural tube in the mouse. *Anat. Embryol. (Berl)* 156, 73-88.

Gelineau-van,W.J., Voss,K.A., Stevens,V.L., Speer,M.C., and Riley,R.T. (2009). Maternal fumonisin exposure as a risk factor for neural tube defects. *Adv. Food Nutr. Res.* 56, 145-181.

Gerrelli,D. and Copp,A.J. (1997). Failure of neural tube closure in the loop-tail (Lp) mutant mouse: analysis of the embryonic mechanism. *Brain Res. Dev. Brain Res.* 102, 217-224.

Giambernardi,T.A., Sakaguchi,A.Y., Gluhak,J., Pavlin,D., Troyer,D.A., Das,G., Rodeck,U., and Klebe,R.J. (2001). Neutrophil collagenase (MMP-8) is expressed during early development in neural crest cells as well as in adult melanoma cells. *Matrix Biol.* 20, 577-587.

Gofflot,F., Hall,M., and Morriss-Kay,G.M. (1997). Genetic patterning of the developing mouse tail at the time of posterior neuropore closure. *Dev. Dyn.* 210, 431-445.

Gofflot,F., Hall,M., and Morriss-Kay,G.M. (1998). Genetic patterning of the posterior neuropore region of curly tail mouse embryos: deficiency of Wnt5a expression. *Int. J. Dev. Biol.* 42, 637-644.

Goldman,D.C., Martin,G.R., and Tam,P.P. (2000). Fate and function of the ventral ectodermal ridge during mouse tail development. *Development* 127, 2113-2123.

Gong,Y., Mo,C., and Fraser,S.E. (2004). Planar cell polarity signalling controls cell division orientation during zebrafish gastrulation. *Nature* 430, 689-693.

Goodrich,L.V. and Strutt,D. (2011). Principles of planar polarity in animal development. *Development* 138, 1877-1892.

Gravel,M., Iliescu,A., Horth,C., Apuzzo,S., and Gros,P. (2010). Molecular and cellular mechanisms underlying neural tube defects in the loop-tail mutant mouse. *Biochemistry* 49, 3445-3455.

Gray,R.S., Abitua,P.B., Wlodarczyk,B.J., Szabo-Rogers,H.L., Blanchard,O., Lee,I., Weiss,G.S., Liu,K.J., Marcotte,E.M., Wallingford,J.B. et al. (2009a). The planar cell polarity effector Fuz is essential for targeted membrane trafficking, ciliogenesis and mouse embryonic development. *Nat. Cell Biol.* 11, 1225-1232.

Gray,R.S., Bayly,R.D., Green,S.A., Agarwala,S., Lowe,C.J., and Wallingford,J.B. (2009b). Diversification of the expression patterns and developmental functions of the dishevelled gene family during chordate evolution. *Dev. Dyn.* 238, 2044-2057.

Greene,N.D. and Copp,A.J. (1997). Inositol prevents folate-resistant neural tube defects in the mouse. *Nat. Med.* 3, 60-66.

Greene,N.D. and Copp,A.J. (2005). Mouse models of neural tube defects: investigating preventive mechanisms. *Am. J. Med. Genet. C. Semin. Med. Genet.* 135C, 31-41.

Greene,N.D. and Copp,A.J. (2009). Development of the vertebrate central nervous system: formation of the neural tube. *Prenat. Diagn.* 29, 303-311.

Greene,N.D., Gerrelli,D., Van Straaten,H.W., and Copp,A.J. (1998). Abnormalities of floor plate, notochord and somite differentiation in the loop-tail (Lp) mouse: a model of severe neural tube defects. *Mech. Dev.* 73, 59-72.

Greene,N.D., Massa,V., and Copp,A.J. (2009). Understanding the causes and prevention of neural tube defects: Insights from the splotch mouse model. *Birth Defects Res. A Clin. Mol. Teratol.* 85, 322-330.

Groenen,P.M., Peer,P.G., Wevers,R.A., Swinkels,D.W., Franke,B., Mariman,E.C., and Steegers-Theunissen,R.P. (2003). Maternal myo-inositol, glucose, and zinc status is associated with the risk of offspring with spina bifida. *Am. J. Obstet. Gynecol.* 189, 1713-1719.

Gros,J., Serralbo,O., and Marcelle,C. (2009). WNT11 acts as a directional cue to organize the elongation of early muscle fibres. *Nature* 457, 589-593.

Gruneberg,H. (1954). Genetical studies on the skeleton of the mouse. VIII. curly tail. *J Genet* 52, 52-67.

Gruneberg,H. (1956). A ventral ectodermal ridge of the tail in mouse embryos. *Nature* 177, 787-788.

Guirao,B., Meunier,A., Mortaud,S., Aguilar,A., Corsi,J.M., Strehl,L., Hirota,Y., Desoeuvre,A., Boutin,C., Han,Y.G. et al. (2010). Coupling between hydrodynamic forces and planar cell polarity orients mammalian motile cilia. *Nat. Cell Biol.* 12, 341-350.

Gustavsson,P., Copp,A.J., and Greene,N.D. (2008). Grainyhead genes and mammalian neural tube closure. *Birth Defects Res. A Clin. Mol. Teratol.* 82, 728-735.

Gustavsson,P., Greene,N.D., Lad,D., Pauws,E., de Castro,S.C., Stanier,P., and Copp,A.J. (2007). Increased expression of Grainyhead-like-3 rescues spina bifida in a folate-resistant mouse model. *Hum. Mol. Genet.* 16, 2640-2646.

Guyot,M.C., Bosoi,C.M., Kharfallah,F., Reynolds,A., Drapeau,P., Justice,M., Gros,P., and Kibar,Z. (2011). A novel hypomorphic Looptail allele at the planar cell polarity Vangl2 gene. *Dev. Dyn.* 240, 839-849.

Habas,R., Dawid,I.B., and He,X. (2003). Coactivation of Rac and Rho by Wnt/Frizzled signaling is required for vertebrate gastrulation. *Genes Dev.* 17, 295-309.

Habas,R., Kato,Y., and He,X. (2001). Wnt/Frizzled activation of Rho regulates vertebrate gastrulation and requires a novel Formin homology protein Daam1. *Cell* 107, 843-854.

Hall,R.J. and Erickson,C.A. (2003). ADAM 10: an active metalloprotease expressed during avian epithelial morphogenesis. *Dev. Biol.* 256, 146-159.

Hamblet,N.S., Lijam,N., Ruiz-Lozano,P., Wang,J., Yang,Y., Luo,Z., Mei,L., Chien,K.R., Sussman,D.J., and Wynshaw-Boris,A. (2002). Dishevelled 2 is essential for cardiac outflow tract development, somite segmentation and neural tube closure. *Development* 129, 5827-5838.

Hamilton,D.L. and Abremski,K. (1984). Site-specific recombination by the bacteriophage P1 lox-Cre system. Cre-mediated synapsis of two lox sites. *J. Mol. Biol.* 178, 481-486.

Hanna,L.A., Foreman,R.K., Tarasenko,I.A., Kessler,D.S., and Labosky,P.A. (2002). Requirement for Foxd3 in maintaining pluripotent cells of the early mouse embryo. *Genes Dev.* 16, 2650-2661.

Harris,M.J. (2009). Insights into prevention of human neural tube defects by folic acid arising from consideration of mouse mutants. *Birth Defects Res. A Clin. Mol. Teratol.* 85, 331-339.

Harris,M.J. and Juriloff,D.M. (2007). Mouse mutants with neural tube closure defects and their role in understanding human neural tube defects. *Birth Defects Res. A Clin. Mol. Teratol.* 79, 187-210.

Harris,M.J. and Juriloff,D.M. (2010). An update to the list of mouse mutants with neural tube closure defects and advances toward a complete genetic perspective of neural tube closure. *Birth Defects Res. A Clin. Mol. Teratol.* 88, 653-669.

Heisenberg,C.P., Tada,M., Rauch,G.J., Saude,L., Concha,M.L., Geisler,R., Stemple,D.L., Smith,J.C., and Wilson,S.W. (2000). Silberblick/Wnt11 mediates convergent extension movements during zebrafish gastrulation. *Nature* 405, 76-81.

Henderson,D.J., Conway,S.J., Greene,N.D., Gerrelli,D., Murdoch,J.N., Anderson,R.H., and Copp,A.J. (2001). Cardiovascular defects associated with abnormalities in midline development in the Loop-tail mouse mutant. *Circ. Res.* 89, 6-12.

Henderson,D.J., Phillips,H.M., and Chaudhry,B. (2006). Vang-like 2 and noncanonical Wnt signaling in outflow tract development. *Trends Cardiovasc. Med.* 16, 38-45.

Heseker,H.B., Mason,J.B., Selhub,J., Rosenberg,I.H., and Jacques,P.F. (2009). Not all cases of neural-tube defect can be prevented by increasing the intake of folic acid. *Br. J. Nutr.* 102, 173-180.

Heydeck,W. and Liu,A. (2011). PCP effector proteins inturned and fuzzy play nonredundant roles in the patterning but not convergent extension of mammalian neural tube. *Dev. Dyn.* 240, 1938-1948.

Heydeck,W., Zeng,H., and Liu,A. (2009). Planar cell polarity effector gene Fuzzy regulates cilia formation and Hedgehog signal transduction in mouse. *Dev. Dyn.* 238, 3035-3042.

Hildebrand,J.D. and Soriano,P. (1999). Shroom, a PDZ domain-containing actin-binding protein, is required for neural tube morphogenesis in mice. *Cell* 99, 485-497.

Hislop,N.R., Caddy,J., Ting,S.B., Auden,A., Vasudevan,S., King,S.L., Lindeman,G.J., Visvader,J.E., Cunningham,J.M., and Jane,S.M. (2008). Grhl3 and Lmo4 play coordinate roles in epidermal migration. *Dev. Biol.* 321, 263-272.

Huang,G.Y., Cooper,E.S., Waldo,K., Kirby,M.L., Gilula,N.B., and Lo,C.W. (1998). Gap junction-mediated cell-cell communication modulates mouse neural crest migration. *J. Cell Biol.* 143, 1725-1734.

Iliescu,A., Gravel,M., Horth,C., Kibar,Z., and Gros,P. (2011). Loss of membrane targeting of Vangl proteins causes neural tube defects. *Biochemistry* 50, 795-804.

Jacinto,A., Woolner,S., and Martin,P. (2002). Dynamic analysis of dorsal closure in Drosophila: from genetics to cell biology. *Dev. Cell* 3, 9-19.

Jacobson,A.G. and Tam,P.P. (1982). Cephalic neurulation in the mouse embryo analyzed by SEM and morphometry. *Anat. Rec.* 203, 375-396.

Jentink,J., Loane,M.A., Dolk,H., Barisic,I., Garne,E., Morris,J.K., and de Jong-van den Berg LT (2010). Valproic acid monotherapy in pregnancy and major congenital malformations. *N. Engl. J. Med.* 362, 2185-2193.

Jessen,J.R. and Solnica-Krezel,L. (2004). Identification and developmental expression pattern of van gogh-like 1, a second zebrafish strabismus homologue. *Gene Expr. Patterns.* 4, 339-344.

Jessen,J.R., Topczewski,J., Bingham,S., Sepich,D.S., Marlow,F., Chandrasekhar,A., and Solnica-Krezel,L. (2002). Zebrafish trilobite identifies new roles for Strabismus in gastrulation and neuronal movements. *Nat. Cell Biol.* 4, 610-615.

Jia,L., Cheng,L., and Raper,J. (2005). Slit/Robo signaling is necessary to confine early neural crest cells to the ventral migratory pathway in the trunk. *Dev. Biol.* 282, 411-421.

Jiang,X., Rowitch,D.H., Soriano,P., McMahon,A.P., and Sucov,H.M. (2000). Fate of the mammalian cardiac neural crest. *Development* 127, 1607-1616.

Juriloff,D.M. and Harris,M.J. (2012a). A consideration of the evidence that genetic defects in planar cell polarity contribute to the etiology of human neural tube defects. *Birth Defects Res. A Clin. Mol. Teratol.* 94, 824-840.

Juriloff,D.M. and Harris,M.J. (2012b). Hypothesis: the female excess in cranial neural tube defects reflects an epigenetic drag of the inactivating X chromosome on the molecular mechanisms of neural fold elevation. *Birth Defects Res. A Clin. Mol. Teratol.* 94, 849-855.

Karner,C.M., Chirumamilla,R., Aoki,S., Igarashi,P., Wallingford,J.B., and Carroll,T.J. (2009). Wnt9b signaling regulates planar cell polarity and kidney tubule morphogenesis. *Nat. Genet.* 41, 793-799.

Keller,R. (2002). Shaping the vertebrate body plan by polarized embryonic cell movements. *Science* 298, 1950-1954.

Keller,R., Davidson,L., Edlund,A., Elul,T., Ezin,M., Shook,D., and Skoglund,P. (2000). Mechanisms of convergence and extension by cell intercalation. *Philos. Trans. R. Soc. Lond B Biol. Sci.* 355, 897-922.

Kibar,Z., Bosoi,C.M., Kooistra,M., Salem,S., Finnell,R.H., De,M.P., Merello,E., Bassuk,A.G., Capra,V., and Gros,P. (2009). Novel mutations in VANGL1 in neural tube defects. *Hum. Mutat.* 30, E706-E715.

Kibar,Z., Salem,S., Bosoi,C.M., Pauwels,E., De,M.P., Merello,E., Bassuk,A.G., Capra,V., and Gros,P. (2010). Contribution of VANGL2 mutations to isolated neural tube defects. *Clin. Genet.*

Kibar,Z., Torban,E., McDearmid,J.R., Reynolds,A., Berghout,J., Mathieu,M., Kirillova,I., De,M.P., Merello,E., Hayes,J.M. et al. (2007). Mutations in VANGL1 associated with neural-tube defects. *N. Engl. J. Med.* 356, 1432-1437.

Kibar,Z., Underhill,D.A., Canonne-Hergaux,F., Gauthier,S., Justice,M.J., and Gros,P. (2001a). Identification of a new chemically induced allele (Lp(m1Jus)) at the loop-tail locus: morphology, histology, and genetic mapping. *Genomics* 72, 331-337.

Kibar,Z., Vogan,K.J., Groulx,N., Justice,M.J., Underhill,D.A., and Gros,P. (2001b). Ltap, a mammalian homolog of Drosophila Strabismus/Van Gogh, is altered in the mouse neural tube mutant Loop-tail. *Nat. Genet.* 28, 251-255.

Kilian,B., Mansukoski,H., Barbosa,F.C., Ulrich,F., Tada,M., and Heisenberg,C.P. (2003). The role of Ppt/Wnt5 in regulating cell shape and movement during zebrafish gastrulation. *Mech. Dev.* 120, 467-476.

Kirke,P.N., Molloy,A.M., Daly,L.E., Burke,H., Weir,D.G., and Scott,J.M. (1993). Maternal plasma folate and vitamin B12 are independent risk factors for neural tube defects. *Q. J. Med.* 86, 703-708.

Kondo,A., Kamihira,O., and Ozawa,H. (2009). Neural tube defects: prevalence, etiology and prevention. *Int. J. Urol.* 16, 49-57.

Krantz,D.A., Hallahan,T.W., and Sherwin,J.E. (2010). Screening for open neural tube defects. *Clin. Lab Med.* 30, 721-725.

Krull,C.E., Lansford,R., Gale,N.W., Collazo,A., Marcelle,C., Yancopoulos,G.D., Fraser,S.E., and Bronner-Fraser,M. (1997). Interactions of Eph-related receptors and ligands confer rostrocaudal pattern to trunk neural crest migration. *Curr. Biol.* 7, 571-580.

Kubota,Y. and Ito,K. (2000). Chemotactic migration of mesencephalic neural crest cells in the mouse. *Dev. Dyn.* 217, 170-179.

Kudryavtseva,E.I., Sugihara,T.M., Wang,N., Lasso,R.J., Gudnason,J.F., Lipkin,S.M., and Andersen,B. (2003). Identification and characterization of Grainyhead-like epithelial transactivator (GET-1), a novel mammalian Grainyhead-like factor. *Dev. Dyn.* 226, 604-617.

Kuo,B.R. and Erickson,C.A. (2010). Regional differences in neural crest morphogenesis. *Cell Adh. Migr.* 4, 567-585.

Kuo,B.R. and Erickson,C.A. (2011). Vagal neural crest cell migratory behavior: a transition between the cranial and trunk crest. *Dev. Dyn.* 240, 2084-2100.

Kuo,J.C., Han,X., Hsiao,C.T., Yates,J.R., III, and Waterman,C.M. (2011). Analysis of the myosin-II-responsive focal adhesion proteome reveals a role for beta-Pix in negative regulation of focal adhesion maturation. *Nat. Cell Biol.* 13, 383-393.

Kuriyama,S. and Mayor,R. (2008). Molecular analysis of neural crest migration. *Philos. Trans. R. Soc. Lond B Biol. Sci.* 363, 1349-1362.

Lane,I.R. (2011). Preventing neural tube defects with folic acid: nearly 20 years on, the majority of women remain unprotected. *J. Obstet. Gynaecol.* 31, 581-585.

Lee,H. and Adler,P.N. (2004). The grainy head transcription factor is essential for the function of the frizzled pathway in the Drosophila wing. *Mech. Dev.* 121, 37-49.

Lee,S.K., Jurata,L.W., Nowak,R., Lettieri,K., Kenny,D.A., Pfaff,S.L., and Gill,G.N. (2005). The LIM domain-only protein LMO4 is required for neural tube closure. *Mol. Cell Neurosci.* 28, 205-214.

Lei,Y.P., Zhang,T., Li,H., Wu,B.L., Jin,L., and Wang,H.Y. (2010). VANGL2 mutations in human cranial neural-tube defects. *N. Engl. J. Med.* 362, 2232-2235.

Letts,V.A., Schork,N.J., Copp,A.J., Bernfield,M., and Frankel,W.N. (1995). A curly-tail modifier locus, mct1, on mouse chromosome 17. *Genomics* 29, 719-724.

Liu,J., Qi,J., Zhu,J., Zhang,L., Liang,Y., Ning,Q., and Luo,X. (2008). Effects of retinoic acid on the expressions of Vangl1 and vangl2 in mouse fetuses. *J. Neurogenet.* 22, 167-179.

Lo,C.W., Cohen,M.F., Huang,G.Y., Lazatin,B.O., Patel,N., Sullivan,R., Pauken,C., and Park,S.M. (1997). Cx43 gap junction gene expression and gap junctional communication in mouse neural crest cells. *Dev. Genet.* 20, 119-132.

Lopez-Escobar,B., De,F.B., Sanchez-Alcazar,J.A., Sasaki,T., Copp,A.J., and Ybot-Gonzalez,P. (2012). Laminin and integrin expression in the ventral ectodermal ridge of the mouse embryo: implications for regulation of BMP signalling. *Dev. Dyn.* 241, 1808-1815.

Lu,X., Borchers,A.G., Jolicoeur,C., Rayburn,H., Baker,J.C., and Tessier-Lavigne,M. (2004). PTK7/CCK-4 is a novel regulator of planar cell polarity in vertebrates. *Nature* 430, 93-98.

Macdonald,K.B., Juriloff,D.M., and Harris,M.J. (1989). Developmental study of neural tube closure in a mouse stock with a high incidence of exencephaly. *Teratology* 39, 195-213.

Marlow,F., Topczewski,J., Sepich,D., and Solnica-Krezel,L. (2002). Zebrafish Rho kinase 2 acts downstream of Wnt11 to mediate cell polarity and effective convergence and extension movements. *Curr. Biol.* 12, 876-884.

Massa,V., Savery,D., Ybot-Gonzalez,P., Ferraro,E., Rongvaux,A., Cecconi,F., Flavell,R., Greene,N.D., and Copp,A.J. (2009). Apoptosis is not required for mammalian neural tube closure. *Proc. Natl. Acad. Sci. U. S. A* 106, 8233-8238.

Matthews,H.K., Marchant,L., Carmona-Fontaine,C., Kuriyama,S., Larrain,J., Holt,M.R., Parsons,M., and Mayor,R. (2008). Directional migration of neural crest cells in vivo is regulated by Syndecan-4/Rac1 and non-canonical Wnt signaling/RhoA. *Development* 135, 1771-1780.

McGrew,M.J., Sherman,A., Lillico,S.G., Ellard,F.M., Radcliffe,P.A., Gilhooley,H.J., Mitrophanous,K.A., Cambray,N., Wilson,V., and Sang,H. (2008). Localised axial progenitor cell populations in the avian tail bud are not committed to a posterior Hox identity. *Development* 135, 2289-2299.

Merte,J., Jensen,D., Wright,K., Sarsfield,S., Wang,Y., Schekman,R., and Ginty,D.D. (2010). Sec24b selectively sorts Vangl2 to regulate planar cell polarity during neural tube closure. *Nat. Cell Biol.* 12, 41-46.

Meyer,D. and Birchmeier,C. (1995). Multiple essential functions of neuregulin in development. *Nature* 378, 386-390.

Meyer,E.J., Ikmi,A., and Gibson,M.C. (2011). Interkinetic nuclear migration is a broadly conserved feature of cell division in pseudostratified epithelia. *Curr. Biol.* 21, 485-491.

Molyneaux,K.A., Stallock,J., Schaible,K., and Wylie,C. (2001). Time-lapse analysis of living mouse germ cell migration. *Dev. Biol.* 240, 488-498.

Montcouquiol,M., Rachel,R.A., Lanford,P.J., Copeland,N.G., Jenkins,N.A., and Kelley,M.W. (2003). Identification of Vangl2 and Scrb1 as planar polarity genes in mammals. *Nature* 423, 173-177.

Montcouquiol,M., Sans,N., Huss,D., Kach,J., Dickman,J.D., Forge,A., Rachel,R.A., Copeland,N.G., Jenkins,N.A., Bogani,D. et al. (2006). Asymmetric localization of Vangl2 and Fz3 indicate novel mechanisms for planar cell polarity in mammals. *J. Neurosci.* 26, 5265-5275.

Morais da,S.S., Hacker,A., Harley,V., Goodfellow,P., Swain,A., and Lovell-Badge,R. (1996). Sox9 expression during gonadal development implies a conserved role for the gene in testis differentiation in mammals and birds. *Nat. Genet.* 14, 62-68.

Moretti,M.E., Bar-Oz,B., Fried,S., and Koren,G. (2005). Maternal hyperthermia and the risk for neural tube defects in offspring: systematic review and meta-analysis. *Epidemiology* 16, 216-219.

Morriss-Kay,G.M. (1981). Growth and development of pattern in the cranial neural epithelium of rat embryos during neurulation. *J. Embryol. Exp. Morphol.* 65 Suppl, 225-241.

MRC. (1991). Prevention of neural tube defects: results of the Medical Research Council Vitamin Study. MRC Vitamin Study Research Group. *Lancet,* 338**,** 131-137.

Mulinari,S. and Hacker,U. (2010). Rho-guanine nucleotide exchange factors during development: Force is nothing without control. *Small GTPases.* 1, 28-43.

Murdoch,J.N., Doudney,K., Paternotte,C., Copp,A.J., and Stanier,P. (2001a). Severe neural tube defects in the loop-tail mouse result from mutation of Lpp1, a novel gene involved in floor plate specification. *Hum. Mol. Genet.* 10, 2593-2601.

Murdoch,J.N., Henderson,D.J., Doudney,K., Gaston-Massuet,C., Phillips,H.M., Paternotte,C., Arkell,R., Stanier,P., and Copp,A.J. (2003). Disruption of scribble (Scrb1) causes severe neural tube defects in the circletail mouse. *Hum. Mol. Genet.* 12, 87-98.

Murdoch,J.N., Rachel,R.A., Shah,S., Beermann,F., Stanier,P., Mason,C.A., and Copp,A.J. (2001b). Circletail, a new mouse mutant with severe neural tube defects: chromosomal localization and interaction with the loop-tail mutation. *Genomics* 78, 55-63.

Narimatsu,M., Bose,R., Pye,M., Zhang,L., Miller,B., Ching,P., Sakuma,R., Luga,V., Roncari,L., Attisano,L. et al. (2009). Regulation of planar cell polarity by Smurf ubiquitin ligases. *Cell* 137, 295-307.

Neumann,P.E., Frankel,W.N., Letts,V.A., Coffin,J.M., Copp,A.J., and Bernfield,M. (1994). Multifactorial inheritance of neural tube defects: localization of the major gene and recognition of modifiers in ct mutant mice. *Nat. Genet.* 6, 357-362.

O'Rahilly,R. and Muller,F. (2002). The two sites of fusion of the neural folds and the two neuropores in the human embryo. *Teratology* 65, 162-170.

Ohta,S., Suzuki,K., Tachibana,K., Tanaka,H., and Yamada,G. (2007). Cessation of gastrulation is mediated by suppression of epithelial-mesenchymal transition at the ventral ectodermal ridge. *Development* 134, 4315-4324.

Oishi,I., Suzuki,H., Onishi,N., Takada,R., Kani,S., Ohkawara,B., Koshida,I., Suzuki,K., Yamada,G., Schwabe,G.C. et al. (2003). The receptor tyrosine kinase Ror2 is involved in non-canonical Wnt5a/JNK signalling pathway. *Genes Cells* 8, 645-654.

Olesnicky Killian,E.C., Birkholz,D.A., and Artinger,K.B. (2009). A role for chemokine signaling in neural crest cell migration and craniofacial development. *Dev. Biol.* 333, 161-172.

Olivera-Martinez,I., Harada,H., Halley,P.A., and Storey,K.G. (2012). Loss of FGF-dependent mesoderm identity and rise of endogenous retinoid signalling determine cessation of body axis elongation. *PLoS. Biol.* 10, e1001415.

Osborne,N.J., Begbie,J., Chilton,J.K., Schmidt,H., and Eickholt,B.J. (2005). Semaphorin/neuropilin signaling influences the positioning of migratory neural crest cells within the hindbrain region of the chick. *Dev. Dyn.* 232, 939-949.

Pai,Y.J., Abdullah,N.L., Mohd-Zin,S.W., Mohammed,R.S., Rolo,A., Greene,N.D., Abdul-Aziz,N.M., and Copp,A.J. (2012). Epithelial fusion during neural tube morphogenesis. *Birth Defects Res. A Clin. Mol. Teratol.* 94, 817-823.

Park,M. and Moon,R.T. (2002). The planar cell-polarity gene stbm regulates cell behaviour and cell fate in vertebrate embryos. *Nat. Cell Biol.* 4, 20-25.

Park,T.J., Haigo,S.L., and Wallingford,J.B. (2006). Ciliogenesis defects in embryos lacking inturned or fuzzy function are associated with failure of planar cell polarity and Hedgehog signaling. *Nat. Genet.* 38, 303-311.

Park,T.J., Mitchell,B.J., Abitua,P.B., Kintner,C., and Wallingford,J.B. (2008). Dishevelled controls apical docking and planar polarization of basal bodies in ciliated epithelial cells. *Nat. Genet.* 40, 871-879.

Paudyal,A., Damrau,C., Patterson,V.L., Ermakov,A., Formstone,C., Lalanne,Z., Wells,S., Lu,X., Norris,D.P., Dean,C.H. et al. (2010). The novel mouse mutant, chuzhoi, has disruption of Ptk7 protein and exhibits defects in neural tube, heart and lung development and abnormal planar cell polarity in the ear. *BMC. Dev. Biol.* 10, 87.

Peeters,M.C., Hekking,J.W., Shiota,K., Drukker,J., and Van Straaten,H.W. (1998a). Differences in axial curvature correlate with species-specific rate of neural tube closure in embryos of chick, rabbit, mouse, rat and human. *Anat. Embryol. (Berl)* 198, 185-194.

Peeters,M.C., Hekking,W.M., Vainas,T., Drukker,J., and Van Straaten,H.W. (1997). Spatio-temporal curvature pattern of the caudal body axis for non-mutant and curly tail mouse embryos during the period of caudal neural tube closure. *Anat. Embryol. (Berl)* 195, 259-266.

Peeters,M.C., Schutte,B., Lenders,M.H., Hekking,J.W., Drukker,J., and Van Straaten,H.W. (1998b). Role of differential cell proliferation in the tail bud in aberrant mouse neurulation. *Dev. Dyn.* 211, 382-389.

Peeters,M.C., Shum,A.S., Hekking,J.W., Copp,A.J., and Van Straaten,H.W. (1996). Relationship between altered axial curvature and neural tube closure in normal and mutant (curly tail) mouse embryos. *Anat. Embryol. (Berl)* 193, 123-130.

Phillips,H.M., Rhee,H.J., Murdoch,J.N., Hildreth,V., Peat,J.D., Anderson,R.H., Copp,A.J., Chaudhry,B., and Henderson,D.J. (2007). Disruption of planar cell polarity signaling results in congenital heart defects and cardiomyopathy attributable to early cardiomyocyte disorganization. *Circ. Res.* 101, 137-145.

Pingault,V., Ente,D., Dastot-Le,M.F., Goossens,M., Marlin,S., and Bondurand,N. (2010). Review and update of mutations causing Waardenburg syndrome. *Hum. Mutat.* 31, 391-406.

Polyak,K. and Weinberg,R.A. (2009). Transitions between epithelial and mesenchymal states: acquisition of malignant and stem cell traits. *Nat. Rev. Cancer* 9, 265-273.

Pryor,S.E., Massa,V., Savery,D., Greene,N.D., and Copp,A.J. (2012). Convergent extension analysis in mouse whole embryo culture. *Methods Mol. Biol.* 839, 133-146.

Pyrgaki,C., Liu,A., and Niswander,L. (2011). Grainyhead-like 2 regulates neural tube closure and adhesion molecule expression during neural fold fusion. *Dev. Biol.* 353, 38-49.

Pyrgaki,C., Trainor,P., Hadjantonakis,A.K., and Niswander,L. (2010). Dynamic imaging of mammalian neural tube closure. *Dev. Biol.* 344, 941-947.

Qian,D., Jones,C., Rzadzinska,A., Mark,S., Zhang,X., Steel,K.P., Dai,X., and Chen,P. (2007). Wnt5a functions in planar cell polarity regulation in mice. *Dev. Biol.* 306, 121-133.

Rachel,R.A., Murdoch,J.N., Beermann,F., Copp,A.J., and Mason,C.A. (2000). Retinal axon misrouting at the optic chiasm in mice with neural tube closure defects. *Genesis.* 27, 32-47.

Rampersaud,E., Bassuk,A.G., Enterline,D.S., George,T.M., Siegel,D.G., Melvin,E.C., Aben,J., Allen,J., Aylsworth,A., Brei,T. et al. (2005). Whole genomewide linkage screen for neural tube defects reveals regions of interest on chromosomes 7 and 10. *J. Med. Genet.* 42, 940-946.

Read,A.P. and Newton,V.E. (1997). Waardenburg syndrome. *J. Med. Genet.* 34, 656-665.

Reaume,A.G., de Sousa,P.A., Kulkarni,S., Langille,B.L., Zhu,D., Davies,T.C., Juneja,S.C., Kidder,G.M., and Rossant,J. (1995). Cardiac malformation in neonatal mice lacking connexin43. *Science* 267, 1831-1834.

Reynolds,A., McDearmid,J.R., Lachance,S., De,M.P., Merello,E., Capra,V., Gros,P., Drapeau,P., and Kibar,Z. (2010). VANGL1 rare variants associated with neural tube defects affect convergent extension in zebrafish. *Mech. Dev.* 127, 385-392.

Richardson,B.E. and Lehmann,R. (2010). Mechanisms guiding primordial germ cell migration: strategies from different organisms. *Nat. Rev. Mol. Cell Biol.* 11, 37-49.

Ricks,D.J., Rees,C.A., Osborn,K.A., Crookston,B.T., Leaver,K., Merrill,S.B., Velasquez,C., and Ricks,J.H. (2012). Peru's national folic acid fortification program and its effect on neural tube defects in Lima. *Rev. Panam. Salud Publica* 32, 391-398.

Rifat,Y., Parekh,V., Wilanowski,T., Hislop,N.R., Auden,A., Ting,S.B., Cunningham,J.M., and Jane,S.M. (2010). Regional neural tube closure defined by the Grainy head-like transcription factors. *Dev. Biol.* 345, 237-245.

Robinson,A., Escuin,S., Doudney,K., Vekemans,M., Stevenson,R.E., Greene,N.D., Copp,A.J., and Stanier,P. (2012). Mutations in the planar cell polarity genes CELSR1 and SCRIB are associated with the severe neural tube defect craniorachischisis. *Hum. Mutat.* 33, 440-447.

Ross,A.J., May-Simera,H., Eichers,E.R., Kai,M., Hill,J., Jagger,D.J., Leitch,C.C., Chapple,J.P., Munro,P.M., Fisher,S. et al. (2005). Disruption of Bardet-Biedl syndrome ciliary proteins perturbs planar cell polarity in vertebrates. *Nat. Genet.* 37, 1135-1140.

Rothman,K.J., Moore,L.L., Singer,M.R., Nguyen,U.S., Mannino,S., and Milunsky,A. (1995). Teratogenicity of high vitamin A intake. *N. Engl. J. Med.* 333, 1369-1373.

Saadai,P. and Farmer,D.L. (2012). Fetal surgery for myelomeningocele. *Clin. Perinatol.* 39, 279-288.

Santiago,A. and Erickson,C.A. (2002). Ephrin-B ligands play a dual role in the control of neural crest cell migration. *Development* 129, 3621-3632.

Sato,A., Scholl,A.M., Kuhn,E.N., Stadt,H.A., Decker,J.R., Pegram,K., Hutson,M.R., and Kirby,M.L. (2011). FGF8 signaling is chemotactic for cardiac neural crest cells. *Dev. Biol.* 354, 18-30.

Satoh,W., Matsuyama,M., Takemura,H., Aizawa,S., and Shimono,A. (2008). Sfrp1, Sfrp2, and Sfrp5 regulate the Wnt/beta-catenin and the planar cell polarity pathways during early trunk formation in mouse. *Genesis.* 46, spcone.

Sauka-Spengler,T. and Bronner-Fraser,M. (2008). A gene regulatory network orchestrates neural crest formation. *Nat. Rev. Mol. Cell Biol.* 9, 557-568.

Schlessinger,K., Hall,A., and Tolwinski,N. (2009). Wnt signaling pathways meet Rho GTPases. *Genes Dev.* 23, 265-277.

Schoenwolf,G.C. (1984). Histological and ultrastructural studies of secondary neurulation in mouse embryos. *Am. J. Anat.* 169, 361-376.

Schoenwolf,G.C., Folsom,D., and Moe,A. (1988). A reexamination of the role of microfilaments in neurulation in the chick embryo. *Anat. Rec.* 220, 87-102.

Schoenwolf,G.C. and Smith,J.L. (1990). Mechanisms of neurulation: traditional viewpoint and recent advances. *Development* 109, 243-270.

Schorah,C. (2009). Dick Smithells, folic acid, and the prevention of neural tube defects. *Birth Defects Res. A Clin. Mol. Teratol.* 85, 254-259.

Schubert,F.R., Fainsod,A., Gruenbaum,Y., and Gruss,P. (1995). Expression of the novel murine homeobox gene Sax-1 in the developing nervous system. *Mech. Dev.* 51, 99-114.

Scott,J.M. (1999). Folate and vitamin B12. *Proc. Nutr. Soc.* 58, 441-448.

Selleck,M.A. and Stern,C.D. (1991). Fate mapping and cell lineage analysis of Hensen's node in the chick embryo. *Development* 112, 615-626.

Shih,J. and Keller,R. (1992). Cell motility driving mediolateral intercalation in explants of Xenopus laevis. *Development* 116, 901-914.

Shima,Y., Copeland,N.G., Gilbert,D.J., Jenkins,N.A., Chisaka,O., Takeichi,M., and Uemura,T. (2002). Differential expression of the seven-pass transmembrane cadherin genes Celsr1-3 and distribution of the Celsr2 protein during mouse development. *Dev. Dyn.* 223, 321-332.

Shnitsar,I. and Borchers,A. (2008). PTK7 recruits dsh to regulate neural crest migration. *Development* 135, 4015-4024.

Shum,A.S. and Copp,A.J. (1996). Regional differences in morphogenesis of the neuroepithelium suggest multiple mechanisms of spinal neurulation in the mouse. *Anat. Embryol. (Berl)* 194, 65-73.

Simons,M. and Mlodzik,M. (2008). Planar cell polarity signaling: from fly development to human disease. *Annu. Rev. Genet.* 42, 517-540.

Smith,A., Robinson,V., Patel,K., and Wilkinson,D.G. (1997). The EphA4 and EphB1 receptor tyrosine kinases and ephrin-B2 ligand regulate targeted migration of branchial neural crest cells. *Curr. Biol.* 7, 561-570.

Smith,J.L. and Schoenwolf,G.C. (1988). Role of cell-cycle in regulating neuroepithelial cell shape during bending of the chick neural plate. *Cell Tissue Res.* 252, 491-500.

Smith,J.L. and Schoenwolf,G.C. (1989). Notochordal induction of cell wedging in the chick neural plate and its role in neural tube formation. *J. Exp. Zool.* 250, 49-62.

Smith,J.L. and Stein,K.F. (1962) Axial elongation in the mouse and its retardation in homozygous looptail mice. *J Embryol Exp Morphol* 10, 73-87.

Smithells,R.W., Sheppard,S., Schorah,C.J., Seller,M.J., Nevin,N.C., Harris,R., Read,A.P., and Fielding,D.W. (1981). Apparent prevention of neural tube defects by periconceptional vitamin supplementation. *Arch. Dis. Child* 56, 911-918.

Song,H., Hu,J., Chen,W., Elliott,G., Andre,P., Gao,B., and Yang,Y. (2010). Planar cell polarity breaks bilateral symmetry by controlling ciliary positioning. *Nature* 466, 378-382.

Srinivas,S., Watanabe,T., Lin,C.S., William,C.M., Tanabe,Y., Jessell,T.M., and Costantini,F. (2001). Cre reporter strains produced by targeted insertion of EYFP and ECFP into the ROSA26 locus. *BMC. Dev. Biol.* 1, 4.

Stamm,D.S., Rampersaud,E., Slifer,S.H., Mehltretter,L., Siegel,D.G., Xie,J., Hu-Lince,D., Craig,D.W., Stephan,D.A., George,T.M. et al. (2006). High-density single nucleotide polymorphism screen in a large multiplex neural tube defect family refines linkage to loci at 7p21.1-pter and 2q33.1-q35. *Birth Defects Res. A Clin. Mol. Teratol.* 76, 499-505.

Steegers-Theunissen,R.P., Boers,G.H., Trijbels,F.J., Finkelstein,J.D., Blom,H.J., Thomas,C.M., Borm,G.F., Wouters,M.G., and Eskes,T.K. (1994). Maternal hyperhomocysteinemia: a risk factor for neural-tube defects? *Metabolism* 43, 1475-1480.

Stein,K.F. and Rudin,I.A. (1953). Development of mice homozygous for loop-tail. *J Hered* 44-59-69.

Steventon,B., Carmona-Fontaine,C., and Mayor,R. (2005). Genetic network during neural crest induction: from cell specification to cell survival. *Semin. Cell Dev. Biol.* 16, 647-654.

Stiefel,D., Copp,A.J., and Meuli,M. (2007). Fetal spina bifida in a mouse model: loss of neural function in utero. *J. Neurosurg.* 106, 213-221.

Stiefel,D., Shibata,T., Meuli,M., Duffy,P.G., and Copp,A.J. (2003). Tethering of the spinal cord in mouse fetuses and neonates with spina bifida. *J. Neurosurg.* 99, 206-213.

Strobl-Mazzulla,P.H. and Bronner,M.E. (2012). Epithelial to mesenchymal transition: new and old insights from the classical neural crest model. *Semin. Cancer Biol.* 22, 411-416.

Strong,L.C. and Hollander,W.F. (1949). Hereditary looptail in the house mouse. *J Hered* 40, 329-334.

Stuhlmiller,T.J. and Garcia-Castro,M.I. (2012). Current perspectives of the signaling pathways directing neural crest induction. *Cell Mol. Life Sci.* 69, 3715-3737.

Tada,M. and Heisenberg,C.P. (2012). Convergent extension: using collective cell migration and cell intercalation to shape embryos. *Development* 139, 3897-3904.

Tada,M. and Smith,J.C. (2000). Xwnt11 is a target of Xenopus Brachyury: regulation of gastrulation movements via Dishevelled, but not through the canonical Wnt pathway. *Development* 127, 2227-2238.

Takada,S., Stark,K.L., Shea,M.J., Vassileva,G., McMahon,J.A., and McMahon,A.P. (1994). Wnt-3a regulates somite and tailbud formation in the mouse embryo. *Genes Dev.* 8, 174-189.

Tam,P.P. and Tan,S.S. (1992). The somitogenetic potential of cells in the primitive streak and the tail bud of the organogenesis-stage mouse embryo. *Development* 115, 703-715.

Tanegashima,K., Zhao,H., and Dawid,I.B. (2008). WGEF activates Rho in the Wnt-PCP pathway and controls convergent extension in Xenopus gastrulation. *EMBO J.* 27, 606-617.

Tang,A.T., Campbell,W.B., and Nithipatikom,K. (2012). ROCK1 feedback regulation of the upstream small GTPase RhoA. *Cell Signal.* 24, 1375-1380.

ten Klooster,J.P., Jaffer,Z.M., Chernoff,J., and Hordijk,P.L. (2006). Targeting and activation of Rac1 are mediated by the exchange factor beta-Pix. *J. Cell Biol.* 172, 759-769.

Theveneau,E., Marchant,L., Kuriyama,S., Gull,M., Moepps,B., Parsons,M., and Mayor,R. (2010). Collective chemotaxis requires contact-dependent cell polarity. *Dev. Cell* 19, 39-53.

Theveneau,E. and Mayor,R. (2012). Neural crest delamination and migration: from epithelium-to-mesenchyme transition to collective cell migration. *Dev. Biol.* 366, 34-54.

Thiesen,S., Kubart,S., Ropers,H.H., and Nothwang,H.G. (2000). Isolation of two novel human RhoGEFs, ARHGEF3 and ARHGEF4, in 3p13-21 and 2q22. *Biochem. Biophys. Res. Commun.* 273, 364-369.

Thomas,P.S., Kim,J., Nunez,S., Glogauer,M., and Kaartinen,V. (2010). Neural crest cell-specific deletion of Rac1 results in defective cell-matrix interactions and severe craniofacial and cardiovascular malformations. *Dev. Biol.* 340, 613-625.

Thompson,D.N. (2009). Postnatal management and outcome for neural tube defects including spina bifida and encephalocoeles. *Prenat. Diagn.* 29, 412-419.

Ting,S.B., Caddy,J., Hislop,N., Wilanowski,T., Auden,A., Zhao,L.L., Ellis,S., Kaur,P., Uchida,Y., Holleran,W.M. et al. (2005). A homolog of Drosophila grainy head is essential for epidermal integrity in mice. *Science* 308, 411-413.

Ting,S.B., Wilanowski,T., Auden,A., Hall,M., Voss,A.K., Thomas,T., Parekh,V., Cunningham,J.M., and Jane,S.M. (2003a). Inositol- and folate-resistant neural tube defects in mice lacking the epithelial-specific factor Grhl-3. *Nat. Med.* 9, 1513-1519.

Ting,S.B., Wilanowski,T., Cerruti,L., Zhao,L.L., Cunningham,J.M., and Jane,S.M. (2003b). The identification and characterization of human Sister-of-Mammalian Grainyhead (SOM) expands the grainyhead-like family of developmental transcription factors. *Biochem. J.* 370, 953-962.

Torban,E., Patenaude,A.M., Leclerc,S., Rakowiecki,S., Gauthier,S., Andelfinger,G., Epstein,D.J., and Gros,P. (2008). Genetic interaction between members of the Vangl family causes neural tube defects in mice. *Proc. Natl. Acad. Sci. U. S. A* 105, 3449-3454.

Torban,E., Wang,H.J., Groulx,N., and Gros,P. (2004). Independent mutations in mouse Vangl2 that cause neural tube defects in looptail mice impair interaction with members of the Dishevelled family. *J. Biol. Chem.* 279, 52703-52713.

Torban,E., Wang,H.J., Patenaude,A.M., Riccomagno,M., Daniels,E., Epstein,D., and Gros,P. (2007). Tissue, cellular and sub-cellular localization of the Vangl2 protein during embryonic development: effect of the Lp mutation. *Gene Expr. Patterns.* 7, 346-354.

Trainor,P.A. (2005). Specification of neural crest cell formation and migration in mouse embryos. *Semin. Cell Dev. Biol.* 16, 683-693.

Trainor,P.A., Sobieszczuk,D., Wilkinson,D., and Krumlauf,R. (2002). Signalling between the hindbrain and paraxial tissues dictates neural crest migration pathways. *Development* 129, 433-442.

Ueno,N. and Greene,N.D. (2003). Planar cell polarity genes and neural tube closure. *Birth Defects Res. C. Embryo. Today* 69, 318-324.

Ulloa,F. and Briscoe,J. (2007). Morphogens and the control of cell proliferation and patterning in the spinal cord. *Cell Cycle* 6, 2640-2649.

Van Straaten,H.W. and Copp,A.J. (2001). Curly tail: a 50-year history of the mouse spina bifida model. *Anat. Embryol. (Berl)* 203, 225-237.

Van Straaten,H.W., Hekking,J.W., Consten,C., and Copp,A.J. (1993). Intrinsic and extrinsic factors in the mechanism of neurulation: effect of curvature of the body axis on closure of the posterior neuropore. *Development* 117, 1163-1172.

Van Straaten,H.W., Hekking,J.W., Copp,A.J., and Bernfield,M. (1992). Deceleration and acceleration in the rate of posterior neuropore closure during neurulation in the curly tail (ct) mouse embryo. *Anat. Embryol. (Berl)* 185, 169-174.

Vandenberg,A.L. and Sassoon,D.A. (2009). Non-canonical Wnt signaling regulates cell polarity in female reproductive tract development via van gogh-like 2. *Development* 136, 1559-1570.

Wallingford,J.B. and Harland,R.M. (2001). Xenopus Dishevelled signaling regulates both neural and mesodermal convergent extension: parallel forces elongating the body axis. *Development* 128, 2581-2592.

Wallingford,J.B. and Harland,R.M. (2002). Neural tube closure requires Dishevelled-dependent convergent extension of the midline. *Development* 129, 5815-5825.

Wallingford,J.B. and Mitchell,B. (2011). Strange as it may seem: the many links between Wnt signaling, planar cell polarity, and cilia. *Genes Dev.* 25, 201-213.

Wallingford,J.B., Rowning,B.A., Vogeli,K.M., Rothbacher,U., Fraser,S.E., and Harland,R.M. (2000). Dishevelled controls cell polarity during Xenopus gastrulation. *Nature* 405, 81-85.

Wang,J., Hamblet,N.S., Mark,S., Dickinson,M.E., Brinkman,B.C., Segil,N., Fraser,S.E., Chen,P., Wallingford,J.B., and Wynshaw-Boris,A. (2006a). Dishevelled genes mediate a conserved mammalian PCP pathway to regulate convergent extension during neurulation. *Development* 133, 1767-1778.

Wang,J., Mark,S., Zhang,X., Qian,D., Yoo,S.J., Radde-Gallwitz,K., Zhang,Y., Lin,X., Collazo,A., Wynshaw-Boris,A. et al. (2005). Regulation of polarized extension and planar cell polarity in the cochlea by the vertebrate PCP pathway. *Nat. Genet.* 37, 980-985.

Wang,Y., Guo,N., and Nathans,J. (2006b). The role of Frizzled3 and Frizzled6 in neural tube closure and in the planar polarity of inner-ear sensory hair cells. *J. Neurosci.* 26, 2147-2156.

Wang,Y. and Nathans,J. (2007). Tissue/planar cell polarity in vertebrates: new insights and new questions. *Development* 134, 647-658.

Wang,Y., Suzuki,H., Yokoo,T., Tada-Iida,K., Kihara,R., Miura,M., Watanabe,K., Sone,H., Shimano,H., Toyoshima,H. et al. (2004). WGEF is a novel RhoGEF expressed in intestine, liver, heart, and kidney. *Biochem. Biophys. Res. Commun.* 324, 1053-1058.

Wansleeben,C., Feitsma,H., Montcouquiol,M., Kroon,C., Cuppen,E., and Meijlink,F. (2010). Planar cell polarity defects and defective Vangl2 trafficking in mutants for the COPII gene Sec24b. *Development* 137, 1067-1073.

Wansleeben,C. and Meijlink,F. (2011). The planar cell polarity pathway in vertebrate development. *Dev. Dyn.* 240, 616-626.

Waterman,R.E. (1976). Topographical changes along the neural fold associated with neurulation in the hamster and mouse. *Am. J. Anat.* 146, 151-171.

Webb,T.S. (2010). Optimizing health care for adults with spina bifida. *Dev. Disabil. Res. Rev.* 16, 76-81.

Weil,M., Jacobson,M.D., and Raff,M.C. (1997). Is programmed cell death required for neural tube closure? *Curr. Biol.* 7, 281-284.

Weinstein,D.C., Altaba,A., Chen,W.S., Hoodless,P., Prezioso,V.R., Jessell,T.M., and Darnell,J.E., Jr. (1994). The winged-helix transcription factor HNF-3 beta is required for notochord development in the mouse embryo. *Cell* 78, 575-588.

Werth,M., Walentin,K., Aue,A., Schonheit,J., Wuebken,A., Pode-Shakked,N., Vilianovitch,L., Erdmann,B., Dekel,B., Bader,M. et al. (2010). The transcription factor grainyhead-like 2 regulates the molecular composition of the epithelial apical junctional complex. *Development* 137, 3835-3845.

Wheelock,M.J., Shintani,Y., Maeda,M., Fukumoto,Y., and Johnson,K.R. (2008). Cadherin switching. *J. Cell Sci.* 121, 727-735.

Wilanowski,T., Caddy,J., Ting,S.B., Hislop,N.R., Cerruti,L., Auden,A., Zhao,L.L., Asquith,S., Ellis,S., Sinclair,R. et al. (2008). Perturbed desmosomal cadherin expression in grainy head-like 1-null mice. *EMBO J.* 27, 886-897.

Wilanowski,T., Tuckfield,A., Cerruti,L., O'Connell,S., Saint,R., Parekh,V., Tao,J., Cunningham,J.M., and Jane,S.M. (2002). A highly conserved novel family of mammalian developmental transcription factors related to Drosophila grainyhead. *Mech. Dev.* 114, 37-50.

Wilkinson,D.G., Bhatt,S., and Herrmann,B.G. (1990). Expression pattern of the mouse T gene and its role in mesoderm formation. *Nature* 343, 657-659.

Wilson,V. and Beddington,R.S. (1996). Cell fate and morphogenetic movement in the late mouse primitive streak. *Mech. Dev.* 55, 79-89.

Wilson,V., Olivera-Martinez,I., and Storey,K.G. (2009). Stem cells, signals and vertebrate body axis extension. *Development* 136, 1591-1604.

Wlodarczyk,B.J., Tang,L.S., Triplett,A., Aleman,F., and Finnell,R.H. (2006). Spontaneous neural tube defects in splotch mice supplemented with selected micronutrients. *Toxicol. Appl. Pharmacol.* 213, 55-63.

Wu,M., Chen,D.F., Sasaoka,T., and Tonegawa,S. (1996). Neural tube defects and abnormal brain development in F52-deficient mice. *Proc. Natl. Acad. Sci. U. S. A* 93, 2110-2115.

Wurdak,H., Ittner,L.M., and Sommer,L. (2006). DiGeorge syndrome and pharyngeal apparatus development. *Bioessays* 28, 1078-1086.

Yamaguchi,T.P., Bradley,A., McMahon,A.P., and Jones,S. (1999). A Wnt5a pathway underlies outgrowth of multiple structures in the vertebrate embryo. *Development* 126, 1211-1223.

Yamaguchi,Y., Shinotsuka,N., Nonomura,K., Takemoto,K., Kuida,K., Yosida,H., and Miura,M. (2011). Live imaging of apoptosis in a novel transgenic mouse highlights its role in neural tube closure. *J. Cell Biol.* 195, 1047-1060.

Yamamoto,S., Nishimura,O., Misaki,K., Nishita,M., Minami,Y., Yonemura,S., Tarui,H., and Sasaki,H. (2008). Cthrc1 selectively activates the planar cell polarity pathway of Wnt signaling by stabilizing the Wnt-receptor complex. *Dev. Cell* 15, 23-36.

Yamanaka,H., Moriguchi,T., Masuyama,N., Kusakabe,M., Hanafusa,H., Takada,R., Takada,S., and Nishida,E. (2002). JNK functions in the non-canonical Wnt pathway to regulate convergent extension movements in vertebrates. *EMBO Rep.* 3, 69-75.

Yamanaka,Y., Tamplin,O.J., Beckers,A., Gossler,A., and Rossant,J. (2007). Live imaging and genetic analysis of mouse notochord formation reveals regional morphogenetic mechanisms. *Dev. Cell* 13, 884-896.

Yang,Y. (2012). Wnt signaling in development and disease. *Cell Biosci.* 2, 14.

Yates,L.L., Papakrivopoulou,J., Long,D.A., Goggolidou,P., Connolly,J.O., Woolf,A.S., and Dean,C.H. (2010a). The planar cell polarity gene Vangl2 is required for mammalian kidney-branching morphogenesis and glomerular maturation. *Hum. Mol. Genet.* 19, 4663-4676.

Yates,L.L., Schnatwinkel,C., Hazelwood,L., Chessum,L., Paudyal,A., Hilton,H., Romero,M.R., Wilde,J., Bogani,D., Sanderson,J. et al. (2013). Scribble is required for normal epithelial cell-cell contacts and lumen morphogenesis in the mammalian lung. *Dev. Biol.* 373, 267-280.

Yates,L.L., Schnatwinkel,C., Murdoch,J.N., Bogani,D., Formstone,C.J., Townsend,S., Greenfield,A., Niswander,L.A., and Dean,C.H. (2010b). The PCP genes Celsr1 and Vangl2 are required for normal lung branching morphogenesis. *Hum. Mol. Genet.* 19, 2251-2267.

Ybot-Gonzalez,P., Cogram,P., Gerrelli,D., and Copp,A.J. (2002). Sonic hedgehog and the molecular regulation of mouse neural tube closure. *Development* 129, 2507-2517.

Ybot-Gonzalez,P. and Copp,A.J. (1999). Bending of the neural plate during mouse spinal neurulation is independent of actin microfilaments. *Dev. Dyn.* 215, 273-283.

Ybot-Gonzalez,P., Gaston-Massuet,C., Girdler,G., Klingensmith,J., Arkell,R., Greene,N.D., and Copp,A.J. (2007a). Neural plate morphogenesis during mouse neurulation is regulated by antagonism of Bmp signalling. *Development* 134, 3203-3211.

Ybot-Gonzalez,P., Savery,D., Gerrelli,D., Signore,M., Mitchell,C.E., Faux,C.H., Greene,N.D., and Copp,A.J. (2007b). Convergent extension, planar-cell-polarity signalling and initiation of mouse neural tube closure. *Development* 134, 789-799.

Yen,W.W., Williams,M., Periasamy,A., Conaway,M., Burdsal,C., Keller,R., Lu,X., and Sutherland,A. (2009). PTK7 is essential for polarized cell motility and convergent extension during mouse gastrulation. *Development* 136, 2039-2048.

Yin,C., Kiskowski,M., Pouille,P.A., Farge,E., and Solnica-Krezel,L. (2008). Cooperation of polarized cell intercalations drives convergence and extension of presomitic mesoderm during zebrafish gastrulation. *J. Cell Biol.* 180, 221-232.

Yin,H., Copley,C.O., Goodrich,L.V., and Deans,M.R. (2012). Comparison of phenotypes between different vangl2 mutants demonstrates dominant effects of the Looptail mutation during hair cell development. *PLoS. One.* 7, e31988.

Yu,H., Smallwood,P.M., Wang,Y., Vidaltamayo,R., Reed,R., and Nathans,J. (2010). Frizzled 1 and frizzled 2 genes function in palate, ventricular septum and neural tube closure: general implications for tissue fusion processes. *Development* 137, 3707-3717.

Yu,H.H. and Moens,C.B. (2005). Semaphorin signaling guides cranial neural crest cell migration in zebrafish. *Dev. Biol.* 280, 373-385.

Yu,Z., Bhandari,A., Mannik,J., Pham,T., Xu,X., and Andersen,B. (2008). Grainyhead-like factor Get1/Grhl3 regulates formation of the epidermal leading edge during eyelid closure. *Dev. Biol.* 319, 56-67.

Yu,Z., Lin,K.K., Bhandari,A., Spencer,J.A., Xu,X., Wang,N., Lu,Z., Gill,G.N., Roop,D.R., Wertz,P. et al. (2006). The Grainyhead-like epithelial transactivator Get-1/Grhl3 regulates epidermal terminal differentiation and interacts functionally with LMO4. *Dev. Biol.* 299, 122-136.

Yu,Z., Mannik,J., Soto,A., Lin,K.K., and Andersen,B. (2009). The epidermal differentiation-associated Grainyhead gene Get1/Grhl3 also regulates urothelial differentiation. *EMBO J.* 28, 1890-1903.

Zeng,H., Hoover,A.N., and Liu,A. (2010). PCP effector gene Inturned is an important regulator of cilia formation and embryonic development in mammals. *Dev. Biol.* 339, 418-428.

Zohn,I.E. (2012). Mouse as a model for multifactorial inheritance of neural tube defects. *Birth Defects Res. C. Embryo. Today* 96, 193-205.